



Doctoral thesis

Micromechanical analysis of blended cement-based composites

carried out for the purpose of obtaining the academic double degree of a “Doctor of Philosophy” (Ph.D.) from CTU in Prague, Faculty of Civil Engineering, and “Doktor der technischen Wissenschaften” (Dr. techn.) from TU Wien – Vienna University of Technology, Department of Civil Engineering

Dissertation

Mikromechanische Analyse von Kompositmaterialien aus Mischzementen

ausgeführt zum Zwecke der Erlangung des akademischen Doppelgrades eines “Doctor of Philosophy” (Ph.D.) eingereicht an der Tschechischen Technischen Universität in Prag, Fakultät für Bauingenieurwesen, und eines Doktors der technischen Wissenschaft eingereicht an der Technischen Universität Wien, Fakultät für Bauingenieurwesen

Ing. Michal Hlobil

Matrikelnummer: 1229375

Supervisor: doc. Ing. Vít Šmilauer, Ph.D.

Department of Mechanics, Czech Technical University in Prague

Supervisor: Assoc. Prof. Dipl.-Ing. Dr. techn. Bernhard Pichler

Institut für Mechanik der Werkstoffe und Strukturen, Technische Universität
Wien

Acknowledgment

It has been a great privilege to work under the dual supervision of both doc. Ing. Vít Šmilauer, Ph.D. during my stay in Prague as well as Assoc. Prof. Dipl.-Ing. Dr. techn. Bernhard Pichler during my stay in Vienna. I thank doc. Šmilauer for his skilled guidance, sharing his knowledge on numerical mechanics and for his tremendous support throughout my studies. I am grateful to Assoc. Prof. Pichler for his continuing encouragement, for introducing me into continuum micromechanics and for his patience and advices that helped me a lot in my personal development.

I would like to acknowledge the support from the industrial-academic nanoscience research network for sustainable cement and concrete ‘NANOCEM’ (<http://www.nanocem.org>), provided within the framework of Core Project 10 entitled “Micromechanical analysis of blended cement-based composites”, which enabled my employment at the Czech Technical University in Prague as well as my stays at the Lafarge Centre de Recherche in Lyon and at TU Wien – Vienna University of Technology. I also gratefully acknowledge CTU grants SGS15/030/OHK1/1T/11 and SGS16/037/OHK1/1T/11.

I wish to thank to two industrial advisors from NANOCEM, namely to Klaus-Alexander Rieder from GCPAP and to Gilles Chanvillard (in memoriam) from LafargeHolcim, who supervised my project, offered advice and contributed to a fruitful project development in an encouraging atmosphere. I appreciated stimulating discussions on NANOCEM events, which further helped me to focus on questions and topics, which are important for the cement industry.

I cannot forget to thank the team at Lafarge Centre de Recherche for their support during my internship, namely Pipat Termkhajornkit for his patience in introducing me into microstructural phase assemblages of cement pastes, Fabienne Begaud for her help with mechanical testing, QuocHuy Vu for his advice and Svatopluk Dobruský for help, not only at the research center.

The team at TU Wien both at Karlsplatz as well as in the Rella Halle deserves my thanks for creating a stimulating atmosphere and helpful discussions. Namely I wish to thank to Markus Königsberger for his help and support with continuum micromechanics and to Wolfgang Dörner for his help with mechanical testing. Thanks to the staff in the department of Mechanics at the Czech Technical Uni-

versity in Prague for creating a calm and friendly atmosphere, especially Petr Hlaváček, Wilson Ricardo Leal da Silva and Fernando Suarez for discussions not only on cement or Python.

For that constant help I wish to thank my parents and my sister. And very special thank goes to my wife Adéla for her strong support not only during my studies.

Abstract

In order to reduce CO₂ emissions associated with the production of building materials, the cement and concrete industry has developed new binders by blending ordinary Portland cement with supplementary cementitious materials such as the industrial waste products blast furnace slag and fly ash, and/or with finely ground inert materials such as limestone and quartz. This is setting the scene for the present thesis which is motivated by the fact that the new binders exhibit different hardening characteristics compared to their predecessors that were produced with ordinary Portland cement alone. In order to improve the predictability of properties of blended cementitious materials, a combined experimental-computational approach is used.

In the *experimental part*, a comprehensive test database is elaborated by combining state-of-the-art microstructural characterization techniques and mechanical testing. Microstructural characterization combines methods including thermogravimetric analysis, X-ray diffraction with Rietveld analysis, and scanning electron microscopy, in order to determine the microstructural phase assemblages of the initial raw products as well as 1, 3, 7, 28, and 91 days after mixing with water. This allows for resolving phase volume evolutions point wisely. Mechanical testing, in turn, includes characterization of stiffness and strength. The early-age evolution of static unloading modulus is determined with a test protocol including cyclic loading-unloading tests which are hourly repeated from 24 hours after production up to material ages of 8 days. Dynamic stiffness is determined based on measurements of ultrasonic pulse velocities of longitudinal and shear waves, evaluated on the basis of elastic wave propagation in isotropic media. The uniaxial compressive strength evolution is determined both on pastes and mortars, crushed 1, 3, 7, 28, and 91 days after production. The tensile splitting strength, in turn, is determined 1, 3, 28, and 91 days after production. All the measured data is then stored in a newly established database “CemBase” along with additional data collected from the literature. At the end of this thesis “CemBase” contained information on 399 entries out of which approx. 20 % were measured during the experimental campaign and approx. 80 % were collected from available literature.

The *computational part* focuses on multiscale strength homogenization in the

frameworks of two complementary modeling methods: multiscale Finite Element-based homogenization and continuum micromechanics. Finite Element-based homogenization uses nonlinear fracture mechanics with an isotropic damage model to establish a link between nanoscopic calcium-silicate-hydrates and the uniaxial compressive strength of cement pastes, emphasizing the nonuniform distribution of C-S-H around clinker grains. The model focuses on the special role of C-S-H as the main material phase contributing to the macroscopic mechanical properties as well as introduces the C-S-H/space ratio as the main microstructural descriptor. In addition, the model identifies key factors influencing the compressive strength of cement pastes. Continuum micromechanics, in turn, is used for elasto-brittle modeling of both compressive and tensile strength. The method accounts for key features of cementitious microstructures in terms of their hierarchical organization, quasi-homogeneous material phases, their volume fractions, characteristic shapes, and mutual interaction. The compressive strength model considers that the macroscopic strength is reached once stress peaks in micron-sized needle-shaped hydrates reach their strength. The latter is described based on a Mohr-Coulomb failure criterion including the angle of internal friction and the cohesion of low-density calcium-silicate-hydrates, as quantified by limit state analysis of nanoindentation tests. The model accounts for stress concentrations in the immediate vicinity of sand grains, and it uses strain energy-related stress averages for the scale transition from cement paste down to needle-shaped hydrates. It is found that microfillers effectively reinforce the hydrate foam, and that hydration of supplementary cementitious materials has a strengthening effect which is not only related to the increase of hydrate volume and the corresponding decrease of capillary porosity, but also to an increase of the cohesion of low-density calcium-silicate-hydrates. The tensile strength model, in turn, is based on up-scaling elasticity and fracture energy from nanoscopic calcium-silicate-hydrates – as quantified by molecular dynamics simulations – all the way up to the uniaxial tensile strength of mortars and concretes. The model considers that cementitious materials suffer from pre-existing cracks which are only somewhat smaller than the maximum aggregate size, and that the tensile strength of the material is reached once these cracks start to propagate. Summarizing, the three developed models define a new state-of-the-art regarding multiscale homogenization of strength properties of cementitious materials.

Abstrakt

Za účelem snížení emisí CO₂ vznikajících při výrobě betonu přistoupil cementářský průmysl k vývinu alternativních pojiv, které vzniknou smícháním Portlandského cementu s doplňkovými cementovými příměsmi jako např. struska a popílek, případně dalšími inertními materiály jako např. mikromletý křemen anebo vápenec. Motivací pro tuto disertační práci byla skutečnost, že směsné cementy vykazují rozdílné vlastnosti v porovnání s Portlandským cementem. Za účelem zlepšení předpovědi výsledných vlastností kompozitů na bázi směsných cementů je v této práci použit komplementární, experimentálně-modelovací přístup.

První část disertační práce se zabývá experimenty a je zde podrobně popsáno vytvoření obsáhlé databáze výsledků získaných kombinací metod určených pro charakterizaci mikrostruktury cementových past a vývoj jejich mechanických vlastností. Charakterizace mikrostruktury byla provedena v 1, 3, 7, 28 a 91 dnech po smíchání cementu s vodou za použití kombinace termické analýzy, RTG difrakce a rastrovacího elektronového mikroskopu s detektorem odražených elektronů. Výstupem byl vývoj objemového zastoupení materiálových fází pro jednotlivé cementové pasty v čase. Následně byl zdokumentován vývoj mechanických vlastností cementových past od okamžiku odbednění vzorku po 24 hodinách až do stáří 91 dnů. Statické měření vývoje modulu pružnosti bylo prováděno každou hodinu během prvních osmi dnů stáří vzorku. Dynamické měření modulu pružnosti bylo prováděno souběžně se statickým měřením podle metodiky vyhodnocení rychlosti šíření ultrazvukové vlny v isotropním materiálu. Vývoj jednoosé tlakové pevnosti byl změřen na vzorcích cementové pasty a malty v časech 1, 3, 7, 28 a 91 dnů. Vývoj tahové pevnosti cementových past byl změřen v časech 1, 3, 28 a 91 dnů. Nově byla založena databáze “CemBase” za účelem shromáždění výsledků zkoušení cementových past nejen v rámci této práce, ale zejména z dostupné literatury. Databáze “CemBase” obsahovala ke dni odevzdání této práce 399 položek, přičemž přibližně 20 % dat bylo naměřeno v rámci této práce a zbývajících přibližně 80 % dat pochází z literatury.

V druhé části disertační práce je popsáno modelování vývoje pevnosti cementových past za pomoci dvou komplementárních přístupů: pomocí metody konečných prvků a pomocí mikromechaniky kontinua. Při homogenizaci metodou konečných prvků je použit materiálový model založený na nelineární lomové mechanice se zohledněním isotropního poškození. Tento materiálový model je použit

při modelování nanoskopických “vápenato-křemičitých hydrátů” (C-S-H) za účelem predikce výsledné jednoosé tlakové pevnosti na úrovni makroskopické cementové pasty s přihlédnutím k nerovnoměrné distribuci C-S-H v okolí slínekových zrn. Model klade důraz na C-S-H jakožto základní stavební kámen mikrostruktury cementových past a nově zavádí popis mikrostruktury za pomoci C-S-H a kapilární porozity. Současně také analyzuje klíčové faktory, které ovlivňují tlakovou pevnost cementových past. Mikromechanika kontinua je použita na predikci jak tlakové, tak i tahové pevnosti. Metoda zohledňuje pět charakteristických vlastností mikrostruktur cementových past: jejich hierarchickou strukturu, jednotlivé materiálové fáze včetně jejich objemového zastoupení, charakteristických tvarů a vzájemné interakce. Model pro tlakovou pevnost je založen na předpokladu, že k porušení cementové pasty dojde v okamžiku dosažení limitního napětí v rámci mikroskopických hydrátů. To je popsáno Mohr-Coulombovým zákonem porušení se zohledněním úhlu vnitřního tření a koheze C-S-H, obou určených za pomoci limitní analýzy u nanoindentačních měření. Model zahrnuje vliv koncentrace napětí v okolí pískových zrn na úrovni malty a využívá průměrování napětí s ohledem na zachování energie pružné deformace mezi úrovní cementové pasty a jednotlivými hydráty. Použití příměsí vede k vyztužení mikrostruktury na úrovni “hydrátové pěny”. Reakce doplňkových cementových příměsí (struska, popílek) má posilující účinek s ohledem na nárůst tlakové pevnosti cementové pasty nejen z důvodu produkce dalšího C-S-H a snížení kapilární porozity, ale také díky zvýšení koheze C-S-H. Model pro tahovou pevnost je založen na škálování pružnosti a lomové energie od nanoskopických hydrátů až po maltu nebo beton na makroskopické úrovni. Základním předpokladem je existence sítě trhlin, které jsou menší než maximální velikost kameniva, a také skutečnost, že tahové pevnosti materiálu je dosaženo v okamžiku, kdy dojde k propagaci trhlin. Celkem byly v rámci této disertační práce sestaveny tři víceúrovňové modely, které otevírají cestu k předpovědi pevností cementových kompozitů.

Contents

Introduction	1
Research objectives	4
Methodology and key results	5
1 Experimental campaign	11
1.1 Material description	11
1.1.1 Ordinary Portland cement	11
1.1.2 Quartz	12
1.1.3 Limestone	13
1.1.4 Blast furnace slag	13
1.1.5 Fly ash	16
1.2 Mix design	18
1.3 Microstructural characterization	19
1.4 Mechanical testing	19
1.4.1 Production of samples	21
1.4.2 Elasticity	22
1.4.3 Compressive strength	29
1.4.4 Splitting tensile strength	32
2 Unloading-Based Stiffness Characterisation of Cement Pastes During the Second, Third and Fourth Day After Production	35
2.1 Introduction	35
2.2 Pure and fly ash-blended cement pastes	38
2.3 Testing overview	39
2.4 Unloading in uniaxial compression	39
2.4.1 Test setup	40

2.4.2	Prescribed loading history	43
2.4.3	Data acquisition	46
2.4.4	Minimization of loading eccentricity	46
2.4.5	Test evaluation and results	48
2.5	Isothermal Differential Calorimetry	49
2.6	Ultrasonics experiments	52
2.7	Discussion	54
2.7.1	Significance for multiscale modeling of concrete containing ITZs	55
2.7.2	Trade-off challenges regarding test design	55
2.7.3	Hydration-induced temperature fluctuations inside young cement paste specimens	57
2.7.4	Extrapolation to the liquid-to-solid transition	60
2.8	Conclusions	61
3	Micromechanical multiscale fracture model for compressive strength of blended cement pastes	63
3.1	Introduction	63
3.2	Finite element analysis	65
3.2.1	Damage material model and its implementation	65
3.2.2	Boundary conditions and intrinsic properties	70
3.3	Multiscale model for cement pastes	71
3.4	Results and discussion	75
3.4.1	Level 0 - C-S-H	76
3.4.2	Level 1 - C-S-H foam	78
3.4.3	Level 2 - cement paste	80
3.4.4	Level 3 - cement paste with air	81
3.4.5	Discussion on FE mesh representations	84
3.4.6	Calibration of $f_{t, glob}$	84
3.4.7	Validation of elastic modulus	87
3.4.8	Example #1 - Portland cement paste w/c=0.51	88
3.4.9	Example #2 - Portland cement paste w/c=0.247	88
3.4.10	Example #3 - slag-blended cement paste w/b=0.53	89
3.4.11	Example #4 - fly ash-blended cement paste w/b=0.60	90
3.4.12	Comparison with Powers' approach	91
3.4.13	Impact of C-S-H fracture energy	92

3.4.14	Impact of void size on strength	93
3.4.15	Global sensitivity analysis by scatter plots	94
3.4.16	Local sensitivity analysis	95
3.5	Conclusions	96
4	Hydration-driven evolution of compressive strength of OPC and blended cementitious materials: microstructural characterization, strength testing, and multiscale modeling	99
4.1	Introduction	99
4.2	Elasto-brittle multiscale strength modeling of ordinary Portland cement pastes and mortars	103
4.2.1	Micromechanical representation	103
4.2.2	Volume fractions and mechanical constants of material phases	104
4.2.3	Concentration of loading imposed on RVEs of mortar into cement paste: quantification of stress peaks	106
4.2.4	Concentration of loading imposed on RVEs of cement paste into hydrates	109
4.2.5	Identification of location and of orientation of most heavily loaded hydrate needles	112
4.2.6	Model validation on OPC pastes	114
4.2.7	Model validation on OPC mortars	116
4.2.8	Location and orientation of most heavily loaded hydrate needles	118
4.3	Strength evolution of blended cement mortars: microstructural characterization, strength testing, and multiscale modeling	119
4.3.1	Microstructural characterization: phase volume evolutions	120
4.3.2	Uniaxial compressive strength testing of blended mortars .	124
4.3.3	Revisiting strength homogenization of OPC mortar based on microstructural characterization results	125
4.3.4	Strength homogenization of inert filler-blended mortars: consideration of quartz and limestone as reinforcements of the hydrate foam	126
4.3.5	Strength homogenization of SCM-blended mortars: the strength-increasing effects of slag and fly ash hydration . .	128
4.4	Discussion	132
4.5	Conclusions	133

5	Molecular-to-macro upscaling of concrete fracture	143
5.1	Introduction	143
5.2	Damage propagation driving force \mathcal{G}_{df} , as derived from molecular-to-macro elasticity homogenization	145
5.3	Damage resistance G_{res} , as determined from C-S-H-to-concrete fracture energy homogenization	152
5.3.1	Relation between damage resistance and fracture energy of mortar/concrete	152
5.3.2	Fracture energy upscaling based on a hierarchical covered spheres model	153
5.4	Damage mechanics and size effect of mortars and concretes subjected to tension	158
5.4.1	Damage propagation criterion under macroscopic uniaxial tension	158
5.4.2	Dimensionless damage evolution law	159
5.4.3	Size effect of concrete tensile strength	160
5.4.4	Direct-tension size effect study on dog bone-shaped concrete specimens carried out by van Mier and van Vliet	161
5.4.5	Identification of intercept quantity $(a_{ini,RVE}/d_{max})$	162
5.4.6	Identification of slope quantity C	165
5.5	Model validation	168
5.5.1	Three-point-bending size effect study on notched mortar prisms, performed by [92]	168
5.5.2	Finite Element model	169
5.5.3	Finite Element model input	171
5.5.4	Sequential elastic FE analyses technique with incremental increase of damage	172
5.5.5	Comparison of model predictions with experimental data	173
5.6	Discussion	174
5.7	Conclusions	176
	Conclusions and further research	183

List of Figures

1.1	SEM micrograph showing the surface texture of a sand-size EAF slag particle, magnified 1200×, source: www.hindawi.com/journals/ace/2011/463638/fig11/	14
1.2	SEM pictures of classes F and C fly ash particles, source: [146]	16
1.3	Phase assemblage of paste compositions plotted as volume fractions with respect to the degree of hydration of OPC. Data points at 1 day for OPC (see Fig. 1.3a) and quartz-blended paste (see Fig. 1.3b) are omitted due to measurement uncertainties.	20
1.4	Test configuration showing paste sample wrapped in a food preservation foil together with five LVDTs evenly spaced around the sample and held in position by Plexiglas rings which were clamped onto the sample (left) and zoom showing the steel cylinder with bottleneck (right)	24
1.5	Typical loading cycle used to assess unloading modulus of cement paste.	25
1.6	The evolution of unloading modulus for all paste compositions as a function of time	26
1.7	Evolution of elastic modulus as a function of time, during the first 7 days (left) and up to 91 days (right)	28
1.8	Comparison of elastic moduli during 7 days for OPC (black) and slag-blended paste (red)	29
1.9	Compressive strength test setup showing steel cylinders with bottlenecks and two layers of Teflon separating them from the sample	31
1.10	Evolution of compressive strength of all paste compositions at 1, 3, 7, 28, and 91 days.	32
1.11	Splitting tensile strength testing	33

1.12	Evolution of splitting tensile strength of investigated paste compositions at 1, 3, 28, and 91 days (left) and the evolution of compressive-to-splitting strength until 91 days (right).	34
2.1	Symmetric upper half of the test setup consisting of a metal cylinder with a bottleneck, the cylindrical specimen, and a plexiglass ring holding five LVDTs which are evenly distributed around the perimeter of the specimen	41
2.2	Threedimensional Finite Element simulations of the chosen loading setup including the bottlenecked metal cylinder and the cement paste specimen: (a) distribution of axial normal stresses, and (b) distribution of shear stresses, indicating a uniform stress field in the central measurement region of the specimens; F = absolute value of applied force, A = cross-sectional area of cylindrical cement paste sample, F/A = absolute value of nominal normal stress in cylindrical cement paste sample	42
2.3	Loading history repeated every hour, essentially consisting of three compressive loading-unloading cycles between 0.10 kN and 0.40 kN	44
2.4	Detail of the unloading event illustrated in Fig. 2.3: the desired unloading speed amounting to 1 kN/s is realized in the central part	44
2.5	Typical measurements of the five LVDTs and their mean values (see circles), after minimization of loading eccentricity	45
2.6	Typical fluctuation of the signals of five LVDTs, captured a few seconds before a loading-unloading cycle began	46
2.7	Model for the central part of the specimen, located between the two plexiglass rings: simply supported beam subjected to a normal force F exhibiting an eccentricity e in the negative z -direction . .	47
2.8	Point-wisely defined stress-strain-diagrams referring to three unloading cycles: the slope of best linear fits to the chains of data points represents the sought unloading modulus; quadratic correlation coefficients between the data points and the linear fits amount to $r^2 = 99.6\%$, to $r^2 = 99.7\%$, and to $r^2 = 99.6\%$, respectively. .	48
2.9	Temporal evolution of unloading modulus of the tested cement pastes; paste 1: circles, paste 2: triangles, fly ash-blended paste 3: crosses	49

2.10	Temporal evolution of heat release rate measured in isothermal differential calorimetry with 10 g solid binder and suitable amounts of distilled water; paste 1: solid lines, paste 2: dashed lines, fly ash-blended paste 3: dash-dotted lines	50
2.11	Temporal evolution of accumulated heat release measured in isothermal differential calorimetry with 10 g solid binder and suitable amounts of distilled water; paste 1: solid lines, paste 2: dashed lines, fly ash-blended paste 3: dash-dotted lines	50
2.12	Temporal evolution of calorimetry-based hydration degree of cement: paste 1: solid line, paste 2: dashed line, fly ash-blended paste 3: dash-dotted line	51
2.13	Unloading modulus as a function of calorimetry-based hydration degree of cement: paste 1: circles, paste 2: triangles, fly ash-blended paste 3: crosses	52
2.14	Ultrasound wave speeds as a function of material age; paste 1: circles, paste 2: triangles, fly ash-blended paste 3: crosses	53
2.15	Dynamic Young's modulus as a function of calorimetry-based hydration degree of cement: paste 1: circles, paste 2: triangles, fly ash-blended paste 3: crosses	54
2.16	Dynamic Poisson's ratio as a function of calorimetry-based hydration degree of cement: paste 1: circles, paste 2: triangles, fly ash-blended paste 3: crosses	54
2.17	Temperature evolution inside cement paste specimens with $w/c = w/s = 0.42$, exposed to a nominal ambient air temperature amounting to 20 °C	57
2.18	Evolution of chemical affinity of cement paste with $w/c = w/s = 0.42$, determined via combination of Eqs. (2.7) and (2.8) as well as (2.12) to (2.15) with the data displayed in Fig. 2.10, as a function of hydration degree determined according to Eq. (2.9)	59
2.19	Comparison of hydration degree evolution obtained (i) for a constant temperature amounting to 20 °C, see solid line, and (ii) for the actual temperature history of Fig. 2.17, see dashed line; determined by means of numerical integration of Eq. (2.12)	59

3.1	Crack evolution during (a) uniaxial tensile stress and (b) compressive stresses. The material contains randomly oriented elliptical voids with negligible area.	66
3.2	Surface at the onset of cracking according to two models under the plane stress condition.	69
3.3	Test of one linear brick element under uniaxial tension / compression with 8 integration points.	69
3.4	Strain localization in shear bands under the uniaxial compression test under plane stress. 20×20 quadrilateral elements (20×20 mm), deformation exaggerated $40 \times$, damage shown for the end of softening.	70
3.5	Four-level hierarchical multiscale model. TEM/SEM images from left to right: Eric Lachowski, S.Y. Hong and F.P. Glasser (http://publish.illinois.edu/concretemicroscopylibrary/transmission-electron-microscopy-tem/); L. Kopecký (CTU in Prague); Paul Stutzman (NIST, http://publish.illinois.edu/concretemicroscopylibrary/magnification-progression-series-1000x/); D. P. Bentz, et al. (Visible Cement Dataset: http://visiblecement.nist.gov)	72
3.6	Spatial distribution of C-S-H between grains for a) early-age pastes and b) for older pastes. A pixel corresponds to $0.95 \mu\text{m}$	73
3.7	The impact of the parameter β on the C-S-H distribution (on level 1) for C-S-H/space ratio $\gamma_{CSH} = 0.7$, UC size $5 \times 5 \times 10 \mu\text{m}$	74
3.8	Compressive strength of pastes with $w/c = 0.45$ measured on cylinders with a diameter of 12.7 mm and height of 25.4 mm [18].	75
3.9	Evolution of the volume fraction of C-S-H _{HD} within C-S-H as a function of capillary porosity and the initial composition from the CEMHYD3D model. C-S-H _{LD} always appears at the beginning of hydration.	77
3.10	UCs for C-S-H _{LD} and C-S-H _{HD} , $20 \times 20 \times 40$ brick elements (UC size $100 \times 100 \times 200$ nm).	78
3.11	Tensile strength of C-S-H depending on the globule packing density. Circles represent results from FE simulations on $20 \times 20 \times 40$ brick elements ($100 \times 100 \times 200$ nm), $\beta = 1.0$ and $G_f = 2 \text{ J/m}^2$	78
3.12	Stress-strain diagram obtained on C-S-H foam using $\gamma_{CSH} = 0.7$, $\beta = 0.6$, and $f_{t,CSH}^0 = 66 \text{ MPa}$	79

3.13	Elastic modulus evolution for level 1 (C-S-H foam), assuming solely C-S-H _{LD} with the globule packing density $\eta_{glob} = \eta_{CSH_{LD}} = 0.63$. Points represent results from FE simulations on UC $20 \times 20 \times 40$ brick elements (UC size $5 \times 5 \times 10 \mu\text{m}$) and the lines are analytical approximations.	79
3.14	Compressive strength evolution for level 1 (C-S-H foam), assuming solely C-S-H _{LD} with the globule packing density $\eta_{glob} = \eta_{CSH_{LD}} = 0.63$ and the corresponding compressive strength $f_{c,CSH}^0 = 528 \text{ MPa}$. Points represent results from FE simulations on UC $20 \times 20 \times 40$ brick elements (UC size $5 \times 5 \times 10 \mu\text{m}$) and lines are analytical approximations.	80
3.15	Elastic modulus evolution for level 2 (cement paste) assuming $E_{foam}^I = 1, 10, 20 \text{ GPa}$. Circles represent results from FE simulations on a 2D microstructure on 100×100 quadrilateral elements (UC size $100 \times 100 \mu\text{m}$) with varying stiffness of the inclusion $E_{incl} = 40, 50, 60, 70, 105, 139.9 \text{ GPa}$	81
3.16	Compressive strength evolution for level 2 (cement paste), assuming $f_{c,foam}^I = 50, 100, 150, 200 \text{ MPa}$. Circles represent results from FE simulations on a 2D microstructure on 100×100 quadrilateral elements (UC size $100 \times 100 \mu\text{m}$) for $f_{c,foam}^I = 50, 100, 150, 200 \text{ GPa}$ with varying stiffness of the inclusion $E_{incl} = 40, 50, 60, 70, 105, 139.9 \text{ GPa}$	82
3.17	Elastic modulus evolution for level 3 (cement paste with air), assuming $E_{CP}^{II} = 20 \text{ GPa}$. Circles represent results from FE simulations on a 2D microstructure on 50×50 quadrilateral elements (UC size $1 \times 1 \text{ mm}$).	82
3.18	Compressive strength evolution for level 3 (cement paste with air). Circles represent results from FE simulations on a 2D microstructure on 50×50 quadrilateral elements (UC size $1 \times 1 \text{ mm}$) for $f_{c,CP}^{II} = 50, 100, 150, 200 \text{ MPa}$	83
3.19	Reduction of cement paste compressive strength with respect to entrapped or entrained air.	83
3.20	Results from FE simulations on level 2 (cement paste) containing 20% of solid inclusions for three mesh sizes.	84
3.21	Validation of model-predicted compressive strength with experiments for $\beta = 1.0$ (a), $\beta = 0.6$ (b), and $\beta = 0.4$ (c).	85

3.22	Impact of the water-to-binder ratio on the C-S-H gradient, represented by the parameter β : (a) dense microstructures with $w/b \leq 0.4$ exhibit a more uniform C-S-H formation signaled by $\beta = 1$, whereas (b) sparse microstructures with $w/b > 0.4$ indicate a higher C-S-H gradient.	87
3.23	Model predicted elastic modulus for $\beta = 1.0$ and $\beta = 0.6$	87
3.24	Volume fractions for OPC paste with $w/b = 0.51$ (a). Experimentally measured compressive strength (b) compared with multiscale model predictions.	88
3.25	Volume fractions for OPC paste with $w/b = 0.247$ (a). Experimentally measured compressive strength (b) compared to model predictions.	89
3.26	Volume fractions for slag-blended paste with $w/b = 0.53$ and the replacement level of 45 % by volume (a). Experimentally measured compressive strength (b) compared to model predictions.	90
3.27	Volume fractions for fly ash-blended paste with $w/b = 0.60$ and the replacement level of 45 % by volume (a). Experimentally measured compressive strength (b) compared to model predictions	91
3.28	Comparison of modeling approaches: Powers' power law fit and proposed model.	92
3.29	Impact of fracture energy of C-S-H on compressive strength of C-S-H foam. FE model from $10 \times 10 \times 20$ brick elements (UC size $5 \times 5 \times 10 \mu\text{m}$) using $\beta = 1.0$	93
3.30	Void size-dependent compressive strength of cement paste obeying the size-effect law.	94
3.31	Important results from global sensitivity analysis; (a) correlation between the compressive strength of C-S-H foam and the CSH/space ratio, and (b) compressive strength of cement paste and volume fraction of air.	95
4.1	Multiscale micromechanics representation of mortar ("material organogram") after [119, 122]; two-dimensional sketches of three-dimensional representative volume elements	104

4.2	Concentration of uniaxial loading imposed on an RVE of mortar, see (4.28), to stress states of cement paste in the immediate vicinity of sand grains: (a) sand grain with global Cartesian base frame $\underline{e}_1, \underline{e}_2, \underline{e}_3$ and local spherical base frame $\underline{e}_r, \underline{e}_\theta, \underline{e}_\phi$; (b) cement paste stress components in the immediate vicinity of the sand-to-cement paste interface \mathcal{I}_{sand}^{cp} as a function of polar angle ψ ; evaluation of (4.13) for $w/c = 0.50$, $s/c = 3.0$, and $\xi_{clin} = 0.50$	108
4.3	Definition of azimuth and zenith angle for identification of the orientation of the needle-shaped hydrates	110
4.4	Model validation on OPC pastes tested at LCR, as for strength data see [122]	115
4.5	Model validation on OPC pastes tested at TUW, as for strength data see [119, 88]	115
4.6	Model validation on OPC pastes tested at EMPA, as for strength data see [157, 175]	116
4.7	Model validation on OPC mortar tested at TUW, as for strength data see [88]	117
4.8	Model validation on OPC mortar tested at LCR in the framework of NANOCEM's Core Project 10	118
4.9	Multiscale failure mechanism in mortar: (a) uniaxially compressed mortar sample, (b) location of failure-inducing stress peaks of cement paste attached to a sand grain, (c) most heavily loaded hydrate needle which is part of the microstructure of cement paste (see also Fig. 4.1), (d) orientation of nanoscopic failure plane inside the most heavily loaded hydrate needle	118
4.10	Phase assemblage of OPC paste: (a) results from microstructural characterization; and (b) subdivision into clinker, hydrates, and capillary pores according to Eq. (4.33)	121
4.11	Phase assemblage of quartz-blended paste: (a) results from microstructural characterization; and (b) subdivision into clinker, hydrates, capillary pores, and quartz according to Eq. (4.34)	121
4.12	Phase assemblage of limestone-blended paste: (a) results from microstructural characterization; and (b) subdivision into clinker, hydrates, capillary pores, and limestone according to Eq. (4.35)	122

4.13	Phase assemblage of slag-blended paste: (a) results from microstructural characterization; and (b) subdivision into clinker, hydrates, capillary pores, and slag according to Eq. (4.36)	122
4.14	Phase assemblage of fly ash-blended paste: (a) results from microstructural characterization; and (b) subdivision into clinker, hydrates, capillary pores, and fly ash according to Eq. (4.37)	123
4.15	RVE of hydrate foam with five types of hydrates (“material organogram”); two-dimensional sketches of three-dimensional representative volume elements	126
4.16	RVEs of hydrate foam including the finely ground fillers quartz or limestone (“material organograms”): (a) one hydrate type, (b) five types of hydrates; two-dimensional sketches of three-dimensional representative volume elements	126
4.17	Comparison of model-predicted strength evolutions with experimental data from Core Project 10 for (a) quartz-blended mortar, and (b) and limestone-blended mortar	128
4.18	RVE of cement paste including SCMs slag or fly ash (“material organogram”); two-dimensional sketches of three-dimensional representative volume elements	128
4.19	Comparison of model-predicted strength evolutions with experimental data from NANOCEM’s Core Project 10 for slag-blended mortar: (a) single hydrate model, and (b) five hydrate model; SCM hydration related strengthening of C-S-H is modeled according to Eq. (4.38) and (4.39).	130
4.20	Comparison of model-predicted strength evolutions with experimental data from NANOCEM’s Core Project 10 for fly ash-blended mortar: (a) single hydrate model, and (b) five hydrate model; SCM hydration related strengthening of C-S-H is modeled according to Eq. (4.38) and (4.39).	131
5.1	Sketch of a damage accumulation zone, also referred to as “fracture process zone” or “crack band” [15, 12]	144
5.2	Hierarchical organization of microcracked mortars and concretes (“material organogram”) used for elasticity homogenization: two-dimensional representations of three-dimensional RVEs.	146

5.3	Covered sphere model employed for homogenization of fracture energy.	154
5.4	Hierarchical organization of microcracked mortars and concretes (“material organogram”) used for homogenization of fracture energy.	155
5.5	Homogenization of fracture energy in case of a porous material, based on a hollow sphere model.	156
5.6	Homogenization of fracture energy in case of covered sphere containing a strong solid core, representing an obstacle for crack propagation.	156
5.7	(a) Geometric dimensions of the dog bone-shaped specimens investigated by van Vliet and van Mier [161]; (a) out of plane dimension $t = 100$ mm was constant for all specimen sizes; elongation measurements refer to the shaded central part of the specimen, see Fig. 5.8; (b) prismatic representation of the central part of the specimens used for re-analysis of the tests including a damage accumulation zone (central white region) adjacent to two undamaged regions.	163
5.8	Force-elongation diagrams: measurement data of van Vliet and van Mier [161], obtained from at least four tests for each specimen size.	164
5.9	Size effect of nominal tensile strength observed by van Vliet and van Mier [161], see circles and scatter bars, as well as Weibull size effect law given in Eq. (5.50).	164
5.10	Force-elongation diagrams: shaded areas cover measurement data of van Vliet and van Mier [161], obtained from at least four tests for each specimen size; black solid lines represent the model prediction, see Eqs. (5.55), (5.56), and (5.58), as well as the input quantities given in Table 5.4.	167
5.11	Geometric dimensions of the notched mortar prisms tested by Le Bellego [92]. The out-of-plane dimension $t = 40$ mm was constant for all specimen sizes.	168
5.12	Force-deflection diagrams: measurement data of Le Bellego et al. [92], obtained from at least 4 tests for each specimen size.	169
5.13	Finite Element mesh used for modeling three-point bending tests.	170

-
- 5.14 Force-deflection diagrams: shaded areas cover measurement data of Le Bellégo et al. [92], obtained from at least 4 tests for each specimen size; black solid lines represent the model prediction. . . 173

List of Tables

1.1	Oxide composition of materials as weight fractions (in %)	12
1.2	Physical properties of materials used	12
1.3	Mineral composition of CEM I 52.5 N as mass fractions (in %) . .	12
1.4	Proposed composition for pure and blended cement pastes	18
2.1	Hydration degrees at the solid-to-liquid transition of the investi- gated materials, estimated by adjusting best linear fits to quasi- static Young’s modulus evolutions (Fig. 2.13) and using them for extrapolating to stiffness values being equal to zero	60
3.1	Intrinsic elastic and apparent fracture properties of relevant che- mical phases considered in the multiscale hierarchical simulation. .	71
3.2	Decrease of strength with upscaling for OPC paste, $w/b = 0.51$ at 28 days (degree of OPC hydration $\xi = 0.836$) using microstructural characterisation as follows: $\gamma_{\text{CSH}} = 0.5815$, $f_{\text{cappor}} = 0.290$, $f_{\text{incl}} =$ 0.3067 , $E_{\text{incl}} = 48.032$ GPa, $f_{\text{air}} = 0.008$, $\beta = 0.6$, and $f_{t,\text{glob}} =$ 320 MPa.	89
3.3	Decrease of strength with upscaling for OPC paste, $w/b = 0.247$ at 28 days (degree of OPC hydration $\xi = 0.515$) using microstruc- tural characterisation as follows: $\gamma_{\text{CSH}} = 0.77564$, $f_{\text{cappor}} = 0.1146$, $f_{\text{incl}} = 0.4892$, $E_{\text{incl}} = 79.033$ GPa, $f_{\text{air}} = 0.041$, $\beta = 0.8$, and $f_{t,\text{glob}} = 320$ MPa.	90
3.4	Local sensitivity analysis on OPC paste, $w/c = 0.51$ at 28 days. .	96
4.1	Isotropic elasticity constants of material phases	105
4.2	Physical properties of materials used	119
4.3	Investigated paste compositions	120
4.4	Elastic and micromorphological hydrate properties	125

5.1	Properties of microstructural constituents of mortar and concrete	150
5.2	Composition of investigated materials: concrete used by van Vliet and van Mier [161] and mortar used by Le Bellego et al. [93]. . . .	162
5.3	Upscaling of elastic and fracture energy from solid C-S-H up to macroscopic concrete.	163
5.4	Concrete properties considered for the re-analysis of the direct tension tests performed by van Vliet and van Mier [161].	165
5.5	Upscaling of elastic and fracture energy from solid C-S-H up to macroscopic mortar.	171
5.6	Mortar properties considered for the re-analysis of the three-point bending tests performed by Le Bellego et al. [92].	171
5.7	Numerical values obtained from simulating with the FE mesh shown in Fig. 5.13, with numerical inputs listed in Table 5.6. . . .	174
5.8	Results of optimal B and D_0 parameters.	176

Introduction

It is estimated that the cement industry produces 5–8 % of total global anthropogenic CO₂ emissions [60]. The reduction of CO₂ emissions became one of the main objectives for the cement and concrete industry in recent years, motivating research on and development of new cementitious binders. One promising approach to reduce the carbon footprint of cement production is to replace part of ordinary Portland cement (OPC) with (i) supplementary cementitious materials (SCMs), such as ground granulated blast furnace slag or fly ash, or with (ii) finely ground inert microfillers such as quartz or limestone, to name a few from the widely used alternative waste products available on the global market today. Clinker substitution rose from 17% in 1990 to 35% in 2010 among the European cement producers [154, 165]. A further shift is expected, motivated by economical, ecological, and sustainability-related benefits [60, 61]. Adding SCMs to OPC results in a challenging chemical complexity [114], such that prediction of reaction kinetics and of microstructural details based on knowledge regarding the actual chemical composition of the binder remain open research questions [25, 39]. Slag addition alters reaction kinetics, but the impact on the resultant microstructure is rather small due to the fact that hydration products of slag exhibit similar stoichiometric composition as the hydration products stemming from pure cement clinker. However their fibrillar morphology may be replaced by a foil-like structure, as concluded by Richardson [131]. Moreover, nanoindentation tests showed that the hydrates in slag blended pastes are considerably stronger than in OPC pastes [178]. The addition of fly ash significantly impacts the workability of the fresh paste as the fly ash particles are near-to-perfect spheres. At the same time, it induces a pozzolanic reaction that transforms Portlandite into C-S-H, which exhibits a smaller Ca/Si ratio as well as a different nanostructure and morphology compared to C-S-H stemming from pure OPC. Using finely ground limestone or quartz leads to overall lower generated hydration heat and to ac-

celerated hydration [94] as they provide preferred precipitation sites for C-S-H hydrates stemming from the hydration of OPC.

Concretes made from blended cements can be competitive on the market only if they exhibit similar or an improved performance compared to concretes from OPC. Standard concrete composition was refined over centuries such that the present-day concrete which is based on Portland cement meets all the industrial demands for an easy-to-produce and durable building material. More specifically, three principal demands of the building industry need to be addressed, namely that (i) concrete remains workable for sufficiently long, i.e. the setting of cement starts after several hours, that (ii) early-age strength develops fast enough such that formworks can be stripped as early as 24 hours after production, and that (iii) the final structure is durable and reliable in order to guarantee serviceability for its entire designed lifetime. Concretes made from blended cements comply with the requirement for workability due to the retarded SCM reaction, and also with long term durability-related requirements. However, the development of early-age strength is slower compared to that of concrete based on OPC. This initiated intensive research focused on early-age mechanical properties of blended cements, see e.g [54, 91, 94, 178]. Notably, also the long-term properties of these materials (using high volume cement replacement levels) are also not well documented. The lack of knowledge results in great challenges for industrial developers and for scientific researchers.

The scientific understanding of concrete microstructures promoted the development of multiscale computational models for predicting mechanical properties. Initially, the primary focus of research was on the elastic properties of cement pastes. Continuum micromechanics not only provides an efficient analytical tool for accessing the elastic properties [22, 137, 120, 148], but also for predicting creep properties [139, 158] and the compressive strength evolution [119, 122] based on “averaged” properties of microstructural constituents. Numerical homogenization by Finite Elements allows for resolving the microstructure in great detail and, hence, allows for analyzing the interaction between the microscopic constituents at a high precision, see e.g. [167] for elasticity predictions and [168] for extension towards viscoelasticity of cement pastes. So far the modeling activities focused on Portland cement pastes due to the detailed knowledge of the microstructure as well as the availability of models for hydration kinetics of clinker [127]. The extension of modeling approaches towards blended cements is difficult due to the

fact that the addition of supplementary cementitious materials results in a substantial modification of the microstructure, rendering analytical approximations of hydration kinetics of blended binders currently out of reach.

The main objective of this thesis is to address the industrial demand for a deeper understanding of blended cement pastes and mortars, and to provide models capable of determining mechanical properties with evolving microstructure. In this context, a comprehensive experimental campaign was launched in order to characterize the evolution of elastic stiffness, compressive strength, and splitting tensile strength of selected blended cement pastes and mortars, see Chapter 1. To this end, a novel approach of determination of the unloading modulus of cement pastes was established, see Chapter 2 for details. In addition to the experimental campaign, two complementary modeling approaches for prediction of mechanical properties were developed: (i) a Finite Element-based model describing nonuniform distribution of hydration products between clinker grains, see Chapter 3, and (ii) a continuum micromechanics approach based on a Mohr-Coulomb strength criterion of hydrates taking into consideration stress concentration around sand grain surfaces, see Chapter 4. Finally, a first analytical multiscale model for tensile fracture is developed in Chapter 5. All chapters in this thesis are written as stand-alone manuscripts; Chapter 1 is planned to be extended to a full journal paper, Chapters 2 and 3 are already published in *Strain* and *Cement and Concrete Research* journals, respectively, and Chapters 4 and 5 are mature drafts soon to be submitted to peer-reviewed journals.

Research objectives

The principal research objectives for this thesis are:

1. Develop predictive micromechanical models for compressive and tensile strength evolution of blended cement pastes. The models should cover a time period from one day after the production up to maturity, i.e. link initial blend composition and hydration degree to macroscopic stiffness and strength evolution.
2. Identify microstructural constituents and key factors governing the evolution of macroscopic mechanical properties of blended cement pastes with increasing degree of hydration.
3. Generate a comprehensive database for cement pastes, produced with pure and blended Portland cements, and test such materials from one day after production up to mature stages. Determine stiffness, compressive and tensile strengths during maturing. Obtain complementary microstructural characterization of individual material phases as a function of degree of hydration.

This thesis is a part of the Core Project 10 entitled “Micromechanical analysis of blended cement-based composites”, funded by the industrial-academic nanoscience research network for sustainable cement and concrete “NANOCEM”.

Methodology and key results

Chapter 1

This Chapter refers to microstructural and mechanical characterization of OPC and blended pastes and mortars, representing the experimental focus of NANOCEM's Core Project 10 entitled "Micromechanical analysis of blended cement-based composites". At the time of finalizing this thesis, it is planned to extend this Chapter to a full journal paper, after completing the PhD studies.

Gilles Chanvillard, Vít Šmilauer, and Bernhard Pichler set up the overall research strategy. Michal Hlobil prepared specimens, tested them mechanically, and documented research results. Pipat Termkhajornkit and Rémi Barbarulo coordinated, supervised, and carried out microstructural characterization. Vít Šmilauer and Michal Hlobil then established the "CemBase" database and used it to store the measured data.

DIGEST: The comprehensive test database is elaborated by combining state-of-the-art microstructural characterization techniques and mechanical testing. Microstructural characterization combines methods including thermo-gravimetric analysis, X-ray diffraction with Rietveld analysis, and scanning electron microscopy, in order to determine the microstructural phase assemblages of the initial raw products as well as 1, 3, 7, 28, and 91 days after mixing with water. This allows for resolving phase volume evolutions point wisely. Mechanical testing includes characterization of stiffness and strength. The early-age evolution of static unloading modulus is determined with a test protocol including cyclic loading-unloading tests which are hourly repeated from 24 hours after production up to material ages of 8 days. Dynamic stiffness is determined based on measurements of ultrasonic pulse velocities of longitudinal and shear waves, evaluated on the basis of elastic wave propagation in isotropic media. The uniaxial compres-

sive strength evolution is determined both on pastes and mortars, crushed 1, 3, 7, 28, and 91 days after production. The tensile splitting strength, in turn, is determined 1, 3, 28, and 91 days after production.

Chapter 2

This chapter is based on a joint publication of Phillip Karte, Michal Hlobil, Roland Reihnsner, Wolfgang Dörner, Olaf Lahayne, Josef Eberhardsteiner, and Bernhard Pichler published in Strain, (2015), vol. 51, pp. 156–169.

Bernhard Pichler and Josef Eberhardsteiner set up the overall research strategy, supervised the research progress, checked key results, and supported the documentation process. Phillip Karte prepared specimens, tested them, evaluated measured data, and documented the research results. Michal Hlobil refined the sample production technique, helped with specimen production and with testing, and prepared software routines for the evaluation of recorded measurement data. Roland Reihnsner operated testing machines and supervised the use of measurement equipment. Wolfgang Dörner designed and manufactured new testing hardware. Olaf Lahayne supervised ultrasonics measurements.

DIGEST:

The stiffness evolution of binder “cement paste” is triggering the stiffness of concrete. In the engineering practice, concrete formworks are typically removed 24 hours after production. This underlines that knowledge on mechanical properties of cementitious materials during the second, third, and fourth day after production are of high relevance for the ongoing construction process. This provides the motivation to perform early-age stiffness characterization on hydrating cement pastes, by means of the following three test methods. Unloading modulus is determined using a novel setup for nondestructive uniaxial compression testing including overdetermined deformation measurements. Dynamic Young’s moduli are obtained from ultrasonics experiments. Isothermal differential calorimetry allows for linking the observed temporal evolution of early-age stiffness to the hydration degree of cement. Pastes with three different compositions are investigated, defined in terms of the initial water-to-cement mass ratio w/c and the initial water-to-solid (binder) mass ratio w/s . Pure cement pastes exhibit $w/c = w/s = 0.50$ and $w/c = w/s = 0.42$, respectively. A fly ash-blended cement

paste refers to a cement mass replacement level of 16 percent, and this is related to $w/c = 0.50$ and $w/s = 0.42$. Both unloading moduli and dynamic Young's moduli of all three materials increase practically linearly with increasing hydration degree, in the investigated regime of hydration degrees ranging from 40 to 60 percent. Fly ash does not contribute significantly to the early-age hydration of the material, i.e. it represents a quasi-inert part of the material's microstructure, exhibiting a significant stiffening effect.

Chapter 3

This chapter is based on a joint publication of Michal Hlobil, Vít Šmilauer, and Gilles Chanvillard published in *Cement and Concrete Research*, (2016), vol. 83, pp. 188–202.

Vít Šmilauer set up the overall research strategy, provided support for Finite Element method, implemented Griffith-Rankine material model into OOFEM code, and documented the theoretical development of the model. Michal Hlobil ran all simulations, postprocessed results and collaborated on the manuscript. Gilles Chanvillard provided insight into the microstructure of cement pastes and offered suggestions to improve the manuscript.

DIGEST:

The evolution of compressive strength belongs to the most fundamental properties of cement paste. Driven by an increasing demand for clinker substitution, the paper presents a new four-level micromechanical model for the prediction of compressive strength of blended cement pastes. The model assumes that the paste compressive strength is governed by apparent tensile strength of the C-S-H globule. The multiscale model takes into account the volume fractions of relevant chemical phases and encompasses a spatial gradient of C-S-H between individual grains. The presence of capillary pores, the C-S-H spatial gradient, clinker minerals, SCMs, other hydration products, and air further decrease compressive strength. Calibration on 95 experimental compressive strength values shows that the apparent tensile strength of the C-S-H globule yields approx. 320 MPa. Sensitivity analysis reveals that the "C-S-H/space" ratio, followed by entrapped or entrained air and the spatial gradient of C-S-H, have the largest influence on compressive strength.

Chapter 4

This chapter contains a quite mature paper draft authored by Michal Hlobil, Markus Königsberger, Pipat Termkhajornkit, Rémi Barbarulo, Christian Hellmich, and Bernhard Pichler. At the time of finalizing this thesis, is planned to submit the paper – in further improved form – to Cement and Concrete Research.

Bernhard Pichler and Christian Hellmich set up the overall research strategy, supervised the research progress, checked key results, and supported the documentation process. Michal Hlobil implemented a software script for compressive strength predictions, produced mortar specimens, tested them, documented research results, and produced diagrams for the paper. Markus Königsberger provided support for Michal Hlobil during model implementation and code verification, produced figures, and wrote the first draft of the paper. Pipat Termkhajornkit and Rémi Barbarulo coordinated, supervised, and carried out microstructural characterization.

DIGEST:

This contribution refers to early-age strength of pastes and mortars produced either with ordinary Portland cement (OPC) or with blended OPC where part of cement clinker is replaced either by quartz, limestone, slag, or fly ash. The study combines multiscale elasto-brittle modeling with microstructural characterization and early-age macroscopic testing of blended mortars. In the context of modeling, the elasto-brittle strength model for cement pastes presented in [CCR 41:467-476, 2011] is extended towards mortars. Loading imposed on mortar samples is first concentrated down to stress peaks in cement paste volumes which are directly bonded to stiff sand grains. Further stress concentration down to micron-sized needle-shaped hydrates is quantified based on *strain energy*-related stress averages. This is motivated by the envisioned failure mode of hydrates, which is *energy*-driven shear cracking at the nanometric scale, with a shear strength that increases with increasing pressure acting on the crack plane. The friction angle and the cohesion intervening in the newly adopted Mohr-Coulomb failure criterion are taken from limit state analysis of grid indentation testing on low-density calcium-silicate-hydrates. Therefore, the model is free of fitting parameters. Blind predictions of the macroscopic compressive strength of OPC pastes and mortars agree very well with experimental results from three different laboratories. This is the motivation to continue with mortars produced with

binders representing blends of OPC and limestone, quartz, slag, and fly ash, respectively. Early-age phase evolutions are quantified based on state-of-the-art microstructural characterization, including thermogravimetric analysis and X-ray diffraction with Rietveld analysis, and scanning electron microscopy. As for modeling, very finely ground quartz and limestone are introduced as reinforcements of the hydrate foam, i.e. they directly interact with needle-shaped hydrates and capillary porosity. The coarser hydraulic supplementary cementitious materials (SCM) slag and fly ash, in turn, are introduced at the same scale as unhydrated clinker grains. Comparison of model-predicted strength evolutions agree well with test results, as long as the blending materials do not hydrate. Hydration of slag and fly ash is shown to increase the hydrate cohesion significantly, and this is consistent with recent nanoindentation studies on mature OPC and blended pastes.

Chapter 5

This chapter contains a mature paper draft authored by Michal Hlobil, Maximilian Göstl, Jacques Burrus, Christian Hellmich, and Bernhard Pichler. At the time of finalizing this thesis, is planned to submit the paper – in further improved form – to the Journal for Mechanics and Physics of Solids.

Bernhard Pichler and Christian Hellmich set up the overall research strategy, supervised the research progress, checked key results, and supported the documentation process. Michal Hlobil contributed the multiscale homogenization approaches for elastic stiffness and fracture energy, the dimensionless versions of the damage evolution law, carried out structural simulations, and documented research results. Maximilian Göstl contributed the first version of the size-effect formulation appearing in the damage evolution law, the Finite Element code for simulation of three-point bending tests, and he documented research results. Jacques Burrus analyzed the direct tension tests, developed the first version of the damage evolution law, and documented research results.

DIGEST:

Macroscopic tensile fracture of cementitious materials results from bond ruptures at the nanoscopic scale of calcium-silicate-hydrates (C-S-H). Here, we use a hierarchical covered spheres model to analytically upscale the fracture energy of the

calcium-silicate-hydrates (C-S-H), as quantified in recently published molecular dynamics simulations, to the material scale of mortar and (cracked) concrete. The latter fracture energy then enters the resistance side of a thermodynamics-based damage propagation criterion, with the crack density parameter as the damage variable quantifying the deterioration state of a representative volume element (RVE) of cracked concrete. The driving force for crack propagation, on the other hand, relates to the change in elastic energy with increasing crack density; the elastic energy being derived from a hierarchical Eshelby-based homogenization scheme, linking the C-S-H level to that of the cracked concrete, the latter with an RVE containing penny-shaped cracks as distinct material phase. These up-scaling relations are complemented by a damage evolution law in the format of a functional relationship between characteristic crack size and crack density, both related to the material phase “cracks” mentioned before, on the one hand, and the maximum aggregate size on the other. This law governs the tensile softening behavior in the three dimensional damage accumulation zone surrounding, by three times the maximum aggregate size, a macrocrack propagating through the considered structure. Thereby, the initial characteristic crack size within an RVE of cracked concrete follows a Weibullian size effect law. Two constants quantifying the aforementioned functional relationship are back-analyzed from direct tensile tests. The thus completed micromechanics model, when fed into 3D structural Finite Element analyses, allows for satisfactory prediction of the behavior of three-point bending experiments on notched mortar beams. This underlines that tension-induced failure of macroscopic structures made of cementitious materials can indeed be explained based on elastic and fracture properties of nanoscopic C-S-H.

Chapter 1

Experimental campaign

This chapter describes the raw materials used within this project, starting with the description of raw materials, followed by specific mix design, then by a microstructural characterization as well as hydration kinetics. In addition, an extensive study of mechanical properties, starting with elasticity measurements performed by means of mechanical loading/unloading cycles as well as by ultrasonic wave speed propagation, followed by uniaxial compressive strength tests and closing with Brazilian splitting strength tests.

1.1 Material description

Lafarge Centre de Recherche provided all the raw materials used in this study. The following raw materials were used to prepare blended cements used within this project: ordinary Portland cement, finely ground quartz sand and limestone, blast furnace slag, and fly ash. For chemical composition of materials used, refer to Table 1.1, for physical properties to Table 1.2.

1.1.1 Ordinary Portland cement

The cement is characterized as CEM I 52.5 N CE CP2 NF and comes from Saint-Pierre-la-Cour plant in northwestern part of France. Microstructural characterization (performed at Lafarge Centre de Recherche) provided insight into the chemical (see Table 1.1) as well as mineral composition (see Table 1.3). Physical

Table 1.1: Oxide composition of materials as weight fractions (in %)

Material	CaO	SiO ₂	Al ₂ O ₃	Fe ₂ O ₃	SO ₃	MgO
OPC	65.59	20.12	4.95	3.04	3.43	0.98
Slag*	42.29	35.82	11.16	0.27	1.99	8.31
Fly ash	10.92	54.70	23.28	3.82	0.16	1.08
Material (cont.)	Na ₂ O	K ₂ O	P ₂ O ₅	TiO ₂	Mn ₂ O ₃	other
OPC	0.16	0.99	0.31	0.21	0.13	0.09
Slag*	0.18	0.34	0.00	0.47	0.22	–
Fly ash	3.15	0.84	0.08	0.67	0.06	1.24

(*) Slag composition does not add to 100 % due to measurement uncertainties.

Table 1.2: Physical properties of materials used

	Mass density [kg/m ³]	Blaine fineness [m ² /kg]	Granulometry			
			d90 [μm]	d50 [μm]	d10 [μm]	d4.3 [μm]
OPC	3 170	363	41.78	15.44	2.45	19.21
Quartz	2 650	617.2	–	–	–	–
Limestone	2 715	–	–	–	–	–
Slag	2 930	340	–	–	–	–
Fly ash	2 090	368.6	–	–	–	–

properties are listed in Table 1.2. During testing, cement was stored in sealed plastic non-transparent barrels to reduce the risk of prehydration.

Table 1.3: Mineral composition of CEM I 52.5 N as mass fractions (in %)

C ₃ S	C ₂ S	C ₃ A (cubic)	C ₃ A (ortho)	C ₄ AF	free lime
57.20	20.80	4.90	1.00	10.30	1.10
gypsum	anhydrite	hemihydrate	calcite	periclase	portlandite
1.30	0.30	2.30	0.40	0.10	0.30

1.1.2 Quartz

The primary reason of substituting a portion of OPC by finely ground quartz sand is to directly reduce the cost of the binder. The addition of quartz helps to disperse clinker particles during mixing which results in a homogeneous mi-

microstructure of hardened cement paste. Quartz sand is a chemically inert material that only acts as an inert filler in the binder. It accelerates the hydration of OPC and the resultant formation of hydration products by providing preferred nucleation sites for precipitation of hydrates [94]. It also helps to progressively decrease the total heat release during the hydration of cement. Table 1.2 contains measured physical properties of quartz used.

1.1.3 Limestone

Finely ground limestone may also be used to substitute part of OPC in the binder, where it acts as a microfiller (similar to quartz). Similar to quartz, limestone influences the hydration of the cementitious binder. First, it slightly accelerates the early-age hydration process by providing *preferred* nucleation sites for C-S-H gel to precipitate on. However, it also reacts with C₃A forming hemi- and monocarbonate phases [40]. The hydrate composition within the microstructure may be changed but the impact on mechanical properties is negligible.

1.1.4 Blast furnace slag

Ground granulated blast-furnace slag (abbrev. GGBS) is a by-product produced during the manufacture of iron in a blast furnace. Iron-rich ore (hematite Fe₂O₃ or magnetite Fe₃O₄) with iron content from 50 % to 70 % is charged directly into the blast furnace, descends through it and is heated with hot air up to 1600 °C. Slag forms in liquid state from the remains of silica and other compounds during the fusion of limestone (and/or dolomite) flux with ash from coke and the siliceous and aluminous residues remaining in the furnace after the reduction and separation of the iron from the ore [110]. Slag is then collected and channeled away from the furnace.

Rapid cooling of molten slag down to 800 °C forms a vitreous structure, resulting in hydraulic properties. Slow cooling leads to a stable solid, which consists of crystalline Ca-Al-Mg silicates, with little or no cementing properties [146]. Slowly-cooled slag can be used as aggregate. There are two methods to rapidly cool blast furnace slag – granulation and pelletization. During *granulation*, molten slag is cooled down by high pressure water jets (0.6 MPa) and forms granules less than 5 mm in diameter. One tonne of slag consumes about three cubic meters of

water [146]. After this process, slag will contain over 95 % of glass [151]. *Pelletization* involves pouring of molten slag onto rotating steel drums with a speed of 300 rpm. These disks throw slag into the air where it is sprayed with water and cooled. The consumption of water is only about one cubic meter per ton of slag. Remaining water content less than 10 %. Taylor [151] states that the proportion of glass decreases with increasing pellet size. Slag is then grounded to a desired fineness, usually the same as Portland cement (see Figure 1.1).

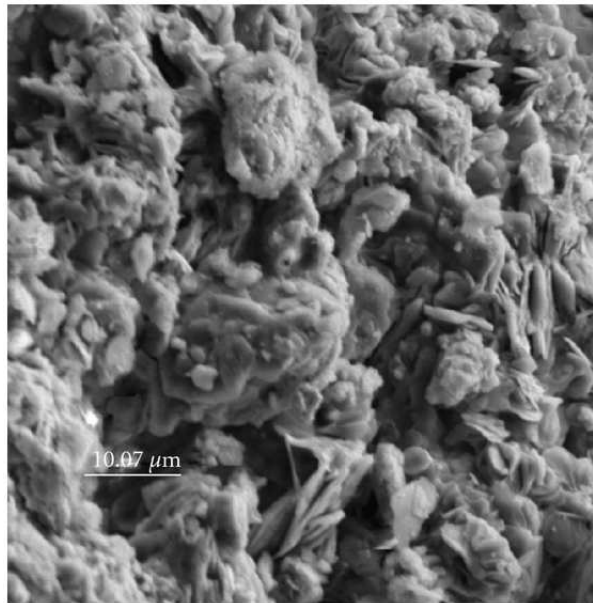


Figure 1.1: SEM micrograph showing the surface texture of a sand-size EAF slag particle, magnified 1200 \times , source: www.hindawi.com/journals/ace/2011/463638/fig11/

Slag particles are irregular in shape but similar in size due to grinding. The final product after grinding has a bright grey colour and a density of approx. 2900 kg/m³. The chemical composition of slag varies greatly from plant to plant with the materials smelted and conditions in the blast furnace but contains SiO₂, CaO, Al₂O₃ and MgO among other metal oxides. But for a given plant, the composition stays relatively similar unless the raw materials change. The more silica slag contains, the more it is reactive. The amount of silica and lime doesn't fluctuate very much in slag (regardless of blast furnace), silica is around 35 % and lime around 40 %. Other constituents vary much more. Glass content is essential for reactivity of slag but most standards do not specify a threshold value.

Replacement of Portland cement

Slag can replace up to 70 % of Portland cement in concrete mixture. It is latently hydraulic therefore needs an activator (either sulfate, alkalis or increase of pH in the system). The reaction rate is rather slow (slower than alite) and depends on quantity and relative proportions of slag and Portland cement, temperature, chemical composition and fineness of slag and cement [110]. Once activated, it begins to form calcium silicate hydrates.

In order to speed up the hydration rate and increase early age strength, it is useful to add alkaline activators (Na_2SiO_3 , Na_2CO_3 , NaOH and Na_2SO_4 , sorted from the most effective to the least) into the cement mixture, especially when high content of slag is present [146]. Once activated, slag offers additional nucleation sites for hydration products to grow, making a denser structure by reducing the connectivity of pores in the paste, resulting in a higher strength. Taylor [151] states that the microstructure of the outer product becomes progressively less fibrillar and more foil-like in character.

The addition of slag does not improve workability and bleeding of the fresh paste due to the fact that its particles are irregular (opposed nearly perfect spheres of fly ash). The hydration rate is slower than Portland cement paste resulting in a slower increase in early age strength. Generated heat is also lower which reduces the risks of thermal cracking [110]. The highest strength of cement paste is obtained when slag contains 15-20 % of Al_2O_3 and 40-50 % of CaO [146]. With increasing amount of Portland cement substituted by slag, the viscosity and yield stress decrease.

Slower hydration also has an effect of formwork removal as these times have to be extended. The structure has to be cured for longer periods. These short-term inconveniences are compensated with a more durable structure. The surface finish has a higher quality, is less permeable to alkalis or sulfates due to finer pore structure and pore distribution [110]. Slag does not however reduce the risk of carbonation of concrete. It can be also noted that the addition of slag creates a brighter colour of the structure which may be used for architectural reasons.

1.1.5 Fly ash

Fly ash is an incombustible residue from materials that coalesced during combustion of coal in power station furnaces between 1250 – 1600 °C [110]. It is filtered and removed from the flue gases using electrostatic precipitators and/or fabric filters before these gases are released into cooling chimneys. Due to pozzolanic properties this waste product is used to replace Portland cement in concrete production. Unused fly ash is stored in landfills.

Fly ash takes the form of fine clay-like particles (see Figure 1.2), spherical in shape up to 100 μm in diameter. Some particles are hollow inside (called cenospheres) and some contain smaller spheres inside (called plerospheres). Particles can contain traces of mullite, crystal quartz (SiO_2), potassium sulfate (K_2SO_4), calcium sulfate (CaSO_4), hematite (Fe_2O_3) and magnetite (Fe_3O_4) adhering on the surface. The particle density depends on grinding and varies from 1900 – 2800 kg/m^3 . Bulk density depends on packing and compaction and fluctuates around 540 – 860 kg/m^3 . Specific chemical composition of fly ash depends on the fuel burned in the power plant but it is generally composed of SiO_2 (amorphous and crystalline), Al_2O_3 , Fe_2O_3 and CaO . When limestone and dolomite are used for desulphurization of the exit gasses, CaO and MgO contents in fly ash will be increased [146]. Depending on the chemical composition, fly ash can be divided into two classes (according to ASTM C 618): *class F* and *class C*.

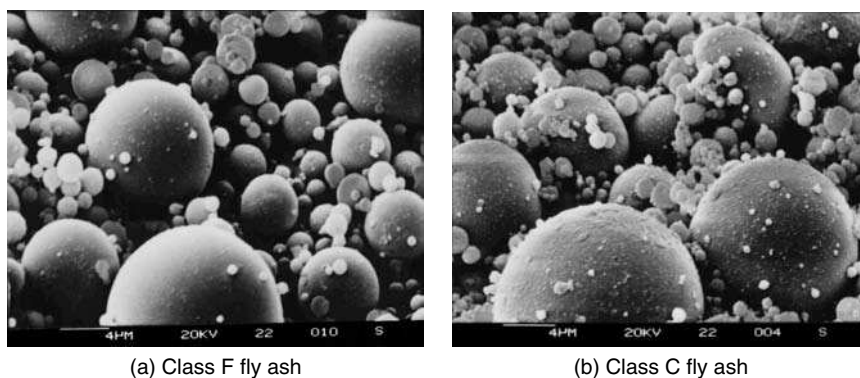


Figure 1.2: SEM pictures of classes F and C fly ash particles, source: [146]

Types of fly ash

- Class F: if $(\text{SiO}_2 + \text{Al}_2\text{O}_3 + \text{Fe}_2\text{O}_3) > 70\%$. Formed when older, black coal (anthracite) is burned. Particles have a clean surface (see Figure 1.2).

Usually has a high content of SiO_2 , Al_2O_3 and Fe_2O_3 while a low content of CaO and has very little cementitious properties.

- Class C: if $50\% < (\text{SiO}_2 + \text{Al}_2\text{O}_3 + \text{Fe}_2\text{O}_3) < 70\%$. Formed during the combustion of lignite (brown coal), has cementing properties. Particles contain additional condensates on their surface (see Figure 1.2). Usually contains more CaO , MgO and SiO_3 and less SiO_2 and Al_2O_3 than class F fly ash. Contains crystalline phases of free CaO , C_3A , C_2S , CaSO_4 and MgO .

Replacement of Portland cement

The addition of fly ash into concrete mixture offers some advantages. From an economic point of view, the substitution of Portland cement by fly ash brings considerable cost savings due to the fact that enormously expensive material (Portland cement) is replaced by a waste product without much affecting the properties of the final product. And when substituted directly by mass, a greater volume of cementitious material can be obtained [110].

Fly ash is added into the concrete mixture to reduce the permeability of concrete and obtain a quality surface area. This increases the chemical resistance (chloride and sulfate attack) and the overall durability of the structure. It pozzolanically reacts with lime, reducing the amount of lime available and reduces the pH of the pore solution to below 13, thus preventing alkali-silica reaction [110]. The reactivity of FA is influenced primary by glass content and composition as well as surface area. Other factors influence the reactivity to a lower degree, such as temperature, humidity and alkali content.

Spherical particles of fly ash improve the dispersion of cement particles, which results in a greater fluidity of fresh concrete. The use of fly ash also enables to reduce the amount of water necessary for workability, decreasing the risks of bleeding and drying shrinkage as well [110]. Fly ash fills the capillary porosity between cement particles, reducing the overall porosity and providing additional nucleation sites for hydration products. This results in an increase of final strength of concrete and reduced porosity. The setting time is increased and the hydration rate is slower when compared to ordinary Portland cement. The presence of FA retards the reaction of alite, in the middle stages the reaction is accelerated due

to the provision of nucleation sites on fly ash particles [110]. Portlandite content is lowered both by the dilution of the clinker by FA and by the pozzolanic reaction [151]. The composition and formation of hydration products differs in Ca/Si (typically 1.55 and lower) and Al/Ca (higher) from OPC paste when FA is used [151]. A significant reduction in hydration heat is observed on mixtures containing fly ash when compared to OPC. In order to accelerate the pozzolanic reaction between portlandite and fly ash and obtain higher early age strengths, alkaline activators can be used. Based on experiments, the most effective seem to be Na_2SO_4 , Na_2SiO_3 and K_2SO_4 [146]. The addition of Na_2SO_4 results in more ettringite (AFt) formation which increases in volume and densifies the structure of the paste.

1.2 Mix design

The basic idea is that all the mixes share identical initial water-to-solid volume ratio, which is equal to 1.60. Then to make blended cements comparable, a substitution rate of 45% cement replacement *by volume* is used. Using a substitution rate by volume, instead of mass, leads to different water-to-solid mass ratios in all the mixes. However, the substitution rate by volume ensures that the total ratio of cement and water stay constant for all blended mixes and enables to directly study the impact of SCM on the hydration process. For specific paste composition, see Table 1.4

Table 1.4: Proposed composition for pure and blended cement pastes

	Initial water/solid volume ratio	Cement replacement by volume	Initial water/cement mass ratio	Initial water/solid mass ratio
OPC	1.60	0 %	0.51	0.51
Quartz blend	1.60	45 %	0.93	0.55
Limestone blend	1.60	45 %	0.93	0.54
Slag blend	1.60	45 %	0.93	0.53
Fly ash blend	1.60	45 %	0.93	0.60

1.3 Microstructural characterization

The dissolution of clinker grains starts upon contact with water, creating a saturated solution. Hydration products precipitate on the surface of clinker grains, interconnecting them in a three-dimensional web, forming a microstructure. Precise identification, separation and quantification of the crystalline and amorphous phases requires a combination of several methods.

The microstructural characterization (as described in [153]) was performed in Lafarge Centre de Recherche and was not part of this Core Project. The following combination of methods were used to quantify volume phases of individual paste constituents. Thermogravimetric analysis determines the amount of bound water. X-ray diffraction combined with Rietveld analysis provides access to the amount of crystalline phases as C_3S , C_2S , C_3A , gypsum, calcite, portlandite (CH), and ettringite (AFt). Calcium-silicate hydrates (C-S-H) and monosulfoaluminate (AFm) exhibit poor crystallinity so their quantities are determined using chemical volume balance equations. Gel porosity was presumed as 40 %. Degree of hydration of supplementary cementitious materials (slag, fly ash) is estimated from thresholded scanning electron microscope images used in backscattered mode, whereas the total degree of hydration can be measured by chemical shrinkage.

The microstructure of all paste compositions was analyzed at 0, 1, 3, 7, 28, and 91 days (see Figure 1.3). The volume fractions of individual components are normalized to a unit volume and plotted as a function of degree of hydration of OPC.

1.4 Mechanical testing

The evolution of mechanical properties from early-age up to maturity for all five paste compositions is investigated at 1, 3, 7, 28, and 91 days after production. Pure OPC paste serves as a reference to which two sets of pastes are compared: the effect of inert fillers (quartz and limestone) and the effect of SCMs (slag and fly ash). The characterization of mechanical properties starts with the determination of elasticity by means of (i) three loading/unloading cycles during uniaxial compression (with load levels well below 30 % of maximal strength) and of (ii) ultrasonic wave speed propagation through the sample. The main focus of the ex-

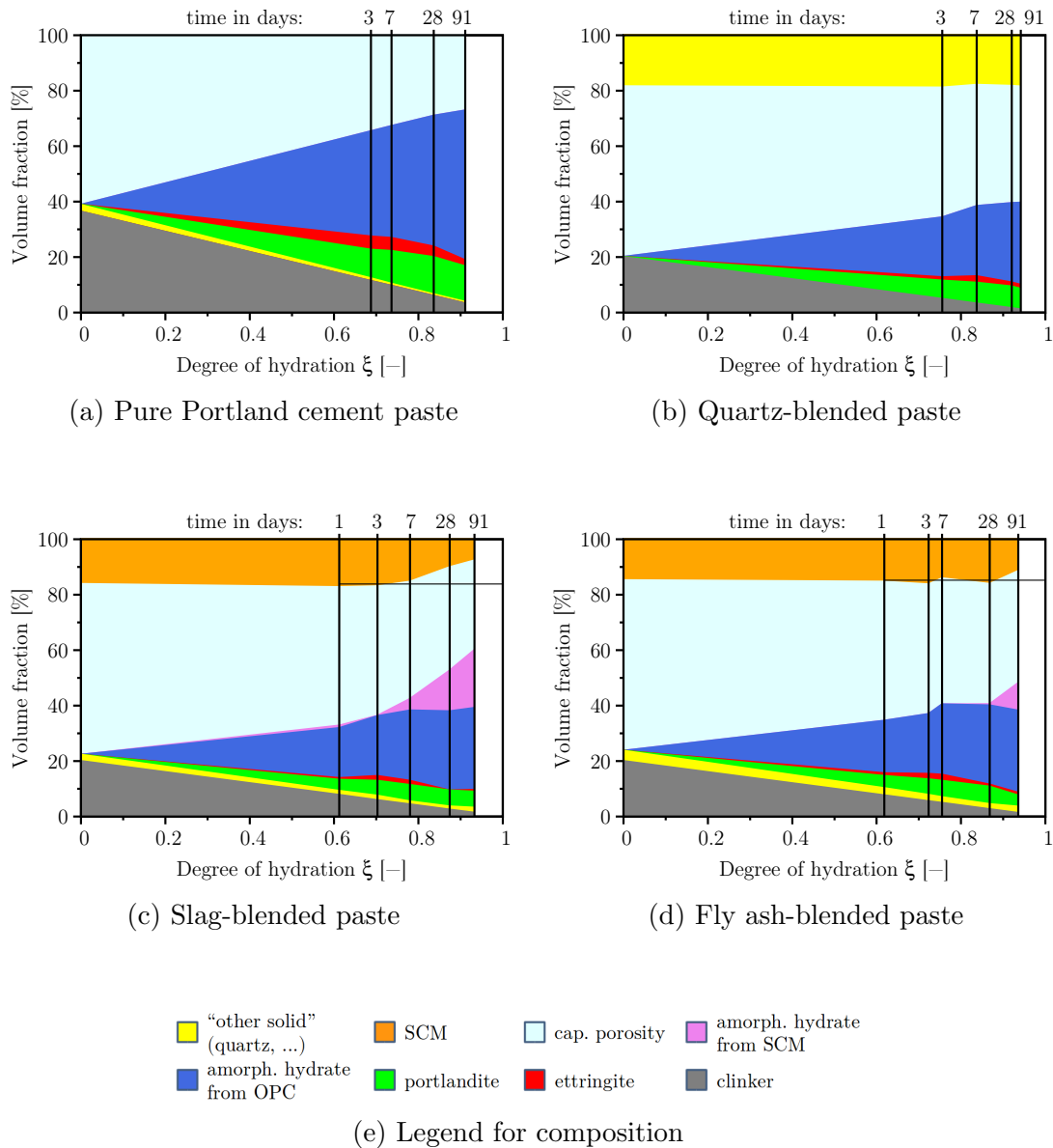


Figure 1.3: Phase assemblage of paste compositions plotted as volume fractions with respect to the degree of hydration of OPC. Data points at 1 day for OPC (see Fig. 1.3a) and quartz-blended paste (see Fig. 1.3b) are omitted due to measurement uncertainties.

perimental part is on compressive strength of samples, followed by determination of tensile strength by means of Brazilian splitting tensile tests.

1.4.1 Production of samples

Macroscopic mechanical testing of cement pastes at early ages is a rather challenging task because any imperfection will contribute to an increased scatter affecting the measurements. It is therefore important to analyze and to optimize every single element in the chain of actions from mixing the material up to the final test.

The production of samples begins by weighting the cementitious binder with a precision up to ± 0.005 g and then emptying it into a mixing bowl (used at TUW or CTU) or a waring blender (used at LCR). We then add SCMs or inert fillers, if necessary, into the bowl/blender and premix both by hand using a metal mallet until a satisfactory blending level is reached, signaled by a more-or-less homogeneous color of the mix without large clusters of any of raw materials used. Water is weighted with the same precision and added into the mixing bowl after the cementitious materials. From this time instant the age of samples is recorded.

We then mix in the mixing bowl using a metal mallet fitted to an electrical screw driver or mixed in the waring blender with the following setup: during the first 30 seconds after water contact with the cementitious powder, we use a lower mixing speed to prevent dusting and to evenly mix all the materials together. Then we increase the mixing speed to the maximum possible and continue to mix again for another 30 seconds. After 1 minute of continuous mixing we stop and manually remove any unmixed clusters of dry cementitious powder from the bottom and sides of the mixing bowl. This interruption in mixing should not take more than 1 minute, i.e. up to 2 minutes since the beginning of mixing. Then we mix the fresh paste once again, this time using only the highest speed for an additional 60 seconds, finishing exactly after 3 minutes from the initial contact between water and cement.

Casting into the mould is the next crucial step to obtain homogeneous specimens without any bubbles of entrapped air. We place the empty formwork on a vibrating table and incline it so that the longitudinal axis of the mould forms an angle around 30° with the horizontal plane of the vibrating table (at TUW) or

directly perpendicular to the table (at LCR and TUW). We then slowly fill the inclined mould by means of sliding the fresh paste through a funnel and then on the side of the inclined formwork rather than letting it simply fall down into the mould. This method reduces the risk of spilling, segregation of fine particles and air entrapment. During filling procedure the mould is constantly vibrated to force air bubbles to the top of the mould. Vibration is then progressively reduced in the sense of a smooth fade-out. Filled moulds are then sealed and placed in a horizontal position (the longitudinal axis of the sample and mould are horizontal) on a roller, which ensures a slow rotation of the specimens (approx. 5 turns per minute around the longitudinal axis of the specimen) during the first 24 hours after casting. The slow rotation prevents segregation of fine cement particles to the bottom of the mould, which causes excessive bleeding of paste near the top of the specimen.

After 24 hours of continuous rotation, we demould and prepare samples for testing. To achieve the desired plan-parallelity of top and bottom surfaces, we carefully scratch the top of the specimen with a Stanley knife, using the top surface of the mould as a guide (at TUW and CTU) or use a precision saw (at LCR). Should the sample contain any large pores or bubbles of entrapped air concentrated on the outer surface near the top (or bottom) of the specimen, we then cut the sample to remove these irregularities and ensure a perfectly prepared sample for testing either by means of a mechanical unloading or by ultrasonic wave speed propagation.

1.4.2 Elasticity

Elasticity is measured either by mechanical unloading or by ultrasonic wave speed propagation, described in subsequent chapters.

Mechanical unloading

We determine the stiffness of the paste specimen by means of quantifying the unloading modulus between two constant load levels during mechanical unloading. In order to come as close as possible to a truly central application of the normal force during stiffness testing, we first attach (using duck tape) a pair of steel cylinders with bottlenecks, in a serial arrangement with the specimen.

The diameter of both steel cylinders is 30 mm so they both align exactly with the specimen. Then we cover the specimen with plastic food preservation foil to reduce evaporation of free (i.e. unbound) water from the otherwise uncovered surface of the specimen.

To quantify strain (and later unloading modulus) of the sample during mechanical unloading, we use the following setup (see Figure 1.4): to obtain over-determined and, hence, redundant measurements of sample deformations during loading and unloading, we use five independent linear variable differential transformers (abbrev. LVDTs) instead of the minimum three, evenly spaced at 72° around the central axis of the specimen. All five LVDTs measure relative displacement of two adapters that are clamped to the specimen at a predefined locations. These adapters are secured to the specimen by means of a continuous contact around the perimeter of the sample. We mount both LVDT-carrying adapters in a distance from the end of the specimens, which amounts to the one times the cylinder diameter (i.e. 30 mm), to minimize the impact of the inevitable self-equilibrated shear forces within the interface between the sample and adjacent metal cylinders. To guarantee a reasonable LVDT measurement length, we use slender specimens (typical height-to-diameter ratio of 5:1). The mean value of the five LVDT measurements together with the distance of the adapters allows for calculation of normal strain in loading direction. Individual displacement fluctuations around the mean value, in turn, are related to bending, resulting mainly from load eccentricity.

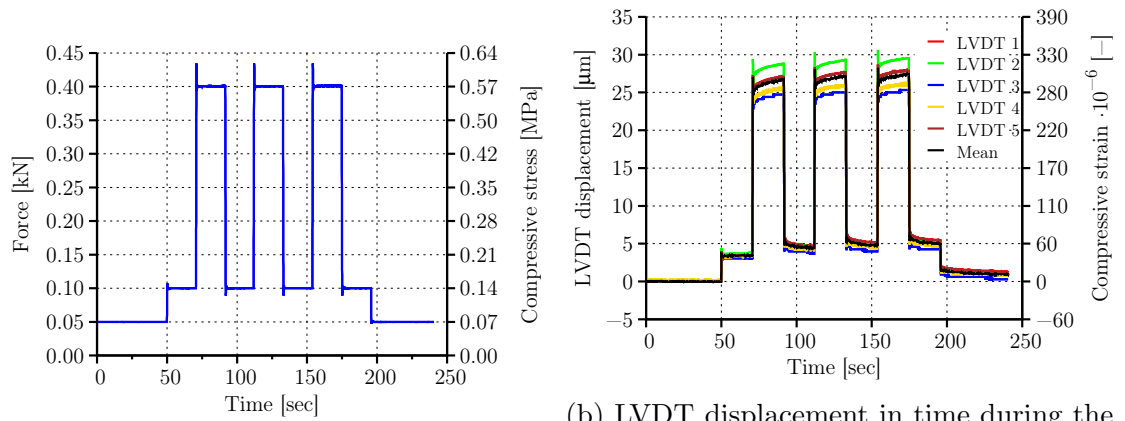
The loading procedure used to determine the unloading modulus will be described next. A preload force amounting to 0.05 kN was used throughout the whole test to stabilize the sample in position and prevent it from tipping over and damaging the LVDTs. During the loading cycle we use a constant loading/unloading speed equal to 1 kN/s to change between different loading levels, regardless whether loading or unloading is applied. The loading cycle alone (see Figure 1.5a) started with an increase of load level up to 0.1 kN which was held as quasi-constant for 20 sec, serving as a bottom force threshold for the loading cycle. The load level was then increased up to 0.4 kN (top force threshold level) and held quasi-constant again for 20 sec forming a top plateau, then followed by unloading down to 0.1 kN (bottom force level) and held quasi-constant for 20 sec forming a bottom plateau. This loading / unloading procedure was repeated two times more to obtain three individual unloading branches which we used to calculate the unloading moduli,



Figure 1.4: Test configuration showing paste sample wrapped in a food preservation foil together with five LVDTs evenly spaced around the sample and held in position by Plexiglas rings which were clamped onto the sample (left) and zoom showing the steel cylinder with bottleneck (right)

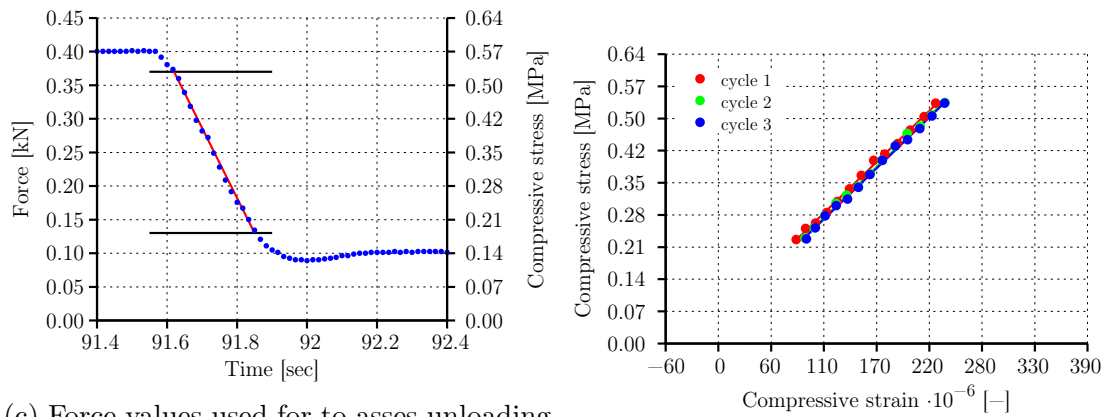
one from each unloading branch. After the first full loading cycle we evaluated the eccentricity of the sample by means of comparing each individual LVDT measurement with the calculated mean value. The use of five independent LVDTs enabled us to precisely reposition the sample so that a uniaxial compression was achieved (see Figure 1.5b).

The whole unloading branch was not considered to calculate the unloading modulus as the points near the top and bottom plateau might be influenced by the fact that the machine has to accelerate/decelerate close to top and bottom force thresholds (the machine is force controlled) and the unloading branch is not linear (see Figure 1.5c). We then considered only points that were more than 10 % apart from the top and bottom force thresholds (see horizontal lines on Figure 1.5c). The unloading modulus (see Figure 1.5d) was then determined by fitting a first order polynomial through the remaining points using a least square approach. In order for this method to be reliable, a minimum number of points had to be considered, which might be a problem for very early age samples (usually samples up to 30 hrs old). We found a reasonable minimum of 6 points to provide reliable result and test repetition. Once the sample becomes older and therefore stiffer, the number of points increases up to 25, providing a very precise polynomial fit.



(a) Force in time during the loading cycle.

(b) LVDT displacement in time during the loading cycle.

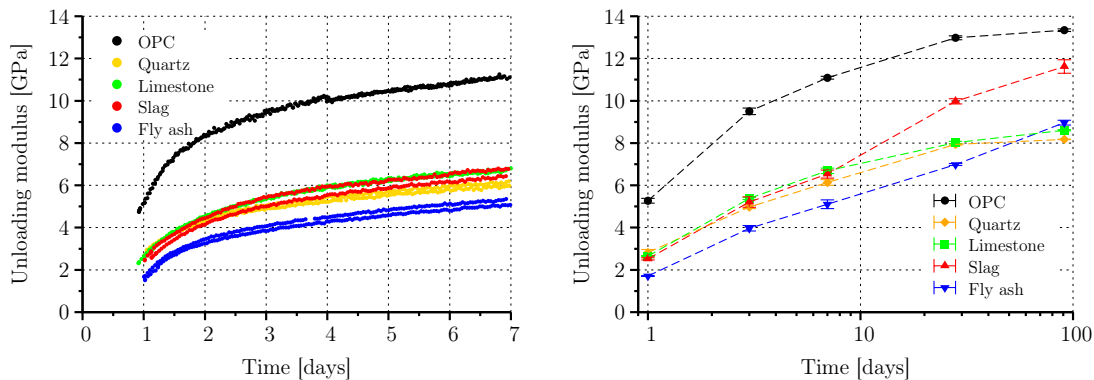


(c) Force values used for to asses unloading modulus.

(d) Stress - strain diagrams for all 3 cycles

Figure 1.5: Typical loading cycle used to asses unloading modulus of cement paste.

This test procedure was designed for a continuous testing, i.e. each cycle consisting of three loading / unloading cycles was performed every 60 minutes, for a sample from 24 hours up to 7 days old. Samples were then stored in a cooling chamber at $20 \pm 1^\circ\text{C}$ / $90 \pm 1\%$ RH ($99 \pm 1\%$ at LCR and CTU), wrapped in a plastic food preservation foil to reduce evaporation of water from the surface and tested again at 28 and 91 days, see Figure 1.6.



(a) Continuous evolution of unloading modulus during the first days with measurements every hour and two tests for each composition (b) Unloading modulus measured at 1, 3, 7, 28, and 91 days with at least 2 tests at 91 days, 4 tests at 28 days, and 6 tests at 7, 3, and 1 day.

Figure 1.6: The evolution of unloading modulus for all paste compositions as a function of time

Summary of mechanical unloading

Unloading modulus at a given time instant was measured on the unloading branch on each of the three loading/unloading cycles, with at least two samples for a given composition. Minimal scatter of results (see Figure 1.6) shows a good reproducibility of experiments. Due to time constraints, the evolution of the unloading modulus was only measured during the first seven days continuously, and then complemented afterwards with single measurements at 28 and 91 days.

Ultrasonic wave speed propagation

To complement elasticity characterization by means of mechanical unloading we use an ultrasonic wave speed propagation technique which allows to directly iden-

tify the components of the isotropic elastic stiffness tensor of the cementitious material. The procedure is described next.

The equipment used for this testing method are two ultrasonic transversal transducers Panametrics NDT V150-RB (0.25 MHz) connected to a pulser receiver Panametrics-NDT 5077 PR and a digital oscilloscope LeCroy waveRunner 62Xi (600 MHz, 10 GS/s (gigasamples per second) dual-channel). The pulser sends an electrical pulse of 200 V which is converted to a mechanical signal (shear wave) in the transducers. The contact surface of both transducers is coated by a highly viscous material (i.e. honey) prior to testing to provide a connection between the transducer and sample surface. One transducer is connected to the top surface of the sample and sends a shear wave. The second transducer collects this signal and transfers it to the oscilloscope, which amplifies it and shows the time a wave needs to travel through the sample. Transversal transducers used emit a shear wave by default, however, the longitudinal wave is also captured and displayed by the oscilloscope. Time needed for each wave is then used to determine the velocity of both waves as

$$v_i = \frac{h}{t_i}, \quad (1.1)$$

where v_i stands for velocity of longitudinal/transversal wave, h for the height of the sample tested, and t_i for the time a longitudinal/transversal wave needs to travel through the sample. The time depends on the composition and age of sample, but as a rule of thumb, the shear wave needs double the time of a longitudinal wave. The wave length λ can then be calculated as

$$\lambda = \frac{v_i}{f}, \quad (1.2)$$

where f is the frequency used by the transducers.

Following the separation of scales requirement from micromechanics, we introduce a representative volume element (RVE). RVE has a characteristic length of ℓ that has to be sufficiently smaller than the characteristic length of stress or strain fluctuations within the structure \mathcal{L} , or, in case of dynamic loading (i.e. ultrasonics), sufficiently smaller than the wave length λ . At the same time, ℓ has to be sufficiently larger than the characteristic length of inhomogeneities d within the RVE. The term ‘‘sufficiently’’ implies a factor of at least 4–5 times smaller or larger. And further, the length of homogeneities d has to be larger

than a certain threshold d_0 under which the continuum micromechanics theory is no longer valid. These statements can be written as

$$d_0 \ll d \ll \ell \ll \{\mathcal{L}, \lambda\} \quad (1.3)$$

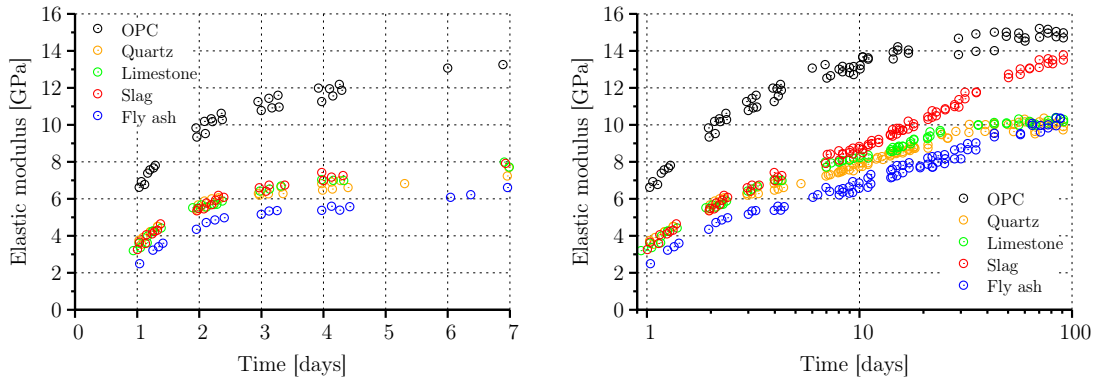
Sought components of the elastic stiffness tensor as a function of the mass density ρ and wave velocity v can be calculated from the general plane wave solution for the displacements within an infinite solid medium with the combination of constitutive equations for linear elastic solids, see [98, 83, 32, 33] as

$$\mathbb{C}_{1111} = \rho \cdot v_L^2 \quad \text{and} \quad \mathbb{C}_{1212} = \rho \cdot v_T^2 \quad (1.4)$$

The two elastic constants characterizing the elastic material (Young's modulus E and Poisson's ratio ν) are in the form

$$E = \frac{\mathbb{C}_{1212} (3 \cdot \mathbb{C}_{1111} - 4 \cdot \mathbb{C}_{1212})}{\mathbb{C}_{1111} - \mathbb{C}_{1212}} \quad \text{and} \quad \nu = \frac{\mathbb{C}_{1111} - 2 \cdot \mathbb{C}_{1212}}{2(\mathbb{C}_{1111} - \mathbb{C}_{1212})} \quad (1.5)$$

For calculated values of the elastic modulus, see Figure 1.7



(a) Evolution of elastic modulus during 7 days with 3-4 measurements per day and modulus until 91 days for all paste compositions two tests for each composition

(b) Continuous evolution of the unloading modulus until 91 days for all paste compositions

Figure 1.7: Evolution of elastic modulus as a function of time, during the first 7 days (left) and up to 91 days (right)

Comparison of elastic moduli obtained from mechanical unloading and ultrasonics

Elastic modulus measured by ultrasonics shows higher values than unloading modulus from mechanical tests (see Figure 1.8). One possible explanation is related to the *loading speed*. Samples subjected to mechanical unloading were loaded by a constant speed equal to 1 kN/s, whereas the speed of wave propagation through the sample was (depending on the age and composition and type of wave) from 1.5–3 km/s for longitudinal waves, roughly half for transversal waves. These values cannot be directly compared to each other, but clearly the loading time and speed of the sample is different. Ultrasonic waves seem to induce pore pressure which apparently increases the stiffness of the sample measured, regardless of time and composition.

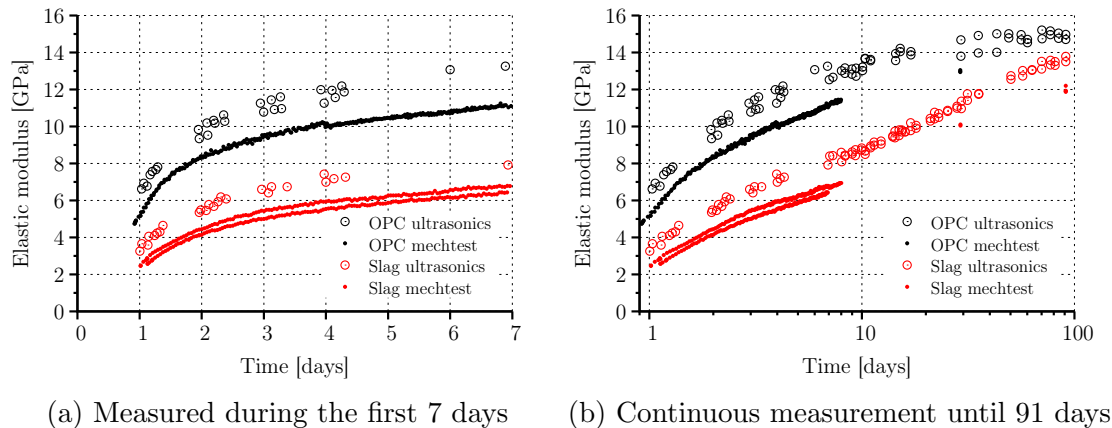


Figure 1.8: Comparison of elastic moduli during 7 days for OPC (black) and slag-blended paste (red)

1.4.3 Compressive strength

The evolution of compressive strength of cement pastes from early-age up to maturity is the main objective of the experimental testing programme. The main focus is on the performance of blended cements, i.e. a direct comparison between both inert fillers (quartz and limestone) and both SCMs (slag and fly ash), at 1, 3, 7, 28, and 91 days to the reference OPC. Samples from all five compositions were tested in two different laboratories (at LCR and TUW) using slightly different testing procedures but with vanishing impact on the compressive strength results.

To make results relevant, from 4 up to 12 samples of a given composition and age were tested at the same time. Samples were cylinders with a diameter of 30 mm and height of approx. 80 mm. Samples used for ultrasonics were also used for compressive stress determination in order to optimize the usage of raw materials. They were cut into halves, both their top and bottom surfaces grinded to ensure close plan-parallelity.

Testing at Lafarge Centre de Recherche

Samples at the age of 3 and 28 days were tested at LCR. After fabrication, they were kept in $20\pm 1^\circ\text{C}$ / $99\pm 1\%$ RH until testing. Any irregularities near the top (or bottom surface) were cut off by ATM Brillant 220 wet abrasive cutting machine prior to testing. This resulted in a varying height of the sample, however, the minimal height recorded after this cutting procedure was 66 mm. Resulting height-to-diameter ratio is always higher than 2:1 for all tested samples. The machine used for compressive testing was Roell Amsler HA 250 dynamic servo-hydraulic testing machine equipped with a Zwick Roell 250 kN load cell.

Once the sample was positioned and centralized on the loading plate, a compressive strength test was started using a prescribed piston displacement speed of $\bar{v} = 0.001$ mm/s. Resultant strain rate is then approx. equal to $\dot{\epsilon} = 1.25 - 1.5 \cdot 10^{-5}$ /s depending on the height of sample used (due to cutting). Duration of each test (until the maximum force was reached) was approx. 5 ± 2 min, depending on the composition and age of sample.

Testing at TUW

Samples at the age of 1, 7, and 91 days were tested at TUW. After fabrication, they were kept in $20\pm 1^\circ\text{C}$ / $90\pm 1\%$ RH until testing. Any irregularities near the top (or bottom surface) were grinded by shaving using a Stanley knife directly after demoulding. The machine used for compressive testing was Walter&Bai LFM 150 electro-mechanical universal static testing machine equipped with a 150 kN load cell.

The “bottleneck” setup was also applied during strength testing, in order to achieve a central load application (see Figure 1.9). Two steel cylinders with bottlenecks and with washers (used to increase the contact area) were attached

to the top and bottom surfaces of the sample. This test setup resulted in no pre-peak spalling of the sample. In order to reduce the undesired shear forces that are created at the interface between two materials with different Poisson's ratios, two sheets of Teflon were placed between the paste sample and the steel cylinders. This setup resulted in axial splitting of the sample without a shear cone, indicating a true material test (as opposed to a structural test where failure of the material is followed by the formation of shear cones on the top and bottom surfaces of the sample).



Figure 1.9: Compressive strength test setup showing steel cylinders with bottle-necks and two layers of Teflon separating them from the sample

Once the sample was positioned and centralized on the loading plate, a compressive strength test was started using a prescribed piston displacement speed of $\bar{v} = 0.006$ mm/s. Resultant strain rate is then approx. equal to $\dot{\epsilon} = 8.5 \cdot 10^{-5}$ /s depending on the height of sample used (due to shaving). Duration of each test (until the maximum force was reached) was approx. 0.5 – 1 min, depending on the composition and age of sample.

Summary of compressive strength measurement

The evolution of compressive strength measured for all pastes is on Figure 1.10. All pastes exhibit a steady increase of strength in time. OPC (black) tested at 91 days exhibits a lower strength than at 28 days. This fact can be attributed to microcracking induced by drying shrinkage, when the samples were not kept

at $99 \pm 1\%$ RH but rather $90 \pm 1\%$ RH. The impact of slag addition (red) is clear from 7 days onwards, when a pozzolanic reaction starts and slag begins to form additional C-S-H. This behavior can clearly be observed on the evolution of unloading modulus (compare with Figure 1.6b) as well as microstructural composition (see Figure 1.3c). The impact of fly ash is also visible between 28 and 91 days for both elasticity and compressive strength testing. It is very hard to tell any difference between the mechanical performance of both inert fillers – quartz and limestone, even if the addition of limestone causes change in the production of hydration products within the microstructure.

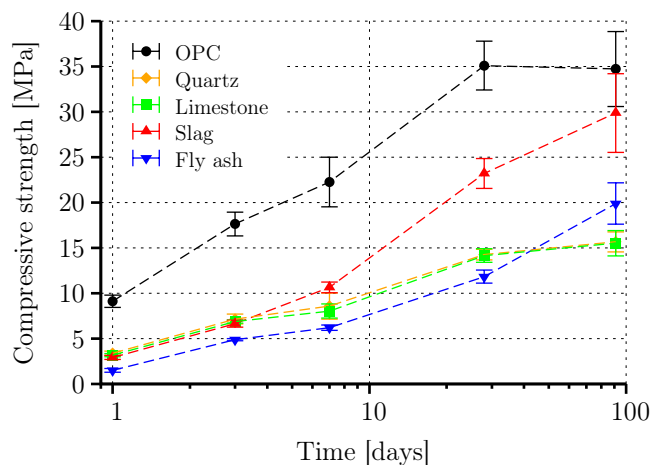


Figure 1.10: Evolution of compressive strength of all paste compositions at 1, 3, 7, 28, and 91 days.

1.4.4 Splitting tensile strength

Direct determination of tensile strength of cementitious materials is a very challenging task due to many reasons. The production of cement paste samples is a tricky part on its own, especially due to the risk of air entrapment during mixing. Very high water-to-cement ratios used for the blended cements ($w/c = 0.93$, see Table 1.4) imply paste bleeding and segregation of clinker particles. Due to this fact, samples have to be agitated (rotated) during the curing period. Cylindrical moulds suit this task very well as they can be sealed and attached to a rotating device easily. However, the production of cement paste prisms or even cubes is due to the above-mentioned reasons extremely challenging. For these reasons we used an indirect method to obtain the tensile strength – Brazilian splitting tests.

Following ASTM standard testing method [6] recommendations for concrete we used the following test setup for the splitting test on cement paste. Dimensions of the sample were identical to those of compressive tests, i.e. 30x80 mm. The sample was positioned on the loading plate, perpendicular to its longitudinal axis. Instead of using thick plywood (as recommended in [6]) we used two thin (< 1 mm) rectangular (30x90 mm) pieces of wood veneer, that were inserted on the top and bottom surfaces of the sample with fiber orientation perpendicular to the longitudinal axis of the sample. Wooden plates even the force distribution, resulting from an uneven surface, along the length of the sample (see Figure 1.11).



Figure 1.11: Splitting tensile strength testing

The loading speed was manually regulated (depending on age and composition of the sample) so that the maximal force measured was achieved within the range 0.5 – 1 min (as in the case of the compressive strength test). This setup ensured axial splitting of the sample (along its longitudinal axis) by a single crack. Maximal force F measured was then recalculated into the splitting strength T as

$$T = 2 \frac{P}{\pi} l d, \quad (1.6)$$

where l and d stand for the length and diameter of the sample, respectively.

Summary of splitting strength measurement

Inert quartz-blended pastes exhibit nearly identical behavior to limestone-blended pastes (see Figs. 1.6b and 1.10) and were excluded from splitting tests. Similar

evolution of mechanical behavior (when compared to compressive strength evolution) is observed for all pastes. Splitting strength of fly ash (blue) observed at 91 days is however unexpected. This can be attributed to the fact that a different testing machine was used for this test. The commonly adapted presumption that the ratio of compressive-to-tensile strength being equal to 8 – 12 is clearly not constant and depends on the age and composition of the sample as it can be seen on Figure 1.12. Splitting strength is used instead of pure tensile strength (which was not measured).

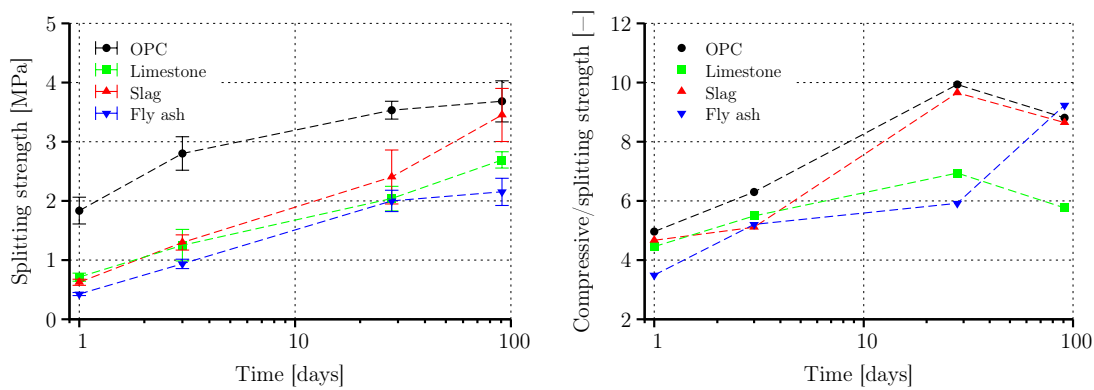


Figure 1.12: Evolution of splitting tensile strength of investigated paste compositions at 1, 3, 28, and 91 days (left) and the evolution of compressive-to-splitting strength until 91 days (right).

Chapter 2

Unloading-Based Stiffness Characterisation of Cement Pastes During the Second, Third and Fourth Day After Production

This chapter is based on a joint publication of Phillip Karte, Michal Hlobil, Roland Reihnsner, Wolfgang Dörner, Olaf Lahayne, Josef Eberhardsteiner, and Bernhard Pichler published in Strain, (2015), vol. 51, pp. 156–169.

2.1 Introduction

Cementitious materials are hierarchically organized. Smallest building blocks are nano-sized calcium-silicate-hydrates (C-S-H) representing the primary product of the chemical hydration reaction between cement clinker and water [75, 4]. C-S-H blocks and nano-sized gel pores constitute C-S-H gel [127]. C-S-H gel and capillary pores built up a porous hydrate foam [119]. Hydrate foam and embedded unhydrated cement grains constitute cement paste. Cement paste and embedded sand grains built up mortar. Finally, mortar and embedded aggregates constitute concrete. The microscopic hydration reaction is responsible for the macroscopic stiffness evolution of cementitious materials, and this was the motivation for the development of multiscale models for upscaling elastic stiffness of cementitious

materials, see, e. g. [22, 137, 120, 148, 9]. Such models consider *constant* material properties of the C-S-H gel. However, recent nuclear magnetic resonance studies [106] show that the density of the C-S-H gel is continuously increasing during hydration, and this motivates the development of further improved multiscale models. Their predictive capabilities are typically checked based on experimental data referring to a scale of observation which is higher than the one of the C-S-H gel. In order to support such validation activities, we here carry out experiments on the cement paste level, because is the smallest scale at which classical macroscopic laboratory testing can be carried out.

Experimental techniques for elastic stiffness characterization include (i) quasi-static methods, such as mechanical unloading, and (ii) dynamic methods, such as ultrasonics or resonance frequency testing. The current state-of-the-art of early-age stiffness characterization on the level of *concrete* is described by Boulay et al. [26, 27], who performed an interesting round-robin-test, involving three laboratories which applied quasi-static and dynamic methods, in order to investigate the stiffness evolution of concrete, starting at very early age and continuing up to the fourth day after production. As for early-age stiffness characterization on hydrating *cement pastes*, in turn, Chamrova [37] carried out quasi-static experiments on two different mixes, 12, 18, 24, and 36 hours after production. Maia et al. [96] tested 17 cement pastes during the first seven days after production. The stiffness evolution was measured continuously, based on resonance frequency testing of composite beams. The comprehensive study involved pastes with initial water-to-cement mass ratios ranging from 0.3 to 0.5, as well as with different contents of limestone filler, fly ash, silica fume, and metakaolin. The dynamic test method allows for testing at very early ages, providing interesting insight into the fluid-to-solid transition of cement pastes, see [97]. The same method was used by Granja et al. [63] who carried out comparisons with ultrasonics, with Vicat needle penetration testing, and with unloading experiments on two different cement pastes with $w/c = 0.50$. These tests were carried out two, three, and seven days after their production.

Testing campaigns on early-age stiffness properties of hydrating cement pastes typically focus on the liquid-solid transition, see, e.g. [97, 140], on the very early-age behavior during the first day after production, see, e.g. [28, 37, 96], or on stiffness properties at mature ages of 28 days or even more, see, e.g., [69, 67]. In practical concrete construction, in turn, formworks are typically removed 24 hours

after production. This underlines that knowledge on mechanical properties of cementitious materials during the second, third, and fourth day after production are of high relevance for the ongoing construction process. This period of time was covered by continuous resonance frequency testing carried out by Maia et al. [96], and Chamrova [37] contributed quasi-static experiments 24 and 36 hours after production. Results from quasi-*continuous* stiffness characterization by means of unloading, however, are – to the best of our knowledge – not yet available in the open literature. This provides the motivation for the present study.

We here develop a novel test setup which allows for repeated unloading experiments on cement pastes, during the second, third, and fourth day after production. Early-age unloading experiments on cement pastes are challenging, because the materials are very prone to be damaged by virtually any mechanical loading. In this context, it is noteworthy that creep deformations of cementitious materials are likely to be associated with damage, as described next. Recent acoustic emission observations carried out in parallel with creep tests on concretes [133], namely, have shown (i) that acoustic events are proportional to the creep deformation, and (ii) that the acoustic event rate (= damage rate) increases with increasing load level. The latter relationship was reproduced by Fischer et al. [55] based on a power law which suggests that creep will damage cement pastes at virtually any load level, even below 30 percent of the strength, which is typically used for cyclic loading-unloading experiments, see, e.g., [37, 63]. In order to protect cement paste samples from accumulation of damage, we here deliberately choose a specifically small compressive stress level. While this allows us to carry out more than 200 loading-unloading cycles (which can be interpreted as creep tests, each with a duration of 20 seconds), we have to tackle several trade-off challenges concerning the layout of the specimens, the realization of the load application, the control of the testing machine, and the strategy for measuring deformations based on Linear Variable Differential Transducers (LVDTs).

The paper is structured as follows. The composition of the analyzed materials as well as the production technique for specimens for stiffness characterization are described in Section “Pure and fly ash-blended cement pastes”. A novel test setup for nondestructive uniaxial compression testing and a related testing procedure for early-age characterization of unloading modulus represent the main original contributions, see Section “Unloading in uniaxial compression”. The calorimetry-based link between material age and hydration degree is the focus

of Section “Isothermal Differential Calorimetry”. Complementary ultrasonics experiment providing access to the early-age evolution of dynamic Young’s modulus is described in Section “Ultrasonics experiments”. The experimental results are discussed in Section “Discussion”, before the paper closes with a concluding section.

2.2 Pure and fly ash-blended cement pastes

Our analyses involve cement pastes with three different compositions, based on a cement of type CEM I 42.5 N, a commercially available fly ash, and distilled water. The compositions are defined in terms of the initial water-to-cement mass ratio w/c and the initial water-to-solid (binder) mass ratio w/s .

- Paste 1 is produced from cement and water only, with $w/c = w/s = 0.50$. This is representative for compositions used in building construction.
- Paste 2 is produced from cement and water only, with $w/c = w/s = 0.42$.
- Paste 3 is a fly ash-blended cement paste exhibiting $w/c = 0.50$ (compare with Paste 1) and $w/s = 0.42$ (compare with Paste 2), i. e. the mass of the solid constituents is composed of 16 % fly ash and of 84 % cement.

As far as the blending strategy for paste 3 is concerned, we here follow the approach used in core-project 10 of the industrial-academic research network on cement and concrete (NANOCEM¹), i. e. we compare different mixes which are based on the *same* type of cement, including mixes where this cement is partly replaced by fly ash, following a recommendation by industrial supervisors from Lafarge and WR Grace.

Cylindrical specimens for stiffness characterization are produced by mixing suitable masses of cement, water, and fly-ash, according to the following procedure. The raw materials are mixed for one minute in a mixer. During the subsequent minute, the suspension is hand-mixed with a spoon, in order to ensure homogeneity of the mix even close to the surface of the mixing bowl. This is followed by another minute of mixing with the mixer. Subsequently, the bowl is dynamically excited on a vibration table, to remove possibly entrapped air from the paste. Finally, we let the material slide – over an extended funnel – into an inclined

¹see <http://www.nanocem.org>

mold. During this action, the mold is placed on the vibrating table, separated from the latter with a sponge, such that the effective vibration energy can be controlled by the force with which the mold is pressed against the sponge.

The cylindrical specimens exhibit a diameter $d = 30$ mm and a height $h = 150$ mm. They are cured in an upright position, inside a climate chamber conditioned to 20 degrees centigrade and to a relative humidity amounting to 95 percent. In order to avoid significant loss of water by means of vaporization, the samples are always sealed against the ambient air, apart from short-term handling operations such as demolding, surface treatments, dimensioning, and weighing, described next. The samples are typically demolded 23 hours after production. This is followed by surface treatment aiming (i) at removing zones which might be affected by segregation effects, both from the bottom and from the top of the specimens, and (ii) at achieving co-planarity of the two circular end surfaces. The best method for these tasks turned out to be careful shaving with a Stanley knife, because standard procedures such as grinding could be shown to damage the tested materials measurably.

2.3 Testing overview

Individual specimens were either subjected to cyclic loading-unloading tests or to ultrasonic testing. As for the loading-unloading tests, the specimens were permanently installed inside a climate chamber (with inside air temperature amounting to 20 ± 0.08 °C) which is integrated into the testing machine. This rendered parallel testing of the same samples with ultrasonics impossible. As for ultrasonics testing, other specimens were stored in a separate climate chamber (with inside air temperature amounting to 20 ± 0.30 °C), they were only taken out for the duration of the tests, and they were returned immediately afterwards.

2.4 Unloading in uniaxial compression

A uniaxial compression experiment complying with scientific accuracy standards requires (i) loading of specimens by means of close-to-perfect uniform normal tractions, and (ii) a countermeasure against undesired shear stresses stemming from friction in the interfaces between specimen and load platens. As for (i) we

note that – in classical setups – load platens are in direct contact with the test specimens such that any imperfection regarding the co-planarity of load platens and of specimen surfaces results in an undesired eccentricity of the loading. This induces stress and strain gradients inside the specimen, contradicting the homogeneous stress and strain fields required for a *material* test. As for (ii) pioneering work goes back to Kupfer et al. [90] who used brush bearing platens to reduce edge effects to a reasonable minimum, see also the review of classical test methods provided by Amieur [5], as well as Boulay et al. [26, 27] for the current state-of-the-art.

We here present a new test setup which allows us to achieve close-to-perfect uniform normal stress fields within the measurement regions of the tested specimens, even for slender specimens and in the presence of small imperfections regarding co-planarity of the two loaded specimen surfaces. In addition, we use compressive load levels which are as small as possible, in order to prevent the specimens from accumulating damage during the tests. While this involves several trade-off challenges which are the focus of Section “Discussion”, we here proceed with describing the developed test setup, the prescribed loading history, the data acquisition system, the strategy for minimize loading eccentricity, as well as test evaluation and results.

2.4.1 Test setup

We use a serial arrangement of the specimen with other elements, including two metal cylinders exhibiting so called bottlenecks: one above and one below the specimen (Fig. 2.1). The bottlenecks exhibit a diameter of 3 mm, and this is one order of magnitude smaller than the diameter of the sample, which amounts to 30 mm (Fig. 2.1). The applied force is transmitted through the entire serial arrangement and, hence, also across the two bottlenecks, such that the loading represents in very good approximation a “point loading” there. Connecting the two loading points by a straight line defines the axis of loading, and our setup is chosen such that the axis of the cylindrical specimen coincides with the axis of loading.

Loading of specimens by means of already quite uniform normal tractions is achieved through the steel cylinders which are directly attached to the specimen. This can be shown based on threedimensional Finite Element simulations

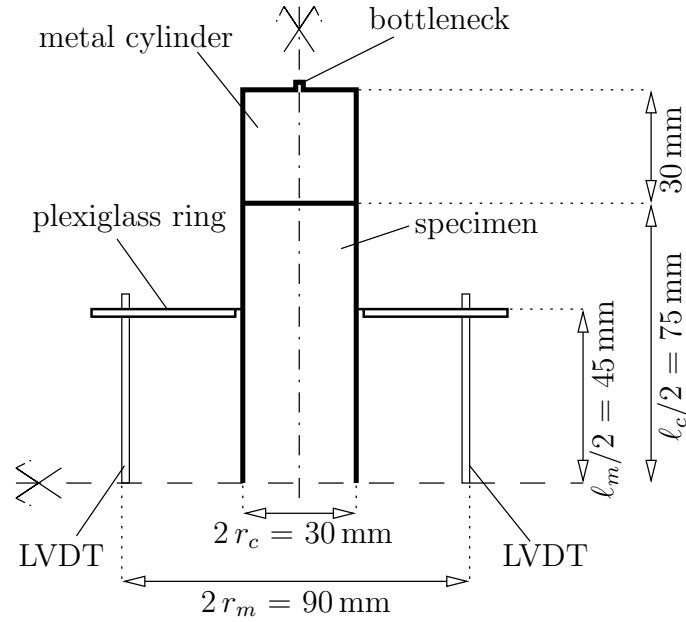


Figure 2.1: Symmetric upper half of the test setup consisting of a metal cylinder with a bottleneck, the cylindrical specimen, and a plexiglass ring holding five LVDTs which are evenly distributed around the perimeter of the specimen

(Fig. 2.2), discussed next. The metal cylinders widen the stress trajectories from the end with the bottleneck, to an almost homogeneous load distribution at the other end, where the metal cylinder is in contact with the specimen, see Figure 2.2(a). Still, metal and cement paste exhibit different Poisson's ratios. This induces – under compressive axial loading – incompatible lateral displacements in the metal-specimen interfaces, resulting in friction-induced shear stresses acting in these interfaces, see Figure 2.2(b). They render the stress field inside the specimen inhomogeneous and multiaxial, contradicting the desired uniform and uniaxial compressive stress state. Notably, the principle of Saint Venant [8] implies that the self-equilibrated shear stresses decrease with increasing distance from the metal-specimen interfaces, such that they reach insignificant magnitudes in a distance amounting to one times the diameter of the specimen, see Figure 2.2. In other words, the top and bottom 30 mm of the specimen are considered to be affected by the undesired and hardly measurable shear stresses, such that these regions are actually to be interpreted as a part of the load application setup. Outside these boundary domains, i. e. in the central part of the specimen, a uniform uniaxial stress state free of significant shear stresses prevails.

Accurate deformation quantification requires measurements directly on the sample. Herein, we use five Linear Variable Differential Transducers (LVDTs) of

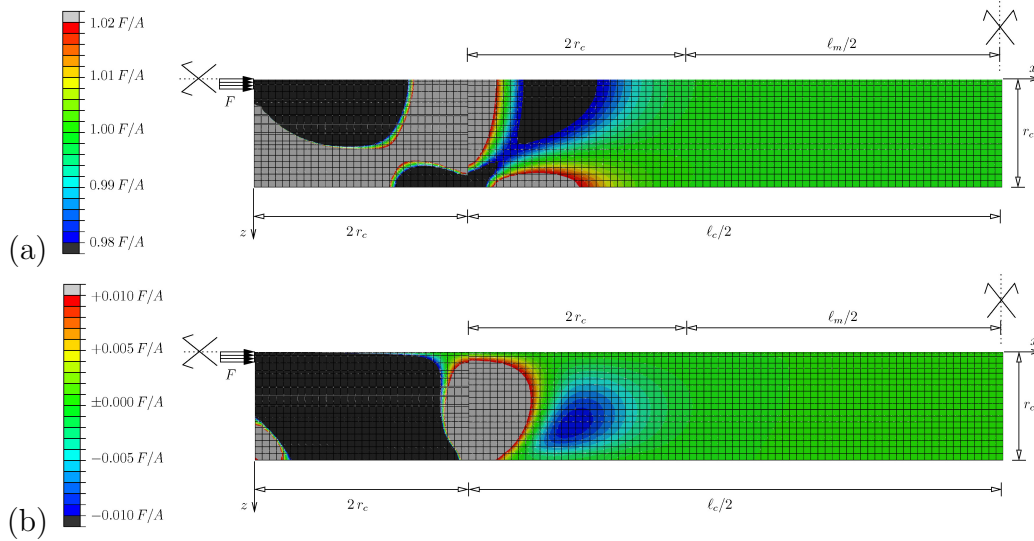


Figure 2.2: Three-dimensional Finite Element simulations of the chosen loading setup including the bottlenecked metal cylinder and the cement paste specimen: (a) distribution of axial normal stresses, and (b) distribution of shear stresses, indicating a uniform stress field in the central measurement region of the specimens; F = absolute value of applied force, A = cross-sectional area of cylindrical cement paste sample, F/A = absolute value of nominal normal stress in cylindrical cement paste sample

type “Solartron”, measuring the relative displacement between two plexiglass rings which are fixed – in a distance of 90 mm – to the aforementioned central part of the specimen (Fig. 2.1). The plexiglass rings are clamped to the specimen such that a continuous contact around the specimen’s diameter is established. The five LVDTs are evenly distributed around the perimeter of the specimen. The stiffness contrast between plexiglass and cement paste does not influence the measurements significantly, because the axial forces transmitted across the five LVDTs is as small as 0.5 N, and this value does not change measurably when considering LVDT length changes up to 10 μm . Therefore, the plexiglass rings behave – in very good approximation – like rigid bodies during the actual tests.

Noting that three LVDTs would be sufficient to measure the relative movement of the two plexiglass rings, our redundant setup with five LVDTs ensures an overdetermined mode of measurements. This increases the measurement accuracy, as quantified in the following based on the standard deviation of the mean of parallel sensors, σ_{mean} . This statistical quantity is a function of the standard deviation σ of the individual LVDTs and of the number n of LVDTs which are used as

parallel sensors:

$$\sigma_{mean} = \frac{\sigma}{\sqrt{n}} \quad (2.1)$$

Comparing the standard deviation of the mean for three and five parallel sensors, respectively, underlines an increase of measurement accuracy by 29 percent:

$$\frac{\sigma_{mean}(n=3) - \sigma_{mean}(n=5)}{\sigma_{mean}(n=3)} = 0.291 \quad (2.2)$$

Also during mechanical testing, the samples are conditioned to 20 degrees centigrade, because they are still undergoing the chemical hydration process which is temperature-activated such that the speed of hydration increases with increasing temperature and vice versa. To this end, the described test setup was placed inside an insulated temperature chamber, conditioned with a temperature control unit “Lauda RK8 KP”, such that the inside air temperature amounts to 20 ± 0.08 °C.

2.4.2 Prescribed loading history

Three loading-unloading cycles are performed every hour, with help of an electromechanical universal testing machine of type “Walter and Bai LFM 150”. During the remaining part of every hour, a permanent compressive force amounting to 0.05 kN ensures that the whole setup (including the sample and the bottlenecks) stays in an upright position without tipping over. All loading and unloading events are carried out under force control, with a desired force rate amounting to 1 kN/s, corresponding to a cement paste-related stress rate amounting to 1.41 MPa/s. Subsequent load level changes are separated from each other by a waiting period amounting to 20 s. First, the compressive load level is increased from the permanent load level up to 0.10 kN (0.14 MPa). This is followed by three loading-unloading cycles up to 0.40 kN (0.57 MPa) and back to 0.10 kN (Fig. 2.3). Finally, the load level is reduced back to the permanent load level.

The PID control settings of the testing machine is chosen such as to maximize the central part of each unloading event, in which the desired force rate (1 kN/s) was actually reached, i. e. to minimize the durations of the initial acceleration period and of the final deceleration period (Fig. 2.4). The optimum PID setup results in overshooting the upper load level (0.40 kN) up to 0.45 kN (0.64 MPa) and of

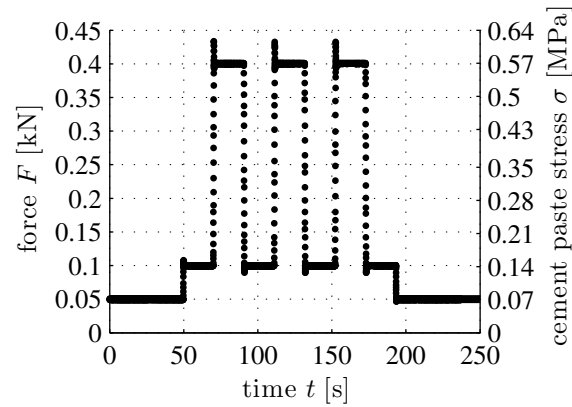


Figure 2.3: Loading history repeated every hour, essentially consisting of three compressive loading-unloading cycles between 0.10 kN and 0.40 kN

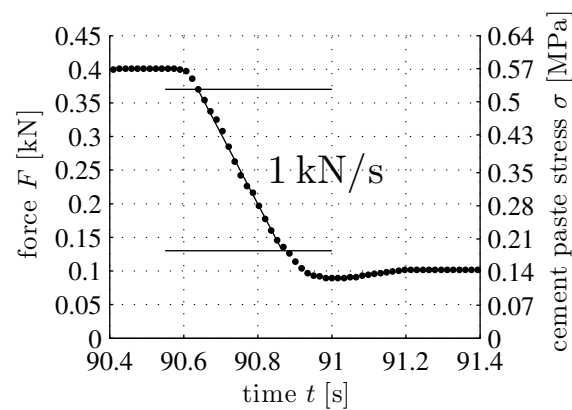


Figure 2.4: Detail of the unloading event illustrated in Fig. 2.3: the desired unloading speed amounting to 1 kN/s is realized in the central part

undershooting the lower load level (0.10 kN) down to 0.08 kN, but the force never fell significantly below the permanent load level (0.05 kN) which ensured to keep the setup in the desired position.

The described loading history ensures (i) nondestructive testing, (ii) at a virtually constant microstructure of the sample, (iii) with a minimum influence of creep on the unloading behavior, but (iv) still suitably large deformations such that the LVDT measurements are reliable. These aspects are discussed next. As for (i), we note that the maximum compressive load, 0.45 kN, corresponds to a compressive normal stress of 0.64 MPa, and this is smaller than 30 percent of the uniaxial compressive strength of the tested materials at any time of testing. In other words, the tests stay out of the so-called nonlinear creep regime [135], which would result in damage of the material [133, 55]. As for (ii), we emphasize that one set of three unloading cycles is finished within 150 seconds. During this period of time, the chemical hydration process does not make significant progress, such that all three unloading events refer to practically the same microstructure. As for (iii), it is noteworthy that each individual unloading event is practically finished within two tenths of a second. This is so short that time-dependent creep deformations do not contribute significantly to the unloading deformations. As for (iv), we note that the unloading-induced elongation of the specimens typically amounts to $5 \mu\text{m}$ (Fig. 2.5), and this is significantly larger the effective signal fluctuation of the individual LVDTs, which is smaller than $0.2 \mu\text{m}$, see LVDTs readings captured right before a test, illustrated in see Fig. 2.6. From the mean

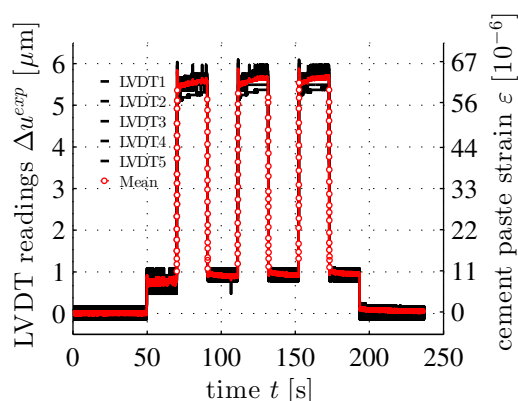


Figure 2.5: Typical measurements of the five LVDTs and their mean values (see circles), after minimization of loading eccentricity

signal of the five LVDTs (Fig. 2.6) we conclude that the effective measurement accuracy of the averaged signals amounts to less than $\pm 0.1 \mu\text{m}$, and this is by a

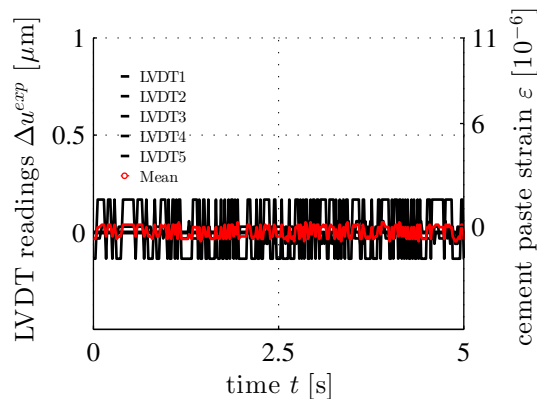


Figure 2.6: Typical fluctuation of the signals of five LVDTs, captured a few seconds before a loading-unloading cycle began

factor of 50 smaller than $5 \mu m$, rendering our measurements sufficiently accurate for our study purpose.

2.4.3 Data acquisition

The measurement signals of the five LVDTs (Fig. 2.5) together with the signal from the force measurement unit of the universal testing machine (Fig. 2.3) are processed and stored inside Excel sheets with help of the digital measurement equipment “Orbit” of “Solartron Metrology”. A visual basic script controls the measurement frequency: during the loading-unloading cycles, 70 individual readings are taken every second; during the rest of the hour (permanent load level), the measurement frequency is reduced to one reading every two seconds.

2.4.4 Minimization of loading eccentricity

Unavoidable eccentricity of the loading results in combined compression *and* bending of the specimen, and bending is responsible for the fact that the five LVDTs do not deliver exactly the same readings. Vice versa, the differences between individual LVDT readings allow for quantifying the effective eccentricity of the applied normal force, as described next. To this end, we evaluate our deformation measurements based on first-order beam theory, i. e. the specimen part between the two plexiglass rings is idealized as a simply supported beam with axial coordinate x . The beam is loaded, at both ends, by a compressive normal force F exhibiting an eccentricity e in the negative z -direction, see Fig. 2.7.

Therefore, both the normal force N and the bending moment M are constant

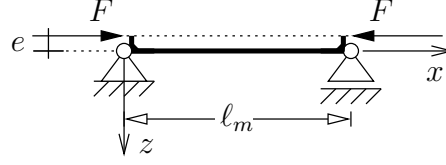


Figure 2.7: Model for the central part of the specimen, located between the two plexiglass rings: simply supported beam subjected to a normal force F exhibiting an eccentricity e in the negative z -direction

along the beam

$$N(x) = -F, \quad M(x) = F e \quad (2.3)$$

The field of the axial displacement component reads, according to first-order beam theory, as

$$u(x, z) = -\frac{Fx}{EA} - \frac{Fe}{EI} \left(\frac{l_0}{2} - x \right) z \quad (2.4)$$

where E stands for Young's modulus and where $EI = E r_c^4 \pi/4$ as well as $EA = E r_c^2 \pi$, respectively, stand for the bending stiffness and for the extensional stiffness of the cylindrical specimen. The beam-theoretical analogon to the measurements of the j -th LVDT is obtained by calculating the difference of the axial displacements between $x = 0$ and $x = l_m$, i. e. $\Delta u^{mod}(z) = u(x = 0, z) - u(x = l_m, z)$, and by specifying the resulting expression for the z -coordinate of the j -th LVDT: $z_j = r_m \cos(\phi_j)$; this delivers

$$\Delta u_j^{mod} = \frac{F l_m}{EA} \left[1 - \frac{e r_m \cos(\phi_j)}{i^2} \right] \quad (2.5)$$

where i denotes the radius of inertia of the cylinder cross-section ($i^2 = I/A$), and where the polar angles ϕ_j with $j \in \{1, 2, 3, 4, 5\}$ follow from $\phi_j = \phi_1 + (j-1) 2\pi/5$. The two unknowns model quantities, i. e. the eccentricity e and the polar angle of the first LVDT, ϕ_1 , are identified through minimization of the sum of the squared differences between measured length changes Δu_j^{exp} and modeled length changes Δu_j^{mod} :

$$\sum_{j=1}^5 [\Delta u_j^{exp} - \Delta u_j^{mod}]^2 \rightarrow \min \quad (2.6)$$

In order to fine-tune the position of our test setup, a preliminary loading-unloading is performed, and the LVDT readings are analyzed in order to de-

termine magnitude and orientation of the effective eccentricity, see Eqs. (2.5) and (2.6). Based on this information, the position of the specimen is improved, and another preliminary loading-unloading cycle is performed, delivering new LVDT readings. Step-by-step, the LVDT readings are used for optimizing the position of the test setup, until the effective force eccentricity is as small as 0.1 mm, see Fig. 2.5 for corresponding LVDT readings. Once a close-to-optimal position of our test setup is found, the described automatic testing procedure is started, typically 24 h after sample production.

2.4.5 Test evaluation and results

Unloading modulus is determined from point-wisely defined stress-strain-diagrams. The stress ordinates are obtained from dividing the force readings by the cross-sectional area of the cylindrical specimens, $A = 7.07 \text{ cm}^2$ (see the right ordinate in Fig. 2.4). As for the required strain ordinates, the average over the five individual LVDT readings is divided by the LVDT measurement length, i. e. by the 90 mm distance of the two plexiglass rings (see the right ordinate in Fig. 2.5). Plotting stress values as a function of corresponding strain values delivers a chain of data points, which can be very accurately fitted by a straight line, the slope of which represents the sought unloading modulus (Fig. 2.8).

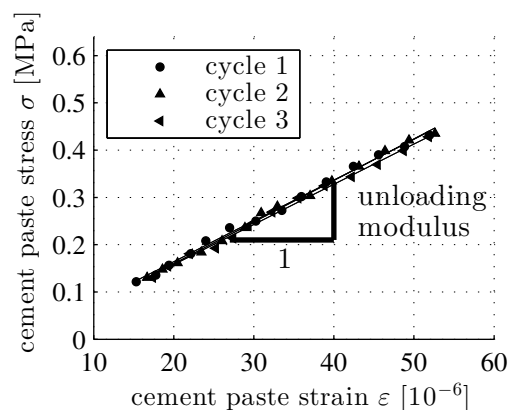


Figure 2.8: Point-wisely defined stress-strain-diagrams referring to three unloading cycles: the slope of best linear fits to the chains of data points represents the sought unloading modulus; quadratic correlation coefficients between the data points and the linear fits amount to $r^2 = 99.6\%$, to $r^2 = 99.7\%$, and to $r^2 = 99.6\%$, respectively.

Our measurements allow us to evaluate three unloading moduli every hour. They

show a very small scatter (Fig. 2.8), indicating a high reproducibility of our tests. Their average value represents the output of each set of three loading-unloading cycles. Plotting these mean values as a function of the age of the materials (Fig. 2.9) underlines that hydration-induced stiffening of the tested materials is underlinear during the second, third, and fourth day after production.

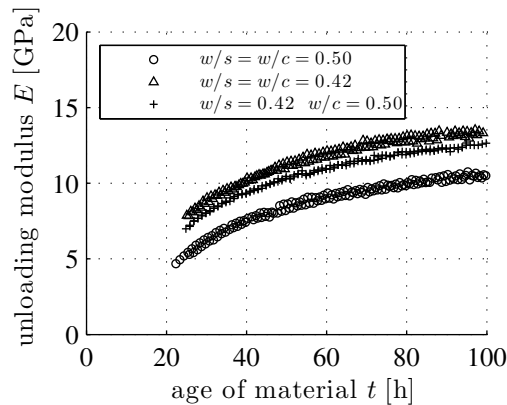


Figure 2.9: Temporal evolution of unloading modulus of the tested cement pastes; paste 1: circles, paste 2: triangles, fly ash-blended paste 3: crosses

For each type of paste, a test repetition was carried out (Fig. 2.9). The evaluated unloading moduli exhibit very satisfactory small differences, underlining the repeatability of our experiments.

2.5 Isothermal Differential Calorimetry

In order to establish a relation between the age of the tested materials and the maturity of their microstructures, isothermal differential calorimetry measurements are carried out at 20 degrees centigrade. Each individual test involves a test tube containing 10 g solid binder and a separated syringe filled with the required amount of distilled water. Both elements are put into a testing cell of a calorimeter “ToniCAL Trio type 7339”. Once a stationary temperature regime is reached, the test is started by injecting the water to the binder and by mixing the paste using a plastic paddle. Notably, both actions are carried out without re-opening the test cell. The primary measurement results are the heat release rate $\dot{Q}(t)$ and the accumulated heat release $Q(t)$, determined during the first four days after mixing, see Figs. 2.10 and 2.11. Two tests are carried out for each

of the three types of pastes. The similarity of results obtained with the same composition indicates a satisfactory reproducibility of the experiments.

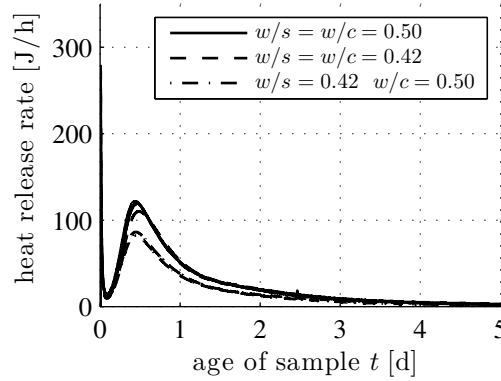


Figure 2.10: Temporal evolution of heat release rate measured in isothermal differential calorimetry with 10 g solid binder and suitable amounts of distilled water; paste 1: solid lines, paste 2: dashed lines, fly ash-blended paste 3: dash-dotted lines

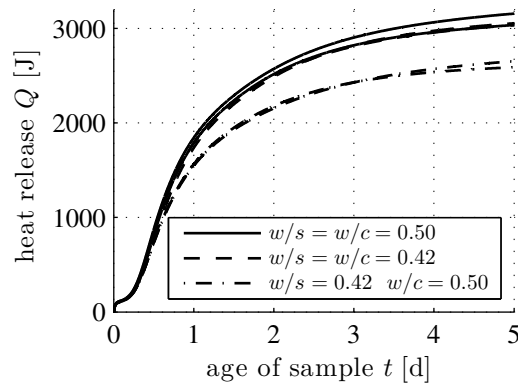


Figure 2.11: Temporal evolution of accumulated heat release measured in isothermal differential calorimetry with 10 g solid binder and suitable amounts of distilled water; paste 1: solid lines, paste 2: dashed lines, fly ash-blended paste 3: dash-dotted lines

Fly ash is well known to exhibit a very small reactivity which is practically negligible during the first days after material production [94]. This suggests that the observed hydration of the fly ash-blended cement paste stems practically speaking from the cement content only.

As to quantify the relation between material age and microstructural maturity, a calorimetry-based estimate of the cement-related hydration degree ξ is determined. To this end, the averaged accumulated heat release $Q(t)$ is divided through

the mass of cement

$$\begin{aligned} m_c &= 10.0 \text{ g} \dots \text{ pastes 1 and 2} \\ m_c &= 8.4 \text{ g} \dots \text{ paste 3} \end{aligned} \quad (2.7)$$

and the result is divided through latent heat of typical CEM I cements [31, 151]

$$\ell_h = 500 \text{ J/g} \quad (2.8)$$

delivering the calorimetry-based hydration degree as

$$\xi(t) = \frac{Q(t)}{m_c \ell_h} \quad (2.9)$$

The described hydration degree increases nonlinearly with time (Fig. 2.12), and all three pastes exhibit virtually the same evolution. This corroborates the ex-

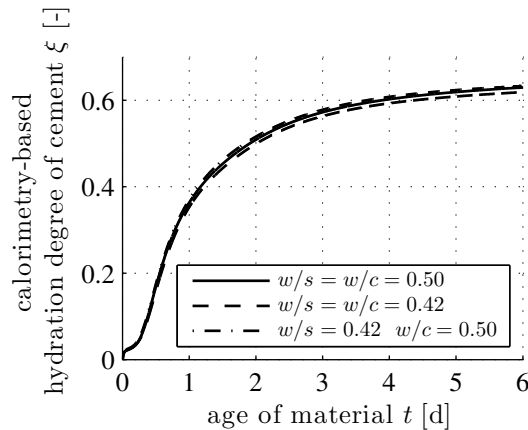


Figure 2.12: Temporal evolution of calorimetry-based hydration degree of cement: paste 1: solid line, paste 2: dashed line, fly ash-blended paste 3: dash-dotted line

pectation that fly ash does not contribute significantly to chemical reactions at the microscale of paste 3. This is consistent with other observations [94] in which it was found that fly ash hydration is hardly reactive at very early ages. In other words, fly ash particles act as practically inert parts of the cement paste microstructure during the performed tests.

Unloading modulus as a function of calorimetry-based hydration degree is obtained from combining the mechanical test data “unloading modulus as a function of material age” with the calorimetry test data “hydration degree as a function of material age”. Unloading moduli of all three analyzed mixes increase practically linearly with increasing hydration degree, in the investigated regime of hydra-

tion degrees ranging from 40 to 60 percent (Fig. 2.13). This is consistent with

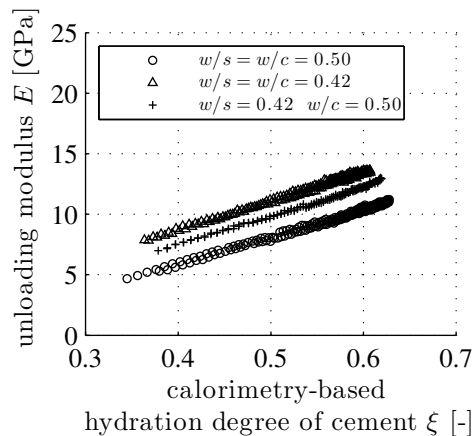


Figure 2.13: Unloading modulus as a function of calorimetry-based hydration degree of cement: paste 1: circles, paste 2: triangles, fly ash-blended paste 3: crosses

findings of Chamrova [37] who carried out quasi-static unloading experiments on two different mixes, 12, 18, 24, and 36 hours after production, corresponding to hydration degrees between 17 and 43 percent, see Fig. 5.14 of [37]. Notably, this is different on the concrete level, where a nonlinear evolution of Young’s modulus is observed with increasing hydration degree, see, e.g., [45].

2.6 Ultrasonics experiments

Ultrasonics experiments provide an independent access to the stiffness of the analyzed cement pastes, namely, to so-called *dynamic* elastic properties. Using an ultrasound frequency amounting to 250 kHz, longitudinal and shear waves are sent through the produced specimens, using a “Panametrics-NDT” equipment. Dividing the cylinder length (= wave travel distance) through the time required for the ultrasound waves to travel through the specimen (= primary measurement result) delivers longitudinal wave speeds v_ℓ and transversal wave speeds v_t , both of which increase with increasing age of the material (Fig. 2.14).

The wave length λ is obtained from dividing wave speeds through the used ultrasound frequency. Notably, the wave lengths were, any time, larger than 4 mm. This underlines that the separation of scales principle [82] was satisfied, i. e. the wavelength values are significantly larger than the size of the representative cement paste volume, amounting to 250 μm ; and this is again sufficiently larger

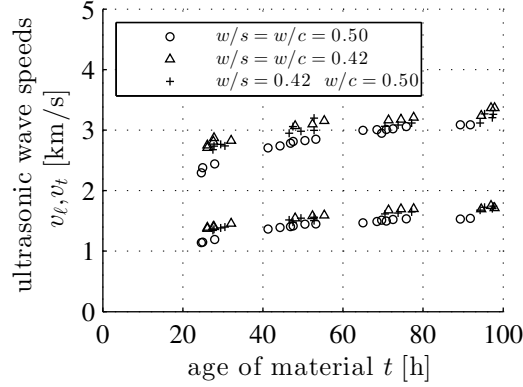


Figure 2.14: Ultrasound wave speeds as a function of material age; paste 1: circles, paste 2: triangles, fly ash-blended paste 3: crosses

than the characteristic size of heterogeneity of the material, which is equal to the characteristic diameter of clinker grains, amounting to $50 \mu\text{m}$.

As for determination of dynamic Young's modulus E_{dyn} , the measured wave velocities (Fig. 2.14) are combined with the mass density ρ of the samples, according to the following relation from the theory of elastic waves traveling through an isotropic elastic body [84]

$$E_{dyn}(\rho, v_t, v_l) = \frac{\rho v_t^2 (3v_l^2 - 4v_t^2)}{v_l^2 - v_t^2} \quad (2.10)$$

Combining ultrasonics results with calorimetry results implies that dynamic Young's moduli increase practically linearly with increasing hydration degree in the investigated regime of hydration degrees ranging from 40 to 60 percent (Fig. 2.15). This is consistent with observations of Boumiz et al. [28], carried out during the first 24 hours after material production, and with observations by Helmuth and Turk [69], carried out on mature cement pastes, six to 24 months after their production.

The measured longitudinal and transversal wave speeds (Fig. 2.14) also allow for quantifying the early-age evolution of dynamic Poisson's ratio

$$\nu_{dyn}(v_t, v_l) = \frac{v_l^2 - 2v_t^2}{2(v_l^2 - v_t^2)} \quad (2.11)$$

Evaluation of our measurement data (Fig. 2.14) according to Eq. (2.11) delivers dynamic Poisson's ratios decreasing from 0.33, at $\xi = 0.40$, to 0.30, at $\xi = 0.60$,

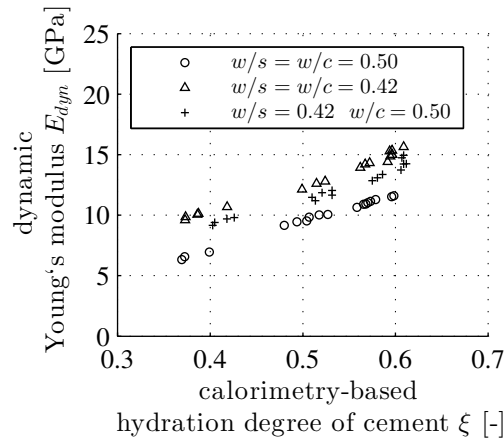


Figure 2.15: Dynamic Young’s modulus as a function of calorimetry-based hydration degree of cement: paste 1: circles, paste 2: triangles, fly ash-blended paste 3: crosses

see Fig. 2.16. This is in very satisfactory agreement with predictions of multiscale

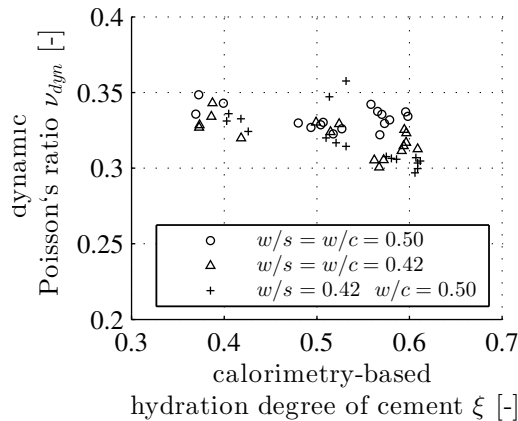


Figure 2.16: Dynamic Poisson’s ratio as a function of calorimetry-based hydration degree of cement: paste 1: circles, paste 2: triangles, fly ash-blended paste 3: crosses

models for cement pastes under undrained conditions, see Fig. 10 of [22].

2.7 Discussion

In the sequel we discuss (i) the significance of the presented study with respect to multiscale modeling of concrete containing interfacial transition zones, (ii) trade-off challenges regarding test design, (iii) hydration-induced temperature

fluctuations inside young cement paste specimens, and (iv) extrapolation of our data to the liquid-to-solid transition at very early ages.

2.7.1 Significance for multiscale modeling of concrete containing ITZs

The presented experimental data are meant to support validation of multiscale models for homogenization of elastic stiffness of hydrating cement paste, starting upscaling from heterogeneities at even smaller scales of observation. Such models will be also beneficial for multiscale models of concrete including consideration of interfacial transition zones (ITZs) covering concrete aggregates. ITZs with a typical thickness of 15 to 30 μm , namely, consist of cement paste, and because of so-called “wall effects” during casting, they exhibit a water-to-cement mass ratio which is increased compared to the bulk paste farther away from the aggregate surface, see, e.g., [143].

2.7.2 Trade-off challenges regarding test design

During the design of our novel test setup, we had to cope with several trade-off challenges. They are discussed next.

The first trade-off concerns relations between the slenderness of the samples and our aim to realize a uniform stress state in the measurement regions of the specimens. The quite slender layout of the specimens was a consequence of our aim to minimize the influence of undesired shear stresses within the deformation measurement region by considering the top and bottom 30 mm of the specimen to be part of the load application setup, see Fig 2.2 (b) for the rationale behind this strategy.

The second trade-off concerns relations between the slenderness of the samples, and the risk of inducing damage into the specimens. For a specific choice of load level, an increasing measurement length (associated with an increasing slenderness of the specimen) would result in larger deformation signals, and this is beneficial for the measurement accuracy of the LVDTs. For a specific choice of the measurement length, in turn, an increasing load level (associated with an increasing risk of damage of the specimen) would result in larger deformation

signals, and this is beneficial for the measurement accuracy of the LVDTs. The possibility to quantify the effective eccentricity of the applied force allowed us to ensure a central load application even in case of a rather slender specimen. Therefore, the length of the cylindrical specimens was set equal to 150 mm, resulting (i) in a length-to-diameter ratio amounting to 5:1, and (ii) in deformation measurement distance between the two plexiglass rings amounting to 90 mm. Given expected Young's moduli between 5 GPa and 15 GPa, a load level as small as 0.40 kN was sufficient to ensure reliable deformation measurements, and this reduced the damage risk to a reasonable minimum.

The third trade-off concerned the question whether to control loading and unloading events via the piston displacement or via the force signal, respectively. In this context, it is noteworthy (i) that we have used two computers, one for controlling the test machine and another one hosting the data acquisition system, and (ii) that they were working independently, such that synchronization of automatic processes was a challenge. It was important that the loading-unloading cycles start, as precisely as possible, one hour after the other, in order to ensure that all tests are recorded by the independent data acquisition system with the highest possible measurement frequency. Force-control has the advantage, that all loading-unloading cycles take the same time, independent of the stiffness of the specimen, and this allowed for keeping both computers synchronized even over 60 hours, which turned out to be beneficial for carrying out automatic testing from Friday evening to Monday morning. A constant force rate results in a constant stress rate, because the cross-sectional area of the specimens is practically constant throughout the tests. Given that the stiffness of cement paste increases with time, a constant stress rate refers to decreasing strain rates. Notably, classical testing is typically based on displacement control, resulting (i) in constant strain rates and (ii) because of the increasing stiffness, in increasing stress rates. Testing under constant stress *and* strain rates is impossible, because of the hydration-induced stiffness increase.

The fourth trade-off concerned the relation between loading speed and the conceptual significance of the obtained unloading moduli. On the one hand, it would be conceptually desirable to change load levels infinitely fast. This would allow for studying purely elastic material behavior, because there would be no time for creep to influence the deformation during unloading. On the other hand, the maximum loading speed that can be realized by the testing machine is limited and

depends on the PID settings of the force-control of the loading machine. Therefore, the PID settings were optimized such as to maximize the force rate while ensuring (i) that the prescribed force rate was realized reliably over a large part of every loading and unloading event (Fig. 2.4) and (ii) that overshooting and undershooting of approached load levels was smaller than 10 percent (Fig. 2.4). This optimization process resulted in a force rate amounting to 1 kN/s.

2.7.3 Hydration-induced temperature fluctuations inside young cement paste specimens

It is interesting to discuss the effective temperature evolution inside the specimens, given that the chemical hardening reaction of cement pastes is exothermic. To this end, we produced two specimens with $w/c = w/s = 0.42$ and measured the internal temperature evolution (Fig. 2.17) in both of them with two embedded temperature sensors each. Although the raw materials were conditioned to

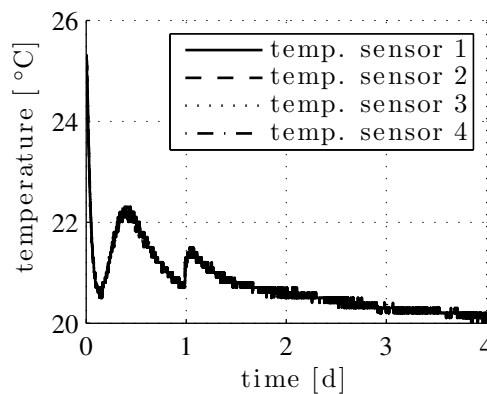


Figure 2.17: Temperature evolution inside cement paste specimens with $w/c = w/s = 0.42$, exposed to a nominal ambient air temperature amounting to 20 °C

the desired 20 °C, mixing of binder and water and the starting chemical hardening reaction resulted in a temperature rise up to 25 °C right after casting. This was followed by a progressive temperature decrease down to 20.7 °C, reached 3.5 hours after production. After that, the characteristic hydration kinetics of cement pastes (Fig. 2.10) resulted in a temperature rise up to 22.2 °C, reached 10 hours after production. This was followed by a temperature decrease down to 20.7 °C, reached one day after production. Demolding and handling of the specimens resulted in a quasi-spontaneous temperature rise up to 21.4 °C. This

was followed by a progressive decrease of temperature down to 20.1 °C, reached 4 days after production.

Because the temperature inside the specimens was always larger than the desired value of 20 °C, the actual evolution of hydration degree differed from the one observed during isothermal calorimetry testing. The actual hydration degree evolution can be determined, based on integrating the following Arrhenius law, see, e.g. [159],

$$\dot{\xi}(t) = \tilde{A}(\xi(t)) \exp\left(-\frac{E_a}{RT(t)}\right) \quad (2.12)$$

In (2.12), $\dot{\xi}$ denotes the rate of the hydration degree, $\tilde{A}(\xi(t))$ denotes the “chemical affinity”, $T(t)$ the temperature history, E_a the activation energy, and R the universal gas constant, with [159]

$$\frac{E_a}{R} = 4000 \text{ K} \quad (2.13)$$

Before we can determine the hydration degree evolution related to the fluctuating temperature history of Fig. 2.17, we need to identify the chemical affinity \tilde{A} based on Eq. (2.12). This is possible based on data from the calorimetry tests which were carried out at a constant temperature amounting to

$$T(t) = 273.15 + 20 = 293.15 \text{ K} \quad (2.14)$$

During calorimetry testing, the evolution of the rate of hydration degree, $\dot{\xi}(t)$, is related to the heat release rate $\dot{Q}(t)$, as follows from the time derivative of Eq. (2.9):

$$\dot{\xi}(t) = \frac{\dot{Q}(t)}{m_c \ell_h} \quad (2.15)$$

Combination of Eqs. (2.7) and (2.8), Eqs. (2.12) to (2.15), and the heat release rate data displayed in Fig. 2.10 allows for determination of the chemical affinity, see Fig. 2.18.

The evolution of hydration degree related to the fluctuating temperature history of Fig. 2.17 follows from (i) specifying Eq. (2.12) for \tilde{A} from Fig. 2.18, for Eq. (2.13), and for $T(t)$ from Fig. 2.17, as well as from (ii) numerical time-integration of the resulting expression for $\dot{\xi}(t)$, see Fig. 2.19.

Assumption of a constant temperature of 20 °C, rather than considering the

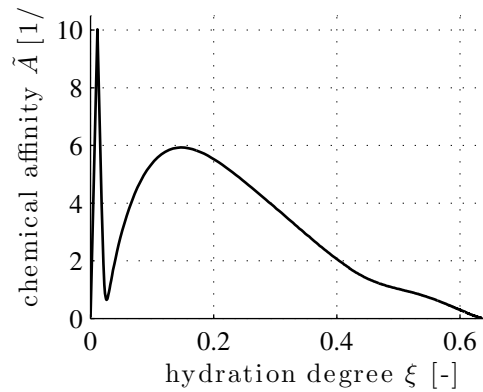


Figure 2.18: Evolution of chemical affinity of cement paste with $w/c = w/s = 0.42$, determined via combination of Eqs. (2.7) and (2.8) as well as (2.12) to (2.15) with the data displayed in Fig. 2.10, as a function of hydration degree determined according to Eq. (2.9)

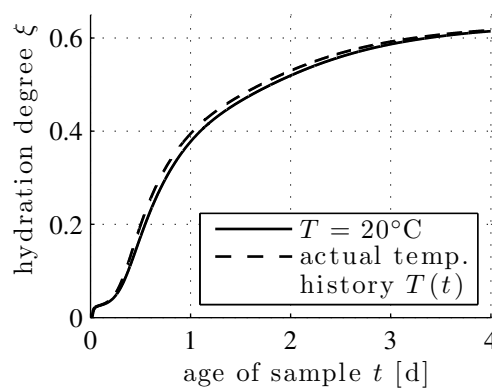


Figure 2.19: Comparison of hydration degree evolution obtained (i) for a constant temperature amounting to 20 °C, see solid line, and (ii) for the actual temperature history of Fig. 2.17, see dashed line; determined by means of numerical integration of Eq. (2.12)

fluctuating temperature evolution of Fig. 2.17, underestimates the hydration degree one day after production by 2.3 percent points, and this deviation decreases progressively down to 1.7 percent points four days after production. This is considered as reliable enough for the present study.

2.7.4 Extrapolation to the liquid-to-solid transition

Direct determination of hydration degrees at the liquid-to-solid transition (so-called hydration degree thresholds) is a very challenging task, because very small loads are sufficient to destroy a freshly formed (and, hence, very fragile) network of solid particles, see, e.g. [140]. Therefore, dynamic testing methods, see, e.g. [28, 97], are clearly preferable over unloading experiments. However, indirect determination of hydration degree thresholds was carried out by Torrenti and Benboudjema [155] who (i) approximated straight line fits to early-age *strength* data of Taplin [150] and (ii) performed extrapolations down to vanishing strength values for the estimation of hydration degree thresholds. Given that the here-measured stiffness evolutions are in very good approximation linear functions of hydration degree, in the investigated regime of hydration degrees ranging from 40 to 60 percent, we implement the same approach in the present context of early-age *stiffness* data. This yields estimated hydration degree thresholds ranging between 4.0 and 14.8 percent, see Table 2.1.

Table 2.1: Hydration degrees at the solid-to-liquid transition of the investigated materials, estimated by adjusting best linear fits to quasi-static Young's modulus evolutions (Fig. 2.13) and using them for extrapolating to stiffness values being equal to zero

mix composition	quadratic correlation coefficient of linear fit	estimated hydration degree threshold (upper bound)
$w/c = w/s = 0.50$	$r^2 = 99.13\%$	$\xi_{\ell \rightarrow s} = 14.8\%$
$w/c = w/s = 0.42$	$r^2 = 99.18\%$	$\xi_{\ell \rightarrow s} = 4.0\%$
$w/c = 0.5, w/s = 0.42$	$r^2 = 99.47\%$	$\xi_{\ell \rightarrow s} = 9.2\%$

Notably, *strength* evolutions have turned out to be overlinear at very early ages, see Fig. 10 of [122], such that straight line extrapolations to very early ages are expected to yield upper bounds for hydration degree thresholds, see Fig. 5 of [121]. Given that similar over-linearities of *stiffness* histories were observed for cement paste at very early age [97], reminiscent of the situation encountered with

concretes [26, 27], it is recommended to interpret the thresholds listed in Table 2.1 as upper bounds.

2.8 Conclusions

We here studied both unloading modulus and dynamic Young's modulus of cement pastes as functions of calorimetry-based hydration degree. Two pure and one fly ash-blended cement paste were characterized during the second, third, and fourth day after production.

As far as the early-age stiffness evolution is concerned, we draw the following conclusions:

- Early-age stiffness of pure and blended cement pastes increases practically linearly with increasing hydration degree, in the investigated regime of hydration degrees ranging from 40 to 60 percent.
- The ultrasound-related dynamic Young's moduli are, 24 hours after production, by 21 percent ($w/c = w/s = 0.42$), by 25 percent ($w/c = 0.5$, $w/s = 0.42$), and by 29 percent ($w/c = w/c = 0.5$) larger than the corresponding unloading moduli. The described ratio reduces monotonously with increasing age of the materials and reaches typical values of 11 to 12 percent, four days after production.
- The difference between dynamic Young's moduli and unloading moduli is likely related to the behavior of water, including the activation of pore pressures in ultrasound testing [164]. This underlines the complexity of cementitious materials, because a similar effect is typically unknown for other media, including tissue engineering scaffolds [95].
- The stiffness evolution of a fly ash-blended cement paste with initial water-to-solid mass ratio $w/s = 0.42$ and initial water-to-cement mass ratio $w/c = 0.50$ falls between the stiffness evolution of a pure cement paste exhibiting $w/c = w/s = 0.42$ and the one of a pure cement paste exhibiting $w/c = w/s = 0.50$. Since fly-ash particles exhibit a significant stiffening effect the stiffness evolution of the blended cement paste is closer to the one of the paste exhibiting $w/c = w/s = 0.42$.

- Performances similar to the one observed here for the fly ash-blended material were the motivation to adjust fineness of cement and the gypsum content in commercial products, in order to improve material properties particularly at early ages.

As far as the hydration kinetics are concerned, we draw the following conclusions:

- During the first four days after production, all three materials exhibit virtually the same cement-related hydration degree, i.e. fly ash particles represent quasi-inert constituents of the microstructure of cement paste.
- At the analyzed blend level of 16 percent of the cement mass, fly-ash does not exhibit a significant “filler effect” [94], i.e. the presence of fly ash particles does not significantly increase the speed of cement hydration by providing preferred nucleation sites for precipitation of calcium silicate hydrates.

Acknowledgments

Funding of the second author provided by the industrial-academic research network on cement and concrete “NANOCEM” (<http://www.nanocem.org>) within the framework of Core Project 10 entitled “Micromechanical Analysis of Blended Cement-Based Composites” is gratefully acknowledged.

Help of system administrator David Kaufmann regarding implementation of a visual basic script allowing for automatic realization of the mechanical compression tests is gratefully acknowledged.

The here-described test setup for the quasi-static unloading experiments is the final result obtained in series of evaluation steps. In this context, interesting discussions with Jaromír Wasserbauer and Ilja Fischer are gratefully acknowledged.

Chapter 3

Micromechanical multiscale fracture model for compressive strength of blended cement pastes

This chapter is based on a joint publication of Michal Hlobil, Vít Šmilauer, and Gilles Chanvillard published in Cement and Concrete Research, (2016), vol. 83, pp. 188–202.

3.1 Introduction

Compressive strength of concrete and its evolution belong to the most important and tested parameters. Due to the multiscale nature of concrete spanning the range from sub-nanometers to meters and its composite nature, several factors on different scales play a role in concrete compressive strength [108]. The most relevant initial factors include the binder type, aggregate type, extent of the interfacial transition zone, and the air content. Time-dependent factors play a role mainly in binder's reaction kinetics which is reflected in the evolution of chemical phases with a direct impact on stiffness and strength evolution.

Up to the time of Hoover Dam construction in the 1930's, a cementitious binder was mostly equivalent to Portland cement. Since that time, Portland clinker has

been substituted more and more by supplementary cementitious materials such as slag, fly ash, limestone or silica fume. The substitution rose from 17% in 1990 to 25% in 2010 among the top world cement producers [154]. A further shift is expected, motivated by economical, ecological and sustainable benefits [60, 61].

The question on the origin of concrete strength becomes reinitiated with the advent of blended binders. The famous Powers' empirical relationship between the gel-space ratio and compressive strength developed for Portland-based materials needs several adjustments when dealing with blended binders [91]. The main reason lies in altered chemistry where a chemically heterogeneous gel differs in chemical phases, e.g. CH may be depleted in pozzolanic reactions or C-A-H phases may emerge. To overcome these deficiencies, micromechanical models taking into account volume fractions directly have been set up for more fundamental understanding.

Continuum micromechanical models able to reproduce the evolution of stiffness and compressive strength have recently been published, e.g. for Portland-based materials [119, 122] or for cocciopesto mortars [109]. Pichler et al. [125] used spherical and acicular representation of hydrates to capture percolation threshold during hydration and the onset on elasticity and strength. Hydrates consisted of solid C-S-H, small and large gel pores and other hydration products. The strength criterion was based on deviatoric strength of hydrates which was identified to be 69.9 MPa. Once the quadratic stress average in arbitrarily oriented needle-shaped hydrates exceeded this strength, the material failed in a brittle manner. Similar modeling approach was also used for C_3S , C_2S , C_3S+C_3A +gypsum pastes, assuming that only C-S-H with the Mohr-Coulomb quasi-brittle failure criterion was responsible for the compressive strength of pastes [153].

Computational micromechanical models generally allow taking into account non-linear elasto-plasto-damage constitutive laws at the expense of computational time. Several 2D and 3D lattice and continuum models were applied for cement paste [58] or concrete [44, 65, 81] to mention a few.

In this paper, a new four-level micromechanical damage model for blended cement pastes is presented, starting from C-S-H globule up to cement paste with entrapped/entrained air. The lowest homogenization level contains C-S-H globules, small and large gel pores [77]. A C-S-H globule is considered to be the only strain-softening component in the multiscale model, leading essentially to failure

at each level. Softening occurs under excessive tension or compression using an elasto-damage constitutive law introduced in Section 3.2.1. Higher levels also use the elasto-damage constitutive law for a phase containing C-S-H globules with an updated homogenized stiffness, strength, and estimated fracture energy. Hence, the strength of cement paste originates from the softening and failure of C-S-H globule. The multiscale model accounts for volume fractions of C-S-H, other hydrates, capillary porosity, clinker, supplementary cementitious materials, entrained / entrapped air and considers the spatial gradient of C-S-H among clinker grains.

The model contains two independent variables that need to be calibrated from experimental data: the apparent tensile strength of C-S-H globules and the spatial gradient of C-S-H. Numerical results for elastic modulus and compressive/tensile strength on each scale are further fitted to microstructure-calibrated analytical expressions, speeding up the whole validation part. Sensitivity analysis identifies key components for the compressive strength of blended pastes.

3.2 Finite element analysis

3.2.1 Damage material model and its implementation

The nonlinear constitutive behavior of quasi-brittle materials, such as cement paste, mortar or concrete, can be generally described by three common theories: plasticity, fracture mechanics, damage mechanics, or their combinations. Plasticity fails to describe stiffness degradation which is needed for strain softening, strain localization, and the size effect, although several extensions were proposed [79]. Linear elastic fracture mechanics can only deal with brittle materials with a negligible process zone ahead of a crack tip and cannot handle microcrack nucleation into a macrocrack.

Damage mechanics, particularly the cohesive crack model, defines the traction-separation law in a plastic zone of an opening crack which is related to the fracture energy of a material and stiffness degradation. Such an approach offers reasonable stress-strain predictions with minimum parameters, reasonable computation time, and captures the size effect of quasibrittle materials [17]. More elaborated plastic-damage models have been successfully used for the mesoscale analysis of concrete [81].

The present material model is based on damage mechanics on all considered four scales. A crack starts to grow when cohesive stress is exceeded anywhere in the material. For uniaxial tension of a homogeneous material, this cohesive stress corresponds obviously to the tensile strength, f_t . Damage mechanics uses the concept of the equivalent strain, $\tilde{\varepsilon}$, as a descriptor of damage evolution. Damage becomes initiated when the equivalent strain, $\tilde{\varepsilon}$, exceeds strain at the onset of cracking, $\varepsilon_0 = f_t/E$, where E is the elastic modulus. The Rankine criterion for tensile failure defines $\tilde{\varepsilon}$ as

$$\tilde{\varepsilon} = \frac{\sigma_1}{E}, \quad \sigma_1 > 0 \quad (3.1)$$

where σ_1 is the maximum positive effective principal stress on undamaged-like material, see Figure 3.1(a).

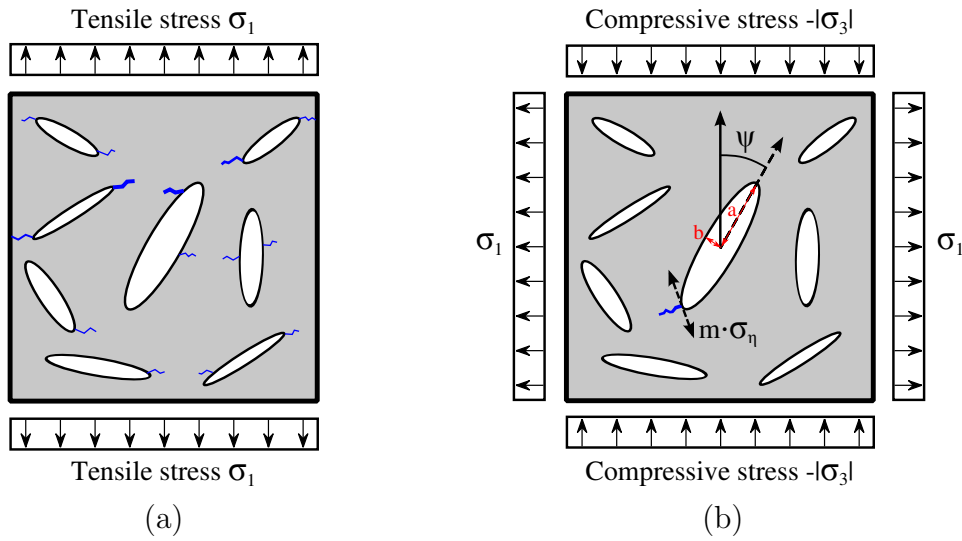


Figure 3.1: Crack evolution during (a) uniaxial tensile stress and (b) compressive stresses. The material contains randomly oriented elliptical voids with negligible area.

Under uniaxial compressive stress, crack initiation occurs under a different mechanism. A homogeneous material experiences only one negative principal stress and the deviatoric stress. Cracking in diagonal, shear band zone is often encountered on cementitious specimens, however, the physical mechanism is again tensile microcracking in voids and defects of the underlying microstructure [17, pp.297]. Such a behavior has already been described in the work of Griffith [66], and McClintock and Walsh [100], and we briefly review this theory and extend it with an equivalent strain to be used in the framework of damage mechanics.

It is assumed that a material contains randomly oriented 2D elliptical flat voids with various aspect ratios $m = b/a$, see Figure 3.1(b). The voids have a negligible area and only represent stress concentrators and internal defects in a material. Under macroscopic biaxial stress, the maximum tensile stress among all voids, $m \cdot \sigma_\eta$, appears on a critically inclined elliptical void under a critical angle ψ

$$\cos 2\psi = \frac{\sigma_3 - \sigma_1}{2(\sigma_3 + \sigma_1)}, \quad \frac{\sigma_1}{\sigma_3} \geq -\frac{1}{3} \quad (3.2)$$

$$m \cdot \sigma_\eta = \frac{-(\sigma_1 - \sigma_3)^2}{4(\sigma_1 + \sigma_3)} \quad (3.3)$$

Crack formation occurs when the tangential tensile stress, $m \cdot \sigma_\eta$, equals to the tensile strength of the matrix. Since σ_η and the crack geometry, m , cannot be measured directly, it is reasonable to relate their product to the uniaxial macroscopic tensile stress, $\bar{\sigma}_1$, as proposed by Griffith [66]

$$\bar{\sigma}_1 = \frac{m \cdot \sigma_\eta}{2} \quad (3.4)$$

The material starts to crack when $\bar{\sigma}_1$ equals to the uniaxial macroscopic tensile strength f_t . Note that the tensile strength of the homogeneous matrix (intrinsic strength) and the crack geometry remain unknown separately and we can assess only apparent macroscopic tensile strength f_t .

Plugging Eq. (3.3) into Eq. (3.4) and further into Eq. (3.1) leads to the definition of the equivalent strain, $\tilde{\varepsilon}$, under compression-dominant loading

$$\tilde{\varepsilon} = \frac{1}{E} \cdot \frac{-(\sigma_1 - \sigma_3)^2}{8(\sigma_1 + \sigma_3)} \quad (3.5)$$

An interesting feature of the Griffith model is that the ratio of the uniaxial compressive-to-tensile strength equals to 8

$$|f_c| = 8f_t \quad (3.6)$$

This can be verified when plugging $\sigma_1 = f_t$ into Eq. (3.1) which leads to $\tilde{\varepsilon} = f_t/E$. Plugging $\sigma_1 = 0$, $\sigma_3 = -8f_t$ into Eq. (3.5) leads to the same equivalent strain.

Since the equivalent strain may arise from the Rankine or Griffith criterion, it is necessary to compare both Eqs. (3.1), (3.5) and to select the higher equivalent

strain. Linear softening is assumed in the simulations. The softening shape has a little effect on the computed macroscopic strength which is the main objective of this paper and naturally affects the post-peak behavior. The linear cohesive law takes the form

$$\sigma = f_t \left(1 - \frac{w}{w_f} \right) \quad (3.7)$$

where w is a crack opening and w_f is the maximum crack opening at zero stress. According to the formulation of the isotropic damage model, the uniaxial tensile stress obeys the law

$$\sigma = (1 - \omega)E\varepsilon \quad (3.8)$$

Let us consider the fracture energy in mode I, G_f , and the effective thickness of a crack band h , which corresponds to the finite element size in the direction of the maximum principal strain [17]. This ensures objective results, independent on finite element size [78]. Notice that $w = h\omega\tilde{\varepsilon}$ and $w_f = 2G_f/f_t$. The evolution of isotropic damage is obtained by combining Eqs. (3.7), (3.8)

$$\omega = \left(1 - \frac{\varepsilon_0}{\tilde{\varepsilon}} \right) \left(1 - \frac{hE\varepsilon_0^2}{2G_f} \right)^{-1} \quad (3.9)$$

The performance of the proposed Griffith-Rankine model under the plane stress condition is demonstrated in Figure 3.2 for the onset of cracking. The Mohr-Coulomb model gives similar results for the friction angle of 51.1° and $c_0/f_t = \sqrt{2}$, which keeps the compressive/tensile strength ratio of 8. The differences in both models are small but the Griffith-Rankine model provides the equivalent strain which is used for damage quantification.

The Griffith-Rankine model was implemented in OOFEM [115]. The basic test covered a uniaxially loaded one brick element under pure tension or compression for $E = 20$ GPa, $G_f = 20$ J/m², $f_t = 5$ MPa and the element size $10 \times 10 \times 10$ mm. Figure 3.3 shows the response in terms of average stress and strain over the element. Note that the linear softening law defined in the integration point may be distorted on the element scale since damage occurs in more integration points and later becomes localized to one integration point. The material model provides fracture energy in compression, which is theoretically 64 times larger

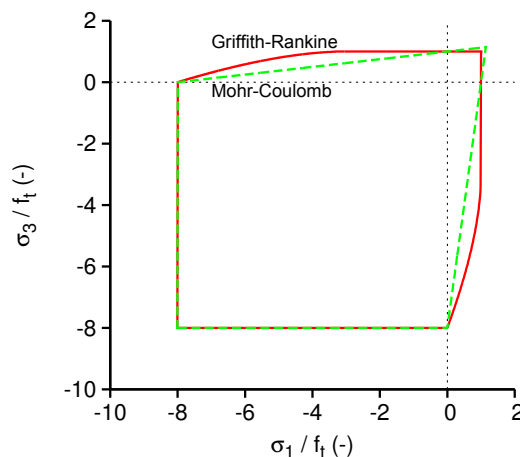


Figure 3.2: Surface at the onset of cracking according to two models under the plane stress condition.

than that in tension. However, such fracture energy in compression is a fictitious value since other mechanisms for energy dissipation occur such as buckling within the microstructure [13].

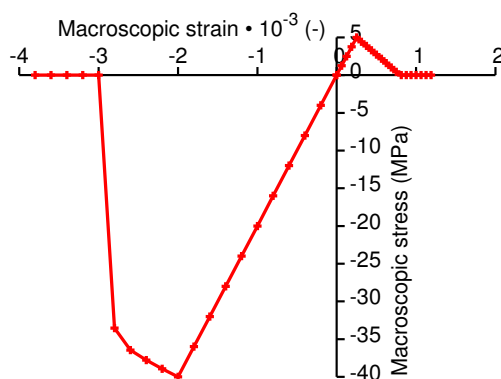


Figure 3.3: Test of one linear brick element under uniaxial tension / compression with 8 integration points.

To demonstrate further the performance of the Griffith-Rankine model, Figure 3.4 shows the strain localization in shear bands under the uniaxial compression test under plane stress condition. A layer of finite elements with steel properties is attached to the top and bottom which restrains the horizontal displacement and induces the horizontal shear stress in the contact. This mimics the situation of the standard uniaxial compression test without teflon pads. Material properties remain the same as in the previous case and the microstructure size 20×20 mm is discretized to 20×20 finite elements. Black lines show crack orientation in damaged parts.

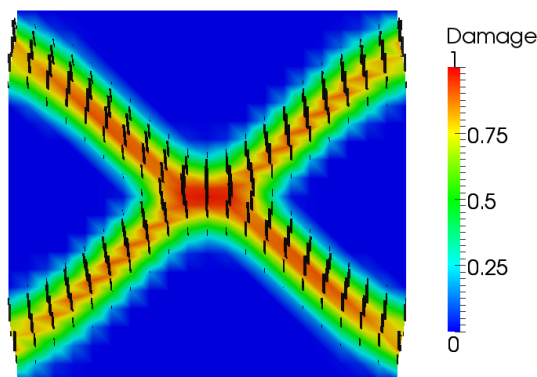


Figure 3.4: Strain localization in shear bands under the uniaxial compression test under plane stress. 20×20 quadrilateral elements (20×20 mm), deformation exaggerated $40 \times$, damage shown for the end of softening.

3.2.2 Boundary conditions and intrinsic properties

The four-level multiscale model utilizes a 2D or 3D finite element analysis on each scale, where the Griffith-Rankine constitutive laws govern the crack growth and material softening. The discretization of the microstructure relies on the length scale considered. Each scale contains relevant chemical phases in correct volume proportions.

The prescribed boundary conditions on a unit cell (UC) reflect uniaxial loading on each scale. Periodic boundary conditions would provide the most reliable estimation of elastic properties when cement paste is considered as a whole at one homogenization level, without any hierarchical approach [169]. However, kinematic boundary conditions in the top and bottom UC's surfaces yield a better match for this hierarchical approach for the elastic modulus. The UC is loaded by eigenstrain increment in the vertical direction which builds up the uniaxial macroscopic compressive stress.

Table 5.1 summarizes intrinsic elastic and apparent fracture properties assigned to relevant phases during simulations. While nanoindentation previously quantified elastic properties [22], the tensile strengths of C-S-H and C-S-H globules need to be estimated by means of downscaling from experimental data on cement pastes, see Section 3.4.6.

The fracture energy of individual components with their interfaces is estimated, based on available data. For example, the C-S-H-C-S-H debonding energy was computed to lay between 0.38 and 2.85 J/m² [62]. However, this energy is too

low and the pull-out mechanism of CH crystals increases this energy to a theoretical range of 7.55–283 J/m², which is more realistic with measured values of fracture energy of cement pastes [62]. Molecular dynamics simulations performed on atomic scale yield fracture energy of C-S-H as 1.72 ± 0.29 J/m²[11]. The value of fracture energy is not very sensitive parameter for the peak stress of a material, see Figure 3.29, but rather influences post-peak behaviour which is not the primary focus of this paper.

Table 3.1: Intrinsic elastic and apparent fracture properties of relevant chemical phases considered in the multiscale hierarchical simulation.

	Elastic modulus (GPa)	Poisson's ratio (-)	Tensile (compressive) strength (MPa)	Fracture energy (J/m ²)	Ref.
C-S-H globule	57.1	0.28	320 (2560)	2 ^a	[153]
C-S-H _{LD}	21.7	0.24	66 (528) ^b	5 ^a	[41]
C-S-H _{HD}	29.4	0.24	107 (856) ^b	5 ^a	[41]
Water-filled porosity	0.001	0.4999	-	-	[169]
CH	38.0	0.305	-	-	[41]
AF _t	22.4	0.25	-	-	[67]
AF _m	42.3	0.324	-	-	[67]
Clinker minerals	139.9	0.30	-	-	[122]
Cement paste	-	-	-	15	[170]

^a) Higher fracture energy leads to the same material strength

^b) Calculated from packing of C-S-H globules

3.3 Multiscale model for cement pastes

The previous success of the gel-space descriptor coined by Powers indicates that strength emerges mainly on submicrometer resolution [122, 127]. A four-level hierarchical model for cement paste, see Figure 5.2, is constructed to account for major and minor effects influencing strength. The coupling between levels occurs through upscaling the elastic modulus, E , and the tensile strength, f_t . The tensile strength on each level is identified from compressive strength, f_c , using the Griffith criterion, which yields a constant ratio $f_c/f_t = 8$, see Section 3.2.1. The fracture energy, G_f , is not directly upscaled, instead, it is explicitly defined at each level, see further discussion in Section 3.4.13.

Level 0: C-S-H considers C-S-H globules packing to densities between C-S-H_{LD}

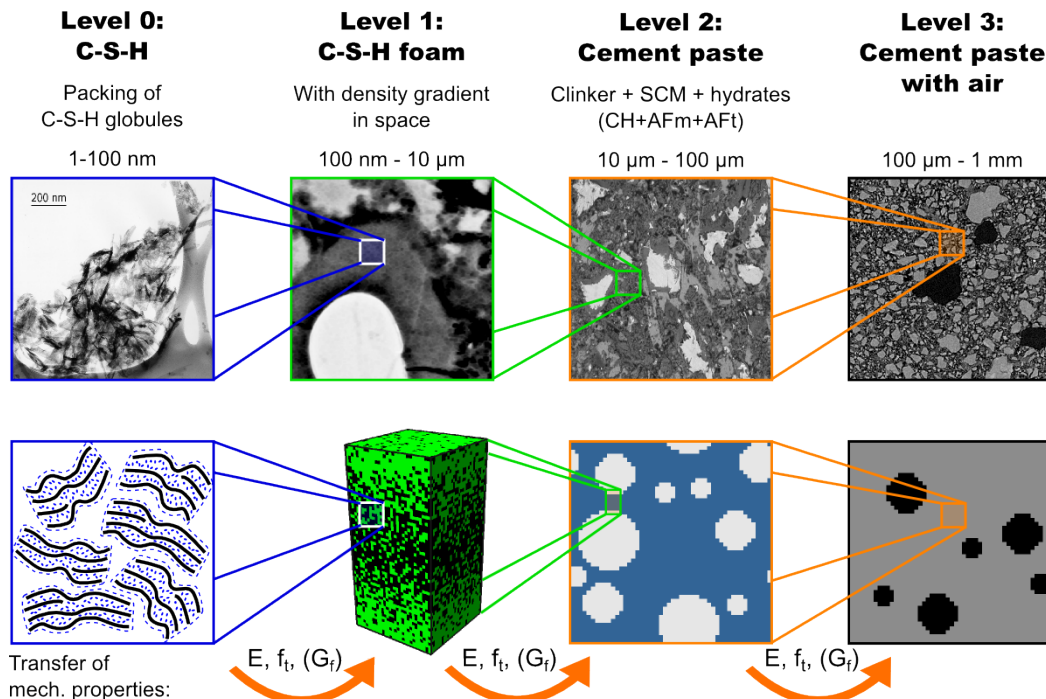


Figure 3.5: Four-level hierarchical multiscale model. TEM/SEM images from left to right: Eric Lachowski, S.Y. Hong and F.P. Glasser (<http://publish.illinois.edu/concretemicroscopylibrary/transmission-electron-microscopy-tem/>); L. Kopecký (CTU in Prague); Paul Stutzman (NIST, <http://publish.illinois.edu/concretemicroscopylibrary/magnification-progression-series-1000x/>); D. P. Bentz, et al. (Visible Cement Dataset: <http://visiblecement.nist.gov>)

and C-S-H_{HD} . Together with Jennings [77], the C-S-H globule consists of calcium silicate sheets, interlayer space, intraglobule space, and monolayer water. The globules become mixed with small and large gel pores ($1 \text{ nm} < d < 12 \text{ nm}$). The characteristic size spans the range of $1 - 100 \text{ nm}$.

Level I: C-S-H foam contains C-S-H together with capillary porosity. To mimic an uneven distribution of C-S-H among grains in cement paste, C-S-H have a spatial gradient. The characteristic size spans the range of $100 \text{ nm} - 10 \mu\text{m}$.

Level II: Cement paste adds unhydrated clinker and all remaining hydration products (CH, AFm, AFt, ...) inside the homogenized C-S-H foam. The characteristic size spans the range of $10 \mu\text{m} - 100 \mu\text{m}$.

Level III: Cement paste with air captures entrained or entrapped air, decreasing the resulting mechanical properties. The characteristic size spans the range of $100 - 1000 \mu\text{m}$.

Level I of C-S-H foam covers a region between individual clinker grains. The size of the region depends on (i) the mean size of clinker grains, and on (ii) the initial composition of cement paste specified by the water-to-binder mass ratio. In modeling, such microstructure was simplified by assigning a constant UC height of $10 \mu\text{m}$.

It is worthy to mention that C-S-H is not a true gel but a precipitate, signaled by the presence of capillary porosity, by a more-or-less constant gel porosity during the C-S-H formation, and by the C-S-H appearance mainly around cement clinker grains [141] which can be observed in SEM/BSE images.

To investigate the spatial distribution of C-S-H between grains, μCT scans of cement pastes from The Visible Cement Dataset created by NIST were used [20]. Two different cement pastes were considered with water/cement ratio equal to 0.3 and 0.45, both produced from a reference cement #133. Cement paste with $w/c=0.3$ was investigated at 8 and 162 hours after mixing whereas cement paste with $w/c=0.45$ was studied at 8 and 124 hours. All μCT scans were sliced to create 2D images, thresholded to separate clinker, hydrates and capillary pores based on known volume fractions. In this particular case, C-S-H corresponded to hydrates.

Figure 3.6 shows the calculated two-point correlation function between hydrates (C-S-H) and the closest grain surface. Thresholded images of pastes tested 8 hours after casting show that C-S-H precipitate mainly around cement grains for both w/c ratios studied. Older pastes exhibit a denser microstructure but a larger w/c ratio (here $w/c=0.45$) indicates a higher gradient of C-S-H.

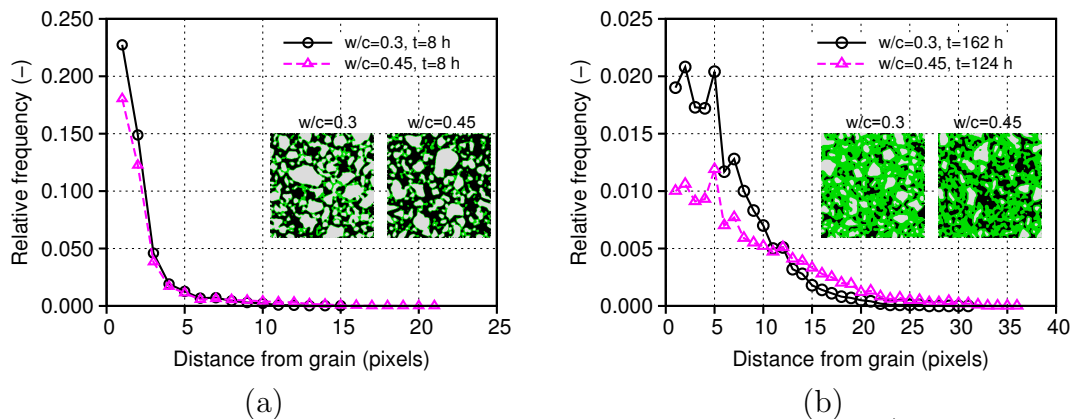


Figure 3.6: Spatial distribution of C-S-H between grains for a) early-age pastes and b) for older pastes. A pixel corresponds to $0.95 \mu\text{m}$.

A common assumption of hydration models is concentric growth of spherical shells representing hydration products around original grains such as HYMOSTRUC [160], [130] or μic [24], [23]. In the proposed multiscale model we approximate the spatial gradient of the C-S-H distribution by a spatial density function ρ as

$$\rho(x, \beta) = \frac{1}{\beta} \exp\left(-\frac{x/\ell_{UC}}{\beta}\right) \quad (3.10)$$

where x stands for the distance from the clinker grain surface, β is a parameter of the exponential distribution and ℓ_{UC} is the characteristic length of UC. Low values of β indicate a high gradient of C-S-H in space. Figure 3.7 illustrates the impact of β on the C-S-H distribution at the level of C-S-H foam.

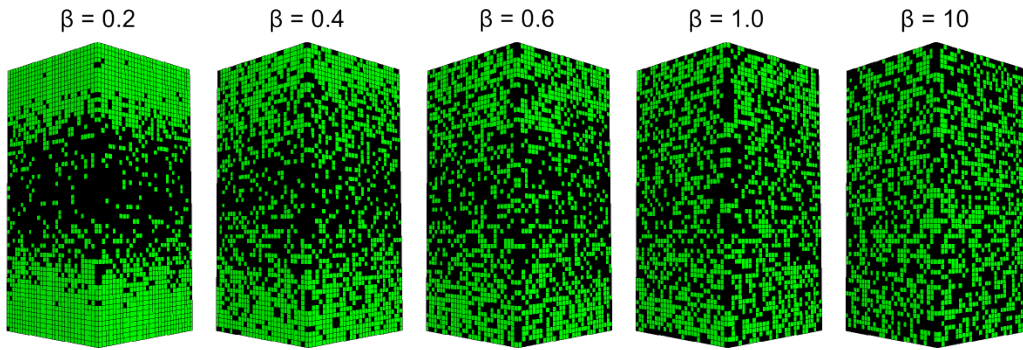


Figure 3.7: The impact of the parameter β on the C-S-H distribution (on level 1) for C-S-H/space ratio $\gamma_{CSH} = 0.7$, UC size $5 \times 5 \times 10 \mu m$.

The term “gel” coined by Powers described a mixture of amorphous C-S-H and all other crystalline hydration products [127]. However, recent detailed modeling of C_3S and C_2S pastes revealed that not all hydration products contribute to the compressive strength equally [153]. In fact, more precise results for the compressive strength prediction were obtained when C-S-H was the only failing component in the cement paste. A similar conclusion is supported by Figure 3.8 which shows the contribution of clinker minerals to the overall compressive strength of hydrated pastes [18]. While minerals producing C-S-H yield comparable results, C_3A generating AFt yields a much lower strength. In the presented multiscale model, C-S-H are considered as the weakest active binding phase, interconnecting other crystalline hydration products, unreacted clinker minerals, and SCMs.

Instead of using the “gel/space ratio”, we define the term “CSH/space ratio” as

$$\gamma_{CSH} = \frac{\phi_{CSH}}{\phi_{CSH} + \phi_{cappor}} \quad (3.11)$$

where ϕ_{CSH} and ϕ_{cappor} stand for the volume fractions of C-S-H (including gel pores) and capillary porosity, respectively.

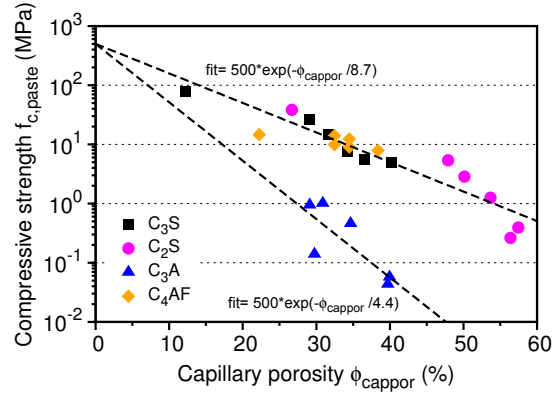


Figure 3.8: Compressive strength of pastes with $w/c = 0.45$ measured on cylinders with a diameter of 12.7 mm and height of 25.4 mm [18].

Level II describes cement paste as a two-phase material. For the reason of simplicity, crystalline hydration products, clinker minerals, and SCMs are merged together into one fictitious isotropic elastic phase, see Figure 5.2. Due to the crystalline morphology, a self-consistent scheme [70] is used to estimate the effective elastic property of this homogenized phase which is based on the volume fractions and elastic properties of individual microstructural constituents according to Table 5.1. The homogenized phase is then embedded into the C-S-H foam where it acts as solid inclusions.

Level III describes the effect of entrapped or entrained air inside the cement paste which has a pronounced impact on the mechanical properties. The microstructure on this level consists of circular voids which are embedded into a homogeneous cement paste.

3.4 Results and discussion

The four-level model aims to predict the elastic modulus and compressive/tensile strength of cement pastes by hierarchical homogenization. The tensile strength

of the C-S-H globule plays the most important role since it is projected onto higher hierarchical levels. This strength value will be calibrated from macroscopic data since no direct experimental method is available today, see Section 3.4.6. The results from finite element simulations are approximated using analytical functions on all hierarchical levels to speed up the validation.

3.4.1 Level 0 - C-S-H

The presented level considers time-dependent and spatially uniform packing density of C-S-H globules as an approximation of a colloidal system of C-S-H gel. The shape of the globule is set as one voxel (5 nm), without specifying globule's orientation, see Figure 3.10. The globule is treated as an isotropic material.

Jennings [76] coined two morphologies of C-S-H (low and high density) which emerge from different packing densities of C-S-H globules. Nanoindentation experiments carried out by Constantinides and Ulm [41] identified elastic properties of C-S-H, see Table 5.1, as well as derived limit packing densities as $\eta_{\text{CSH}_{\text{LD}}} = 0.63$ and $\eta_{\text{CSH}_{\text{HD}}} = 0.76$ [42].

A packing density of globules is estimated from the CEMHYD3D hydration model [19] with the implemented confinement algorithm [169] and it is a function of the initial water-to-binder mass ratio, w/b , and the time-dependent capillary porosity, ϕ_{cappor} . Figure 3.9 shows the evolution for three w/b ratios with the approximation

$$\phi_{\text{CSH}_{\text{HD}}} = \left[1 + 5000 \phi_{\text{cappor}}^{(2.5+5 w/b)} \right]^{-1} \quad (3.12)$$

The confinement algorithm makes no difference between various solid phases, hence it captures both OPC and blended cements [169].

Depending on the volume fraction of C-S-H_{HD} within C-S-H, we interpolate the actual packing density of globules as

$$\eta_{\text{glob}} = \eta_{\text{CSH}_{\text{LD}}} + (\eta_{\text{CSH}_{\text{HD}}} - \eta_{\text{CSH}_{\text{LD}}}) \phi_{\text{CSH}_{\text{HD}}} = 0.63 + 0.14 \phi_{\text{CSH}_{\text{HD}}} \quad (3.13)$$

Similarly, Young's modulus of C-S-H spans the range between $E_{\text{CSH}_{\text{LD}}} = 21.7$ GPa

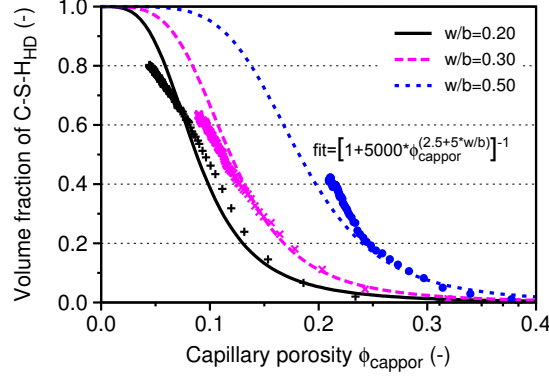


Figure 3.9: Evolution of the volume fraction of C-S-H_{HD} within C-S-H as a function of capillary porosity and the initial composition from the CEMHYD3D model. C-S-H_{LD} always appears at the beginning of hydration.

and $E_{\text{CSH}_{\text{HD}}} = 29.4 \text{ GPa}$, see Table 5.1.

$$E_{\text{CSH}}^0 = E_{\text{CSH}_{\text{LD}}} + (E_{\text{CSH}_{\text{HD}}} - E_{\text{CSH}_{\text{LD}}}) \phi_{\text{CSH}_{\text{HD}}} = 21.7 + 7.7 \phi_{\text{CSH}_{\text{HD}}} \quad (3.14)$$

The apparent tensile strength of the globule governs strength at higher hierarchical levels. Section 3.4.6 shows that the globule's apparent tensile strength was identified as

$$f_{t, \text{glob}} = 320 \text{ MPa} \quad (3.15)$$

Figure 3.10 shows UCs for C-S-H_{LD} and C-S-H_{HD} types used for finite element simulations. Figure 3.11 displays the evolution of the C-S-H tensile strength depending on the packing density. The approximation reads

$$f_{t, \text{CSH}}^0 = f_{t, \text{glob}} \exp \left(-1.101 \frac{1 - \eta_{\text{glob}}^{5.133}}{\eta_{\text{glob}}} \right) \quad (3.16)$$

which yields the apparent tensile strength of C-S-H_{LD} and C-S-H_{HD} as $f_{t, \text{CSH}_{\text{LD}}}^0 = 66 \text{ MPa}$ and $f_{t, \text{CSH}_{\text{HD}}}^0 = 107 \text{ MPa}$, respectively. By extrapolation to globule packing density $\eta_{\text{glob}} = 1$ we identify the apparent tensile strength of the globule as 320 MPa. The compressive strength of C-S-H can be obtained from the Griffith criterion in Eq. (3.6), which yields the apparent compressive strength $f_{c, \text{CSH}_{\text{LD}}}^0 = 528 \text{ MPa}$, and $f_{c, \text{CSH}_{\text{HD}}}^0 = 856 \text{ MPa}$.

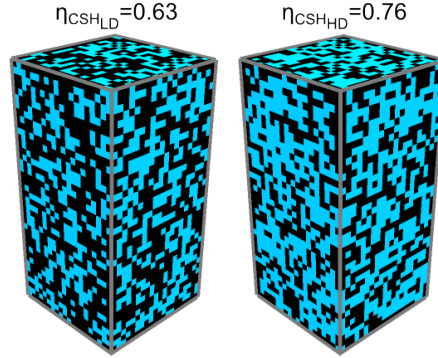


Figure 3.10: UCs for C-S-H_{LD} and C-S-H_{HD}, 20×20×40 brick elements (UC size 100×100×200 nm).

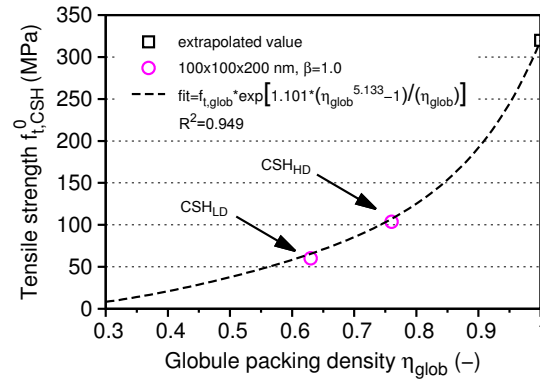


Figure 3.11: Tensile strength of C-S-H depending on the globule packing density. Circles represent results from FE simulations on 20×20×40 brick elements (100×100×200 nm), $\beta = 1.0$ and $G_f = 2 \text{ J/m}^2$.

3.4.2 Level 1 - C-S-H foam

C-S-H precipitating in the region between individual clinker grains forms a spatial gradient, see Figure 3.7. This level contains only C-S-H which is intermixed with capillary porosity. The computational UC is composed from a 3D uniform mesh, consisting of 20×20×40 brick elements with linear displacement interpolations and with a resolution of 0.25 $\mu\text{m}/\text{voxel}$, yielding the UC size of 5×5×10 μm . The proposed setup assumes that the top and bottom planes of UC touch the surfaces of clinker grains and C-S-H precipitates in between. C-S-H is generated randomly in UC but its spatial distribution follows Eq. (3.10).

Figure 3.12 shows the stress-strain diagram obtained from a FE model of C-S-H foam consisting solely of C-S-H_{LD} using the C-S-H/space ratio $\gamma_{\text{CSH}} = 0.7$, $\beta = 0.6$, and $f_{t,\text{CSH}}^0 = 66 \text{ MPa}$.

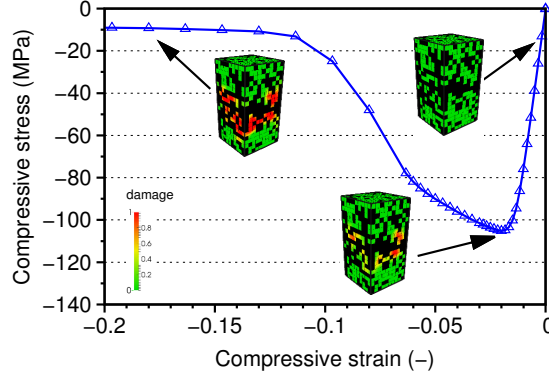


Figure 3.12: Stress-strain diagram obtained on C-S-H foam using $\gamma_{\text{CSH}} = 0.7$, $\beta = 0.6$, and $f_{t,\text{CSH}}^0 = 66$ MPa.

The results from numerical simulations on the level of C-S-H foam show that the spatial gradient has only a weak impact on elasticity. The elastic modulus for percolated microstructures linearly increases with the increasing CSH/space ratio, see Figure 3.13.

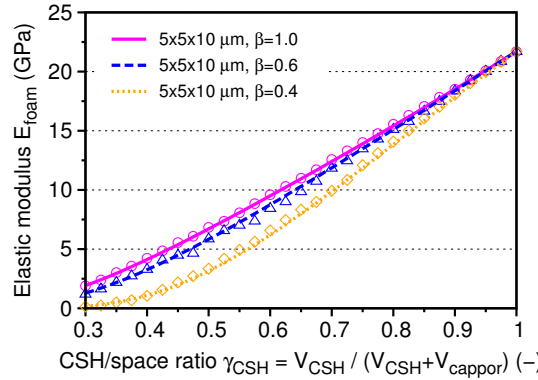


Figure 3.13: Elastic modulus evolution for level 1 (C-S-H foam), assuming solely C-S-H_{LD} with the globule packing density $\eta_{\text{glob}} = \eta_{\text{CSH}_{\text{LD}}} = 0.63$. Points represent results from FE simulations on UC $20 \times 20 \times 40$ brick elements (UC size $5 \times 5 \times 10 \mu\text{m}$) and the lines are analytical approximations.

An analytical approximation to numerical results of the elastic modulus of C-S-H foam yields

$$E_{\text{foam}}^I = E_{\text{CSH}}^0 \exp \left(A_1 \frac{\gamma_{\text{CSH}}^{B_1} - 1}{\gamma_{\text{CSH}}} \right) \quad (3.17)$$

$$A_1 = 0.820 \exp \left(-4.949 \frac{\beta^{0.02} - 1}{\beta^{2.8}} \right), \quad \beta \in \langle 0.4; 1.0 \rangle \quad (3.18)$$

$$B_1 = 1.818 \exp \left(4.310 \frac{\beta^{0.02} - 1}{\beta^{2.8}} \right), \quad \beta \in \langle 0.4; 1.0 \rangle \quad (3.19)$$

where $\beta \in \langle 0.4; 1.0 \rangle$. Higher β values are equivalent to a uniform distribution.

Compressive strength determined on identical microstructures exhibits a high sensitivity on the spatial gradient, see Figure 3.14. This can be explained by

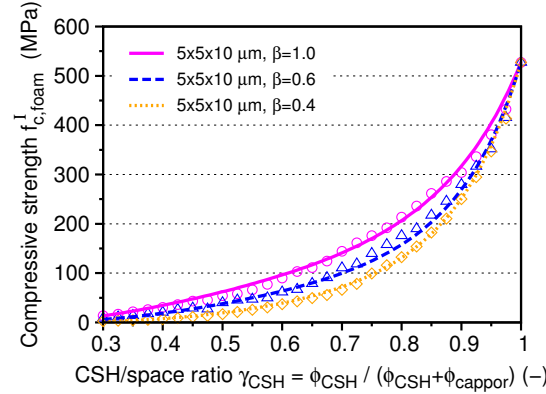


Figure 3.14: Compressive strength evolution for level 1 (C-S-H foam), assuming solely C-S-H_{LD} with the globule packing density $\eta_{glob} = \eta_{CSH_{LD}} = 0.63$ and the corresponding compressive strength $f_{c,CSH}^0 = 528$ MPa. Points represent results from FE simulations on UC $20 \times 20 \times 40$ brick elements (UC size $5 \times 5 \times 10 \mu\text{m}$) and lines are analytical approximations.

the stress concentration in diluted areas which decrease the load-bearing capacity. The analytical approximation to numerical data results in more complicated equations, capturing the effect of the CSH/space ratio γ_{CSH} and the spatial gradient by means of the parameter β as

$$f_{c,foam}^I = f_{c,CSH}^0 \exp\left(-C_1 \frac{1 - \gamma_{CSH}^{D_1}}{\gamma_{CSH}}\right) \quad (3.20)$$

$$C_1 = 1.101 \exp\left(-0.296 \frac{\beta - 1}{\beta}\right), \beta \in \langle 0.4; 1.0 \rangle \quad (3.21)$$

$$D_1 = -11.058 \beta^{1.987} + 16.191 \beta, \beta \in \langle 0.4; 1.0 \rangle \quad (3.22)$$

3.4.3 Level 2 - cement paste

Level 2 uses a 2D uniform mesh composed of 100×100 quadrilateral elements (UC size of $100 \times 100 \mu\text{m}$) with linear displacement interpolations. The comparison with 3D UC proved that 2D model under plane stress yields very similar results for elasticity and peak stress. The 2D model allows capturing larger and more detailed microstructures. The damage model was assigned to a homogeneous C-S-H foam. The actual size of inclusions follows a step-wise particle size distribution with circles of 5, 10, and $15 \mu\text{m}$ in diameter.

Introducing a solid inclusion into a homogeneous C-S-H foam results in an increase of the stiffness of the reinforced foam on the one hand, and in a decrease of the compressive strength on the other hand. Results from FE simulations show that the overall stiffness of cement paste proportionally increases with the quantity of inclusions as well as their stiffness, see Figure 3.15.

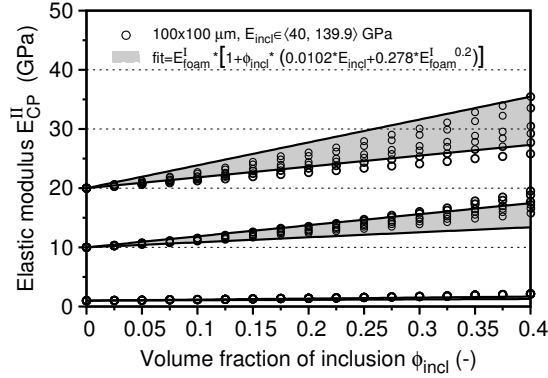


Figure 3.15: Elastic modulus evolution for level 2 (cement paste) assuming $E_{foam}^I = 1, 10, 20$ GPa. Circles represent results from FE simulations on a 2D microstructure on 100×100 quadrilateral elements (UC size $100 \times 100 \mu\text{m}$) with varying stiffness of the inclusion $E_{incl} = 40, 50, 60, 70, 105, 139.9$ GPa.

An analytical approximation yields

$$E_{CP}^{II} = E_{foam}^I \left[1 + \phi_{incl} \left(0.0102 E_{incl} + 0.278 E_{foam}^{I 0.2} \right) \right] \quad (3.23)$$

The high stiffness contrast between solid inclusions and the C-S-H foam influences stress trajectories to concentrate between inclusions, resulting in a decrease of the nominal strength of cement paste, see Figure 3.16. The impact of inclusion's stiffness on the resultant decrease of compressive strength is insignificant.

An analytical approximation yields

$$f_{c,CP}^{II} = f_{c,foam}^I \left[0.758 + (1 - 0.758) \exp(-29.3 \phi_{incl}) \right] \quad (3.24)$$

3.4.4 Level 3 - cement paste with air

Level 3 again uses a 2D uniform mesh composed of 50×50 quadrilateral elements (UC size $1000 \times 1000 \mu\text{m}$). To account for the random size of entrapped or entrained air bubbles in real cement pastes, the size of the bubbles follows a step-wise particle size distribution with spheres of 20, 60, and $100 \mu\text{m}$ in diameter.

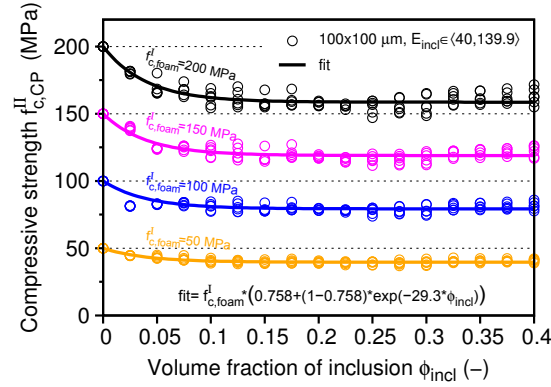


Figure 3.16: Compressive strength evolution for level 2 (cement paste), assuming $f_{c,foam}^I = 50, 100, 150, 200$ MPa. Circles represent results from FE simulations on a 2D microstructure on 100×100 quadrilateral elements (UC size $100 \times 100 \mu\text{m}$) for $f_{c,foam}^I = 50, 100, 150, 200$ GPa with varying stiffness of the inclusion $E_{incl} = 40, 50, 60, 70, 105, 139.9$ GPa.

The presence of air in the cement paste significantly reduces both observed mechanical properties. Figure 3.17 shows the decrease of the elastic modulus with the increasing volume fraction of the air content ϕ_{air} .

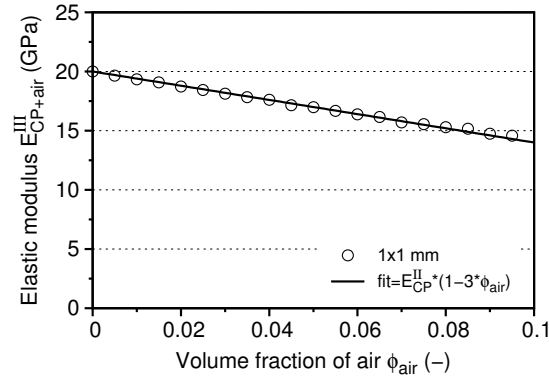


Figure 3.17: Elastic modulus evolution for level 3 (cement paste with air), assuming $E_{CP}^{II} = 20$ GPa. Circles represent results from FE simulations on a 2D microstructure on 50×50 quadrilateral elements (UC size 1×1 mm).

An analytical approximation reads

$$E_{CP+air}^{III} = E_{CP}^{II} (1 - 3 \phi_{air}) \quad (3.25)$$

Every 1 % of entrained (or entrapped) air results in a proportional decrease of the elastic modulus by 3 %.

Voids in a homogeneous matrix cause the concentration of stress, effectively reducing the compressive strength, see Figure 3.18.

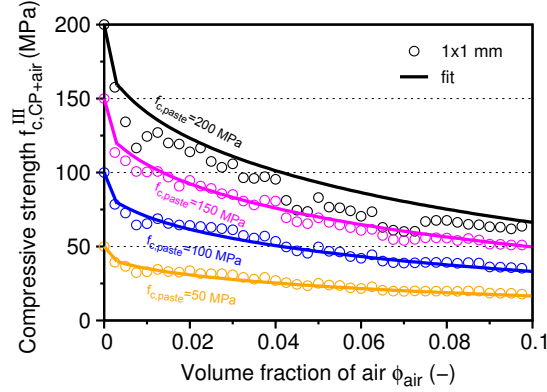


Figure 3.18: Compressive strength evolution for level 3 (cement paste with air). Circles represent results from FE simulations on a 2D microstructure on 50×50 quadrilateral elements (UC size 1×1 mm) for $f_{c,CP}^{II} = 50, 100, 150, 200$ MPa.

An analytical approximation to numerical simulations reads

$$f_{c,CP+air}^{III} = \begin{cases} f_{c,CP}^{II} - 0.2 f_{c,CP}^{II} \frac{\phi_{air}}{0.0025} & \text{for } \phi_{air} \leq 0.0025 \\ 0.8 f_{c,CP}^{II} \exp\left(\frac{-4.056 (\phi_{air} - 0.0025)^{1.6452}}{\phi_{air}}\right) & \text{for } \phi_{air} > 0.0025 \end{cases} \quad (3.26)$$

Figure 3.19 shows that introducing only 0.1 % of air decreases compressive strength by approximately 20 %. This sharp decrease could hardly be measured experimentally since it compares a material without any defects such as macro-defect-free cements with a material with only a few voids or cracks. However, going to the region after this initial reduction yields a strength reduction of approx. 5 % per 1 % of entrained air, which is already consistent with the observation on the concrete scale [108, p.557].

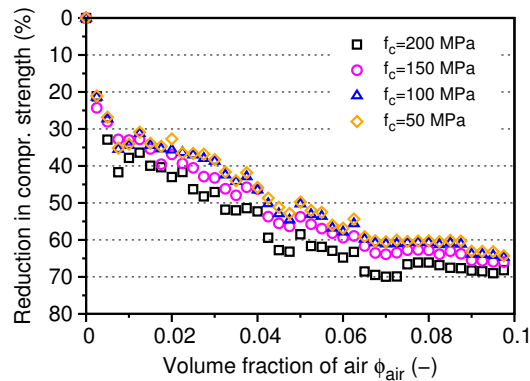


Figure 3.19: Reduction of cement paste compressive strength with respect to entrapped or entrained air.

3.4.5 Discussion on FE mesh representations

To demonstrate representativeness of a mesh, a cement paste from level 2 was taken with the size $100 \times 100 \mu\text{m}$. Three sets of microstructures were generated using different mesh sizes, yielding 50×50 , 100×100 , and 200×200 quadrilateral elements. Five randomly generated microstructures in each set aimed at capturing statistical effect with 20% volume fraction of solid inclusions with stepwise particle size distribution using 5, 10, and $15 \mu\text{m}$ circular inclusions.

Simulations show that the predicted compressive strength of cement paste is almost insensitive to the mesh size, see Figure 3.20. However, increasing mesh size results in a decrease of scatter in predicted compressive strengths, in accordance with theoretical predictions [80].

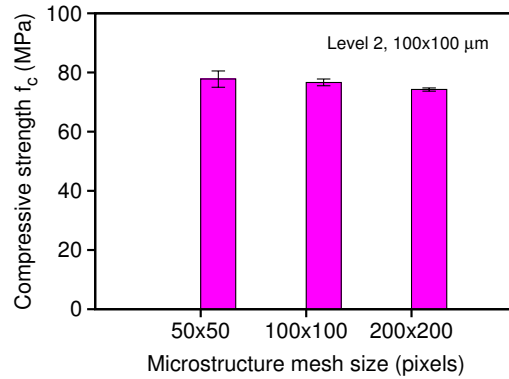


Figure 3.20: Results from FE simulations on level 2 (cement paste) containing 20% of solid inclusions for three mesh sizes.

3.4.6 Calibration of $f_{t,glob}$

The proposed multiscale model contains two independent variables which need to be calibrated from experimental data

- The apparent tensile strength of C-S-H globules, $f_{t,glob}$.
- The spatial gradient of C-S-H described by the parameter β .

In this regard, we created the CemBase database version 1.0, containing experimental results from testing cement pastes and mortars. The data contained in this PostgreSQL database are structured and systematically sorted into individual categories starting from the characterization of raw materials, followed by the

mixture composition, volume fractions of relevant phases, and measured mechanical properties. Individual categories are cross-linked to remove any duplicities.

Up to date, CemBase contains mechanical tests of 399 microstructures: 297 pastes and 102 mortars for water-to-binder ratios between 0.157 and 0.68. Complete volume fractions are not available for every microstructure due to missing experimental data. Whenever possible, the quantities of phases were calculated using a CEMHYD3D hydration model [19] to complement missing microstructural information.

Compressive strength is recorded for 353 microstructures between 1 and 750 days, however, our multiscale model was only validated against 95 paste compressive strength values as sufficient microstructural compositions are available here. Out of 95 strength values, 76 are from OPC pastes, 5 from slag-blended pastes, 5 from fly ash-blended pastes, 5 from limestone-blended pastes, and 4 from finely ground quartz-blended pastes. The volume of air is only recorded for 44 microstructures with an average value of 0.8 %. The latter was assigned to the remaining microstructures as a default value.

During the calibration of our multiscale model, the parameter was initially fixed to $\beta = 1$, which signaled a nearly uniform distribution of C-S-H in space as well as the highest possible compressive strength prediction. The apparent tensile strength for the C-S-H globule was identified using 95 experimental results of compressive strength as

$$f_{t, glob} = 320 \text{ MPa} \quad (3.27)$$

This strength is the highest value which is only exceeded by 6 out of 95 measured compressive $f_{c, paste}$ strength values, see Figure 3.21(a).

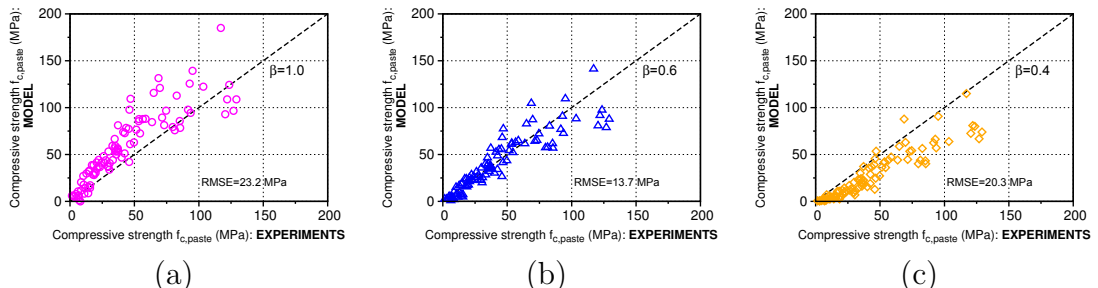


Figure 3.21: Validation of model-predicted compressive strength with experiments for $\beta = 1.0$ (a), $\beta = 0.6$ (b), and $\beta = 0.4$ (c).

A further reduction of the model-predicted compressive strength is achieved by decreasing β , i. e. effectively by creating a gradient of C-S-H within capillary pores. The value $\beta = 0.6$ globally fits the strength data best, however, the range $\beta \in \langle 0.4, 1 \rangle$ can accommodate almost all experimental results. Pastes from blended cements do not exhibit any substantial variations from the trend described by the C-S-H/space ratio, we, therefore, expect that the C-S-H formed from SCMs exhibits similar mechanical properties when compared to the C-S-H from pure OPC.

The theoretical tensile strength for cohesive brittle material is related to the E modulus through surface energy. Typical estimates are $f_t \in (0.01 - 0.10) E$ [53, 59]. This gives a theoretical tensile strength of the C-S-H globule in the range $f_t \in (571 - 5710)$ MPa which already shows high values on the small scale. Our apparent tensile strength for the C-S-H globule lies at the bottom range which already signalizes defects on this small scale.

Recently, tensile strength was measured indirectly on cantilever beams 20 μm long by means of bending [111]. The beams were prepared from 7 year old cement paste via FIB technique. Tensile strength of outer product (mainly CSH_{LD}) corresponded to 264.1 ± 73.4 MPa, inner product (mainly CSH_{HD}) 700.2 ± 198.5 MPa. This clearly demonstrates increase of strength with size decrease and supports the high tensile strength of C-S-H globule.

The formation of the C-S-H gradient inevitably leads to a decrease of compressive strength. A possible way of interpreting the C-S-H gradient is that as C-S-H precipitates on clinker grains it starts to grow onwards, filling capillary porosity. For cement pastes with a relatively high w/b ratio clinker grains are widely spaced apart from each other, C-S-H fail to interconnect neighbouring grains to create a solid structural network. Densifying the microstructure, either by lowering w/b ratio, by providing additional mineral surfaces for C-S-H to precipitate onto or by filling capillary porosity by a fine material (such as silica fume), inevitably leads to a more dispersed C-S-H. This results in a low gradient of C-S-H (described by a high parameter β) and corresponds to high strength predictions, see Figure 3.22(a) for pastes with $w/b \leq 0.4$. Pastes with a higher water-to-binder ratio ($w/b > 0.4$) tend to exhibit a larger gradient of C-S-H (described by a low parameter β) due to a less dense packing of clinker grains, see Figure 3.22(b).

The scaling parameter β takes into account several factors, notably heterogeneous

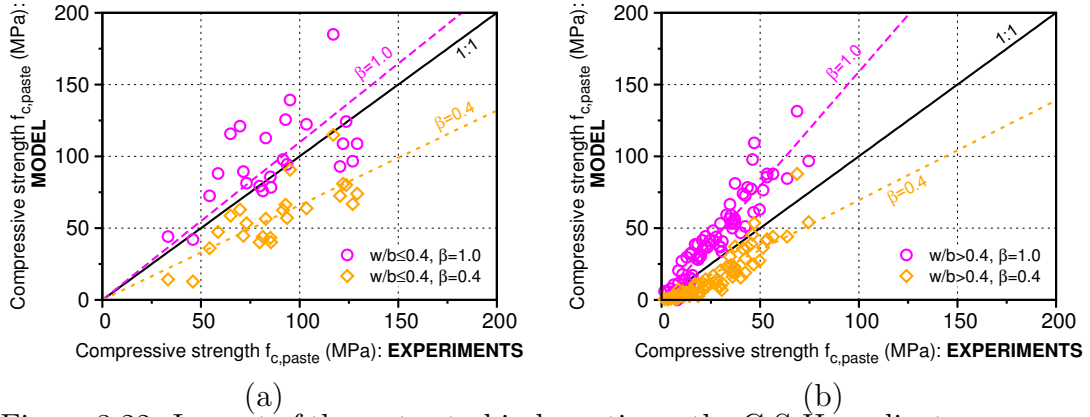


Figure 3.22: Impact of the water-to-binder ratio on the C-S-H gradient, represented by the parameter β : (a) dense microstructures with $w/b \leq 0.4$ exhibit a more uniform C-S-H formation signaled by $\beta = 1$, whereas (b) sparse microstructures with $w/b > 0.4$ indicate a higher C-S-H gradient.

nucleation and precipitation of C-S-H and cement fineness. These factors are normally overlooked since calibration data usually come from similar cements without seeding agents or with various blend levels. Recognizing this effect opens a way to optimize distribution of C-S-H and to improve a binder.

3.4.7 Validation of elastic modulus

The elastic modulus of cement paste was validated against 27 experimental results from CemBase. The validation assumed $\beta = 1.0$ and $\beta = 0.6$ for all experimental results, see Figure 3.23. Lower values of β lead to slightly lower model predictions.

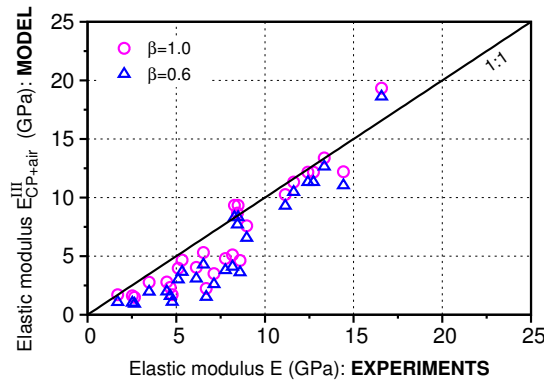


Figure 3.23: Model predicted elastic modulus for $\beta = 1.0$ and $\beta = 0.6$.

3.4.8 Example #1 - Portland cement paste $w/c=0.51$

This example illustrates the performance of the multiscale model on OPC with $w/b = 0.51$. The microstructural characterization in Figure 3.24(a) was performed at 3, 7, 28, and 91 days at Lafarge Centre de Recherche according to the test protocol described in [153] using a combination of XRD/Rietveld together with thermal gravimetric analysis and volume balance equations and provides the necessary volume fractions for the model. A high water-to-binder ratio creates a sparsely filled microstructure which, at the same time, results in a high gradient of C-S-H. Figure 3.24(b) shows a validation where a low parameter $\beta = 0.6$ fits the best experimental results. The last experimental strength value measured at 91 days shows no increase when compared to 28 days. In this particular case the specimen had dried out, which is further supported by mass measurements taken directly after demoulding of the specimen and before testing. The specimen was kept for 91 days in a cooling chamber with 95% RH, 20 °C and was wrapped in a food-preservation plastic foil to further reduce water evaporation. However, such precautions were insufficient and surface microcracks were very likely formed which resulted in a lower-than-expected compressive strength. Table 3.2 shows a decrease of model-predicted tensile and compressive strength with upscaling.

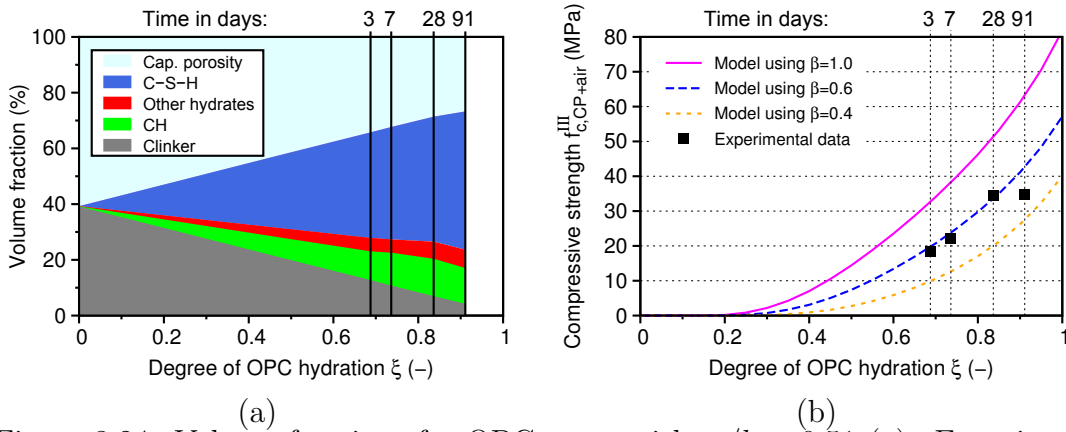


Figure 3.24: Volume fractions for OPC paste with $w/b = 0.51$ (a). Experimentally measured compressive strength (b) compared with multiscale model predictions.

3.4.9 Example #2 - Portland cement paste $w/c=0.247$

To study the impact of the water-to-binder ratio on observed mechanical properties, we extract a sub-stoichiometric cement paste with $w/b = 0.247$ from Cem-

Table 3.2: Decrease of strength with upscaling for OPC paste, $w/b = 0.51$ at 28 days (degree of OPC hydration $\xi = 0.836$) using microstructural characterisation as follows: $\gamma_{\text{CSH}} = 0.5815$, $f_{\text{cappor}} = 0.290$, $f_{\text{incl}} = 0.3067$, $E_{\text{incl}} = 48.032$ GPa, $f_{\text{air}} = 0.008$, $\beta = 0.6$, and $f_{t, \text{glob}} = 320$ MPa.

	Level 0 C-S-H	Level 1 C-S-H foam	Level 2 Cement paste	Level 3 Cement paste with air	
f_t^i	68.958	7.605	5.765	4.185	MPa
f_c^i	551.667	60.843	46.121	33.481	MPa

Base. Volume fractions were calculated by CEMHYD3D hydration model [19] using raw material characterization found in [101]. The necessary input for the multiscale model comes from the volume fraction in Figure 3.25(a). A relatively low $w/b = 0.247$ indicates a dense microstructure, forcing C-S-H to evenly precipitate within capillary pores. This is best described by $\beta = 0.8$, see Figure 3.25(b). Table 3.3 shows a decrease of model-predicted tensile and compressive strength with upscaling.

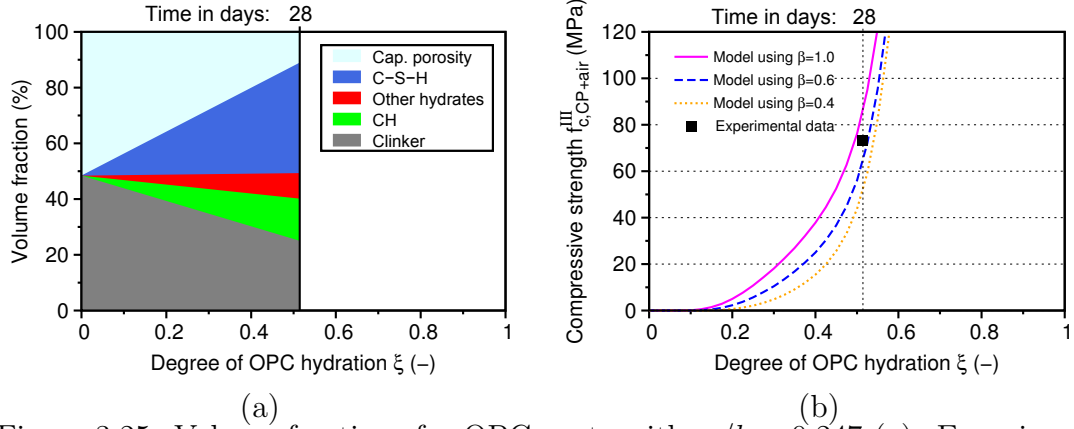


Figure 3.25: Volume fractions for OPC paste with $w/b = 0.247$ (a). Experimentally measured compressive strength (b) compared to model predictions.

3.4.10 Example #3 - slag-blended cement paste $w/b=0.53$

The results from a microstructural characterization carried out on a slag-blended paste with $w/b = 0.53$ by mass ($w/b = 1.6$ by volume), the 45 % cement replacement level are shown in Figure 3.26(a). The characterization of individual chemical phases was performed at 1, 3, 7, 28, and 91 days in the same way

Table 3.3: Decrease of strength with upscaling for OPC paste, $w/b = 0.247$ at 28 days (degree of OPC hydration $\xi = 0.515$) using microstructural characterisation as follows: $\gamma_{\text{CSH}} = 0.77564$, $f_{\text{cappor}} = 0.1146$, $f_{\text{incl}} = 0.4892$, $E_{\text{incl}} = 79.033$ GPa, $f_{\text{air}} = 0.041$, $\beta = 0.8$, and $f_{t,\text{glob}} = 320$ MPa.

	Level 0	Level 1	Level 2	Level 3	
	C-S-H	C-S-H foam	Cement paste	Cement paste with air	
f_t^i	80.764	24.404	18.498	9.289	MPa
f_c^i	646.115	195.236	147.998	74.313	MPa

as in Section 3.4.8. The model-predicted compressive strength is shown in Figure 3.26(b). The most appropriate value is $\beta = 0.5$.

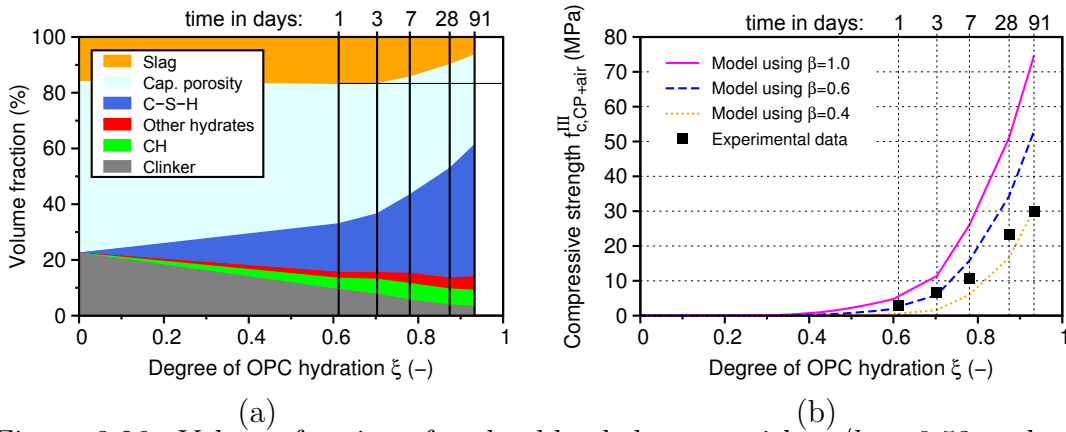


Figure 3.26: Volume fractions for slag-blended paste with $w/b = 0.53$ and the replacement level of 45 % by volume (a). Experimentally measured compressive strength (b) compared to model predictions.

3.4.11 Example #4 - fly ash-blended cement paste $w/b=0.60$

The results from a microstructural characterization carried out on a fly ash-blended paste with $w/b = 0.60$ by mass ($w/b = 1.6$ by volume), the 45 % cement replacement level are shown in Figure 3.27(a). The characterization of individual chemical phases was performed at 1, 3, 7, 28, and 91 days in the same way as in Section 3.4.8. The model-predicted compressive strength is shown in Figure 3.27(b). The most appropriate value is $\beta = 0.5$.

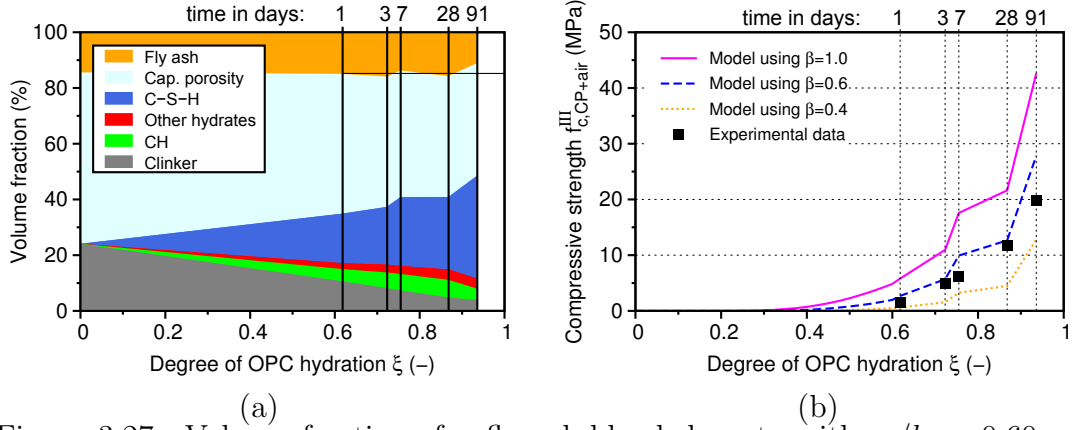


Figure 3.27: Volume fractions for fly ash-blended paste with $w/b = 0.60$ and the replacement level of 45 % by volume (a). Experimentally measured compressive strength (b) compared to model predictions

3.4.12 Comparison with Powers' approach

Direct comparison of Powers' gel/space model [128] and the presented model is not straightforward because both are based on different microstructural descriptors. However, we will show that under some reasonable assumptions both approaches yield comparable results. Powers coined an empirical relation between the microstructure of pure cement pastes and their compressive strength using "gel/space" ratio (GSR) as a microstructural descriptor. This relation can be expressed by a power law function as

$$f_{c,paste} = f_0 \text{GSR}^b \quad (3.28)$$

where f_0 stands for the intrinsic compressive strength of the material and b for the best fit coefficient. Similar power law function can also be identified when the microstructure is described by "C-S-H/space" ratio, γ_{CSH} , see Figure 3.28.

The presented multiscale model uses four hierarchical levels to describe the microstructure. To simplify the strength prediction into a single equation, we make the following assumptions: (i) on level 0 we assume the ratio of C-S-H_{LD}:C-S-H_{HD} equal to 4:1; (ii) on level 1 the spatial gradient of C-S-H by $\beta = 0.6$; (iii) on level 2 the volume fraction of inclusions equals to 0.15; (iv) on level 3 the volume of entrained air equals to 0.008. The expression of compressive strength of then

simplifies into a single exponential equation

$$f_{c,paste} = 320 \exp \left(-1.3412 \frac{1 - \gamma_{CSH}^{5.7072}}{\gamma_{CSH}} \right) \quad (3.29)$$

Figure 3.28 shows the comparison of both approaches with very similar results. However, just by varying the scaling parameter β results in upper and lower bounds that can cover almost all experimental data points.

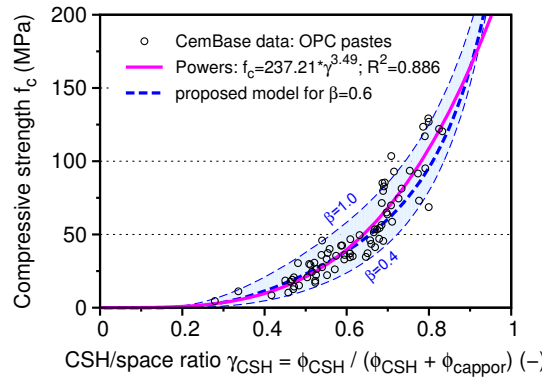


Figure 3.28: Comparison of modeling approaches: Powers' power law fit and proposed model.

3.4.13 Impact of C–S–H fracture energy

It is an interesting feature of the four-level model that compressive or tensile strength always decreases on upscaling. Fracture energy may increase on upscaling if other mechanisms occur during the crack propagation, e.g. crack arresting, shielding, or pulling out an inclusion. It is also known from concrete experiments that fracture energy increases with the size of aggregates [174].

A direct experimental characterization of fracture energy for C-S-H is currently, up to our best knowledge, beyond experimental evidence. C-S-H as an amorphous precipitate contains micro-crystalline seeds of CH and other crystalline hydration products (AFm, AFt) which increase the observed fracture energy. Modeling of frictional pull-out tests [62] of CH from the C-S-H matrix tend to increase the fracture energy due to intermolecular interactions between C-S-H globules.

Numerical modeling on level 1, see Figure 3.29, shows that the fracture energy of C-S-H only has an insignificant impact on the predicted compressive strength.

Decreasing $G_{f,CSH}^0$ below 2 J/m^2 would increase the apparent tensile strength of a globule, $f_{t,glob}$, [62].

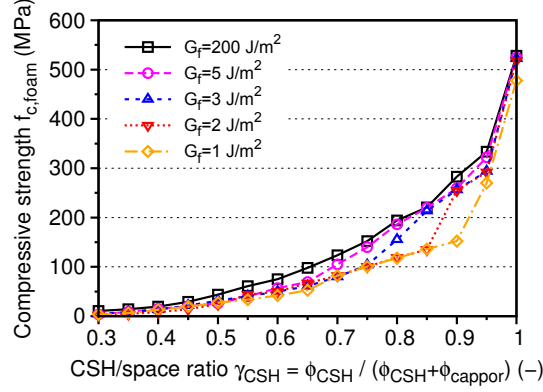


Figure 3.29: Impact of fracture energy of C-S-H on compressive strength of C-S-H foam. FE model from $10 \times 10 \times 20$ brick elements (UC size $5 \times 5 \times 10 \mu\text{m}$) using $\beta = 1.0$.

3.4.14 Impact of void size on strength

Voids in cement paste occur on different length scales either as capillary pores (size $10 \text{ nm} - 10 \mu\text{m}$) or as entrained air ($10 \mu\text{m} - 500 \mu\text{m}$) or entrapped air ($> 1 \text{ mm}$). In quasi-brittle materials the size of voids matters as the scaling of compressive (tensile) strength obeys the size-effect law [17]

$$\sigma_{N,c} = B f'_c \left(1 + \frac{d}{d_0} \right)^{-\frac{1}{2}} \quad (3.30)$$

where d is the void diameter, d_0, B, f'_c are constants for identification. In a perfectly ductile material, the diameter of a void does not matter. The level of C-S-H foam resembles this situation with the size up to $10 \mu\text{m}$, see Figure 3.12, which renders the foam less brittle with larger softening part. Capillary pores residing in the foam influence strength by their volume only, while the shape and their distribution have a little influence. This is the reason why the total amount of capillary porosity controls compressive / tensile strength, but neither their pore distribution nor their shape.

The situation changes for entrapped/entrained air voids which have a much larger size than capillary voids. In a perfectly brittle material, increasing a void size four-times would decrease the strength twice according to linear elastic fracture

mechanics. Also, the shape of void influences the strength of material. Cement paste is a quasibrittle material hence the scaling of strength occurs between ductile and brittle asymptotic limits.

Figure 3.30 shows results from a size effect study on a 2D microstructure (100×100 quadrilateral elements). The model is not directly associated to any homogenization level in particular, see Figure 5.2, but covers the whole range of sizes. The model consists of a homogeneous matrix ($f_c = 100$ MPa and $G_f = 15$ J/m²) with voids. The actual void diameter is kept constant at 10 elements whereas the volume fraction changes from 0 up to 10 %. Changing the element resolution creates different sizes of the identical microstructure, starting from 1×1 μm with void size 0.1 μm up to 2×2 cm with void size 2 mm. It is clear that void diameters $d > 50$ μm reduce the strength more than only by their volume amount. This is due to a more brittle behavior of the cement paste than the foam. The presence of entrapped air with $d > 1$ mm is the most detrimental.

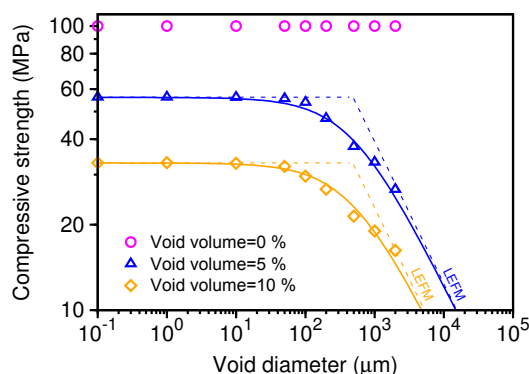


Figure 3.30: Void size-dependent compressive strength of cement paste obeying the size-effect law.

3.4.15 Global sensitivity analysis by scatter plots

Sensitivity analysis by a sampling-based method identifies the key global factors influencing compressive/tensile strength. Compressive strength is calculated using a full factorial design from a combination of all input variables on each scale. Model inputs for each level were chosen by uniform sampling over all admissible model input as follows:

- C-S-H/space ratio $\gamma_{\text{C-S-H}} \in \langle 0.3, 1 \rangle$ for level 1.
- Volume fraction of C-S-H_{HD} within C-S-H: $\phi_{\text{CSH}_{\text{HD}}} \in \langle 0, 1 \rangle$ for level 1.

- Parameter for C-S-H spatial gradient: $\beta \in \langle 0.4, 1 \rangle$ for level 1.
- Volume fraction of inclusion: $\phi_{incl} \in \langle 0, 1 \rangle$ for level 2.
- Volume fraction of entrapped / entrained air: $\phi_{air} \in \langle 0, 0.1 \rangle$ for level 3.

Compressive strength is plotted against a combination of individual input variables in a scatter plot which provides a visual indication of the sensitivity of a given input value. Spearman's rank correlation coefficient ρ is used to quantify sensitivity; the closer the $|\rho|$ is to 1, the more monotonically related the observed variables are.

Input variables on all levels cover a wide range of possible combinations of admissible data for the multiscale model. Figure 3.31 shows the most correlated input variables globally; the C-S-H/space ratio and the volume fraction of entrapped / entrained air.

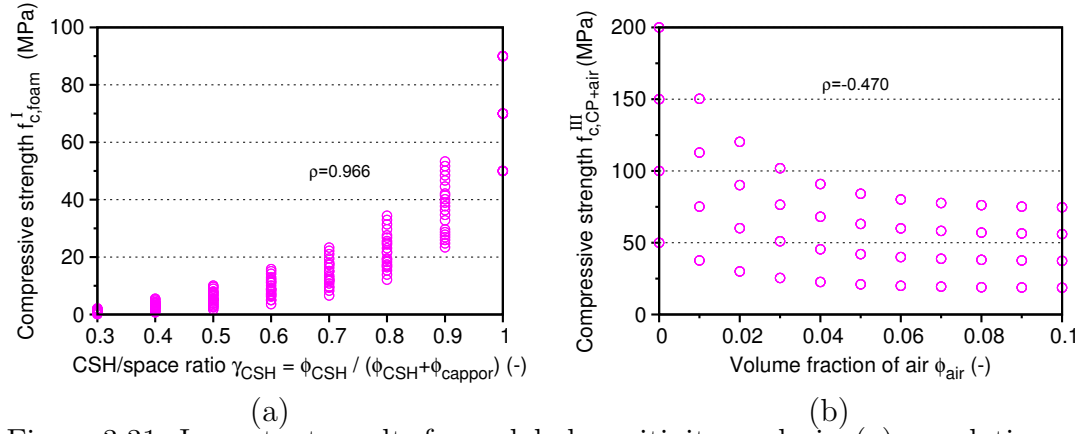


Figure 3.31: Important results from global sensitivity analysis; (a) correlation between the compressive strength of C-S-H foam and the CSH/space ratio, and (b) compressive strength of cement paste and volume fraction of air.

3.4.16 Local sensitivity analysis

To further highlight the impact of individual input parameters on model predictions, local sensitivity analysis was carried out for selected cement pastes. Local sensitivity analysis the effect of small perturbations of one model input variable (X_i) to the compressive strength while keeping the other inputs constant (\mathbf{X})

$$\left. \frac{\partial Y}{\partial X_i} \right|_{\mathbf{X}} \quad (3.31)$$

The partial derivative in Eq. (3.31) is solved using a forward difference method with the step length equal to 1 % of the input value. The higher the absolute value of the partial derivation, the more sensitive the input parameter. However, the step length is kept equal for assessment of all input variables, disregarding the actual range for the input parameter. This results in unequal model predictions because changing the volume fraction of air by 1 % (with a range from 0 to 0.1) reduces predicted compressive strength significantly more than changing, e.g. β by 1 % (with a range from 0.4 to 1). Therefore the presented local sensitivity analysis only shows trends and highlights key microstructural factors rather than comparing absolute values of the partial derivation.

Local sensitivity analysis was performed on all mixes in four examples (OPC with $w/b = 0.51$, OPC with $w/b = 0.247$, slag-blended paste with 45 % clinker replacement, and fly ash-blended paste with 45 % clinker replacement). The results were very similar and only the OPC paste $w/b = 0.51$ is shown in Table 3.4.

Table 3.4: Local sensitivity analysis on OPC paste, $w/c = 0.51$ at 28 days.

Model input X_i	Default value \mathbf{X}	Impact on compressive strength $\left. \frac{\partial f_{c,CP+air}^{III}}{\partial X_i} \right _{\mathbf{x}}$
Air volume fraction ϕ_{air}	0.008	-491.67
C-S-H/space ratio γ_{CSH}	0.608	181.85
Spatial gradient of C-S-H β	0.600	58.37
C-S-H _{HD} volume fraction $\phi_{CSH_{HD}}$	0.094	19.16
Inclusion volume fraction ϕ_{incl}	0.267	-0.15
Elastic modulus of inclusion E_{incl}	48.032	0.00

Results highlighted that apart from the C-S-H/space ratio and entrapped air, the spatial gradient of C-S-H plays a key role for the compressive strength and elastic modulus of cement paste.

3.5 Conclusions

The paper describes a four-level micromechanical model for blended cement pastes aimed at predicting compressive strength. The multiscale model uses a newly-proposed ‘‘C-S-H/space’’ ratio as the primary microstructural descriptor which is applicable for pure as well as blended cements. The model introduces a spatial

C-S-H gradient, mimicking nonuniform distribution between individual grains. The most relevant findings and conclusions can be summarized as follows:

1. The C-S-H globule was taken as the only failing phase which obeys an elasto-damage law. Other chemical phases were treated elastically. Validation proved that this assumption can cover all experimental data on OPC and blended pastes with the addition of slag, fly ash, limestone and quartz and w/b in the range of 0.157 up to 0.68 from approximately 1 day of hydration under room temperature.
2. The CemBase database version 1.0 was assembled for validating the multiscale model. The database now contains 399 experimental data.
3. The apparent tensile strength of the C-S-H globule was identified as $f_{t, glob} = 320$ MPa by evaluating the model predicted compressive strength against 95 experimental values. Although there is no direct experimental evidence of such high tensile strength, the theoretical limit value can be as high as 5700 MPa [53, 59].
4. The C-S-H/space ratio was found to be the most fundamental parameter for compressive/tensile strength, in accordance with Powers [127]. The volume of entrained / entrapped air and the spatial gradient of C-S-H are further factors governing the compressive strength of blended pastes.
5. Precipitating C-S-H around grains exhibit a spatial gradient which has a strong impact on the compressive strength of cement paste. The densification of the microstructure due to a decrease of the initial water-to-binder ratio or by progressing hydration leads to a more uniform distribution of C-S-H. This assumption needs further experimental refinement by statistical descriptors based on true μ CT or SEM images.
6. The multiscale model needs further elaboration for systems beyond the OPC basis producing C-S-H. Particularly alkali-activated systems (N-A-S-H gel), calcium aluminate cements (C-A-H gel), oxychloride, phosphatic cements, etc.
7. The multiscale model captures the strain-softening behavior on each scale and handles energy dissipation by upscaling E , f_t and assigning G_f . This ensures a correct localization limiter on each scale and the transfer of microstructurally-based fracture properties between scales [177].

Acknowledgement

The authors gratefully acknowledge “NANOCEM” funding within Core Project 10 “Micromechanical Analysis of Blended Cement-Based Composites” and support from CTU grant SGS15/030/OHK1/1T/11. We appreciate stimulating discussions on NANOCEM events, particularly contributions from Bernhard Pichler (TU Wien) and Klaus-Alexander Rieder (WR Grace). NANOCEM’s funding further allowed Michal Hlobil’s internship in Lafarge Centre de Recherche during 2012-2013.

Chapter 4

Hydration-driven evolution of compressive strength of OPC and blended cementitious materials: microstructural characterization, strength testing, and multiscale modeling

This chapter contains a quite mature paper draft authored by Michal Hlobil, Markus Königsberger, Pipat Termkhajornkit, Rémi Barbarulo, Christian Hellmich, and Bernhard Pichler. At the time of finalizing this thesis, is planned to submit the paper – in further improved form – to Cement and Concrete Research.

4.1 Introduction

The hydration-induced development of strength of cementitious materials is of highest practical relevance, because the uniaxial compressive strength of concrete is the central material property for classification and design used by codes and regulations [56, 1, 113]. In the second half of the 20th century, concrete technology was challenged to satisfy high – and to a certain extent contradicting – demands

from construction industry. This includes the following requirements.

- As for flexible construction, fresh concrete shall remain workable for hours, i.e. significant hydration of cement shall not start prior to placement of concrete.
- As for efficient construction, hydration shall be a speedy process after placement, i.e. early-age strength shall develop so fast that formworks can be stripped 24 hours after production.
- The final product shall be durable, in order to guarantee serviceability of structures over their entire designed lifetime.

Available concrete mixes based on ordinary Portland cement (OPC) satisfy the described demands. At the end of the 20th century, in turn, reduction of CO₂ emissions became an additional challenging requirement. The favorite solution was to replace part of OPC clinker either by hydraulic waste materials from other industries, such as the supplementary cementitious materials (SCMs) blast furnace slag or fly ash from combustion power plants, or by inert fillers, such as quartz or limestone. The resulting blended binders make the sought reduction of CO₂ emissions possible, they comply with the requirements regarding fresh concrete properties and the long-term performance, but the early-age strength development is slower compared to traditional OPC. This has initiated intensive research on early-age properties of cementitious materials produced with blended binders, see e.g. [54, 91, 114, 94, 178, 72].

Use of blended binders adds, on the one hand, a lot of flexibility for the development of innovative mix designs, given that different clinker replacement ratios can be used and that several clinker replacement materials are available, see above. On the other hand, the early-age evolutions of mechanical properties such as stiffness and strength are significantly different as compared to pure OPC materials. First and foremost, this is a consequence of modified hydration kinetics [114]. Finely ground non-reactive fillers made of limestone or quartz are known to speed up reaction kinetics, since the small particles represent preferred precipitation sites for hydrates [94], although the fillers themselves do not dissolve considerably [176, 172]. While SCM particles exhibit (to a certain extent) a similar filler effect, they start to hydrate typically much later than OPC, because the pH value of the pore solution must exceed a certain threshold to initiate SCM hydration [94]. Delayed hydration results in the delayed development of

early-age stiffness and strength. In addition to the influence on reaction kinetics, interaction between SCM hydration and clinker hydration may lead to chemical hydrate compositions which are significantly different from those precipitating in pure OPC pastes [25, 39]. The fibrillar morphology of hydrates, known from OPC, may gradually change into a more foil-like morphology under the influence of blast furnace slag [131]. Fly ash, in turn, may result in a more uniform microstructure and a decreased average pore size relative to the OPC reference [39]. Other sources report on an influence of grinding fineness on the resulting pore size distribution [39] and, consequently, also on the macroscopic compressive strength [38]. Finally, nanoindentation tests imply that hydrates in SCM-blended pastes are considerably stronger than in OPC paste [178], while inert calcareous fillers do not alter the hydrates' strength [162].

The present contribution further extends this line of research by studying the strength evolution of (cement pastes and) mortars produced with pure OPC or blended binders, in the framework of a combined experimental-computational approach. Given that predictive modeling of the phase evolution of blended pastes is out of reach, state-of-the-art microstructural characterization techniques are combined in order to quantify the phase volume evolutions of one pure OPC paste and of four blended pastes, where 45% of the clinker volume are replaced either by quartz, limestone, slag, or fly ash. In addition, blended mortar cylinders are crushed under uniaxial compression at material ages amounting to 3 days and to 28 days. This experimental database serves as the motivation for related modeling activities, which are based on methods of continuum micromechanics [180]. As for OPC materials, these methods have shown to be valuable for homogenization of elastic stiffness [22, 137, 120, 148, 9, 164], creep [139, 87], and strength [120, 119, 122]. Notably, the elasto-brittle strength models consider that the macroscopic strength of OPC cement pastes is reached, once stresses in microscopic hydration products reach the corresponding hydrate strength. In the context of the present paper, aspects of the strength model [119, 122] are further elaborated:

1. The range of applicability of the strength models [119, 122] is first extended from cement pastes to mortars. The latter are considered as matrix-inclusion composites, with rather stiff sand grains embedded in a less stiff cement paste matrix. Because of the stiffness contrast, we consider that stress peaks of the cement paste matrix occur in representative volumes that are directly attached to the surface of sand grains. Such stress peaks

are evidenced by the formation of cracks in this region [145, 144]. We here quantify these stress peaks by means of the stress concentration concept developed in [85, 86].

2. Envisioning that hydrate failure is related to shear cracking at the nanoscopic scale, and that the corresponding shear strength increases with increasing pressure acting on the crack plane, the *von Mises*-type elastic limit criterion used in [119, 122] is replaced by a *Mohr-Coulomb* criterion. Related strength constants are taken from limit state analysis of nanoindentation studies on low-density calcium-silicate-hydrates [138].
3. When it comes to the scale transition from cement paste down to micron-sized needle-shaped hydrates, we consider that cracking of hydrates is an *energy*-driven phenomenon. Therefore, we quantify principal hydrate stresses intervening in the Mohr-Coulomb criterion based on *energy density*-related stress averages, i.e. we provide a mechanical explanation why so-called “higher-order” or “second-order” stress averages intervene in the strength models [119, 122], rather than simple volume averages which are also referred to as “first-order” averages.
4. While the models [119, 122] are based on only one *average* hydrate type, we here extend the microstructural representation towards all types of hydrates that are identified by means of microstructural characterization, and they include C-S-H, portlandite, ettringite, monosulfate, etc.
5. Finally, consideration of blended binders (rather than pure OPC cements) requires an extension of the microstructural representation towards consideration of the cement replacement materials quartz, limestone, slag, and fly ash.

The paper is structured as follows. Section 4.2 refers to strength of OPC pastes and mortars. We extend the multiscale strength homogenization model of [119, 122] by newly adding the scale of mortar and by implementing the Mohr-Coulomb criterion for hydrate failure. The extended model is validated for OPC cement pastes and mortars, by comparing blind predictions of early-age strength evolutions with experimental data from three different laboratories. Section 4.3 refers to strength of pastes and mortars produced with blended binders. Phase volume evolutions of four blended binders and of the underlying OPC are quantified based on state-of-the-art methods for microstructural characterization. Com-

pressive strength values are determined on mortar samples at ages of 3 days and 28 days. The strength model of Section 4.2 is further extended towards consideration of the replacement materials and of all hydrate types that were identified by means of microstructural characterization. Model predicted strength values are compared with their experimental counterparts. Finally, the paper is closed with a discussion (Section 4.4) and conclusions (Section 4.5).

4.2 Elasto-brittle multiscale strength modeling of ordinary Portland cement pastes and mortars

Following the concept of quasi-brittle strength upscaling developed by Pichler et al. [125, 120] and Pichler and Hellmich [119], it is considered that the macroscopic strength of cement paste or mortar is reached once microstresses in hydration products reach the hydrate strength. Therefore, a multiscale representation of cementitious materials is required, which accounts for key features of their microstructure.

4.2.1 Micromechanical representation

In continuum micromechanics a material is understood as a micro-heterogeneous representative volume element (RVE) with characteristic size ℓ fulfilling the separation of scales requirement [180]:

$$d \ll \ell \ll D, \quad (4.1)$$

where d and D , respectively, stand for the characteristic sizes of inhomogeneities and of the structure containing the RVE (such as structural dimensions or the wavelength of loading). RVEs of cementitious materials are too complex to be resolved in full detail. As a remedy, quasi-homogeneous material subdomains (referred to as material phases), are identified as microstructural key features. The overall (“homogenized”) mechanical properties of cementitious materials are governed by the mechanical properties of the material phases, their shapes, volume dosages, and mutual interaction.

Following Pichler et al. [119] as well as Pichler and Hellmich [122], we resolve the microstructure of mortar across three separated scales of observation, see Fig. 4.1. At the largest scale of observation, we envision a centimeter-sized RVE of mor-

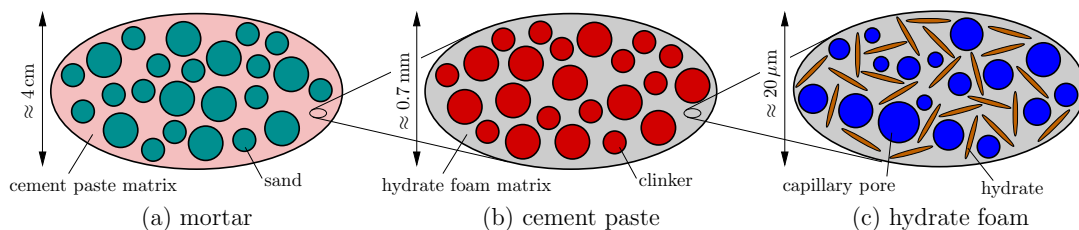


Figure 4.1: Multiscale micromechanics representation of mortar (“material organogram”) after [119, 122]; two-dimensional sketches of three-dimensional representative volume elements

tar, which consists of spherical sand grains that are embedded in a cement paste matrix, see Fig. 4.1(a). At the intermediate scale of observation, we envision a (sub-)millimeter-sized RVE of cement paste, which consists of spherical unhydrated clinker grains that are embedded in a hydrate foam matrix, see Fig. 4.1(b). At the smallest scale of observation, we envision a micrometer-sized RVE of hydrate foam, which consists of spherical capillary pores and needle-shaped hydrates that are uniformly orientated in all space directions, see Fig. 4.1(c).

4.2.2 Volume fractions and mechanical constants of material phases

The Powers-Acker model [2, 127] provides analytical expressions for phase volume fractions as functions of the initial water-to-cement mass ratio w/c , the initial sand-to-cement mass ratio s/c , and the degree of clinker hydration ξ_{clin} , defined as the volume of already hydrated clinker divided by its initial volume. At the scale of mortar, the volume fractions of sand f_{sand}^{mor} and of the cement paste matrix f_{cp}^{mor} read as [22]

$$f_{sand}^{mor} = \frac{\frac{s/c}{\rho_{sand}}}{\frac{1}{\rho_{clin}} + \frac{w/c}{\rho_{H_2O}} + \frac{s/c}{\rho_{sand}}}, \quad f_{cp}^{mor} = 1 - f_{sand}^{mor}. \quad (4.2)$$

At the scale of cement paste, the volume fractions of clinker f_{clin}^{cp} and of the hydrate foam matrix f_{hf}^{cp} read as [2, 127, 119]

$$f_{clin}^{cp} = \frac{20(1 - \xi_{clin})}{20 + 63w/c} \geq 0, \quad f_{hf}^{cp} = 1 - f_{clin}^{cp}. \quad (4.3)$$

At the scale of the hydrate foam, the volume fractions of capillary pores f_{pore}^{hf} and of hydrates f_{hyd}^{hf} read as [119]

$$f_{pore}^{hf} = \frac{63(w/c - 0.367\xi_{clin})}{20\xi + 63w/c} \geq 0, \quad f_{hyd}^{hf} = 1 - f_{pore}^{hf}. \quad (4.4)$$

All material phases are considered to exhibit isotropic elastic properties, which allows for expressing the phase stiffness tensor \mathbb{C}_i in terms of bulk moduli k_i and shear moduli μ_i

$$\mathbb{C}_i = 3k_i\mathbb{I}^{vol} + 2\mu_i\mathbb{I}^{dev}, \quad (4.5)$$

where index i refers to the material phase i , see Table 5.1 for phase-specific constants. In Eq. (4.5), \mathbb{I}^{vol} and \mathbb{I}^{dev} denote the volumetric and deviatoric parts of the symmetric fourth-order identity tensor \mathbb{I} , defined as $I_{ijkl} = 1/2(\delta_{ik}\delta_{jl} + \delta_{il}\delta_{jk})$, $\mathbb{I}^{vol} = 1/3(\mathbf{1} \otimes \mathbf{1})$, and $\mathbb{I}^{dev} = \mathbb{I} - \mathbb{I}^{vol}$, respectively, whereby $\mathbf{1}$ denotes the second-order identity tensor with components equal to the Kronecker delta δ_{ij} , namely $\delta_{ij} = 1$ for $i=j$, and 0 otherwise.

Table 4.1: Isotropic elasticity constants of material phases

	Bulk modulus	Shear modulus	Source
	k [GPa]	μ [GPa]	
clinker	k_{clin}	116.58	μ_{clin} 53.81 [163]
hydrates	k_{hyd}	18.69	μ_{hyd} 11.76 [119]
quartz	k_{quartz}	36.44	μ_{quartz} 31.20 [3]
limestone	$k_{limestone}$	67.19	$\mu_{limestone}$ 29.24 [129]
slag	k_{slag}	36.44	μ_{slag} 31.19 [112]
fly ash	k_{FA}	58.33	μ_{FA} 43.75 [171]
sand	k_{sand}	35.35	μ_{sand} 29.91 [166]
pores	k_{pore}	0.00	μ_{pore} 0.00

As for strength properties, we consider that hydrates are the weakest links in cementitious microstructures. In [119, 122], it was considered that hydrate failure follows a (von Mises-type) elastic limit criterion and the corresponding (shear failure-related) deviatoric hydrate strength was identified by top-down analysis,

i.e. from macroscopic strength measurements on young cement pastes. Considering the nanogranular nature of C-S-H [42], we now consider a Mohr-Coulomb-type elastic limit criterion [43, 103], expressing that the shear strength of gliding planes increases with increasing normal pressure acting on the gliding planes:

$$f(\boldsymbol{\sigma}_{hyd}) = \sigma_{hyd,I} \frac{1 + \sin \varphi_{hyd}}{2 c_{hyd} \cos \varphi_{hyd}} - \sigma_{hyd,III} \frac{1 - \sin \varphi_{hyd}}{2 c_{hyd} \cos \varphi_{hyd}} - 1 \leq 0, \quad (4.6)$$

where $\boldsymbol{\sigma}_{hyd}$ denotes the hydrate stress tensor (with $\sigma_{hyd,I}$ and $\sigma_{hyd,III}$ as largest and smallest principal stress component), φ_{hyd} the angle of internal friction, and c_{hyd} the cohesion. Notably, $f < 0$ refers to elastic hydrate behavior and $f = 0$ corresponds to hydrate failure. The material constants of low density calcium-silicate-hydrates are considered to be representative for all the hydrates [123], and they were quantified using limit state analysis of nanoindentation test data [41, 138] as

$$\varphi_{hyd} = 12^\circ, \quad c_{hyd} = 50 \text{ MPa}. \quad (4.7)$$

Evaluation of the the Mohr-Coulomb criterion (4.6) requires quantification of hydrate stress states $\boldsymbol{\sigma}_{hyd}$. They follow from concentration of macrostress states imposed on RVEs of cement paste or mortar down to the level of needle-shaped hydrates, discussed next.

4.2.3 Concentration of loading imposed on RVEs of mortar into cement paste: quantification of stress peaks

Because sand grains are stiffer than the cement paste matrix (particularly so at early ages), sand grains exhibit – on average – larger stresses than the cement paste matrix. Therefore stress peaks of cement paste occur in the immediate vicinity of the sand grains. In order to quantify these stress peaks, we follow the two-step procedure developed by Königsberger et al. [85], i.e. we concentrate first the loading imposed on RVEs of mortar down to average stresses and strains of sand grains. Subsequently, we apply firm bond-related stress and strain compatibility conditions at the sand-to-cement paste interface \mathcal{I}_{sand}^{cp} , in order to obtain the sought cement paste stress states representing stress peaks in the immediate vicinity of sand grains, as detailed next.

Concentration from homogeneous macrostresses imposed on an RVE of mortar,

Σ_{mor} , down to average stresses of sand grains, σ_{sand} , reads as

$$\sigma_{sand} = \mathbb{B}_{sand}^{mor} : \Sigma_{mor}, \quad (4.8)$$

with \mathbb{B}_{sand}^{mor} as the stress concentration tensor which is a function of the volume fractions and of the elastic properties of sand grains and cement paste. Based on the micromechanical representation of mortar as a matrix-inclusion composite, see Fig. 4.1, a Mori-Tanaka-scheme [105, 21] is appropriate for homogenization [180]. The scheme provides analytical access to the concentration tensor \mathbb{B}_{sand}^{mor} , see Appendix 4.5 for details. Averages strains of sand grains, ϵ_{sand} , are obtained from the elasticity law

$$\epsilon_{sand} = (\mathbb{C}_{sand})^{-1} : \sigma_{sand}, \quad (4.9)$$

where \mathbb{C}_{sand} stands for the isotropic stiffness tensor of sand, see Eq. (4.5) and Table 5.1.

Consideration of firm bond between sand grains and the surrounding cement paste matrix, implies interfacial continuity conditions of tractions and displacements. Displacement continuity can be expressed as the following relation [136, 85] between sand strains ϵ_{sand} and cement paste strains $\epsilon_{cp}(\underline{x})$

$$\underline{t}_1(\underline{x}) \cdot [\epsilon_{sand} - \epsilon_{cp}(\underline{x})] \cdot \underline{t}_2(\underline{x}) = 0 \quad \forall \underline{x} \in \mathcal{I}_{sand}^{cp}, \quad (4.10)$$

where $\underline{t}_1(\underline{x})$ and $\underline{t}_2(\underline{x})$ denote all possible pairs of tangent vectors in the tangential plane to the interface \mathcal{I}_{sand}^{cp} at position \underline{x} . Traction continuity, in turn, can be expressed as the following relation [136, 85] between sand stresses σ_{sand} and cement paste stresses $\sigma_{cp}(\underline{x})$

$$[\sigma_{sand} - \sigma_{cp}(\underline{x})] \cdot \underline{n}(\underline{x}) = 0 \quad \forall \underline{x} \in \mathcal{I}_{sand}^{cp}, \quad (4.11)$$

where $\underline{n}(\underline{x})$ denotes a unit vector orientated perpendicular to the interface \mathcal{I}_{sand}^{cp} at position \underline{x} . Stresses and strains of cement paste are related to each other by isotropic elasticity law

$$\sigma_{cp}(\underline{x}) = \mathbb{C}_{cp} : \epsilon_{cp}(\underline{x}), \quad (4.12)$$

where \mathbb{C}_{cp} denotes the homogenized stiffness of cement paste, which is obtained by two-step upscaling starting at needle-shaped hydrates and capillary pores. Their polycrystalline arrangement (direct mutual interaction) renders the self-

consistent scheme [70, 89, 71] appropriate for homogenization of the hydrate foam. Subsequent homogenization of the matrix-inclusion composite cement paste is carried out based on the abovementioned Mori-Tanaka scheme, see Appendix 4.5 for details.

The sought cement paste stress states prevailing in the immediate vicinity of the sand-to-cement paste interface \mathcal{I}_{sand}^{cp} follow from combination of relations (4.8)-(4.12) as [85]

$$\boldsymbol{\sigma}_{cp}(\underline{x}) = \mathbb{B}_{cp}^{sand}(\underline{x}) : \boldsymbol{\sigma}_{sand} = \mathbb{B}_{cp}^{sand}(\underline{x}) : \mathbb{B}_{sand}^{mor} : \boldsymbol{\Sigma}_{mor} \quad \forall \underline{x} \in \mathcal{I}_{sand}^{cp}, \quad (4.13)$$

with \mathbb{B}_{cp}^{sand} denoting the sand-to-cement paste stress concentration tensor, see Appendix 4.5 for details. Notably, the stress states $\boldsymbol{\sigma}_{cp}$ depend on the location vector \underline{x} , e.g. stress concentrations around the equator of the sand grains are quite different from the ones at the poles [85], see Fig. 4.2.

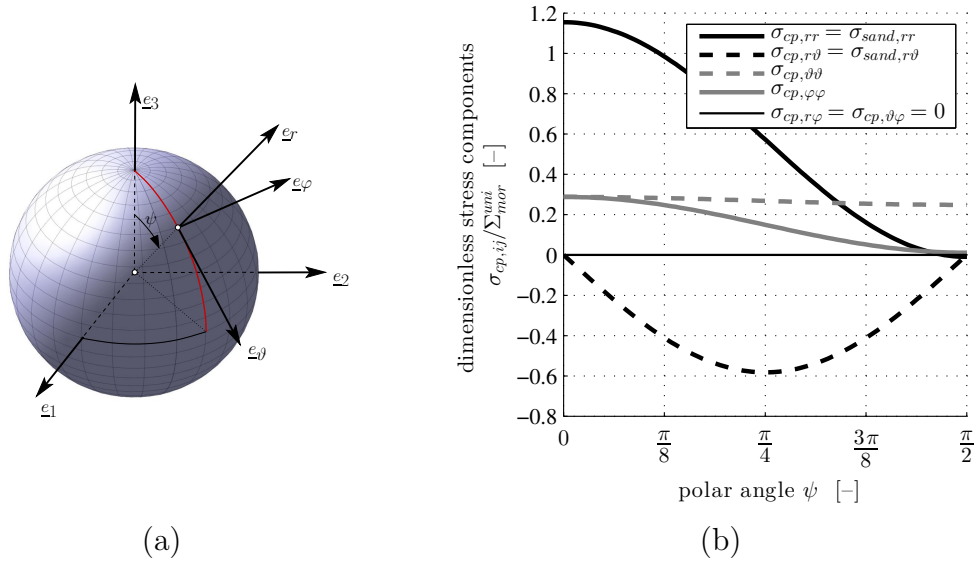


Figure 4.2: Concentration of uniaxial loading imposed on an RVE of mortar, see (4.28), to stress states of cement paste in the immediate vicinity of sand grains: (a) sand grain with global Cartesian base frame $\underline{e}_1, \underline{e}_2, \underline{e}_3$ and local spherical base frame $\underline{e}_r, \underline{e}_\theta, \underline{e}_\phi$; (b) cement paste stress components in the immediate vicinity of the sand-to-cement paste interface \mathcal{I}_{sand}^{cp} as a function of polar angle ψ ; evaluation of (4.13) for $w/c = 0.50$, $s/c = 3.0$, and $\xi_{clin} = 0.50$

4.2.4 Concentration of loading imposed on RVEs of cement paste into hydrates

As for quantification of hydrates stresses $\boldsymbol{\sigma}_{hyd}$ intervening in the Mohr-Couomb criterion (4.6), we now consider, at any point \underline{x} of the interface \mathcal{I}_{sand}^{cp} , the microstructure of cement paste in terms of a three-dimensional RVE, such as illustrated in Fig. 4.1(b). In agreement with that, we consider specific stress states $\boldsymbol{\sigma}_{cp}(\underline{x})$ from (4.13) as “macroscopic” loading imposed on RVEs of cement paste, $\boldsymbol{\Sigma}_{cp}$, representing the starting point for further multiscale stress concentration, i.e. $\boldsymbol{\sigma}_{cp}(\underline{x}) \rightarrow \boldsymbol{\Sigma}_{cp}$.

The Mohr-Coulomb criterion (4.6) implies that failure of hydrates is governed by cracking processes at the nanometric scale *inside* hydrate needles which is not explicitly resolved herein. Given that cracking is a dissipative phenomenon, failure of hydrates is a strain energy-dependent process, and this provides the motivation to perform strain energy-related stress concentration into hydrate needles [49, 125, 120], rather than quantifying spatial averages of stresses. To this end, the elastic energy W stored in the RVE of cement paste is expressed both macroscopically (W^{macro}) and microscopically (W^{micro}). In the latter case, it is considered that cement paste is made up of three constituents: isotropically orientated hydrate needles, capillary pores, and clinker grains:

$$W = W^{macro} = \frac{V_{cp}}{2} \mathbf{E}_{cp} : \mathbf{C}_{cp} : \mathbf{E}_{cp}, \quad (4.14)$$

$$W = W^{micro} = \int_0^{2\pi} \int_0^{\pi} \int_{V_{hyd;\varphi,\vartheta}} \frac{1}{2} \boldsymbol{\varepsilon}(\underline{x}) : \mathbf{C}_{hyd} : \boldsymbol{\varepsilon}(\underline{x}) dV \frac{\sin \vartheta}{4\pi} d\vartheta d\varphi \\ + \int_{V_{pore}} \frac{1}{2} \boldsymbol{\varepsilon}(\underline{x}) : \mathbf{C}_{pore} : \boldsymbol{\varepsilon}(\underline{x}) dV + \int_{V_{clin}} \frac{1}{2} \boldsymbol{\varepsilon}(\underline{x}) : \mathbf{C}_{clin} : \boldsymbol{\varepsilon}(\underline{x}) dV \quad (4.15)$$

whereby φ and ϑ define the orientation of the hydrate needles by azimuth and zenith angle (see Fig. 4.3), $\boldsymbol{\varepsilon}(\underline{x})$ denotes the microscopic strain field, and V_i and \mathbf{C}_i denote the volume and the elastic stiffness tensor of material phase i ; whereby i refers to hydrates, to capillary pores, to clinker grains, or to cement paste, $i \in \{hyd, cpor, clin, cp\}$. Again, \mathbf{C}_{cp} is the homogenized stiffness of cement paste, see Appendix 4.5 for details. In Eq. (4.14), \mathbf{E}_{cp} refers to the macro-homogeneous strain state at the considered RVE of cement paste. The strains \mathbf{E}_{cp} are related

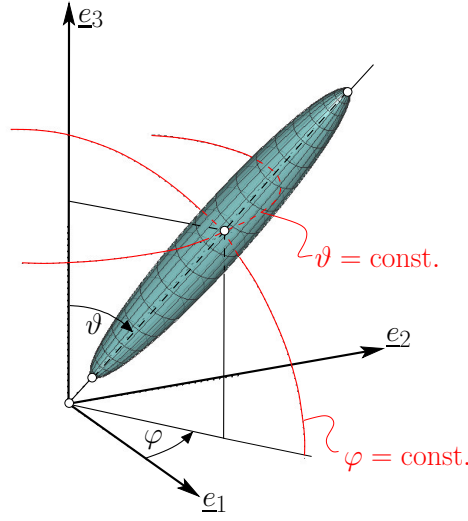


Figure 4.3: Definition of azimuth and zenith angle for identification of the orientation of the needle-shaped hydrates

to the stresses Σ_{cp} by the isotropic elasticity law

$$\mathbf{E}_{cp} = (\mathbf{C}_{cp})^{-1} : \Sigma_{cp}. \quad (4.16)$$

Setting equal the microscopic and the macroscopic expressions of the elastic energy, see Eqs. (4.14) and (4.15), and deriving them either with respect to bulk modulus or to shear modulus of φ, ϑ -orientated hydrate needles (Fig. 4.3), yields under consideration of isotropic phases (4.5) and kinematically admissible displacement fields [49]

$$\frac{\partial W}{\partial k_{hyd;\varphi,\vartheta}} = \frac{V_{cp}}{2} \mathbf{E}_{cp} : \frac{\partial \mathbf{C}_{cp}}{\partial k_{hyd;\varphi,\vartheta}} : \mathbf{E}_{cp} = \frac{3}{2} \int_{V_{hyd;\varphi,\vartheta}} \boldsymbol{\varepsilon}(\underline{x}) : \mathbb{I}^{vol} : \boldsymbol{\varepsilon}(\underline{x}) dV, \quad (4.17)$$

$$\frac{\partial W}{\partial \mu_{hyd;\varphi,\vartheta}} = \frac{V_{cp}}{2} \mathbf{E}_{cp} : \frac{\partial \mathbf{C}_{cp}}{\partial \mu_{hyd;\varphi,\vartheta}} : \mathbf{E}_{cp} = \int_{V_{hyd;\varphi,\vartheta}} \boldsymbol{\varepsilon}(\underline{x}) : \mathbb{I}^{dev} : \boldsymbol{\varepsilon}(\underline{x}) dV, \quad (4.18)$$

where $V_{hyd;\varphi,\vartheta}$, $k_{hyd;\varphi,\vartheta}$, and $\mu_{hyd;\varphi,\vartheta}$ denote the volume, the bulk modulus, and the shear modulus of the hydrate needles orientated in φ, ϑ -direction. Under consideration of the definition of volumetric/deviatoric strain decomposition $\boldsymbol{\varepsilon} = \boldsymbol{\varepsilon}^{vol} + \boldsymbol{\varepsilon}^{dev}$, with $\boldsymbol{\varepsilon}^{vol} = \mathbb{I}^{vol} : \boldsymbol{\varepsilon}$ and $\boldsymbol{\varepsilon}^{dev} = \mathbb{I}^{dev} : \boldsymbol{\varepsilon}$, Eqs. (4.17) and (4.18) are

divided by $V_{hyd;\varphi,\vartheta}$ and rearranged as

$$\frac{1}{3 f_{hyd;\varphi,\vartheta}^{cp}} \mathbf{E}_{cp} : \frac{\partial \mathbf{C}_{cp}}{\partial k_{hyd;\varphi,\vartheta}} : \mathbf{E}_{cp} = \frac{1}{V_{hyd;\varphi,\vartheta}} \int_{V_{hyd;\varphi,\vartheta}} \boldsymbol{\varepsilon}^{vol}(\underline{x}) : \boldsymbol{\varepsilon}^{vol}(\underline{x}) dV = \left(\overline{\overline{\varepsilon}}_{hyd;\varphi,\vartheta}^{vol} \right)^2 \quad (4.19)$$

$$\frac{1}{2 f_{hyd;\varphi,\vartheta}^{cp}} \mathbf{E}_{cp} : \frac{\partial \mathbf{C}_{cp}}{\partial \mu_{hyd;\varphi,\vartheta}} : \mathbf{E}_{cp} = \frac{1}{V_{hyd;\varphi,\vartheta}} \int_{V_{hyd;\varphi,\vartheta}} \boldsymbol{\varepsilon}^{dev}(\underline{x}) : \boldsymbol{\varepsilon}^{dev}(\underline{x}) dV = \left(\overline{\overline{\varepsilon}}_{hyd;\varphi,\vartheta}^{dev} \right)^2 \quad (4.20)$$

where $f_{hyd;\varphi,\vartheta}^{cp} = V_{hyd;\varphi,\vartheta}/V_{cp}$ stands for the cement paste-related volume fraction of φ, ϑ -orientated hydrate needles, and $\overline{\overline{\varepsilon}}_{hyd;\varphi,\vartheta}^{vol}$ and $\overline{\overline{\varepsilon}}_{hyd;\varphi,\vartheta}^{dev}$ are scalars representing strain energy-related averages of volumetric and deviatoric strains in hydrate needles orientated in φ, ϑ -direction. Corresponding scalar stress averages can be quantified as [48]

$$\overline{\overline{\sigma}}_{hyd;\varphi,\vartheta}^{vol} = 3 k_{hyd} \overline{\overline{\varepsilon}}_{hyd;\varphi,\vartheta}^{vol} = \sqrt{\frac{3 k_{hyd}^2}{f_{hyd;\varphi,\vartheta}^{cp}} \mathbf{E}_{cp} : \frac{\partial \mathbf{C}_{cp}}{\partial k_{hyd;\varphi,\vartheta}} : \mathbf{E}_{cp}}, \quad (4.21)$$

$$\overline{\overline{\sigma}}_{hyd;\varphi,\vartheta}^{dev} = 2 \mu_{hyd} \overline{\overline{\varepsilon}}_{hyd;\varphi,\vartheta}^{dev} = \sqrt{\frac{2 \mu_{hyd}^2}{f_{hyd;\varphi,\vartheta}^{cp}} \mathbf{E}_{cp} : \frac{\partial \mathbf{C}_{cp}}{\partial \mu_{hyd;\varphi,\vartheta}} : \mathbf{E}_{cp}}. \quad (4.22)$$

While details about the numerical computation of the partial derivatives in (4.21) and (4.22) are given in [125, 120], Eqs. (4.19)-(4.22) allow for expressing the volume average of elastic strain energy stored in hydrate needles orientated in φ, ϑ -direction as

$$\frac{1}{V_{hyd;\varphi,\vartheta}} \int_{V_{hyd;\varphi,\vartheta}} \frac{1}{2} \boldsymbol{\varepsilon}(\underline{x}) : \mathbf{C}_{hyd} : \boldsymbol{\varepsilon}(\underline{x}) dV = \frac{1}{2} \left(\overline{\overline{\sigma}}_{hyd;\varphi,\vartheta}^{vol} \overline{\overline{\varepsilon}}_{hyd;\varphi,\vartheta}^{vol} + \overline{\overline{\sigma}}_{hyd;\varphi,\vartheta}^{dev} \overline{\overline{\varepsilon}}_{hyd;\varphi,\vartheta}^{dev} \right) \quad (4.23)$$

We are left with calculating the largest and the smallest principal stress intervening in the Mohr-Coulomb criterion (4.6) based on the scalar stress measures $\overline{\overline{\sigma}}_{hyd;\varphi,\vartheta}^{vol}$ and $\overline{\overline{\sigma}}_{hyd;\varphi,\vartheta}^{dev}$. This requires access to the full tensorial expression of the strain energy-related stress tensor $\overline{\overline{\boldsymbol{\sigma}}}_{hyd;\varphi,\vartheta}$. The latter is estimated by scaling the volume-averaged stress tensor $\overline{\overline{\boldsymbol{\sigma}}}_{hyd;\varphi,\vartheta}$ such that it is related to the same strain energy as $\overline{\overline{\boldsymbol{\sigma}}}_{hyd;\varphi,\vartheta}$, see (4.23). To this end, we decompose the sought stress tensor $\overline{\overline{\boldsymbol{\sigma}}}_{hyd}$ into its volumetric and deviatoric part as

$$\overline{\overline{\boldsymbol{\sigma}}}_{hyd;\varphi,\vartheta} = \overline{\overline{\boldsymbol{\sigma}}}_{hyd;\varphi,\vartheta}^{vol} + \overline{\overline{\boldsymbol{\sigma}}}_{hyd;\varphi,\vartheta}^{dev}. \quad (4.24)$$

and we express these parts as being equal to their volume-averaged counterparts $\overline{\overline{\sigma}}_{hyd;\varphi,\vartheta}^{vol}$ and $\overline{\overline{\sigma}}_{hyd;\varphi,\vartheta}^{dev}$, multiplied with scalar scaling factors

$$\overline{\overline{\sigma}}_{hyd;\varphi,\vartheta}^{vol} = \overline{\sigma}_{hyd;\varphi,\vartheta}^{vol} \frac{\overline{\overline{\sigma}}_{hyd;\varphi,\vartheta}^{vol}}{\overline{\sigma}_{hyd;\varphi,\vartheta}^{vol}}, \quad \overline{\overline{\sigma}}_{hyd;\varphi,\vartheta}^{dev} = \overline{\sigma}_{hyd;\varphi,\vartheta}^{dev} \frac{\overline{\overline{\sigma}}_{hyd;\varphi,\vartheta}^{dev}}{\overline{\sigma}_{hyd;\varphi,\vartheta}^{dev}}. \quad (4.25)$$

The volume-averaged stress tensor $\overline{\overline{\sigma}}_{hyd;\varphi,\vartheta}$ follows from the stress concentration rule which involves stress concentration tensor $\mathbb{B}_{hyd;\varphi,\vartheta}^{cp}$ as

$$\overline{\overline{\sigma}}_{hyd;\varphi,\vartheta} = \mathbb{B}_{hyd;\varphi,\vartheta}^{cp} : \Sigma_{cp}, \quad (4.26)$$

for details see Appendix A, and the scalar stress quantities $\overline{\overline{\sigma}}_{hyd;\varphi,\vartheta}^{vol}$ and $\overline{\overline{\sigma}}_{hyd;\varphi,\vartheta}^{dev}$ follow by analogy to Eqs. (4.19)-(4.22) as

$$\overline{\overline{\sigma}}_{hyd;\varphi,\vartheta}^{vol} = \sqrt{\overline{\sigma}_{hyd;\varphi,\vartheta} : \mathbb{I}^{vol} : \overline{\sigma}_{hyd;\varphi,\vartheta}}, \quad \overline{\overline{\sigma}}_{hyd;\varphi,\vartheta}^{dev} = \sqrt{\overline{\sigma}_{hyd;\varphi,\vartheta} : \mathbb{I}^{dev} : \overline{\sigma}_{hyd;\varphi,\vartheta}}. \quad (4.27)$$

4.2.5 Identification of location and of orientation of most heavily loaded hydrate needles

Herein, we consider that uniaxial compressive loading in \underline{e}_3 -direction is either imposed on an RVE of mortar or of cement paste

$$\Sigma_i = -\Sigma_i^{uni} \underline{e}_3 \otimes \underline{e}_3, \quad i \in \{mor, cp\} \quad (4.28)$$

where Σ_i^{uni} denotes the absolute value of the imposed uniaxial traction. The *location* in the immediate vicinity of sand grains and the *orientation* of most heavily loaded hydrate needles inside RVEs of cement paste are identified as follows.

As for strength predictions for cement paste, macroloading Σ_{cp} is first concentrated into strain energy-related stress averages of hydrate needles, using Eqs. (4.16), (4.21) and (4.22), (4.26)-(4.27), and (4.25) and (4.24). The obtained hydrate stress tensors are functions of the macroloading and of the orientation angles φ and ϑ of the hydrate needles

$$\overline{\overline{\sigma}}_{hyd} = \overline{\overline{\sigma}}_{hyd}(\Sigma_{cp}^{uni}; \varphi, \vartheta). \quad (4.29)$$

The largest and smallest eigenvalues of $\overline{\overline{\sigma}}_{hyd}$, i.e. $\overline{\overline{\sigma}}_{hyd,I}(\Sigma_{cp}^{uni}; \varphi, \vartheta)$ and $\overline{\overline{\sigma}}_{hyd,III}(\Sigma_{cp}^{uni}; \varphi, \vartheta)$, are inserted into the Mohr-Coulomb failure criterion, see (4.6) and (4.7). Next, the intensity of macroscopic loading Σ_{cp}^{uni} is conceptually increased (starting from zero) and the failure criteria are checked in all hydrate orientations, i.e. for all φ, ϑ -directions (see Fig. 4.3). The specific orientation angles φ_{fail} and ϑ_{fail} , for which the corresponding failure criterion is satisfied first, refer to the most heavily loaded hydrate orientation, and the corresponding load intensity represents the uniaxial compressive strength of cement paste, $\Sigma_{cp}^{uni,ult}$.

As for strength predictions for mortar, macroloading Σ_{mor} according to (4.28) is first concentrated into cement paste stress states around sand grains, see Eq. (4.13). This problem exhibits axial symmetry with respect to the macroscopic loading direction, i.e. cement paste stress states are a function of the polar angle ψ (see Fig. 4.2):

$$\sigma_{cp} = \sigma_{cp}(\Sigma_{mor}^{uni}; \psi) . \quad (4.30)$$

The calculated stress states represent macroscopic loading of cement paste RVEs, i.e. $\sigma_{cp} \rightarrow \Sigma_{cp}$, and further stress concentration down to hydrate needles is performed as described in the preceding paragraph, such that hydrate stress tensors are also functions of the orientation angles φ and ϑ of hydrate needles

$$\overline{\overline{\sigma}}_{hyd} = \overline{\overline{\sigma}}_{hyd}(\Sigma_{mor}^{uni}; \psi; \varphi, \vartheta) . \quad (4.31)$$

The largest and smallest eigenvalues of $\overline{\overline{\sigma}}_{hyd}$, i.e. $\overline{\overline{\sigma}}_{hyd,I}(\Sigma_{mor}^{uni}; \psi; \varphi, \vartheta)$ and $\overline{\overline{\sigma}}_{hyd,III}(\Sigma_{mor}^{uni}; \psi; \varphi, \vartheta)$ are inserted into the Mohr-Coulomb failure criterion, see (4.6) and (4.7), and the intensity of macroscopic loading, Σ_{mor}^{uni} is conceptually increased (starting from zero). The Mohr-Coulomb failure criteria are checked for all polar angles ψ marking positions of cement paste RVEs around sand grains [see Fig. 4.2(a)] as well as for all angles φ and ϑ defining the orientation of hydrate needles within RVEs of cement paste (see Fig. 4.3). The specific position and orientation angles ψ_{fail} , φ_{fail} , and ϑ_{fail} , for which the corresponding failure criterion is satisfied first, refer to the most heavily loaded hydrate location and orientation, and the corresponding load intensity represents the uniaxial compressive strength of mortar, $\Sigma_{mor}^{uni,ult}$. Appendix 4.5 contains details about the numerical realization.

Notably, the described multiscale model for strength of OPC-based cementitious materials does not contain any fitting parameters. The only input parameters

are the initial water-to-cement mass ratio w/c , the initial sand-to-cement mass ratio s/c , and the degree of hydration ξ_{clin} , intervening in the expressions of phase volume fractions, see Eqs. (4.2)-(4.4). All other inputs, i.e. the elastic properties of all involved material phases as well as the strength properties of hydrates, are material *constants*, see Table 5.1 and Eq. (4.7).

4.2.6 Model validation on OPC pastes

Herein, the presented micromechanical model is used to predict strength tests on cement pastes performed at Lafarge Centre de Recherche (LCR), TU Wien – Vienna University of Technology (TUW), and Swiss Federal Laboratories for Materials Science and Technology (EMPA), respectively. All considered strength tests were performed on elongated samples (either cylinders or prisms), such that determined strength values can be interpreted as genuine (“material”) uniaxial compressive strength values and *not* as shear-enhanced (“structural”) cube compressive strength values.

Four sets of tests were carried out at LCR on cement paste cylinders (with a diameter of 7 mm and a height of 22 mm) exhibiting w/c ratios ranging from 0.33 up to 0.508 produced from three distinct OPC cements (referred to as LCR I, LCR II, and LCR III), see Pichler et al. [122] for more details. Specimens were cured at 20 °C, tested 1, 3, 7, and 28 days after production, and their hydration degree was determined by XRD/Rietveld coupled with thermogravimetric analysis, as specified in [152]. Blind model predictions agree well with experimental results, see Fig. 4.4, as quantified through the quadratic correlation coefficient $R^2 = 0.897$ for samples with $w/c = 0.33$, and $R^2 = 0.867$ for samples with $w/c \approx 0.50$.

Two sets of independent strength tests were performed at TUW, referred to as TUW I and TUW II. The testing campaign TUW I was carried out on cylindrical cement paste specimens (with diameter of 29.0 ± 0.3 mm and a height of 58.0 ± 1.3 mm) exhibiting $w/c = 0.42$ from commercial CEM I 42.5 N cement and distilled water, see Pichler et al. [122] for details. After demoulding, the specimens were cured in lime-saturated water at 25 °C until testing. The clinker hydration degree was identified from isothermal calorimetry carried out at 25 °C. In the testing campaign TUW II, cement paste prisms (with dimensions of $40 \times 40 \times 80$ mm³) were tested 24 h after production, immediately after de-

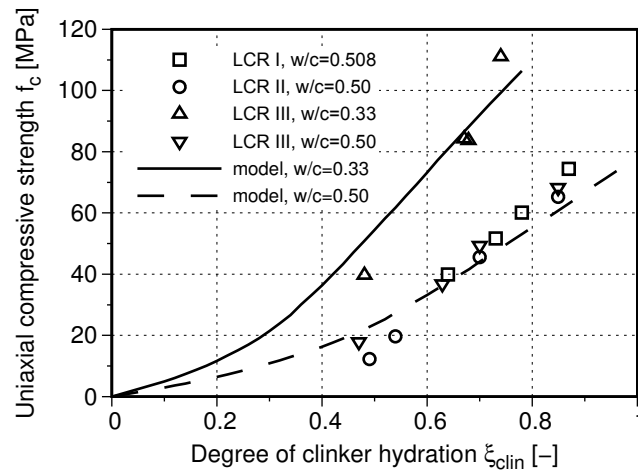


Figure 4.4: Model validation on OPC pastes tested at LCR, as for strength data see [122]

moulding [88]. Clinker type (CEM I) and mix design ($w/c = 0.42$) were the same as in test campaign TUW I. Molded specimens were continuously stored in a climate chamber at 20°C , and isothermal calorimetry tests were carried out at the same temperature to get access to the hydration degree. Model predicted strength evolutions for $w/c = 0.42$ agree very well with both experimental campaigns; the corresponding quadratic correlations coefficient amounts to $R^2 = 0.977$.

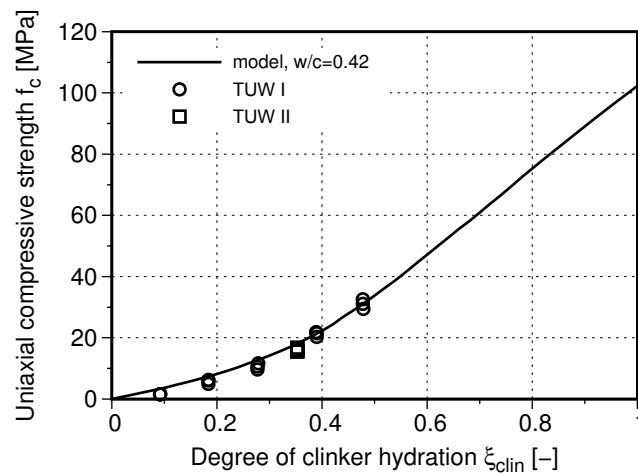


Figure 4.5: Model validation on OPC pastes tested at TUW, as for strength data see [119, 88]

Strength values of another test campaign performed at EMPA were provided in the framework of the COST action TU1404 [157], see also Wyrzykowski and Lura [175]. Prismatic cement paste samples ($25 \times 25 \times 100 \text{ mm}^3$) were produced in vacuum from CEM I 42.5 N with two different water-to-cement mass ratios $w/c =$

{0.25, 0.30}, cured under sealed conditions at 20 °C, and tested 1, 3, and 7 days after production. The hydration degree was measured by isothermal calorimetry, see [175]. Model predictions agree very well with experimental results, see Fig. 4.6, as quantified by quadratic correlation coefficients amounting to $R^2 = 0.994$ for $w/c = 0.25$ and to $R^2 = 0.993$ for $w/c = 0.30$.

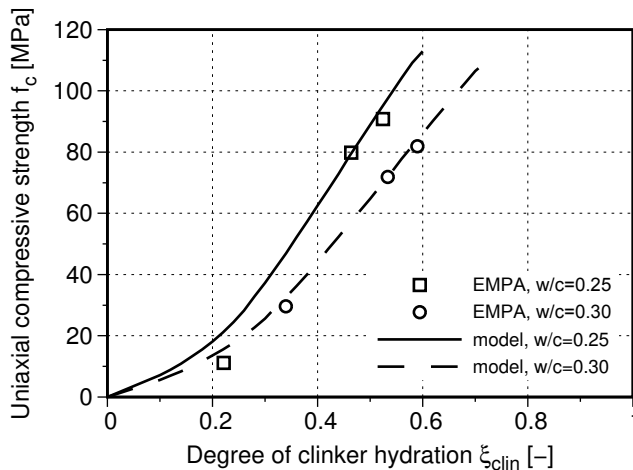


Figure 4.6: Model validation on OPC pastes tested at EMPA, as for strength data see [157, 175]

4.2.7 Model validation on OPC mortars

After the successful model validation at the level of cement paste, we now proceed at the mortar scale, where we consider two sets of experimental data: tests performed at TUW and a test campaign carried out at LCR within the framework of NANOCEM’s Core Project 10 (CP 10), see the acknowledgment.

Mortar tests at TUW were carried out on prisms with volume $4 \times 4 \times 8 \text{ cm}^3$, produced with $w/c = 0.50$ (CEM I 42.5 N and distilled water) and sand-to-cement ratio of $s/c = 3.0$, using oven-dried standard quartz sand from the company “Normensand”, with diameters smaller than 2 mm. The same material was also characterized by means of hourly repeated three-minute-long creep tests [74], which allowed for quantification of internal curing processes, i.e. water is partly uptaken – upon mixing of raw materials – by the open porosity of the quartz grains, and – during hydration – this water is progressively soaked back into the cement paste matrix, such that the effective water-to-cement mass ratio w_{cp}/c

increases linearly with increasing hydration degree

$$w_{cp}/c = 0.47 + 0.0317 \xi_{clin} \leq 0.50. \quad (4.32)$$

Given that strength tests were carried out one day after production, and that calorimetry implies that the degree of clinker hydration reached $\xi_{clin} = 0.353$ at that time, Eq. (4.32) allows for quantifying the effective water-to-cement mass ratio of the tested specimens as $w_{cp}/c = 0.481$. Evaluation of the described strength model for these inputs delivers predictions which agree very well with the measured strength values, see Fig. 4.7.

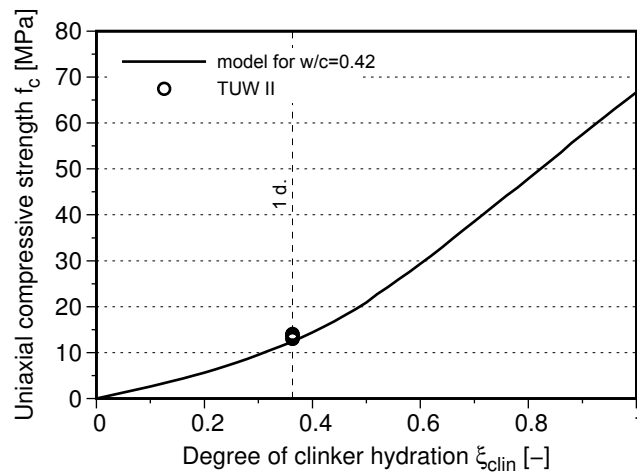


Figure 4.7: Model validation on OPC mortar tested at TUW, as for strength data see [88]

Experiments from CP 10 were carried out on cylindrical mortar specimens (with a diameter of 70 mm and a height of 150 mm) produced using sand-to-cement mass ratio $s/c = 3.0$ and initial water-to-cement mass ratio $w/c = 0.51$ from CEM I 52.5 N. Moulds were removed 24 hours after production and the specimens were subsequently exposed to air conditioned to 20 °C and 99% relative humidity until testing. Tests were carried out 3 and 28 days after production. The clinker hydration degree was identified from XRD/Rietveld and thermogravimetric analysis, amounting to $\xi_{clin} = 0.69$ and $\xi_{clin} = 0.84$ at material ages of 3 days and 28 days, respectively, see also Section 4.3.1 for more details. Evaluating the model for the tested composition and comparing the results with the experimentally determined strength values, see the thick solid line in Fig. 4.8, shows that the model predicts the strength evolution in OPC mortars quite reliably, as quantified by $R^2 = 0.809$.

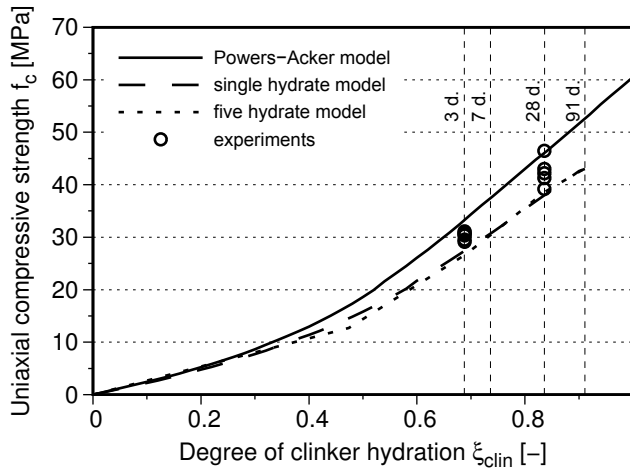


Figure 4.8: Model validation on OPC mortar tested at LCR in the framework of NANOCEM’s Core Project 10

4.2.8 Location and orientation of most heavily loaded hydrate needles

For all analyzed OPC mortars, the model-predicted location and orientation of the most heavily loaded hydrate needle is the same, i.e. location angle $\psi_{fail} \approx \pi/6$, and orientation angles $\vartheta_{fail} = 0$, $\varphi_{fail} \in [0; 2\pi]$. Polar angle $\psi_{fail} \approx \pi/6$ indicates that strength-relevant stress peaks in cement paste occur at the shoulder of sand grains, approximately one third of the distance between the poles and the equator, see Fig. 4.9(b). At the microscale of cement paste, the most heavily loaded hydrate needle is virtually aligned with the direction of macroscopic loading ($\vartheta \approx 0$), see Fig. 4.9(c), and the normal of the nanoscopic plane of shear failure is inclined by an angle of $\approx \pi/4$ with respect to the loading direction, see Fig. 4.9(d).

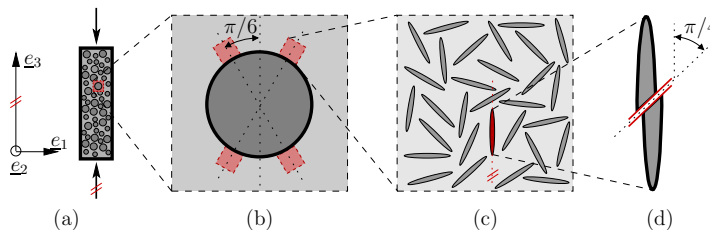


Figure 4.9: Multiscale failure mechanism in mortar: (a) uniaxially compressed mortar sample, (b) location of failure-inducing stress peaks of cement paste attached to a sand grain, (c) most heavily loaded hydrate needle which is part of the microstructure of cement paste (see also Fig. 4.1), (d) orientation of nanoscopic failure plane inside the most heavily loaded hydrate needle

4.3 Strength evolution of blended cement mortars: microstructural characterization, strength testing, and multiscale modeling

The satisfactory model performance regarding OPC pastes and mortars is the motivation to extend our study to blended cement materials. Four blended cement binders were obtained by replacing 45% of cement volume either by finely ground fillers (quartz or limestone, respectively) or by supplementary cementitious materials (ground granulated blast furnace slag or fly ash, respectively), for mass densities and Blaine fineness values see Table 4.2. The fifth binder, i.e. pure ordinary Portland cement, served as a reference. Replacing cement clinker by

Table 4.2: Physical properties of materials used

	Mass density [kg/m ³]	Blaine fineness [m ² /kg]	Granulometry			
			d90 [μ m]	d50 [μ m]	d10 [μ m]	d4.3 [μ m]
OPC	3 170	363	41.78	15.44	2.45	19.21
Quartz	2 650	617.2	–	–	–	–
Limestone	2 715	–	–	–	–	–
Slag	2 930	340	–	–	–	–
Fly ash	2 090	368.6	–	–	–	–

volume (rather than by mass) ensures that the composition of the different materials is identical in terms of initial volume fractions. Also to this end, the initial water-to-solid volume ratio amounting to 1.6 is the same for all pastes. Consequently, pure OPC paste exhibited a water-to-cement mass ratio amounting to $w/c = 0.53$ while this mass ratio was equal to 0.93 for all blended mixes. Notably, water-to-solid *mass* ratios differed from mix to mix, because of the differences in specific mass densities of blending materials, see Table 4.3. All materials were demoulded 1 day after production and subsequently exposed to air conditioned to 20 °C and 99% relative humidity.

Table 4.3: Investigated paste compositions

	Initial water/solid volume ratio	Cement replacement by volume	Initial water/cement mass ratio	Initial water/solid mass ratio
OPC	1.60	0 %	0.51	0.51
Quartz blend	1.60	45 %	0.93	0.55
Limestone blend	1.60	45 %	0.93	0.54
Slag blend	1.60	45 %	0.93	0.53
Fly ash blend	1.60	45 %	0.93	0.60

4.3.1 Microstructural characterization: phase volume evolutions

Microstructural characterization was performed on the dry binders as well as on pastes 1, 3, 7, 28, and 91 days after their production, in order to quantify the evolution of paste volume fractions, see Figs. 4.10(a)-4.14(a). To this end, several methods were combined as follows. Thermogravimetric analysis and X-ray diffraction including Rietveld refinement allowed for determination of the crystalline phases clinker, portlandite (CH), and ettringite (AFt) as well as the amount of total amorphous matter together with the hydration degree of clinker. The amounts of the poorly crystalline amorphous phases calcium silicate hydrates C-S-H, monosulfoaluminate (AFm), and monosulfocarboaluminates (AFmC) are obtained as follows. Volume and mass balance equations allowed for relating C-S-H and portlandite to hydration of C_3S and C_2S under the assumption that both clinker phases lead to the same type of C-S-H, as suggested also by TEM analysis [131]. The amount of AFm hydrates was determined based on the amount of dissolved C_3A which was not transformed into ettringite. Finally, the capillary pore volume was calculated as the total paste volume minus the solid volume. As for the supplementary cementitious materials, the degree of reaction of slag and fly ash was determined based on SEM/BSE image analysis. A pozzolanic reaction is assumed for both slag and fly ash materials leading to the formation of additional C-S-H (with a lower calcium-to-silica ratio) and consumption of portlandite in such pastes.

Results from microstructural characterization underline that C-S-H is by far the most frequently produced hydration product, followed by portlandite and by aluminate hydrates, see Figs. 4.10-4.14. As for OPC, the limestone blend, and the

quartz blend, the overall hydrate volume increases in very good approximation *linearly* with increasing degree of cement clinker reaction. Although quartz and limestone volumes remain virtually constant throughout the hydration process, they increase the speed of the hydration, compare hydration degrees reached 3, 7, 28, and 91 days after production in Figs. 4.10-4.12. This is typically referred to as a “microfiller effect” [94]. In addition, the presence of limestone seems to have an influence on the composition of the produced aluminate hydrates, which is in agreement with previous experimental observations [151].

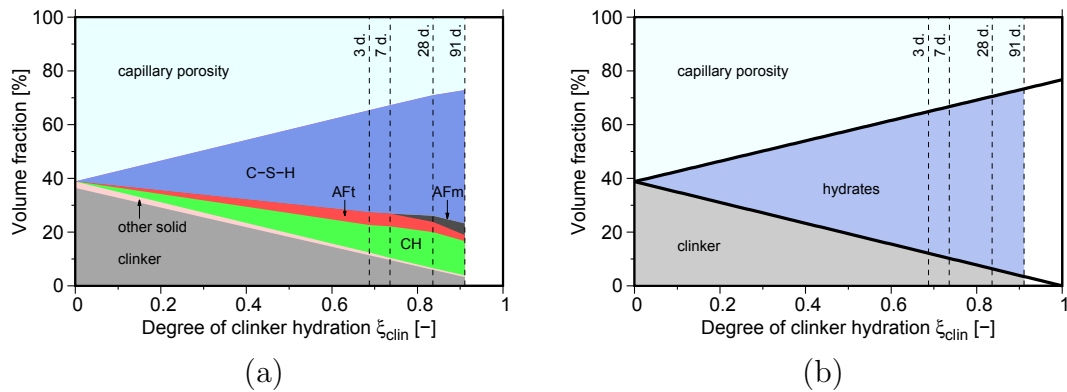


Figure 4.10: Phase assemblage of OPC paste: (a) results from microstructural characterization; and (b) subdivision into clinker, hydrates, and capillary pores according to Eq. (4.33)

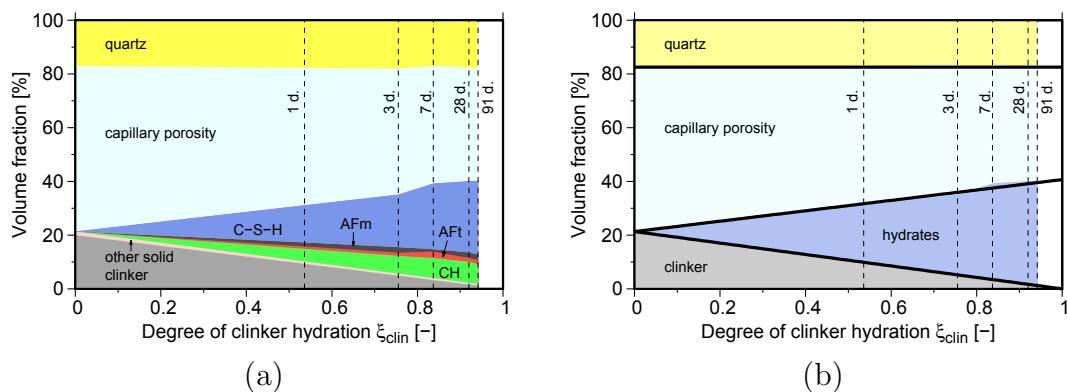


Figure 4.11: Phase assemblage of quartz-blended paste: (a) results from microstructural characterization; and (b) subdivision into clinker, hydrates, capillary pores, and quartz according to Eq. (4.34)

As for slag- and fly ash-blended pastes, the overall hydrate volume increases *linearly* with increasing degree of cement clinker hydration, as long as the supplementary cementitious materials remain inert. Slag hydration appears to start

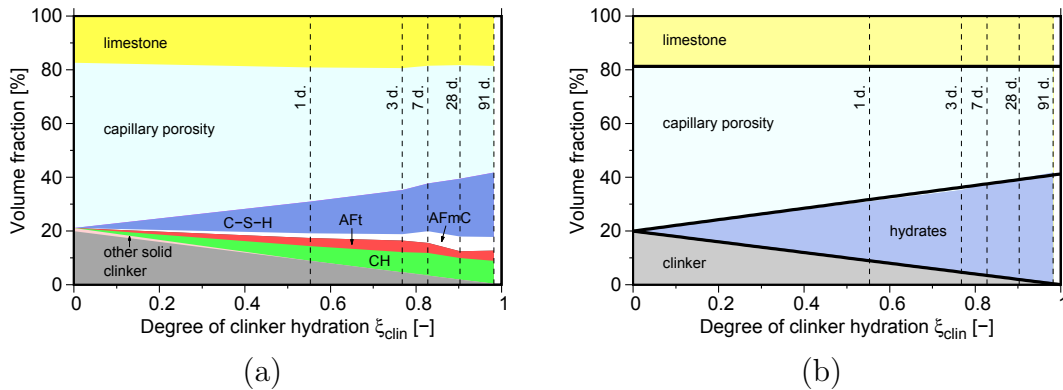


Figure 4.12: Phase assemblage of limestone-blended paste: (a) results from microstructural characterization; and (b) subdivision into clinker, hydrates, capillary pores, and limestone according to Eq. (4.35)

around 3 days after production, and the subsequent increase of the degree of slag reaction is virtually a linear function of the degree of clinker hydration. Fly ash hydration, in turn, appears to start around 7 days after production, and the subsequent increase of the degree of fly ash hydration appears to be an overlinear function of the degree of clinker hydration. Notably, the unexpected kink in the C-S-H volume fraction developing between the 3rd and the 7th day after production [Fig. 4.14(a)] indicates that microstructural characterization was particularly challenging for the fly ash-blended material. The microfiller effects of the used SCMs was less effective than the one observed with the inert fillers, compare hydration degrees reached 3, 7, 28, and 91 days after production in Figs. 4.10-4.14.

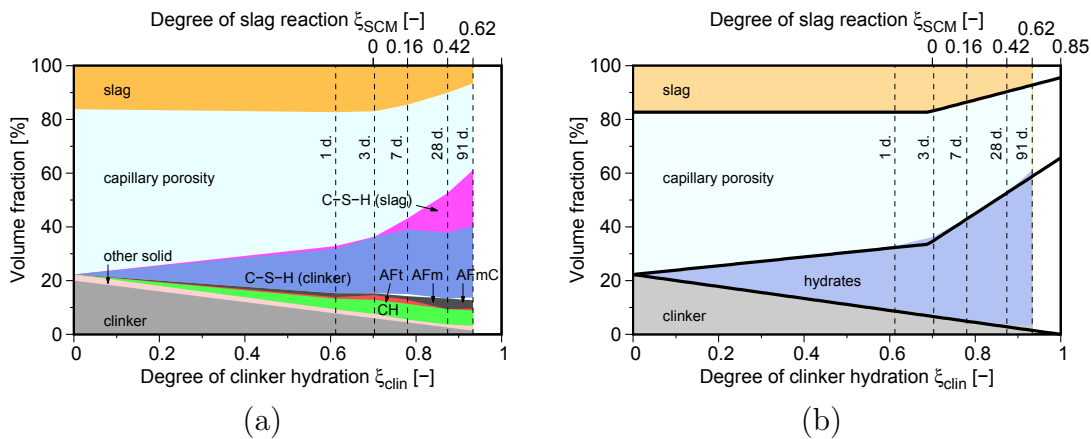


Figure 4.13: Phase assemblage of slag-blended paste: (a) results from microstructural characterization; and (b) subdivision into clinker, hydrates, capillary pores, and slag according to Eq. (4.36)

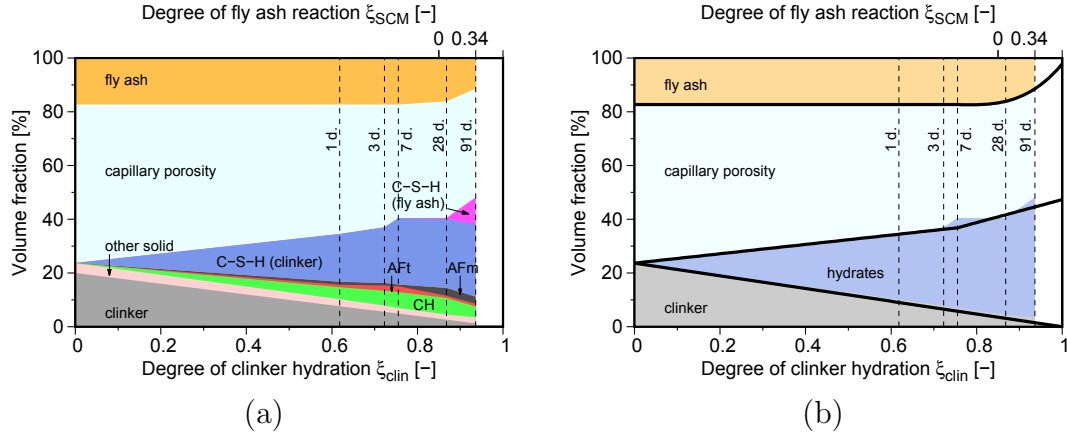


Figure 4.14: Phase assemblage of fly ash-blended paste: (a) results from microstructural characterization; and (b) subdivision into clinker, hydrates, capillary pores, and fly ash according to Eq. (4.37)

In order to obtain simple closed-form expressions describing monotonous evolutions of phase volumes of clinker, hydrates, capillary porosity, and blending solids, the point-wisely measured phase volume evolutions are approximated by linear, piecewise linear, and piecewise cubic fitting functions. The latter are computed based on a least square approach, which is constrained by the requirement that the volume fractions must sum up to one. The obtained volume fraction evolutions are depicted in Figs. 4.10(b)-4.14(b), and the corresponding functions are given next. For the OPC paste, they read as

$$f_{clin}^{cp} = 0.388 (1 - \xi_{clin}) , \quad f_{hyd}^{cp} = 0.767 \xi_{clin} , \quad f_{pore}^{cp} = 1 - f_{clin}^{cp} - f_{hyd}^{cp} , \quad (4.33)$$

for the quartz-blended paste, they read as

$$\begin{aligned} f_{clin}^{cp} &= 0.213 (1 - \xi_{clin}) , & f_{quartz}^{cp} &= 0.174 , \\ f_{hyd}^{cp} &= 0.407 \xi_{clin} , & f_{pore}^{cp} &= 1 - f_{clin}^{cp} - f_{quartz}^{cp} - f_{hyd}^{cp} , \end{aligned} \quad (4.34)$$

for limestone-blended paste, they read as

$$\begin{aligned} f_{clin}^{cp} &= 0.200 (1 - \xi_{clin}) , & f_{limestone}^{cp} &= 0.188 , \\ f_{hyd}^{cp} &= 0.412 \xi_{clin} , & f_{pore}^{cp} &= 1 - f_{clin}^{cp} - f_{limestone}^{cp} - f_{hyd}^{cp} , \end{aligned} \quad (4.35)$$

for the slag-blended paste, they reads as

$$\begin{aligned}
 f_{clin}^{cp} &= 0.223 (1 - \xi_{clin}) \\
 f_{slag}^{cp} &= \begin{cases} 0.173 & \text{if } \xi_{clin} < 0.69 \\ 0.173 - 0.415 (\xi_{clin} - 0.69) & \text{if } \xi_{clin} \geq 0.69 \end{cases} \\
 f_{hyd}^{cp} &= \begin{cases} 0.387 \xi_{clin} & \text{if } \xi_{clin} < 0.69 \\ 0.387 \xi_{clin} + 0.872 (\xi_{clin} - 0.69) & \text{if } \xi_{clin} \geq 0.69 \end{cases} \\
 f_{pore}^{cp} &= 1 - f_{clin}^{cp} - f_{slag}^{cp} - f_{hyd}^{cp},
 \end{aligned} \tag{4.36}$$

and for fly ash-blended paste, they read as

$$\begin{aligned}
 f_{clin}^{cp} &= 0.237 (1 - \xi_{clin}) \\
 f_{FA}^{cp} &= \begin{cases} 0.173 & \text{if } \xi_{clin} < 0.755 \\ 0.173 - 1.081 (\xi_{clin} - 0.755)^3 + 0.031 (\xi_{clin} - 0.755) & \text{if } \xi_{clin} \geq 0.755 \end{cases} \\
 f_{hyd}^{cp} &= \begin{cases} 0.411 \xi_{clin} & \text{if } \xi_{clin} < 0.755 \\ 0.411 \xi_{clin} + 0.254 (\xi_{clin} - 0.755) & \text{if } \xi_{clin} \geq 0.755 \end{cases} \\
 f_{pore}^{cp} &= 1 - f_{clin}^{cp} - f_{FA}^{cp} - f_{hyd}^{cp}
 \end{aligned} \tag{4.37}$$

4.3.2 Uniaxial compressive strength testing of blended mortars

Blended mortars were produced with paste compositions according to Table 4.3 as well as standard sand with mass ratio of sand-to-“sum of cement clinker and of replacement materials” amounting to 3.0. Fresh mortar was cast into cylindrical steel moulds with diameters amounting to 70 mm and heights amounting to 150 mm. Specimens were demoulded after 24 hours and subsequently exposed to air conditioned to 20 °C and 99% relative humidity until testing. Top and bottom surfaces of the mortar cylinders were ground prior to testing in order to ensure close-to-perfect coplanarity required for a central load application. Five to six specimens of each given composition were tested 3 and 28 days after production.

4.3.3 Revisiting strength homogenization of OPC mortar based on microstructural characterization results

Herein, we perform two sensitivity analyses complementing the OPC mortar predictions of Subsections 4.2.7: At first, we stay with representing all hydrates as isotropically orientated needles [see Fig. 4.1(c)], with elastic constants according to Table 5.1 and strength properties according to Eqs. (4.7), but rather than using the Powers-Acker phase evolution model (4.2)-(4.4), we now use the *measured* phase volume evolutions as illustrated in Fig. 4.10(b), see also Eqs. (4.33). Obtained model predictions, referred to as “single hydrate” model (see the dashed line in Fig. 4.8), explain the available strength data similarly well as the Powers-Acker model-related predictions (see the thick solid line in Fig. 4.8), but the former are by some 15 % smaller than the latter. This is because the microstructural characterization results suggest that hydration products are denser than foreseen by the Powers-Acker model, and denser hydrates result in an increased capillary porosity which effectively reduces the strength of the material.

As for the second sensitivity analysis, we consider five types of hydrates within the RVE of hydrate foam (rather than only one type), see Fig. 4.15 for a conceptual illustration and Table 4.4 for elastic properties and characteristic phase shapes. The Mohr-Coulomb strength properties of Eqs. (4.7) are now assigned to C-S-H only. Corresponding strength homogenization results, referred to as “five hydrates” model (see the thin dashdotted line in Fig. 4.8), are very similar to the ones obtained using the “single hydrate” approach. The sensitivity analyses suggest that investments into a reliable quantification of the overall phase volume fraction of *all hydrates* is more important than investments into a very detailed representation of *different hydration products*; at least for OPC mortars.

Table 4.4: Elastic and micromorphological hydrate properties

	Bulk modulus k [GPa]	Shear modulus μ [GPa]	Source	Shape
C-S-H gel	$k_{CSH} = 18.7$	$\mu_{CSH} = 11.8$	[119]	needle [119, 132]
portlandite	$k_{CH} = 40.00$	$\mu_{CH} = 16.00$	[73, 104]	sphere
ettringite	$k_{AFt} = 27.20$	$\mu_{AFt} = 9.45$	[147]	needle [142, 132]
monosulfate	$k_{AFm} = 40.00^*$	$\mu_{AFm} = 16.00^*$	[-]	sphere
monocarbonate	$k_{AFmC} = 40.00^*$	$\mu_{AFmC} = 16.00^*$	[-]	sphere

* chosen to be equal to portlandite, see also [153]

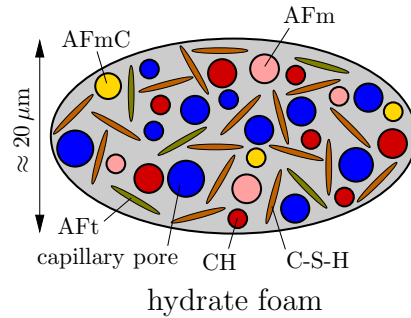


Figure 4.15: RVE of hydrate foam with five types of hydrates (“material organogram”); two-dimensional sketches of three-dimensional representative volume elements

4.3.4 Strength homogenization of inert filler-blended mortars: consideration of quartz and limestone as reinforcements of the hydrate foam

When it comes to include quartz or limestone fillers into the micromechanical representation of mortar (Fig. 4.1), it is noteworthy that the Blaine fineness of the used fillers is considerably higher than the one of the cement clinker, see Table 4.2. Higher Blaine values imply smaller particle sizes, and this motivates us to introduce the fillers as spherical inclusions at the scale of the hydrates, i.e. one scale below the cement clinker, see Fig. 4.16. In addition, the finely ground filler grains

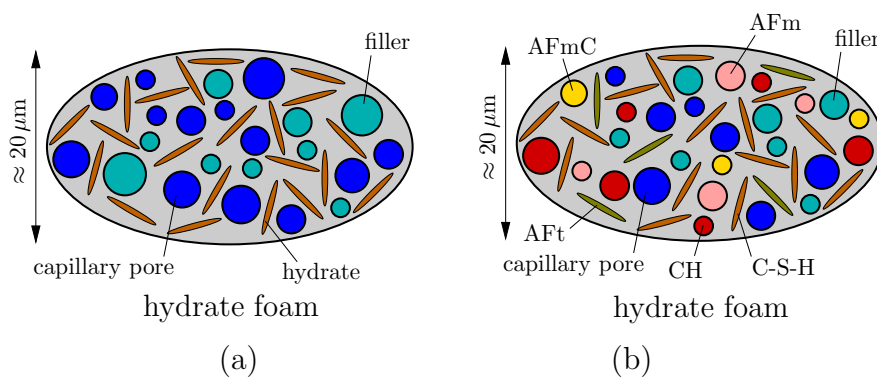


Figure 4.16: RVEs of hydrate foam including the finely ground fillers quartz or limestone (“material organograms”): (a) one hydrate type, (b) five types of hydrates; two-dimensional sketches of three-dimensional representative volume elements

act as preferred precipitation sites for hydrates, as underlined by the observed microfiller effect, and this is a further argument to consider filler particles as part of the hydrate foam matrix. By analogy to the sensitivity analysis described in

the previous subsection, we compare two modeling options: (i) consideration of one hydrate type [see Fig. 4.16(a)] with elastic constants, strength properties and phase volume evolutions according to Table 5.1, Eq. (4.7), and Figs. 4.11(b) and 4.12(b), respectively; and (ii) five hydrate types [see Fig. 4.16(b)] with elastic properties and shapes according to Table 4.4 as well as phase volume evolutions according to Fig. 4.11(a) and 4.12(a). Strength values predicted by the “single hydrate” model overestimate strength values measured 3 days after production and underestimate 28 day strength values, see the dashed lines and the circles in Figs. 4.17(a) and (b). The multiscale model with the more detailed representation of hydrates (“five hydrates” model), in turn, explains the strength values measured after 3 days very reliably, but also underestimates the 28 day strength values, see the solid lines and circles in Figs. 4.17(a) and (b).

Model-predicted strength evolutions as function of hydration degree of cement clinker exhibit the following remarkable features. While compressive strength is well known to increase initially overlinearly and later virtually linearly [150, 119, 122], the obtained strength evolution of both filler-blended mortars show a surprising *underliner* increase of strength as function of hydration degree during the age period from 3 to 28 days, see the solid lines in Figs. 4.17. This phenomenon particularly concerns the quartz-blended mortar. It is a consequence of the microstructural characterization results which have served as input for strength homogenization, see particularly Fig. 4.11, where the difference quotient $\Delta f_{CSH}^{cp} / \Delta \xi_{clin}$ (i.e. the increase of the C-S-H volume fraction over the increase of the hydration degree of cement clinker) in the age interval from 3 to 7 days is *larger* than in the age interval from 7 to 28 days. This suggests that microstructural characterization is particularly challenging 28 and 91 days after production, because extrapolating, in Fig. 4.17(a), the model-predicted strength evolution from 7 to 28 days, based on the obtained trend from 0 to 7 days, would explain the strength data measured 28 days after production. While this suggests a considerable uncertainty regarding the microstructural characterization results at mature stages, model-predicted strength evolutions also suggest that consideration of only one hydrate type or several hydrate types renders a considerable difference for strength homogenization of inert filler-blended mortars, see Figs. 4.17.

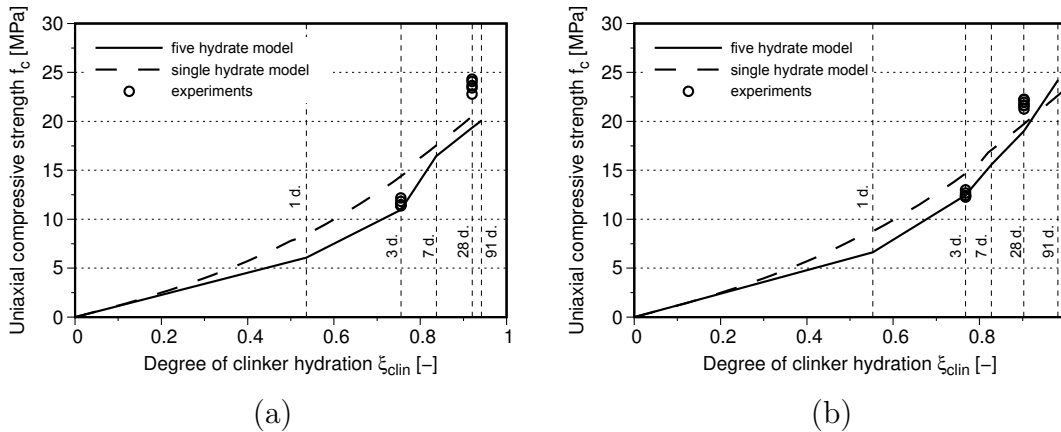


Figure 4.17: Comparison of model-predicted strength evolutions with experimental data from Core Project 10 for (a) quartz-blended mortar, and (b) and limestone-blended mortar

4.3.5 Strength homogenization of SCM-blended mortars: the strength-increasing effects of slag and fly ash hydration

As for including slag or fly ash into the microstructural representation of mortar (Fig. 4.1), it is noteworthy that the Blaine fineness of the used SCMs is comparable or smaller than to the one of the OPC clinker, see Table 4.2. Similar Blaine values imply similar particle sizes, and this motivates us to introduce SCMs as spherical inclusions at the same scale as the clinker grains, see Fig. 4.18. In ad-

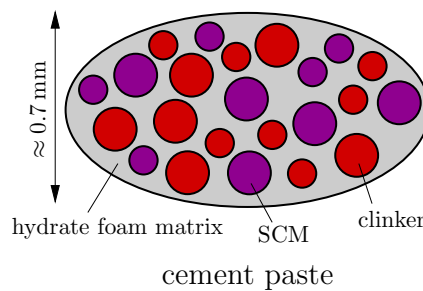


Figure 4.18: RVE of cement paste including SCMs slag or fly ash (“material organogram”); two-dimensional sketches of three-dimensional representative volume elements

dition, the microfiller effect of the SCMs was significantly less effective compared to the one of the inert fillers, and this is a further argument to consider SCM particles at the *same* scale as clinker grains.

Slag and fly ash are inert during the first few days after production, such that the

OPC-related hydrate strength values (4.7) are expected to apply for macroscopic strength predictions. However, as soon as the SCMs start to react, the characteristic hydrate strength increases, as described next. Nanoindentation experiments of Zadeh and Bobko [178] showed that the strength-related indentation hardness of low density C-S-H in mature slag- and fly ash-blended pastes is by almost 50 % larger than the one in conventional OPC. This SCM hydration-related strength increase is even more pronounced for high density C-S-H [178]. Stiffness-related indentation moduli, however, are virtually unaffected by SCM hydration [178]. The increased strength might origin from the fact that slag and fly ash contain significantly more silicon oxide than clinker, yielding a smaller calcium-to-silica ratio of C-S-H [54, 91]. Using rigidity theory of glass science, Bauchy et al. [10] showed that decreasing calcium-to-silica ratio increases the hydrates' strength, because more bonds between the atoms develop. In order to capture this effect in the model, the hydrates' cohesion is considered to increase as soon as slag or fly ash start to react. In the sense of a first approach, the increase of the cohesion is considered to be proportional to the volume of already consumed SCM, ΔV_{SCM} , divided by the volume of already consumed clinker, ΔV_{clin} :

$$c_{hyd} = \left(1 + \alpha_{SCM} \frac{\Delta V_{SCM}}{\Delta V_{clin}} \right) 50 \text{ MPa} \quad \forall SCM \in \{slag, FA\} \quad (4.38)$$

with α_{SCM} denoting a dimensionless proportionality constant. The hydrates' friction angle, in contrast, is considered to remain constant, motivated by the fact that low and high density C-S-H exhibit markedly different cohesion values but the *same* friction angle [138]. As for the unknown quantities α_{slag} and α_{FA} , we perform sensitivity analyses, as discussed next. Motivated by the aforementioned nanoindentation results [178], we consider that slag-blended hydrates are, 28 days after production, by 50 % stronger than OPC hydrates, implying that $\alpha_{slag} = 1.812$, see Eq. (4.38). This serves as a starting point for the sensitivity analyses for slag- and fly ash blended pastes, i.e.

$$\alpha_{SCM} \in \{0.000, 0.906, 1.812, 3.624\} \quad (4.39)$$

is considered for the study. In addition, we compare the modeling approach with one type of hydrate [Fig. 4.1(c)] with the alternative approach based on five hydrates (Fig. 4.15). Both modeling approaches slightly underestimate measured strength values 3 days after production, see Figs. 4.19 and 4.20. As for slag-

blended mortars, the measured strength evolution from 3 to 28 days after production is nicely reproduced based on $\alpha_{slag} = 1.812$ of the studied interval (4.39), see Fig. 4.19. As for fly ash-blended mortars, the volume ratio $\Delta V_{SCM}/\Delta V_{clin}$ is quite small at 28 days after production. Consequently, also the strengthening effect is rather small, see Figs. 4.20. Reminiscent of the situation encountered with the quartz-blended mortar, the underestimated strength values 28 days after production might well be a consequence of the microstructural characterization results, see the kinky evolution of the point-wisely resolved phase volume evolutions from 3 days to 91 days after production (Fig. 4.14). The corresponding uncertainties render a detailed assessment of the used multiscale strength model in the context of the fly ash-blended mortar impossible.

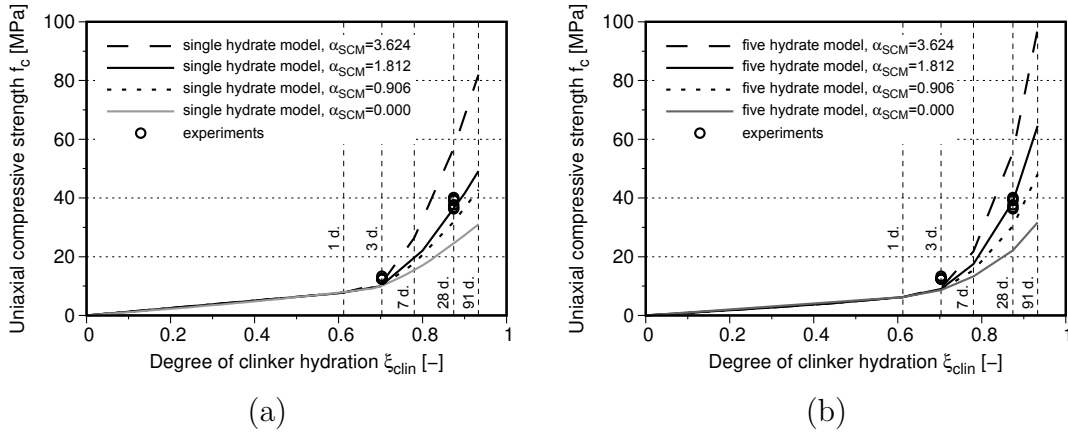


Figure 4.19: Comparison of model-predicted strength evolutions with experimental data from NANOCEM’s Core Project 10 for slag-blended mortar: (a) single hydrate model, and (b) five hydrate model; SCM hydration related strengthening of C-S-H is modeled according to Eq. (4.38) and (4.39).

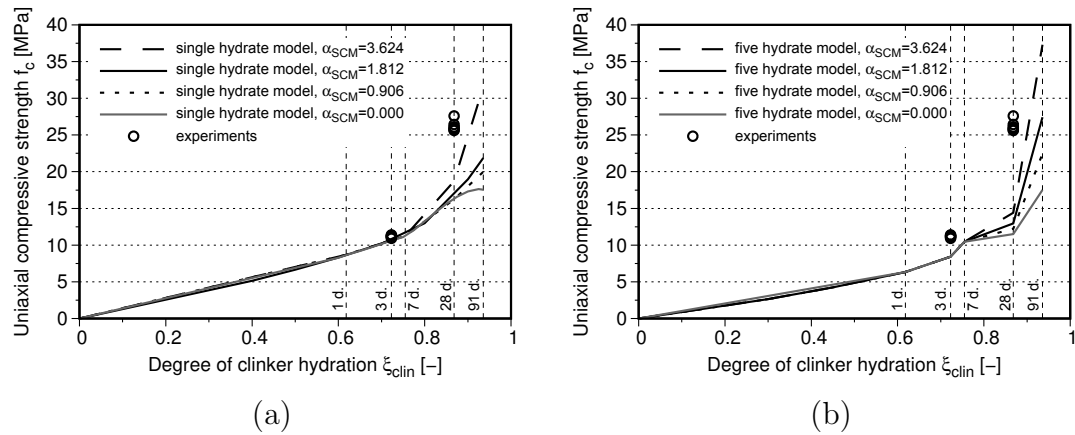


Figure 4.20: Comparison of model-predicted strength evolutions with experimental data from NANOCEM’s Core Project 10 for fly ash-blended mortar: (a) single hydrate model, and (b) five hydrate model; SCM hydration related strengthening of C-S-H is modeled according to Eq. (4.38) and (4.39).

4.4 Discussion

Two aspects related to multiscale stress concentration deserve discussion: (i) stress redistributions resulting from potential partial debonding of sand grains from the surrounding cement paste matrix, prior to reaching the uniaxial compressive strength of mortar, and (ii) stress peaks in the hydrate foam occurring in the immediate vicinity of unhydrated clinker grains.

As regards uniaxial compressive strength tests on *concretes*, it is well known that partial debonding of aggregates from the surrounding cement paste matrix typically starts once the macroscopic loading exceeds one third of the compressive strength [99]. Debonding is driven by tensile stresses, and it may either develop in form of cracking *inside* the 15 to 30 microns thin interfacial transition zone (ITZ) which is located between the aggregates and the cement paste matrix, or in form of separation of the ITZ from the aggregate [85, 86]. In addition, debonding is spatially limited to regions where significant tensile stresses occur, and – under macroscopic uniaxial compression – this is observed only in lateral parts of aggregates [85, 86]. Therefore, debonding results in rather localized stress re-distributions, and the latter are on the order of magnitude of the debonding strength. Because the latter is by one order of magnitude smaller than the compressive strength, debonding-induced stress redistributions are of secondary importance for compression-dominated stress states in the shoulder region of aggregates, where cement paste fails once the compressive strength of concrete is reached. Therefore, consideration of firm bonding between sand grains and the surrounding cement paste matrix is a reasonable assumption when it comes to quantifying compression-dominated stress states of cement paste in the immediate vicinity of sand grains.

Unhydrated clinker grains are significantly stiffer than the average stiffness of the surrounding hydrate foam matrix. This raises the question whether failure of the hydrate foam starts in the immediate vicinity of clinker grains, by analogy to the situation encountered with sand grains and the cement paste matrix, see above. In this context, it is noteworthy that the hydrate foam exhibits density gradients. Close to unhydrated clinker grains, namely, so called “inner products” form, and they are denser than the “outer products” forming in the interstitial space between unhydrated clinker grains [150, 131]. Considering that mass density, stiffness, and strength are typically well-correlated properties, also stiffness and

strength of the hydrate foam decrease with increasing distance from unhydrated clinker grains. The stiffer a microstructural region, in turn, the larger is the stress concentration, and vice versa [136]. Therefore, also hydrate foam stresses decrease with increasing distance from the unhydrated clinker grains [72], such that failure of the hydrate foam will start in characteristic distance from unhydrated clinker grains, where the stress-to-strength ratio reaches a maximum. This is likely to happen in the domain of outer products, i.e. in the region of low-density C-S-H, rather than in the immediate vicinity of the unhydrated clinker grains. This explains why we have used different modes of stress concentration around sand grains and around unhydrated clinker grains, respectively. In addition, it is noteworthy that the hydrate foam densifies progressively during hydration, i.e. *quantitatively* the density increases, while the density *distribution* can be expected to stay *qualitatively* the same, as suggested recently by Finite Element-based homogenization of cement pastes [72]. This renders simple consideration of hydration-dependent *average* hydrate foam properties (density and stiffness) reasonable for quantification of stress concentration.

4.5 Conclusions

In order to study the early-age strength evolution of OPC and blended mortars, we have carried out several extensions of the multiscale elasto-brittle strength model of Pichler and Hellmich [119]:

- As for the extension towards mortars, the presented model accounts for stress peaks in representative volumes of cement paste, which are directly attached to the surface of sand grains.
- The elasto-brittle failure criterion of micron-sized hydrate needles was extended from a *von Mises* approach to a *Mohr-Coulomb* approach.
- The microstructural representation of “hydrates” was extended from on one *average* hydrate type towards several types of hydrates, including C-S-H, portlandite, ettringite, monosulfate, etc.
- The microstructural representation of the “binder” phase was extended from consideration of cement clinker towards additional consideration of the cement replacement materials quartz, limestone, slag, and fly ash.

From the satisfactory model performance regarding blind predictions of strength of OPC pastes and mortars, tested in three different laboratories, we draw the following conclusions:

- When subjecting mortars to uniaxial compression, the most heavily loaded representative volume of cement paste is directly attached to sand grains. Related stress peaks of cement paste can be quantified by calculation of spatial averages of stresses and strains in sand grains, and by “translating” them to adjacent cement paste volumes which are directly attached to the sand grains. As for this sand-to-cement paste transition, it is adequate to consider firm bond-related continuity conditions for displacements and tractions in the interfaces between sand grains and cement paste.
- As for the stress concentration from (stress peaks of) cement paste down to micron-sized needle-shaped hydrates, strain energy-related stress averages, i.e. so called “higher-order” or “second-order” stress averages, are relevant, because hydrate failure is very likely related to *energy-driven* shear cracking at nanometric scales *inside* hydrate needles, whereby the shear strength increases with increasing pressure acting on the crack plane.
- The described failure mode of hydrate needles is accounted for by the newly adopted Mohr-Coulomb criterion. As for OPC materials, the two involved strength constants of hydrates, i.e. the cohesion and the angle of internal friction, may be set equal to the corresponding quantities of low-density C-S-H, which are known from limit state analysis of grid nanoindentation studies [138].
- Virtually the same model-predicted strength evolutions of OPC mortars are obtained, no matter whether just one *average* hydrate type was considered or several types of hydrates.
- Microstructural characterization has delivered phase volume evolutions that are related to denser hydrates, compared to the Powers-Acker phase volume evolution model. Denser hydrates, in turn, result in larger amounts of capillary pores, and this results in smaller model-predicted strength values.

As for cementitious materials produced with blended binders, phase evolution models are, unfortunately, still out of reach. Therefore, microstructural characterization data are required prerequisites for multiscale strength predictions. In

this context, the following conclusions are drawn

- Microstructural characterization based on thermogravimetric analysis, X-ray diffraction with Rietveld refinement, and scanning electron microscopy remains to be a challenging task. The nowadays achievable accuracy is, unfortunately, not high enough as to allow for a *detailed* assessment of the predictive capabilities of multiscale strength models which use the microstructural characterization results as an input. Still, the following additional conclusions appear to be justified.
- Compared to OPC mortars, strength predictions for blended mortars appear to be significantly more sensitive to the microstructural representation of hydrates either in form of just one *average* hydrate type or in form of several different types of hydrates. The latter more detailed representation appears to deliver better strength predictions.
- Finely ground inert fillers (quartz and limestone) exhibit a significant filler effect. It is well-known that they are accelerating hydration kinetics, because small filler particles represent preferred precipitation sites for hydrates. In addition to this “filler effect on reaction kinetics”, the present study suggests that finely ground fillers also exhibit a “mechanical filler effect”, because they appear to act as strength-increasing reinforcements of the hydrate foam, i.e. at the fine scale of observation of individual hydration products and of capillary porosity.
- Supplementary cementitious materials (slag and fly ash) are hydraulic materials which are well known to react – during the first few days after production – significantly slower than ordinary Portland cement. Notably, the present study suggests that SCM hydration *significantly* increases the strength of cementitious materials already during the second, third, and fourth week after production, and – very remarkably – this strengthening effect appears to be not only related to an increase of hydrate volume and to a corresponding decrease of capillary porosity, but also to an increase of the strength of those hydrates which represent the weakest links of the microstructure. While this hydrate strengthening effect of SCMs is consistent with results from nanoindentation testing of pure OPC and blended pastes, see [178], and with theoretical considerations inspired by glass physics [10], a more detailed analysis is required to identify the evolution of the increase

of the hydrate strength, driven by the hydration of SCMs.

Acknowledgments

Funding of the first author provided by the industrial academic nanoscience research network for sustainable cement and concrete “NANOCEM” (<http://www.nanocem.org>) within the framework of Core Project 10 entitled “Micromechanical Analysis of Blended Cement-Based Composites” is gratefully acknowledged. In addition, we appreciate stimulating discussions at NANOCEM events, particularly with Dr. Gilles Chanvillard (Lafarge) and Dr. Klaus-Alexander Rieder (GCPAT).

A Scale transitions, stiffness upscaling and stress concentrations

Stiffness homogenization starts with the hydrate foam (Fig. 4.1). Given the polycrystalline arrangement of hydrate needles and capillary pores, the self consistent scheme [70, 89, 71] is appropriate for homogenization, yielding the following implicit expression for the homogenized stiffness of the hydrate foam [120]

$$\begin{aligned} \mathbf{C}_{hf} = & \left(f_{pore}^{hf} \mathbf{C}_{pore} : \left\{ \mathbf{I} + \mathbf{P}_{sph}^{hf} : [\mathbf{C}_{pore} - \mathbf{C}_{hf}] \right\}^{-1} \right. \\ & \left. + f_{hyd}^{hf} \mathbf{C}_{hyd} : \int_0^{2\pi} \int_0^{\pi} \left\{ \mathbf{I} + \mathbf{P}_{cyl}^{hf}(\varphi, \vartheta) : [\mathbf{C}_{hyd} - \mathbf{C}_{hf}] \right\}^{-1} \frac{\sin \vartheta}{4\pi} d\vartheta d\varphi \right) : \\ & \left(f_{pore}^{hf} \left\{ \mathbf{I} + \mathbf{P}_{sph}^{hf} : [\mathbf{C}_{pore} - \mathbf{C}_{hf}] \right\}^{-1} \right. \\ & \left. + f_{hyd}^{hf} \int_0^{2\pi} \int_0^{\pi} \left\{ \mathbf{I} + \mathbf{P}_{cyl}^{hf}(\varphi, \vartheta) : [\mathbf{C}_{hyd} - \mathbf{C}_{hf}] \right\}^{-1} \frac{\sin \vartheta}{4\pi} d\vartheta d\varphi \right)^{-1}. \end{aligned} \quad (4.40)$$

whereby f_j^{hf} denote the hydrate foam-related phase volume fractions and \mathbf{C}_j denote the elastic phase stiffness for hydrates and capillary pores $j \in \{hyd, cpor\}$. The spherical and cylindrical phase shape, respectively, is taken into account by

using the corresponding Hill tensors \mathbb{P}_{sph}^{hf} and \mathbb{P}_{cyl}^{hf} , see [120] for details. Notably, orientation angles φ and ϑ refer to the azimuth and zenith angles of the hydrate needle. As for the homogenization of the matrix-inclusion composites cement paste and mortar, the Mori-Tanaka scheme [105, 21] is appropriate, resulting in homogenized stiffness tensors of cement paste reading as [120]

$$\mathbb{C}_{cp} = \left(\{1 - f_{clin}^{cp}\} \mathbb{C}_{hf} + f_{clin}^{cp} \mathbb{C}_{clin} : \left\{ \mathbb{I} + \mathbb{P}_{sph}^{hf} : [\mathbb{C}_{clin} - \mathbb{C}_{hf}] \right\}^{-1} \right) : \left(\{1 - f_{clin}^{cp}\} \mathbb{I} + f_{clin}^{cp} \left\{ \mathbb{I} + \mathbb{P}_{sph}^{hf} : [\mathbb{C}_{clin} - \mathbb{C}_{hf}] \right\}^{-1} \right)^{-1}, \quad (4.41)$$

with cement paste-related clinker volume fraction f_{clin}^{cp} , and in the homogenized stiffness tensor of mortar as [122]

$$\mathbb{C}_{mor} = \left(\{1 - f_{sand}^{mor}\} \mathbb{C}_{cp} + f_{sand}^{mor} \mathbb{C}_{sand} : \left\{ \mathbb{I} + \mathbb{P}_{sph}^{cp} : [\mathbb{C}_{sand} - \mathbb{C}_{cp}] \right\}^{-1} \right) : \left(\{1 - f_{sand}^{mor}\} \mathbb{I} + f_{sand}^{mor} \left\{ \mathbb{I} + \mathbb{P}_{sph}^{cp} : [\mathbb{C}_{sand} - \mathbb{C}_{cp}] \right\}^{-1} \right)^{-1}, \quad (4.42)$$

with mortar-related sand volume fraction f_{sand}^{mor} and cement paste-related Hill tensor \mathbb{P}_{sph}^{mor} .

As for downscaling of macrostresses to the spatial average of hydrate stresses (first-order concentration) the following stress concentration tensors are used: \mathbb{B}_{sand}^{mor} , \mathbb{B}_{cp}^{sand} , and $\mathbb{B}_{hyd;\varphi,\vartheta}^{cp}$, see Eqs. (4.8) and (4.26). The mortar-to-sand stress concentration tensor \mathbb{B}_{sand}^{mor} is isotropic and reads as [85] reads as

$$\mathbb{B}_{sand}^{mor} = \mathbb{C}_{sand} : \left\{ \mathbb{I} + \mathbb{P}_{sph}^{cp} : [\mathbb{C}_{sand} - \mathbb{C}_{cp}] \right\}^{-1} : \left(\{1 - f_{sand}^{mor}\} \mathbb{I} + f_{sand}^{mor} \left\{ \mathbb{I} + \mathbb{P}_{sph}^{cp} : [\mathbb{C}_{sand} - \mathbb{C}_{cp}] \right\}^{-1} \right)^{-1} : (\mathbb{C}_{mor})^{-1} \quad (4.43)$$

The aggregate-to-cement paste stress concentration tensor \mathbb{B}_{cp}^{sand} can be given in a compact form in a local spherical base frame with base vectors $\underline{e}_r, \underline{e}_\theta, \underline{e}_\phi$ moving

along the sand grain surface. The non-zero components read as [85]

$$\begin{aligned}
 B_{cp,rrrr}^{sand} &= 1 \\
 B_{cp,\theta\theta\theta\theta}^{sand} &= B_{cp,\phi\phi\phi\phi}^{sand} = \mu_{cp} (3 k_{sand} k_{cp} + 2 k_{sand} \mu_{cp} + 2 k_{cp} \mu_{sand}) / \Delta \\
 B_{cp,\theta\theta\phi\phi}^{sand} &= B_{cp,\phi\phi\theta\theta}^{sand} = 2 \mu_{cp} (k_{cp} \mu_{sand} - k_{sand} \mu_{cp}) / \Delta \\
 B_{cp,\theta\theta rr}^{sand} &= B_{cp,\phi\phi rr}^{sand} = [3 k_{sand} k_{cp} (\mu_{sand} - \mu_{cp}) - 2 \mu_{sand} \mu_{cp} (k_{sand} - k_{cp})] / \Delta \\
 B_{cp,r\theta r\theta}^{sand} &= B_{cp,r\phi r\phi}^{sand} = \frac{1}{2} \quad B_{cp,\theta\phi\theta\phi}^{sand} = \frac{\mu_{cp}}{2 \mu_{sand}}
 \end{aligned} \tag{4.44}$$

with $\Delta = k_{sand} \mu_{sand} (3 k_{cp} + 4 \mu_{cp})$ and symmetries $B_{cp,ijkl}^{sand} = B_{cp,jikl}^{sand} = B_{cp,ijlk}^{sand} = B_{cp,jilk}^{sand}$. Finally, the stress concentration from the cement paste scale to φ, ϑ -orientated hydrates, quantified by the stress concentration tensor $\mathbb{B}_{hyd;\varphi,\vartheta}^{cp}$ is discussed. It is readily obtained by combining the two stress concentrations, first the one from the cement paste to the hydrate foam scale, with the one from the hydrate foam to the hydrate, reading as

$$\begin{aligned}
 \mathbb{B}_{hyd;\varphi,\vartheta}^{cp} &= \mathbb{C}_{hyd} : \left(\{1 - f_{clin}^{cp}\} \mathbb{C}_{hf} + f_{clin}^{cp} \mathbb{C}_{clin} : \left\{ \mathbb{I} + \mathbb{P}_{sph}^{hf} : [\mathbb{C}_{clin} - \mathbb{C}_{hf}] \right\}^{-1} \right) : \\
 &\quad \left\{ \mathbb{I} + \mathbb{P}_{cyl}^{hf}(\varphi, \vartheta) : [\mathbb{C}_{hyd} - \mathbb{C}_{hf}] \right\}^{-1} : \left(f_{pore}^{hf} \left\{ \mathbb{I} + \mathbb{P}_{sph}^{hf} : [\mathbb{C}_{pore} - \mathbb{C}_{hf}] \right\}^{-1} \right. \\
 &\quad \left. + f_{hyd}^{hf} \int_0^{2\pi} \int_0^{\pi} \left\{ \mathbb{I} + \mathbb{P}_{cyl}^{hf}(\varphi, \vartheta) : [\mathbb{C}_{hyd} - \mathbb{C}_{hf}] \right\}^{-1} \frac{\sin \vartheta}{4\pi} d\vartheta d\varphi \right)
 \end{aligned} \tag{4.45}$$

B Numerical realization of the strength criterion

Herein, we describe the strategy to find the critical position along the sand grain surface, the critical hydrate orientation, and correspondingly, the critical macroscopic stress magnitude (macroscopic material strength) which governs the material failure according to the microscopic Mohr-Coloumb strength criterion (4.6). In order to minimize the amount of the time consuming derivatives related to the critical hydrate orientation, the macroscopic loading is rotated while only the \underline{e}_3 -orientated hydrate is considered, see also [125]. Provided the symmetry of the problem, the azimuth and zenith angle related to the loading rotation are resolved

for 31 homogeneously distributed points within the interval $[0, \pi/2]$, respectively. The zenith angle ψ , which marks the position of the critical cement paste RVE at the sand grain surface, in turn, is resolved for 91 points within the interval $[0, \pi/2]$. In summary, we are checking $31 \times 31 \times 91 = 87,451$ combinations for position with (respect to the aggregate surface) and orientation of the critical hydrate.

C Nomenclature

Abbreviations

The following symbols are used in the paper:

<i>AFt</i>	ettringite hydrates
<i>AFm</i>	monosulfoaluminate hydrates
<i>AFmC</i>	monocarbo-sulfoaluminate hydrates
<i>clin</i>	cement clinker
<i>CH</i>	portlandite hydrates
<i>cp</i>	cement paste
<i>cyl</i>	cylindrical (needle-shaped)
<i>C-S-H, CSH</i>	calcium-silicate-hydrates
<i>hf</i>	hydrate foam
<i>H₂O</i>	water
<i>hyd</i>	hydrates
<i>mor</i>	mortar
<i>pore</i>	pores
RVE	representative volume element
<i>sph</i>	spherical
<i>SCM</i>	supplementary cementitious materials

Mathematical operators

\cdot	inner product
$:$	second-order tensor contraction
\otimes	dyadic product

∂	partial derivative
d	derivative

Mathematical symbols

$\mathbf{1}$	second-order identity tensor
\mathbb{B}_{cp}^{sand}	stress concentration tensor relating sand stresses down to stresses in the cement paste
\mathbb{B}_{sand}^{mor}	stress concentration tensor relating mortar stresses down to stresses in the sand grains
$\mathbb{B}_{hyd;\varphi,\vartheta}^{cp}$	stress concentration tensor relating cement paste stresses down to stresses in the φ, ϑ -orientated hydrate needles
\mathbb{C}_j	elastic stiffness tensor of phase j with $j \in \{clin, cp, hf, hyd, mor, pore\}$
c_{hyd}	cohesion of hydrates
d	characteristic size of the inclusion in an RVE
D	characteristic size of the structure containing an RVE
$\underline{e}_1, \underline{e}_2, \underline{e}_3$	unit base vectors of the global Cartesian base frame
$\underline{e}_r, \underline{e}_\theta, \underline{e}_\phi$	unit base vectors of the local spherical base frame
\mathbf{E}_{cp}	macroscopic strain tensor at the cement paste scale
f_j^{cp}	cement paste-related volume fraction of phase j with $j \in \{clin, hf, hyd, pore; quartz, limestone, slag, FA\}$
$f_{hyd;\varphi,\vartheta}^{cp}$	cement paste-related volume fraction of φ, ϑ -orientated hydrate needles
f_j^{hf}	hydrate foam-related volume fraction of phase j with $j \in \{hyd, pore\}$
f_j^{mor}	mortar-related volume fraction of phase j with $j \in \{cp, sand\}$
\mathbb{I}	fourth-order identity tensor
$\mathbb{I}^{vol}, \mathbb{I}^{dev}$	volumetric and deviatoric parts of fourth-order identity tensor
\mathcal{I}_{sand}^{cp}	sand-to-cement paste interface
k_j	bulk modulus of phase j with $j \in \{clin, cp, hf, hyd, pore, sand; quartz, limestone, slag, FA; CSH, CH, AFt, AFm, AFmC\}$
$k_{hyd;\varphi,\vartheta}$	bulk modulus of φ, ϑ -orientated hydrates
ℓ	characteristic size of an RVE

\underline{n}	unit (outward) normal vector acting perpendicular to the interface \mathcal{I}_{sand}^{cp}
\mathbb{P}_j^{hf}	Hill tensor of an inclusion with shape j , embedded in an infinite hydrate foam matrix, $j \in \{sph, cyl\}$
\mathbb{P}_{sph}^{cp}	Hill tensor of a spherical inclusion embedded in an infinite cement paste matrix
R^2	quadratic correlation coefficient
s/c	initial sand-to-cement mass ratio
$\underline{t}_1, \underline{t}_2$	pairs of tangent vectors in the tangential plane to the interface \mathcal{I}_{sand}^{cp}
V_j	volume of phase j with $j = \{hyd; \varphi, \vartheta\}$ or $j = \{pore\}$
w/c	initial water-to-cement mass ratio
w_{cp}/c	effective water-to-cement mass ratio
W	elastic energy stored in an RVE, expressed macroscopically W^{macro} and microscopically W^{micro}
\underline{x}	position vector
α_{SCM}	dimensionless proportionality constant for slag ($SCM = slag$) or fly ash ($SCM = FA$)
δ_{ij}	Kronecker delta
Δ	Auxiliary variable
$\Delta V_{SCM}, \Delta V_{clin}$	volume of already consumed SCM or clinker
$\boldsymbol{\varepsilon}_j$	strain tensor of phase j with $j \in \{cp, sand\}$
$\boldsymbol{\varepsilon}^{vol}, \boldsymbol{\varepsilon}^{dev}$	volumetric and deviatoric part of the strain tensor
$\overline{\varepsilon}_{hyd;\varphi,\vartheta}^{vol}, \overline{\varepsilon}_{hyd;\varphi,\vartheta}^{dev}$	volumetric and deviatoric strain scalars of the strain energy-related strain tensor of φ, ϑ -orientated hydrate needles
ϑ	zenith angle marking the orientation of hydrate needles
ϑ_{fail}	azimuth angle ϑ of failing hydrate needles
μ_j	shear modulus of phase j with $j \in \{clin, cp, hf, hyd, pore, sand; quartz, limestone, slag, FA; CSH, CH, AFt, AFm, AFmC\}$
ξ_{clin}	hydration degree of cement clinker
ξ_{SCM}	hydration degree of SCM
ρ_j	mass density of phase j with $j \in \{sand, H_2O, clin\}$
$\boldsymbol{\sigma}_j$	stress tensor of phase j with $j \in \{cp, hyd, sand\}$
$\overline{\boldsymbol{\sigma}}_{hyd}$	strain energy-related stress tensor of hydrates

$\bar{\sigma}_{hyd;\varphi,\vartheta}$	volume average-related stress tensor of φ, ϑ -orientated hydrates
$\bar{\sigma}_{hyd;\varphi,\vartheta}^{vol}, \bar{\sigma}_{hyd;\varphi,\vartheta}^{dev}$	volumetric and deviatoric part of $\bar{\sigma}_{hyd;\varphi,\vartheta}$
$\bar{\bar{\sigma}}_{hyd;\varphi,\vartheta}$	strain energy-related stress tensor of φ, ϑ -orientated hydrates
$\bar{\bar{\sigma}}_{hyd;\varphi,\vartheta}^{vol}, \bar{\bar{\sigma}}_{hyd;\varphi,\vartheta}^{dev}$	volumetric and deviatoric part of $\bar{\bar{\sigma}}_{hyd;\varphi,\vartheta}$
$\bar{\sigma}_{hyd;\varphi,\vartheta}^{vol}, \bar{\sigma}_{hyd;\varphi,\vartheta}^{dev}$	volumetric and deviatoric stress scalars of $\bar{\sigma}_{hyd;\varphi,\vartheta}$
$\bar{\bar{\sigma}}_{hyd;\varphi,\vartheta}^{vol}, \bar{\bar{\sigma}}_{hyd;\varphi,\vartheta}^{dev}$	volumetric and deviatoric stress scalars of $\bar{\bar{\sigma}}_{hyd;\varphi,\vartheta}$
$\sigma_{hyd,I}, \sigma_{hyd,III}$	largest and smallest principal stress component of σ_{hyd}
$\bar{\bar{\sigma}}_{hyd,I}, \bar{\bar{\sigma}}_{hyd,III}$	largest and smallest principal stress component of $\bar{\bar{\sigma}}_{hyd}$
Σ_j	macroscopic stress tensor at scale j with $j \in \{cp, mor\}$
Σ_j^{uni}	absolute value of imposed uniaxial loading at scale j with $j \in \{cp, mor\}$
$\Sigma_j^{uni,ult}$	magnitude of Σ_j^{uni} corresponding to the macroscopic material strength at scale j with $j \in \{cp, mor\}$
φ	azimuth angle marking the orientation of hydrate needles
φ_{fail}	azimuth angle φ of failing hydrate needles
φ_{hyd}	angle of internal friction of hydrates
ψ	polar angle marking locations at the sand grain surface
ψ_{fail}	polar angle ψ of most heavily loaded RVE of cement paste

Chapter 5

Molecular-to-macro upscaling of concrete fracture

This chapter contains a mature paper draft authored by Michal Hlobil, Maximilian Göstl, Jacques Burrus, Christian Hellmich, and Bernhard Pichler. At the time of finalizing this thesis, is planned to submit the paper – in further improved form – to the Journal for Mechanics and Physics of Solids.

5.1 Introduction

Macroscopic cracking of solids can be traced back to breaking of intermolecular bonds and, hence, represents a multiscale problem originating from the nanometric scale. Cracks propagating through cementitious materials (with regular strength, not high performance materials) avoid, as a rule, aggregate and unhydrated clinker inclusions. Thus, crack propagation is predominantly taking place along the surface or through the volume of the reaction products between clinker and water, the so-called hydrates. The major part of the latter is made up by the calcium-silicate hydrates (C-S-H). Hence, there is great interest in the fracture properties of C-S-H. However, a direct experimental access to those properties is still out of reach. Therefore various computational approaches have been proposed for estimating the fracture energy of C-S-H, i.e. the amount of energy required to produce a unit crack area at the surface or within the bulk of an elementary block of C-S-H: Ghebrab and Soroushian [62] estimated the fracture energy needed to separate two C-S-H globules from Van-der-Waals forces, arriv-

ing at values ranging from 0.38 to 2.85 J/m². Hlobil et al. [72] back-analyzed a similarly large value from a suite of material simulations at the levels of C-S-H, of hydrate foam, and of cement paste: they proposed a hydrate fracture energy of 2.0 J/m². The most "direct" access to the C-S-H fracture energy available today seem to be the molecular dynamics simulations of Bauchy et al. [11], who analyzed mode I crack propagation in the interlayer spaces of C-S-H. Based on the stoichiometry provided by Pellenq et al. [116], they arrive at a fracture energy of

$$G_{CSH} = 1.72 \pm 0.29 \text{ J/m}^2 \quad (5.1)$$

This value is the starting point for the present paper. It is probably the first to provide an analytical upscaling approach, for the C-S-H-related fracture energy given in Eq. (5.1), up to the material scales of mortars and concretes. In this way, it will allow for the prediction of macroscopic cracking phenomena, as they are occurring in direct tension tests on concretes or three-point bending tests on mortars.

In this context, we concentrate on the so-called damage accumulation zone, which surrounds, by three times the maximum aggregate diameter, a macrocrack propagating through a concrete structure [15, 12, 16, 102], see Fig. 5.1. This zone

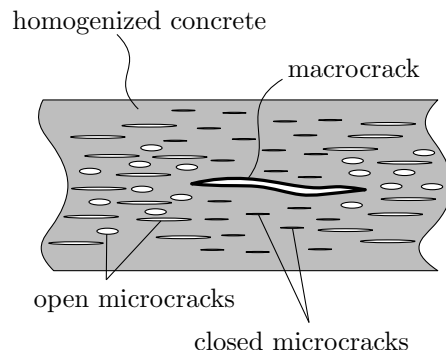


Figure 5.1: Sketch of a damage accumulation zone, also referred to as "fracture process zone" or "crack band" [15, 12]

is represented as being made up by representative volume elements (RVEs) of cracked concrete, for which a thermodynamics-based damage propagation law is formulated in the line of Dormieux et al. [47]. The corresponding free energy density of cracked concrete depends on the (macroscopic) strain \mathbf{E} and on a damage variable ω , $\Psi = \Psi(\mathbf{E}, \omega)$. Accordingly, the dissipation \mathcal{D} reads as

$$\mathcal{D} = \frac{\partial \Psi}{\partial \omega} \dot{\omega} = \mathcal{G}_{df} \dot{\omega} \geq 0 \quad (5.2)$$

with the damage propagation driving force $\mathcal{G}_{df} = \partial\Psi/\partial\omega$; leading to an increase of ω , $\dot{\omega} \geq 0$, under conditions analogous to those of Melan-Kuhn-Tucker in the context of elastoplasticity

$$\mathcal{G}_{df} - \mathcal{G}_{res} \leq 0 \quad \dot{\omega} \geq 0 \quad (\mathcal{G}_{df} - \mathcal{G}_{res}) \dot{\omega} = 0 \quad (5.3)$$

where the damage resistance \mathcal{G}_{res} is the analogon to a strength property in elastoplasticity. The remainder of the paper is devoted to the quantification of the cracked concrete-related quantities \mathcal{G}_{df} and \mathcal{G}_{res} from the material's hierarchical microstructure, down to the nanoscale where elasticity and strength of C-S-H emerge. The paper is structured as follows: Section 5.2 concerns the driving force \mathcal{G}_{df} , which is related to the elastic energy dissipated per unit of crack growth; this energy following from a hierarchical micromechanics approach based on Eshelby's matrix-inclusion problem. Section 5.3 covers the determination of \mathcal{G}_{res} , from fracture energies encountered throughout the different material scales; based on a hierarchical covered spheres model. Section 5.4 introduces a novel damage evolution law, as well as the determination of its two governing quantities from direct tensile tests. Thereafter, the new micromechanics model is experimentally validated by means of three-point bending tests in Section 5.5; which is followed by a final discussion, contained in Section 5.6.

5.2 Damage propagation driving force \mathcal{G}_{df} , as derived from molecular-to-macro elasticity homogenization

According to Eq. (5.1), the driving force for damage propagation is the change of the elastic energy density in a piece of cracked concrete, with changing damage variable ω . Upon a macroscopic stress Σ acting on such a piece of cracked concrete, with elasticity tensor \mathbb{C}_{crcon} , this driving force may be mathematically expressed as

$$\mathcal{G}_{df} = \frac{1}{2} \Sigma : \frac{\partial(\mathbb{C}_{crcon})^{-1}}{\partial\omega} : \Sigma \quad (5.4)$$

As damage variable, we adopt the crack density parameter, which for n_c penny shaped cracks of radius a_i , within volume Ω of an RVE of cracked concrete reads

as [30, 29, 46]

$$\omega = \frac{1}{|\Omega|} \sum_{i=1}^{n_c} a_i^3 \quad (5.5)$$

In order to render this expression applicable to real cracks with general shapes, we express the crack radii in Eq. (5.5) in terms of the crack areas of penny-shaped cracks, $A_i = \pi a_i^2$, $i \in \{1, 2, \dots, n_c\}$, yielding

$$\omega = \frac{1}{|\Omega| \pi^{\frac{3}{2}}} \sum_{i=1}^{n_c} A_i^{\frac{3}{2}} \quad (5.6)$$

From now on, A_i in (5.6) stands for the area of the i -th real crack.

The stiffness C_{ccon} is quantified from a multistep homogenization scheme as depicted in Fig. 5.2: Homogenized properties of materials with heterogeneous

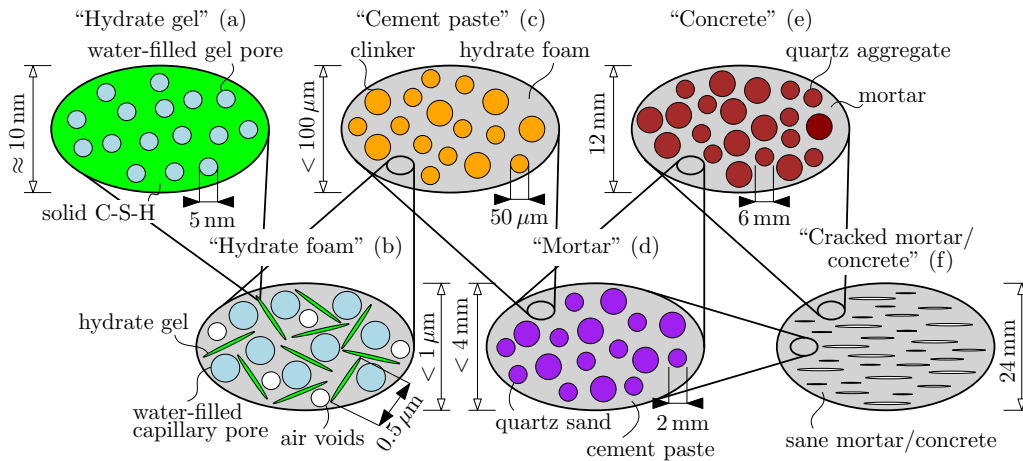


Figure 5.2: Hierarchical organization of microcracked mortars and concretes (“material organogram”) used for elasticity homogenization: two-dimensional representations of three-dimensional RVEs.

microstructures are defined on representative volume elements (RVEs) satisfying the separation of scales principle

$$d \ll \ell \ll \mathcal{L} \quad (5.7)$$

where ℓ stands for the characteristic size of the RVE, d for the average size of heterogeneities within the RVE, and \mathcal{L} for the characteristic size of the structure containing the RVE, such as structural dimensions or wavelengths of loads. Notably, “ \ll ” in the left of the inequalities (5.7) does not necessarily imply more than a factor of two [50].

As every detail of the microstructure within an RVE is anyway unaccessible, the key microstructural features are represented in terms of homogeneous subdomains called material phases. The latter are characterized by elastic properties, volume fraction, shape, and mutual interaction. Homogenization of elasticity over each of the RVEs depicted in Fig. 5.2 is performed in the framework of continuum micromechanics [71, 149, 179, 180], based on Hill's expression for the homogenized stiffness \mathbf{C}_{hom} , see [71]

$$\mathbf{C}_{hom} = \sum_{i=1}^{n_p} f_i \mathbf{C}_i : \mathbf{A}_i \quad (5.8)$$

where f_i^{hom} , \mathbf{C}_i , and \mathbf{A}_i stand for the volume fraction, for the fourth-order stiffness tensor, and for the fourth-order strain concentration tensor of phase i while n_p is the number of material phases. When representing each of the individual phases as an inclusion in a fictitious infinite matrix as occurring in Eshelby's matrix-inclusion problem [52], the strain concentration tensors can be given in an explicit analytical format, reading as [21, 179, 180]

$$\mathbf{A}_i = \left[\mathbb{I} + \mathbf{P}_i : (\mathbf{C}_i - \mathbf{C}_\infty) \right]^{-1} : \left\{ \sum_{j=1}^{n_p} f_j \left[\mathbb{I} + \mathbf{P}_j : (\mathbf{C}_j - \mathbf{C}_\infty) \right]^{-1} \right\}^{-1} \quad (5.9)$$

where \mathbb{I} stands for the fourth-order unity tensor, with the components $I_{ijkl} = (\delta_{ik} \delta_{jl} + \delta_{il} \delta_{jk})/2$, where the Kronecker delta δ_{ij} is defined as $\delta_{ij} = 1$ if $i = j$, and $\delta_{ij} = 0$ otherwise; \mathbf{P}_i stands for the fourth-order Hill tensor of phase i , reading as

$$\mathbf{P}_i = \mathbf{S}_i : \mathbf{C}_\infty^{-1} \quad (5.10)$$

with \mathbf{C}_∞ as the symmetric fourth-order stiffness tensor of the infinite matrix in the Eshelby problems [52], and \mathbf{S}_i as the fourth-order Eshelby tensor, accounting for the shape of material phase i embedded in an infinite isotropic matrix with stiffness \mathbf{C}_∞ . The Eshelby tensor of a spherical inclusion is isotropic and reads as [107]

$$\mathbf{S}_{sph} = \frac{3k_\infty}{3k_\infty + 4\mu_\infty} \mathbb{I}_{vol} + \frac{6(k_\infty + 2\mu_\infty)}{5(3k_\infty + 4\mu_\infty)} \mathbb{I}_{dev} \quad (5.11)$$

where k_∞ and μ_∞ stand for the bulk and shear moduli, respectively, of the infinite matrix. In addition, $\mathbb{I}_{vol} = (\mathbf{1} \otimes \mathbf{1})/3$ and $\mathbb{I}_{dev} = \mathbb{I} - \mathbb{I}_{vol}$, respectively, stand for the volumetric and deviatoric parts of \mathbb{I} , and where $\mathbf{1}$ denotes the second-order identity tensor with components identical to the Kronecker delta δ_{ij} . The components of the Eshelby tensor of a cylindrical inclusion with its axis point-

ing in \underline{e}_3 -direction and embedded in an isotropic matrix with stiffness \mathbf{C}_∞ reads as [107, 125]

$$\begin{aligned}
 S_{cyl,1111} &= S_{cyl,2222} = \frac{9}{4} \frac{k_\infty + \mu_\infty}{3k_\infty + 4\mu_\infty} \\
 S_{cyl,1122} &= S_{cyl,2211} = \frac{1}{4} \frac{3k_\infty - 5\mu_\infty}{3k_\infty + 4\mu_\infty} \\
 S_{cyl,1133} &= S_{cyl,2233} = \frac{1}{2} \frac{3k_\infty - 2\mu_\infty}{3k_\infty + 4\mu_\infty} \\
 S_{cyl,1212} &= \frac{1}{4} \frac{3k_\infty + 7\mu_\infty}{3k_\infty + 4\mu_\infty} \\
 S_{cyl,1313} &= S_{cyl,2323} = \frac{1}{4}
 \end{aligned} \tag{5.12}$$

The Eshelby tensor exhibits minor symmetries, i.e. $\forall\{i, j, k, l\}$, $S_{ijkl} = S_{jikl} = S_{ijlk} = S_{jilk}$. The choice of the fictitious stiffness \mathbf{C}_∞ depends on the mechanical interaction between the material phases. In case of matrix-inclusion problems, \mathbf{C}_∞ is set equal to the stiffness of the matrix of the RVE [179, 180]. This leads to the Mori-Tanaka scheme [105, 21]. As for polycrystalline microstructures, in turn, the stiffness of the infinite matrix is set equal to the stiffness of the RVE [179, 180]. This leads to the self consistent scheme [30, 70, 89, 71]. In addition, the isotropic spatial orientation of “hydrate gel” needles representing all hydrates found in an RVE of hydrate foam, see Fig. 5.2(b), requires introduction of infinitely many cylindrical phases, and the corresponding infinite sum in Eq. (5.9) can be expressed as a double-integral over all space orientations [57, 120]

$$\begin{aligned}
 \mathbf{A}_i &= \left[\mathbf{I} + \mathbf{P}_i : (\mathbf{C}_i - \mathbf{C}_{hf}) \right]^{-1} : \left\{ f_{pore}^{hf} \left[\mathbf{I} + \mathbf{P}_{sph} : (\mathbf{C}_{pore} - \mathbf{C}_{hf}) \right]^{-1} \right. \\
 &\quad \left. + f_{gel}^{hf} \int_{\varphi=0}^{2\pi} \int_{\vartheta=0}^{\pi} \left[\mathbf{I} + \mathbf{P}_{cyl}(\vartheta, \varphi) : (\mathbf{C}_{gel} - \mathbf{C}_{hf}) \right]^{-1} \frac{\sin \vartheta}{4\pi} d\vartheta d\varphi \right\}^{-1}
 \end{aligned} \tag{5.13}$$

where ϑ and φ are the two position angles in a spherical coordinate system. Eq. (5.13) also considers mutual mechanical interaction between the disordered needle arrangement and the finite capillary pore phase seen in Fig. 5.2(b). The corresponding expression for the homogenized stiffness of hydrate foam, as an

extension of Eq. (5.8) to infinite many phases, reads as

$$\begin{aligned} \mathbf{C}_{hf}^{hom} = & \left(f_{pore}^{hf} \mathbf{C}_{pore} : \left\{ \mathbf{I} + \mathbb{P}_{sph}^{hf} : [\mathbf{C}_{pore} - \mathbf{C}_{hf}^{hom}] \right\}^{-1} \right. \\ & \left. + f_{gel}^{hf} \mathbf{C}_{gel} : \int_0^{2\pi} \int_0^{\pi} \left\{ \mathbf{I} + \mathbb{P}_{cyl}^{hf}(\varphi, \vartheta) : [\mathbf{C}_{gel} - \mathbf{C}_{hf}^{hom}] \right\}^{-1} \frac{\sin \vartheta}{4\pi} d\vartheta d\varphi \right) : \\ & \left(f_{pore}^{hf} \left\{ \mathbf{I} + \mathbb{P}_{sph}^{hf} : [\mathbf{C}_{pore} - \mathbf{C}_{hf}^{hom}] \right\}^{-1} \right. \\ & \left. + f_{gel}^{hf} \int_0^{2\pi} \int_0^{\pi} \left\{ \mathbf{I} + \mathbb{P}_{cyl}^{hf}(\varphi, \vartheta) : [\mathbf{C}_{gel} - \mathbf{C}_{hf}^{hom}] \right\}^{-1} \frac{\sin \vartheta}{4\pi} d\vartheta d\varphi \right)^{-1}. \end{aligned} \quad (5.14)$$

We are left with discussing stiffness estimates for damage accumulation zones in mortars and concretes. The latter are represented as matrix-inclusion composites consisting of a mortar or concrete matrix (index *mat*), and embedded parallel cracks [Fig. 5.2(f)]. In this case, the crack density parameter (5.5) intervenes in the transversely isotropic Mori-Tanaka expression for the homogenized stiffness of damage accumulation zones containing parallel cracks [48]

$$\mathbf{C}_{dam} = \mathbf{C}_{mat} : \left(\mathbf{I} + \frac{4\pi}{3} \omega \mathbb{T} \right)^{-1} \quad (5.15)$$

where the fourth-order tensor \mathbb{T} accounts for the anisotropic damage effect of parallel cracks [118]. Provided that the normal to the crack planes points in \underline{e}_3 -direction, the non-vanishing components of \mathbb{T} read as

$$\begin{aligned} T_{3311} &= T_{3322} = \frac{4\nu_{mat}(1-\nu_{mat})}{\pi(1-2\nu_{mat})} \\ T_{1313} &= T_{2323} = \frac{2(1-\nu_{mat})}{\pi(2-\nu_{mat})} \\ T_{3333} &= \frac{4(1-\nu_{mat})^2}{\pi(1-2\nu_{mat})} \end{aligned} \quad (5.16)$$

where ν_{mat} denotes Poisson's ratio of the isotropic matrix material surrounding the cracks; which is – in the present case – made of either (uncracked) mortar or (uncracked) concrete. The \mathbb{T} tensor exhibits minor symmetries, i.e. $\forall \{i, j, k, l\}$, $T_{ijkl} = T_{jikl} = T_{ijlk} = T_{jilk}$.

Next, we identify the elastic properties and volume fractions of the phases occurring in the hierarchical organization of mortars and concretes in Fig. 5.2: The matrix-inclusion composite “hydrate gel” is the smallest RVE of mortars and concretes, with characteristic size $\ell_{gel} \approx 10$ nm. It consists of a “solid C-S-H” matrix with embedded spherical gel pore inclusions [Fig. 5.2 (a)]. Adopting the random packing limit given by Constantinides and Ulm [42], the corresponding volume fractions read as

$$f_{CSH}^{gel} = 0.64; \quad f_{pore}^{gel} = 1 - f_{CSH}^{gel} \quad (5.17)$$

The elastic properties of solid C-S-H follow from the molecular dynamics simulations of Pellenq et al. [116], see Table 5.1.

Table 5.1: Properties of microstructural constituents of mortar and concrete

	Bulk modulus k [GPa]	Shear modulus μ [GPa]	Fracture energy G [J/m ²]	Source
solid C-S-H	$k_{CSH} = 49.00$	$\mu_{CSH} = 23.00$	$G_{CSH} = 1.72$	[117],[11]
pore	$k_{pore} = 0.00$	$\mu_{pore} = 0.00$	–	[120]
clinker	$k_{clin} = 116.58$	$\mu_{clin} = 53.81$	–	[163]
quartz sand	$k_{sand} = 35.35$	$\mu_{sand} = 29.91$	–	[166]
quartz aggregate	$k_{agg} = 35.35$	$\mu_{agg} = 29.91$	–	[166]

The polycrystalline composite “hydrate foam”, with characteristic size $\ell_{hf} = 1$ μ m, is a highly disordered arrangement of isotropically oriented “hydrate gel” needles with elastic properties following from the homogenization over the RVE of Fig. 5.2(a), according to Eq. (5.8)–(5.11). As given through Eq. (5.13) and (5.14) this arrangement is in direct mechanical interaction with spherical capillary pores which are drained, and therefore assigned to a vanishing stiffness [Fig. 5.2 (b)]. The “hydrate foam”-related volume fractions are functions (i) of the material composition in terms of the initial water-to-cement mass ratio w/c and (ii) of the maturity in terms of the hydration degree ξ ; they reads as [122]

$$f_{gel}^{hf} = \frac{43.15 \xi}{20 \xi + 63 (w/c)}; \quad f_{pore}^{hf} = 1 - f_{gel}^{hf} \quad (5.18)$$

The matrix-inclusion composite “cement paste”, with characteristic size $\ell_{cp} \approx 100$ μ m, consists of a “hydrate foam” matrix and spherical cement clinker grain inclusions [Fig. 5.2 (c)]. The “cement paste”-related volume fractions follow from

the Powers-Acker hydration model [127, 2], see e.g. Pichler and Hellmich [119], as

$$f_{clin}^{cp} = \frac{20(1-\xi)}{20+63(w/c)}; \quad f_{hf}^{cp} = 1 - f_{clin}^{cp} \quad (5.19)$$

The matrix-inclusion composite “mortar”, with characteristic size amounting to two to three times the maximum sand grain diameter, consists of a “cement paste” matrix and spherical sand grain inclusions [Fig. 5.2 (d)]. The “mortar”-related volume fractions are functions of the material composition in terms of the initial water-to-cement and sand-to-cement mass ratios (w/c and s/c , respectively) as well as of the mass densities of clinker, water, and sand (ρ_{clin} , ρ_{H_2O} , and ρ_{sand} , respectively, Table 5.1), and they read as [68]

$$f_{sand}^{mor} = \frac{(s/c) \frac{\rho_{clin}}{\rho_{sand}}}{1 + (w/c) \frac{\rho_{clin}}{\rho_{H_2O}} + (s/c) \frac{\rho_{clin}}{\rho_{sand}}}; \quad f_{cp}^{mor} = 1 - f_{sand}^{mor} \quad (5.20)$$

Finally, the matrix-inclusion composite “concrete”, with a characteristic size amounting to two to three times the maximum aggregate diameter, consists of a “mortar” matrix and spherical aggregate inclusions [Fig. 5.2 (e)]. The “concrete”-related volume fractions are functions of the material composition in terms of the initial water-to-cement, sand-to-cement, and aggregate-to-cement mass ratios (w/c , s/c , and a/c , respectively) as well as of the mass densities of clinker, water, sand, and aggregates (ρ_{clin} , ρ_{H_2O} , ρ_{sand} and ρ_{agg} , respectively, Table 5.1), and they read as

$$f_{agg}^{con} = \frac{(a/c) \frac{\rho_{clin}}{\rho_{agg}}}{1 + (w/c) \frac{\rho_{clin}}{\rho_{H_2O}} + (s/c) \frac{\rho_{clin}}{\rho_{sand}} + (a/c) \frac{\rho_{clin}}{\rho_{agg}}}; \quad f_{mor}^{con} = 1 - f_{agg}^{con} \quad (5.21)$$

5.3 Damage resistance G_{res} , as determined from C-S-H-to-concrete fracture energy homogenization

5.3.1 Relation between damage resistance and fracture energy of mortar/concrete

We start with establishing a relation between the resistance against damage propagation \mathcal{G}_{res} and the material-specific fracture energy G_{mat} . To this end, \mathcal{G}_{res} is multiplied with the rate of the crack density parameter, in order to quantify the dissipation \mathcal{D} in an RVE of cracked mortar or concrete in the damage accumulation zone, see [47],

$$\mathcal{G}_{res} \dot{\omega} = \mathcal{D} \quad (5.22)$$

The expression (5.22) is now specified for real crack networks. On the one hand, we consider that, due to “crack shielding”, not all but only some cracks within the damage accumulation zone will propagate simultaneously, such that the rate of the crack density parameter, see (5.6), is related to the rates of the crack areas of all the aforementioned propagating cracks

$$\dot{\omega} = \frac{1}{|\Omega| \pi^{\frac{3}{2}}} \sum_{i=1}^{n_c} \frac{3}{2} A_i^{\frac{1}{2}} \dot{A}_i, \quad (5.23)$$

where $|\Omega|$ stands for the volume of the damage accumulation zone, $\dot{A}_i > 0$ for a propagating crack and $\dot{A}_i = 0$ for a stationary (non-propagating) crack, respectively. On the other hand, we consider that a material-specific fracture energy G_{mat} is consumed during creation of a unit crack area, such that the dissipation follows as

$$\mathcal{D} = \frac{1}{|\Omega|} \sum_{i=1}^{n_c} G_{mat} \dot{A}_i \quad (5.24)$$

The sought relation between the thermodynamic resistance against crack propagation, \mathcal{G}_{res} , and the material-specific fracture energy G_{mat} follows from specification of Eqs. (5.22) for (5.23) and (5.24), and from solving the resulting expression

for \mathcal{G}_{res} :

$$\mathcal{G}_{res} = \frac{\pi^{\frac{3}{2}} \sum_{i=1}^{n_c} \dot{A}_i}{\frac{3}{2} \sum_{i=1}^{n_c} A_i^{\frac{1}{2}} \dot{A}_i} G_{mat} \quad (5.25)$$

The current scientific understanding of fracture processes within a damage accumulation zone does not allow for the prediction of the number and sizes of propagating and stationary cracks. As a remedy, we introduce a as the radius of a *representative* circular crack, which is equivalent to all *propagating* (= “active”) cracks, as expressed by the following definition

$$\sum_{i=1}^{n_c} A_i^{\frac{1}{2}} \dot{A}_i = \sqrt{a^2 \pi} \sum_{i=1}^{n_c} \dot{A}_i \quad (5.26)$$

This definition of the representative crack size a significantly simplifies the relation between \mathcal{G}_{res} and G_{mat} , as follows from insertion of (5.26) into (5.25):

$$\mathcal{G}_{res} = \frac{2\pi}{3} \frac{G_{mat}}{a} \quad (5.27)$$

Notably, the initial value of the representative crack size, a_{ini} , quantifies the active crack network at the initiation of the damage propagation. The latter is associated with the tensile strength of the investigated material.

5.3.2 Fracture energy upscaling based on a hierarchical covered spheres model

Macroscopic cracking of cementitious materials originates from breaking of intermolecular bonds at the nanoscopic scale, where debonding events (“nano-cracks”) propagate predominantly through the volume or along the surface of C-S-H. In the sequel, we present a covered sphere model (Fig. 5.3) for upscaling the fracture energy of solid C-S-H, see Eq. (5.1), all the way up to the material scales of mortars and concretes. Thereby, it is considered that cracks propagate along pathways of minimum resistance, i.e. they pass *through* gel and capillary pores, as well as *around* strong obstacles, such as cement clinker particles, sand grains, or aggregates. This leads to crack surfaces exhibiting significant roughness at several separated scales of observation, which may be seen as kind of a fractal

surface geometry [34, 36, 35].

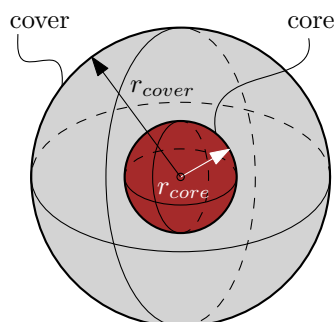


Figure 5.3: Covered sphere model employed for homogenization of fracture energy.

In order to provide a means for step-by-step upscaling of fracture energy of C-S-H, we here employ a covered sphere model, which is typically used for introducing basic thoughts in microporoelasticity [48]. Such covered sphere models are introduced at each scale of observation, see Fig. 5.4, where they are identified with the corresponding real materials (hydrate gel, hydrate foam, cement paste, mortar, or concrete, respectively), in terms of involved material phases and volume fractions, as explained next.

Cover and core materials of the covered sphere models are selected among the two constituents of the real materials, see Fig. 5.4. As for matrix-inclusion composites (“hydrate gel”, “cement paste”, “mortar”, and “concrete”, respectively), the cover is made of the matrix material and the core is made of the inclusion phase. As for polycrystalline “hydrate foam”, the cover is made of the solid phase “hydrate gel” and the core is a “capillary pore”.

The radii of cover and core spheres (r_{cover} and r_{core} , respectively) are chosen such that the volume fractions of cover and core are identical to the volume fractions of the real material phases. The volume fractions of cover and core read as

$$f_{core} = \frac{\frac{4\pi r_{core}^3}{3}}{\frac{4\pi r_{cover}^3}{3}} = \left(\frac{r_{core}}{r_{cover}}\right)^3 \quad f_{cover} = 1 - f_{core} \quad (5.28)$$

As for the volume fractions of the real material phases, see Eqs. (5.17) – (5.21).

When it comes to homogenization of fracture energy based on covered sphere models, two cases are distinguished. The first case refers to a hollow sphere, used to model porous two-phase materials. The second case refers to a solid core which

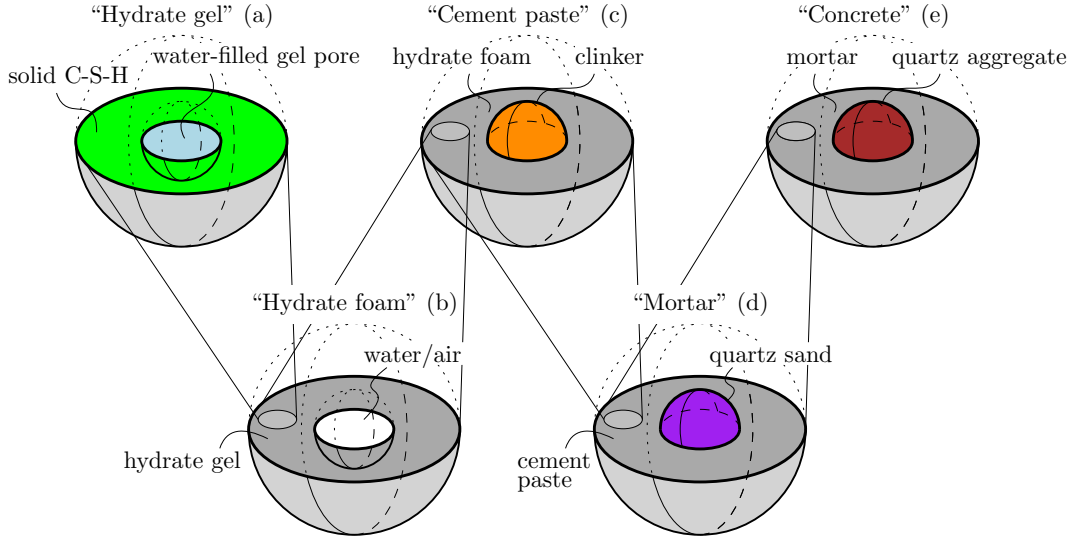


Figure 5.4: Hierarchical organization of microcracked mortars and concretes (“material organogram”) used for homogenization of fracture energy.

represents an obstacle for crack propagation.

In the first case of a hollow sphere, cracking through the cover is modeled by fictitiously cutting through the hollow sphere, with a plane that intersects the center of the pore [Fig. 5.5 (a)]. The energy required to create this crack is equal to the annulus area along which the crack runs through the cover, $\pi (r_{cover}^2 - r_{core}^2)$, multiplied with the fracture energy of the cover material, G_{cover} ; while no energy is required to cut through a pore. Similarly, we cut through the center of a homogeneous sphere made from the homogenized material [Fig. 5.5 (b)]. The energy required to create this crack is equal to the area of the total cutting plane, πr_{cover}^2 , multiplied with the sought fracture energy of the homogenized material, G_{hom} . Setting the two energies equal to each other, while considering Eq. (5.28), yields

$$\pi (r_{cover}^2 - r_{core}^2) G_{cover} = \pi r_{cover}^2 G_{hom} \quad \Rightarrow \quad G_{hom} = \left[1 - (f_{core})^{\frac{2}{3}} \right] G_{cover} \quad (5.29)$$

In the second case of a strong solid core, cracking through the covered sphere is modeled by cutting (i) through the cover with a plane that intersects the center of the sphere, and (ii) around one hemisphere of the core obstacle [Fig. 5.6 (a)]. The energy required to create this crack is equal to the fracture energy of the cover material G_{cover} multiplied with the created crack area, i. e. with the sum of the

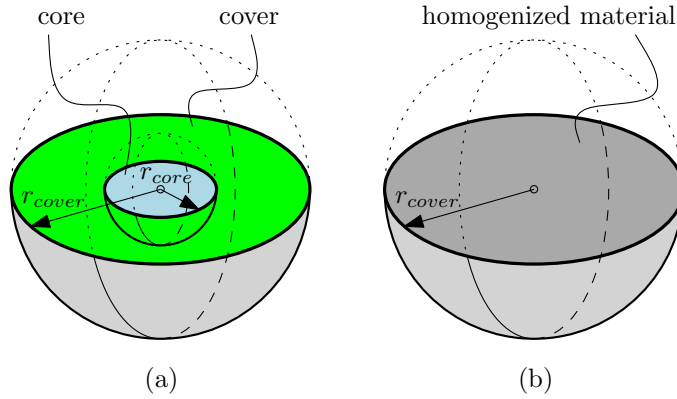


Figure 5.5: Homogenization of fracture energy in case of a porous material, based on a hollow sphere model.

annulus area $\pi (r_{cover}^2 - r_{core}^2)$ and the hemisurface of the core inclusion, $2\pi r_{core}^2$. Similarly, we cut through the center of a sphere made from the homogenized material [Fig. 5.6 (b)]. The energy required to create this crack is equal to the area of the total cutting plane, πr_{cover}^2 , multiplied with the sought fracture energy of the homogenized material, G_{hom} . Setting the two energies equal to each other, while considering (5.28), yields

$$\pi (r_{cover}^2 + r_{core}^2) G_{cover} = \pi r_{cover}^2 G_{hom} \quad \Rightarrow \quad G_{hom} = \left[1 + (f_{core})^{\frac{2}{3}} \right] G_{cover} \quad (5.30)$$

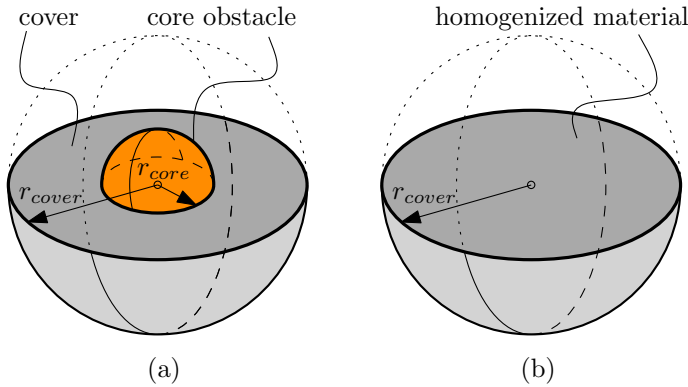


Figure 5.6: Homogenization of fracture energy in case of covered sphere containing a strong solid core, representing an obstacle for crack propagation.

Step-by-step homogenization of the fracture energy of mortars and concretes starts with “hydrate gel”. The corresponding covered sphere model consists of a “solid C-S-H” cover surrounding a “gel pore” core [Fig. 5.4 (a)]. The homogenized fracture energy of “hydrate gel” follows from specialization of Eq. (5.29)

for $G_{hom} = G_{gel}$, for $f_{core} = f_{gpor}^{gel}$ from (5.17), and for $G_{cover} = G_{CSH}$ from (5.1), as

$$G_{gel} = \left[1 - 0.36^{\frac{2}{3}} \right] \times 1.72 \text{ J/m}^2 = 0.850 \text{ J/m}^2 \quad (5.31)$$

The homogenized fracture energy of “hydrate foam”, represented as a “hydrate gel” cover surrounding a “porous” core [Fig. 5.4 (b)], follows from specialization of Eq. (5.29) for $G_{hom} = G_{hf}$, for $f_{core} = f_{pore}^{hf}$ from (5.18), and for $G_{cover} = G_{gel}$ from (5.31), as

$$G_{hf} = \left[1 - \left(1 - \frac{43.15 \xi}{20 \xi + 63 (w/c)} \right)^{2/3} \right] \times 0.850 \text{ J/m}^2 \quad (5.32)$$

The homogenized fracture energy of “cement paste”, represented as a “hydrate foam” cover surrounding a “clinker” core [Fig. 5.4 (c)], follows from specialization of Eq. (5.30) for $G_{hom} = G_{cp}$, for $f_{core} = f_{clin}^{cp}$ from (5.19), and for $G_{cover} = G_{hf}$, see (5.32), as

$$G_{cp} = \left[1 + \left(\frac{20 (1 - \xi)}{20 + 63 (w/c)} \right)^{2/3} \right] G_{hf} \quad (5.33)$$

The homogenized fracture energy of “mortar”, represented as a “cement paste” cover surrounding a “sand grain” core [Fig. 5.4 (d)] follows from specialization of Eq. (5.30) for $G_{hom} = G_{mor}$, for $f_{core} = f_{sand}^{mor}$ from (5.20), and for $G_{cover} = G_{cp}$, see (5.33), as

$$G_{mor} = \left[1 + \left(\frac{(s/c) \frac{\rho_{clin}}{\rho_{sand}}}{1 + (w/c) \frac{\rho_{clin}}{\rho_{H_2O}} + (s/c) \frac{\rho_{clin}}{\rho_{sand}}} \right)^{2/3} \right] G_{cp} \quad (5.34)$$

The homogenized fracture energy of “concrete”, represented as a “mortar” cover surrounding a “aggregate” core [Fig. 5.4 (e)], follows from specialization of Eq. (5.30) for $G_{hom} = G_{con}$, for $f_{core} = f_{agg}^{con}$ according to (5.21), and for $G_{cover} = G_{mor}$, see (5.34), as

$$G_{con} = \left[1 + \left(\frac{(a/c) \frac{\rho_{clin}}{\rho_{agg}}}{1 + (w/c) \frac{\rho_{clin}}{\rho_{H_2O}} + (s/c) \frac{\rho_{clin}}{\rho_{sand}} + (a/c) \frac{\rho_{clin}}{\rho_{agg}}} \right)^{2/3} \right] G_{mor} \quad (5.35)$$

5.4 Damage mechanics and size effect of mortars and concretes subjected to tension

5.4.1 Damage propagation criterion under macroscopic uniaxial tension

The microstructures of mortars and concretes contain defects stemming from the production and the curing process, i.e. they exist even prior to any mechanical loading. Tensile loading on such materials can be monotonously increased up to the tensile strength level, at which unstable damage propagation is initiated. The relation between the uniaxial tensile strength Σ^{ult} and the initial representative crack size within damage accumulation zone a_{ini} follows from specification of the damage propagation criterion (5.3) for the driving force (5.4) and damage resistance (5.27), as

$$\Sigma^{ult} \propto 1/\sqrt{a_{ini}} \quad (5.36)$$

The stiffness estimate given in Eq. (5.15) gives precise access to the driving force for damage propagation according to Eq. (5.4). Envisioning uniaxial tension aligned with the crack normal, $\Sigma = \Sigma_{33} \mathbf{e}_3 \otimes \mathbf{e}_3$, the driving force is obtained from specifying \mathbf{C}_{hom} in (5.4) for \mathbf{C}_{dam} from (5.15), as

$$\mathcal{G}_{df} = \frac{8 \Sigma_{33}^2 (1 - \nu_{mat}^2)}{3 E_{mat}} \quad (5.37)$$

The driving force for damage propagation in the format (5.37), in turn, allows for specification of the damage propagation criterion (5.3), thus providing a relation between the tensile stress Σ_{33} and the characteristic crack size a . The latter relation follows from specifying Eq. (5.3) for (5.37) and (5.27), as well as from solving the resulting expression for Σ_{33} , as

$$\Sigma_{33} \leq \sqrt{\frac{G_{mat} E_{mat} \pi}{4 a (1 - \nu_{mat}^2)}} = \frac{K_{Ic,mat}}{2} \sqrt{\frac{\pi}{a}} \quad (5.38)$$

with E_{mat} as the Young's modulus of the material surrounding the cracks, i.e. that of (uncracked) mortar or (uncracked) concrete. In addition, the standard plane-strain relation between fracture energy G_{mat} and the mode I fracture toughness

K_{Ic} for isotropic materials was considered:

$$G_{mat} = \frac{1 - \nu_{mat}^2}{E_{mat}} K_{Ic,mat}^2 \quad (5.39)$$

The mathematical structure of Eq. (5.38) is identical to the one of a problem from linear elastic fracture mechanics, where an infinitely large solid with isotropic stiffness (Young's elastic modulus E_{mat} and Poisson's ratio ν_{mat}), containing one circular crack of radius a , is subjected, at the infinitely remote boundary, to uniaxial tension aligned with the crack normal [124]. In the present context, however, a is representative for all propagating cracks inside the damage accumulation zone, see Eq. (5.26).

5.4.2 Dimensionless damage evolution law

Intuitively, one expects that the characteristic crack size a would increase with increasing crack density ω , and this functional relationship may be referred to as a "damage evolution law". We here develop such a relation in the framework of dimensional analysis [7], where the first step consists of identifying quantities which influence the functional relationship of interest. In ordinary concrete, the cracks propagate around aggregate stones, such that the aggregate size distribution is likely to influence the damage evolution process. Aggregate size distributions of mortars and concretes, in turn, are similar in the sense that they aim at reducing the space for the expensive binder cement paste to a reasonable minimum. In this line of reasoning, we consider that the diameter of the largest aggregate stones, d_{max} , is representative of the grain size distribution and influences the damage evolution process.

Dimensional analysis [7] delivers the following dimensionless format of a functional relationship between the representative crack size a , the crack density ω , and the maximum aggregate size d_{max} :

$$\frac{a}{d_{max}} = \mathcal{F}\left(\frac{a_{ini}}{d_{max}}, \omega\right) \quad (5.40)$$

where a_{ini} denotes the initial value of the representative crack size. In Eq. (5.40), \mathcal{F} stands for a dimensionless function. The simplest version of it is a linear

function of the form

$$\frac{a}{d_{max}} = \frac{a_{ini}}{d_{max}} + C \omega \quad (5.41)$$

When regarded as a function of ω , the quantity (a_{ini}/d_{max}) plays the role of an “intercept”, while C can be referred to as “slope”. Remarkably, the quantity a_{ini} is of statistical nature, as described next.

5.4.3 Size effect of concrete tensile strength

The initial representative crack size a_{ini} exhibits a statistical size effect, i.e. it depends on the investigated volume of concrete, as explained next. In this context, we consider that the smallest RVE of mortar/concrete exhibits a characteristic size which is three-times the maximum aggregate size [15, 12, 16, 102], i.e.

$$\ell = 3 d_{max} \quad (5.42)$$

Eq. (5.42) suggests that the smallest cubic RVE of concrete exhibits a volume amounting to

$$V_{RVE} = (3 d_{max})^3 \quad (5.43)$$

Already the tensile strength of such concrete RVEs is a statistical quantity, i.e. different RVEs of concrete, being identical in the sense that they exhibit the same volume, will exhibit tensile strength values scattering around the expected value, i.e. around the mean (or “nominal”) tensile strength denoted as Σ_{RVE}^{ult} . This scatter stems from details of the microstructural arrangement of aggregates, sand grains, the cement paste matrix, and initially existing defects, which differ from RVE to RVE.

The volume-dependence of tensile strength (“statistical size effect”) will be observed when testing concrete bodies (i) which consist of more than one RVE and (ii) which are subjected to tensile loading in a way that a *nominally uniform*¹ stress state prevails within the entire body. The strength of such a body will be equal to the strength of the weakest RVE, and – for statistical reasons – the latter strength will be the smaller, the more RVEs are contained inside the body. This is Weibull’s weakest link idea [173], according to which the mean tensile strength Σ^{ult} of a concrete body decreases with increasing volume V , expressed through

¹Due to the absence of nominal stress gradients, stress fluctuations will exclusively stem from the heterogeneous microstructure of the material.

the size effect law

$$\Sigma^{ult}(V) = \Sigma_{RVE}^{ult} \left(\frac{V}{V_{RVE}} \right)^{-\frac{1}{m}} \quad (5.44)$$

In Eq. (5.44), m denotes the dimensionless Weibull modulus which is to be identified from experiments. For concrete subjected to uniaxial tension it was quantified by Zech and Wittmann [181] as

$$m = 12 \quad (5.45)$$

Size effect law (5.44) together with $\Sigma^{ult} \propto 1/\sqrt{a_{ini}}$, see Eq. (5.36), suggest that the expected value for the initial characteristic crack size increases with increasing volume of a body of concrete, i.e. the size effect law for a_{ini} is formally identical to Eq. (5.44), except for the exponent which now reads as $+2/m$:

$$a_{ini}(V) = a_{ini,RVE} \left(\frac{V}{V_{RVE}} \right)^{+\frac{2}{m}} \quad (5.46)$$

Specifying a_{ini} in the damage evolution law given in Eq. (5.41) as $a_{ini}(V)$ according to Eq. (5.46), yields

$$\frac{a}{d_{max}} = \frac{a_{ini,RVE}}{d_{max}} \left(\frac{V}{V_{RVE}} \right)^{+\frac{2}{m}} + C \omega \quad (5.47)$$

The format (5.47) of the damage evolution law allows for identification of the “intercept” ($a_{ini,RVE}/d_{max}$) and “slope” C from the results of a direct-tension size effect study on dog bone-shaped specimens, carried out by van Vliet and van Mier [161]. This is described next.

5.4.4 Direct-tension size effect study on dog bone-shaped concrete specimens carried out by van Mier and van Vliet

Van Vliet and van Mier [161] tested concrete with a maximum aggregate size amounting to

$$d_{max} = 8 \text{ mm} \quad (5.48)$$

for more composition details, see Table 5.2. The experiments involved dog bone-shaped specimens exhibiting self-similar two-dimensional scaling of the character-

Table 5.2: Composition of investigated materials: concrete used by van Vliet and van Mier [161] and mortar used by Le Bellego et al. [93].

investigated material cement type used	concrete [161] Portland, type B		mortar [93] CPA CEM I 42.5	
	mass* [kg]	density [kg/m ³]	mass* [kg]	density [kg/m ³]
cement	375	3140**	639	3140**
water	187.5	1000	256	1000
sand: 0.125 – 4 mm	1268	2610**	–	–
sand: 0.16 – 3.15 mm	–	–	1380	2555**
aggregates: 4 – 8 mm	540	2610**	–	–
mix overview				
water/cement ratio	0.5		0.4	
sand/cement ratio	3.38		2.16	
aggregate/cement ratio	1.44		–	
*per 1 m ³ of concrete	**estimated			

istic in-plane specimen dimension L_s (Fig. 5.7) and constant thickness amounting to $t = 100$ mm. The specimens were subjected to slightly eccentric tension. Stable damage propagation was achieved by controlling the magnitude of the imposed load based on the recordings of displacement sensors measuring the elongation of the central part of the specimens [Fig. 5.7 (a)]. This way, force-elongation relationships could be captured with great precision, even in the post-peak softening regime (Fig. 5.8).

Upscaling elastic stiffness and fracture energy from nanoscopic solid C-S-H, see Eq. (5.1) and Table 5.1, up to the macroscale of concrete follows the Eqs (5.8)–(5.21) and (5.31)–(5.35). Input values are the composition of concrete, see Table 5.2, as well as the degree of hydration ξ which is set equal to 90% given that concrete specimens were tested 57 – 61 days after their production. For relevant volume fractions of gel, hydrates, and clinker see Eqs. (5.17), (5.18) and (5.19), respectively. Notably, elastic properties and fracture energy change from scale to scale, but they stay on the same order of magnitude, see Table 5.3.

5.4.5 Identification of intercept quantity ($a_{ini,RVE}/d_{max}$)

The first dimensionless constant, a_{ini}/d_{max} , is identified from explaining the measured peak loads based on the size effect laws (5.44) and (5.46) as well as on the damage propagation criterion (5.38). Notably, van Vliet and van Mier deter-

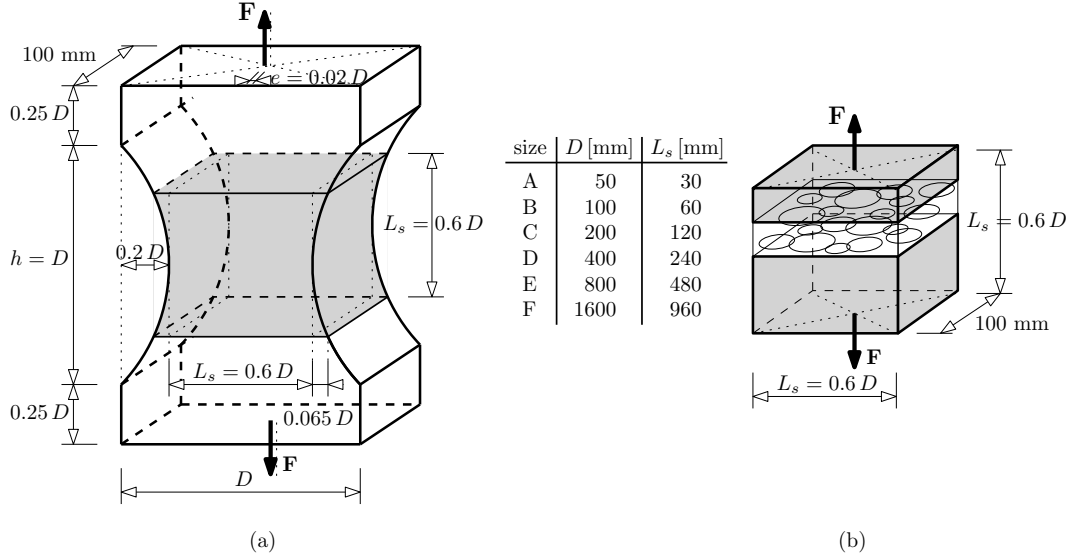


Figure 5.7: (a) Geometric dimensions of the dog bone-shaped specimens investigated by van Vliet and van Mier [161]; (a) out of plane dimension $t = 100$ mm was constant for all specimen sizes; elongation measurements refer to the shaded central part of the specimen, see Fig. 5.8; (b) prismatic representation of the central part of the specimens used for re-analysis of the tests including a damage accumulation zone (central white region) adjacent to two undamaged regions.

Table 5.3: Upscaling of elastic and fracture energy from solid C-S-H up to macroscopic concrete.

	Solid C-S-H	C-S-H gel	Hydrate foam	Cement paste	Mortar	Concrete	
Young's modulus	59.67*	28.04	16.12	17.15	37.49	42.50	GPa
Poisson's ratio	0.30*	0.27	0.25	0.25	0.21	0.20	–
Fracture energy	1.72**	0.85	0.54	0.61	1.04	1.41	J/m ²

*recalculated from k_{CSH} and μ_{CSH} given in Table 5.1

**taken from Bauchy et al. [11], see also Eq. (5.1)

mined the nominal tensile strength values of the tested concrete specimens, Σ^{ult} , by dividing the measured peak loads F_{peak} through the cross-sectional area at the center of the specimens $A = t L_s$, see the circles and scatter bars in Fig. 5.9. As for the re-analysis, we consider the central portion of the specimens to be cuboids (Fig. 5.7), with volumes

$$V = t L_s^2 \tag{5.49}$$

These volumes are larger than the smallest cubic RVE of concrete, with volume $(3 d_{agg})^3$. Therefore, the cuboids consist of several concrete RVEs, and damage propagation will initiate within the weakest RVE, as described by size effect law Eq. (5.44). Specifying the latter for the Weibull modulus in Eq. (5.45), for cuboid

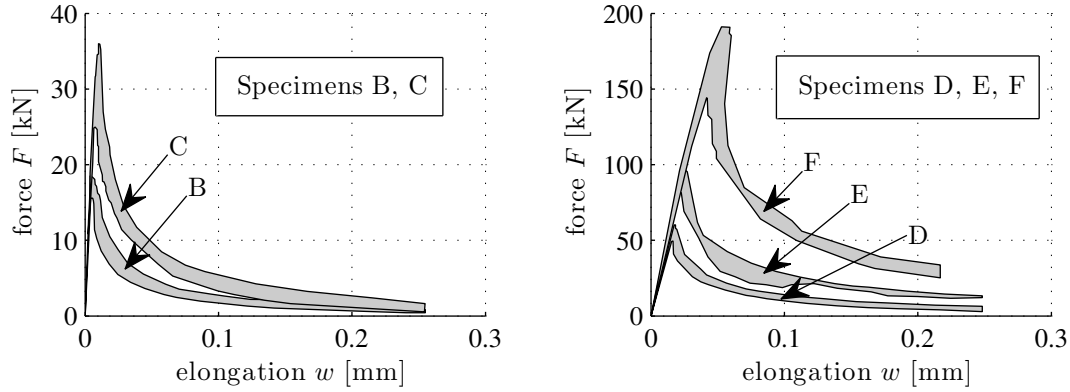


Figure 5.8: Force-elongation diagrams: measurement data of van Vliet and van Mier [161], obtained from at least four tests for each specimen size.

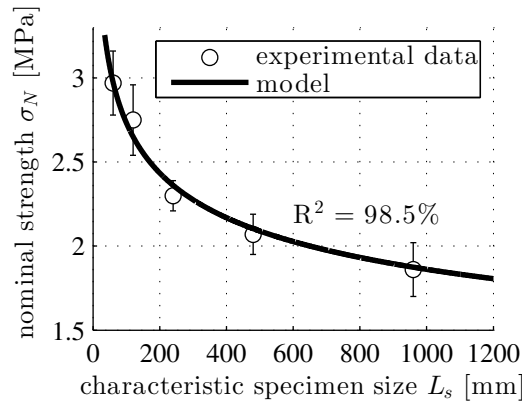


Figure 5.9: Size effect of nominal tensile strength observed by van Vliet and van Mier [161], see circles and scatter bars, as well as Weibull size effect law given in Eq. (5.50).

volume in Eq. (5.49), and for the RVE volume Eq. (5.43), delivers

$$\Sigma^{ult}(V) = \Sigma_{RVE}^{ult} \left(\frac{t^{-\frac{1}{12}}}{(3d_{max})^{-\frac{1}{4}}} \right) L_s^{-\frac{1}{6}} \quad (5.50)$$

The only unknown on the right-hand-side of Eq. (5.50) is Σ_{RVE}^{ult} , the nominal tensile strength of the smallest concrete cube. It is identified such that Eq. (5.50) explains the measured size-dependent strength values (Fig. 5.9) as good as possible, under consideration of the maximum aggregate size given in Eq. (5.48), the specimen thickness $t = 100$ mm, and the scaled specimen sizes L_s given in Fig. 5.7. This delivers

$$\Sigma_{RVE}^{ult} = 3.90 \text{ MPa} \quad (5.51)$$

The initial value of the characteristic crack size, $a_{ini,RVE}$, follows from specifying the “ \leq ” sign in damage propagation law (5.38) for the “ $=$ ” sign, from replacing index *mat* by index *con* standing for concrete, from specifying Σ_{33} for Σ_{RVE}^{ult} according to Eq. (5.51), as well as a for $a_{ini,RVE}$, and from consideration of elastic and fracture properties of concrete taken from Table 5.3, as

Table 5.4: Concrete properties considered for the re-analysis of the direct tension tests performed by van Vliet and van Mier [161].

property	value	source
maximum aggregate size	$d_{max} = 8 \text{ mm}$	[161]
Young’s elastic modulus	$E_{con} = 42.5 \text{ GPa}$	upscaled (Table 5.3)
Poisson’s ratio	$\nu_{con} = 0.20$	upscaled (Table 5.3)
fracture energy	$G_{con} = 1.41 \text{ J/m}^2$	upscaled (Table 5.3)
Weibull modulus	$m = 12$	[181, 161]
tensile strength of concrete RVE	$\Sigma_{RVE}^{ult} = 3.90 \text{ MPa}$	Eq. (5.51)
initial characteristic crack size	$a_{ini,RVE} = 3.22 \text{ mm}$	Eq. (5.52)
dimensionless initial crack size	$a_{ini,RVE}/d_{max} = 0.402$	Eq. (5.53)
damage evolution factor	$C = 0.396$	Eq. (5.58)

$$a_{ini,RVE} = \frac{G_{con} E_{con} \pi}{4 (1 - \nu_{con}^2) (\Sigma_{RVE}^{ult})^2} = 3.22 \text{ mm} \quad (5.52)$$

Dividing $a_{ini,RVE}$ according to Eq. (5.52) through the maximum aggregate size d_{max} according to Eq. (5.48), provides access to the first of the sought dimensionless quantities:

$$\frac{a_{ini,RVE}}{d_{max}} = 0.402 \quad (5.53)$$

5.4.6 Identification of slope quantity C

The second of the sought dimensionless quantities, C , is identified from the post-peak softening behavior measured in the direct tension experiments, see Fig. 5.8. To this end, we consider that (i) the damage accumulation zone will grow, starting at the weakest RVE, in a plane orthogonal to the loading axis, and that (ii) the width of the damage accumulation zone, i.e. its size measured in loading direction, is equal to $3 d_{max}$. This is the motivation to subdivide our analysis cuboid into three serially arranged subcuboids: two subcuboids which remain undamaged and one central subcuboid representing an RVE of the damage accumulation zone, exhibiting width = $3 d_{max}$, length = L_s , and depth = t [Fig 5.7 (b)]. This complies

with the separation of scales requirement (5.7), as long as (i) crack openings are small compared to $3 d_{max}$, and (ii) in-plane crack sizes are small compared to the width L_s and the depth t of the damage accumulation zone. Both conditions are satisfied in the vicinity of the peak load, but the latter condition will be violated at later stages in the post peak regime, when the specimen falls into two pieces. In the sequel, we will check corresponding limits.

As for the identification of C based on measured post-peak force-elongation relationships, see Fig. 5.10, we are left with deriving expressions for both the force F and the elongation $\Delta\ell$, as functions of the crack density ω . In this context, it is noteworthy that throughout the entire softening regime, the damage propagation law (5.3) will be satisfied in the sense that $\mathcal{G}_{df} - \mathcal{G}_{res} = 0$ and $\dot{\omega} > 0$. In other words, the “equal sign” is valid in the damage propagation law (5.38), and combining this expression with the size effect law (5.47) delivers the softening tensile strength of the crack law as a function of crack density parameter ω , as

$$\Sigma_{33}(\omega) = \sqrt{\frac{G_{con} E_{con} \pi}{4(1 - \nu_{con}^2) d_{max}} \left[\frac{a_{ini,RVE}}{d_{max}} \left(\frac{V}{V_{RVE}} \right)^{\frac{2}{m}} + C \omega \right]^{-1}} \quad (5.54)$$

Because of the serial arrangement, the same nominal stress prevails in all three subcuboids, and the external tensile force F is equal to $\Sigma_{33}(\omega)$ according to Eq. (5.54) multiplied with the cross sectional area $t L_s$ of the subcuboids:

$$F(\omega) = t L_s \Sigma_{33}(\omega) \quad (5.55)$$

As for expressing the elongation of the three-zoned cuboid as a function of the damage variable, we again consider that the same nominal stress prevails in all three subcuboids. The strains in the three cuboids are equal to the stress Σ_{33} divided by Young’s elastic modulus of the respective subcuboid, being equal to the same Young’s elastic modulus E_{con} outside the damage accumulation zone, and $E_{daz}(\omega)$ inside the latter. The elongation of the body is obtained by summing up the elongations of the three subcuboids, being equal to the strain of each zone, multiplied with size of the zone, measured in loading direction:

$$\Delta\ell(\omega) = \Sigma_{33}(\omega) \left(\frac{L_s - 3 d_{max}}{E_{con}} + \frac{3 d_{max}}{E_{daz}(\omega)} \right) \quad (5.56)$$

The micromechanics-based estimate of Young’s elastic modulus of the damage

accumulation zone, in loading direction, follows from Eq. (5.15) as

$$E_{daz}(\omega) = E_{con} \left[1 + \frac{16\omega}{3} (1 - \nu_{con}^2) \right]^{-1} \quad (5.57)$$

Evaluating parameter forms $F(\omega)$ and $\Delta\ell(\omega)$, see Eqs. (5.55) and (5.56), for the quantitative values listed in the eight upper rows of Table 5.4, allows for comparing model-predicted force-elongation relationships with their measured counterparts as functions of differently chosen values for C . Subsequent search for the maximum value of the quadratic correlation coefficients R^2 characterizing the agreement between model predictions and experimental data for each of the load-displacement curves of samples B to F (see Figure 5.10), allows for identification of the optimal value of the sought dimensionless constant C , providing a satisfactory agreement between model outputs and experimental data, see Fig. 5.10,

$$C = 0.396. \quad (5.58)$$

The corresponding maximum quadratic correlation coefficients amount to $R_B^2 = 98.91\%$, $R_C^2 = 99.45\%$, $R_D^2 = 99.32\%$, $R_E^2 = 97.78\%$, and $R_F^2 = 96.96\%$, for the different specimen sizes labeled “B” through “F”. Very remarkably, C according to (5.58) does not only allow for a satisfactory description of the initial post-peak behavior, in the immediate vicinity of the peak load, but it also provides a satisfactory description of most of the softening paths, well away from the peak load, see Fig. 5.10.

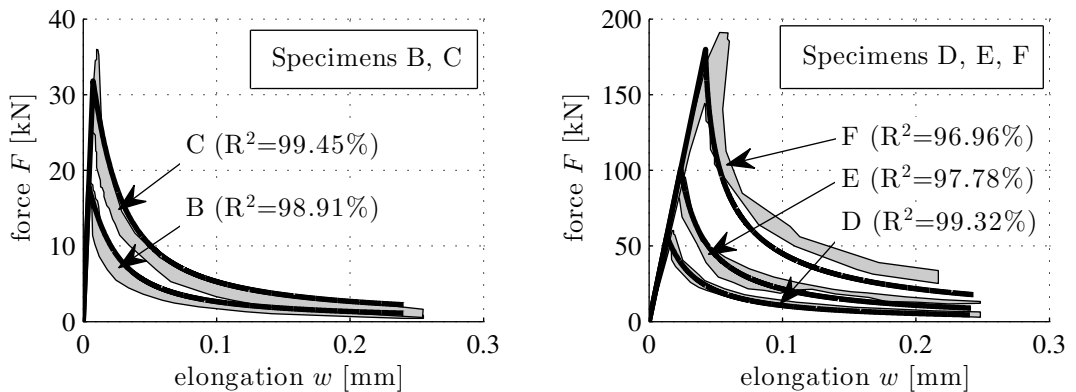


Figure 5.10: Force-elongation diagrams: shaded areas cover measurement data of van Vliet and van Mier [161], obtained from at least four tests for each specimen size; black solid lines represent the model prediction, see Eqs. (5.55), (5.56), and (5.58), as well as the input quantities given in Table 5.4.

5.5 Model validation

With the identification of $(a_{ini,RVE}/d_{max})$ and C , see Eqs. (5.53) and (5.58), our model developments are completed. Hence, the material-specific model input parameters are restricted to just the initial material composition in terms of water, cement, sand, and aggregate masses, as well as the material maturity in terms of the hydration degree. We now proceed with assessing the predictive capabilities of the model, i.e. we apply it to the analysis of a three-point-bending size effect study on notched mortar prisms, performed by Le Bellego et al. [92]. All inputs required for the numerical simulations are derived from the results of the preceding section and from composition data regarding the mortar tested by Le Bellego et al. [92, 93]. This way, our model predictions are independent of the measurements by Le Bellégo et al..This allows us to rigorously assess the predictive capabilities of the developed model.

5.5.1 Three-point-bending size effect study on notched mortar prisms, performed by [92]

Le Bellego [92] investigated the size effect of mortar strength in the framework of notched rectangular prisms subjected to three-point bending (Fig. 5.11 and Table 5.2). Prior to testing, the specimens were allowed to cure for four months

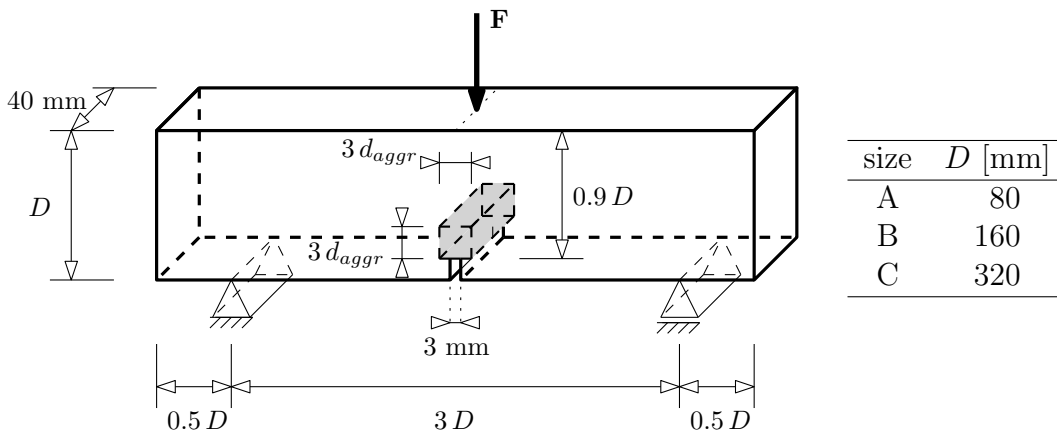


Figure 5.11: Geometric dimensions of the notched mortar prisms tested by Le Bellego [92]. The out-of-plane dimension $t = 40$ mm was constant for all specimen sizes.

at 23°C and under a relative humidity of 100%. The experiments were carried out

under notch opening control. The test results are reported in the form of force-deflection diagrams (Fig. 5.12), whereby the vertical displacement was measured in the cross-section of the notch, at mid-height of the beam.

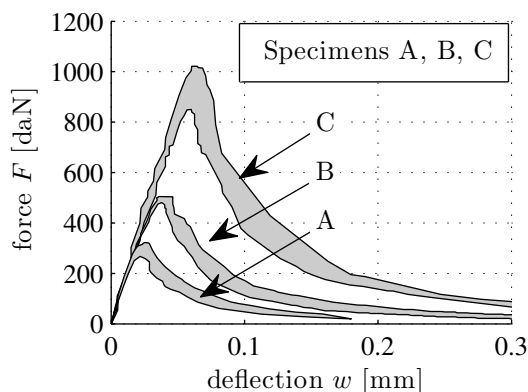


Figure 5.12: Force-deflection diagrams: measurement data of Le Bellego et al. [92], obtained from at least 4 tests for each specimen size.

5.5.2 Finite Element model

For plane stress Finite Element analyses of the three-point bending tests, quadrilateral elements with bilinear displacement interpolation are employed. This results in element-wise constant stress and strain states at the levels of the RVEs of Figure 5.2(d) and 5.2(e), respectively, as concerns uncracked and cracked mortar elements, respectively. Considering a symmetric problem with respect to the notch plane, one half of the structure is discretized (Fig. 5.13). According to [15], the width of the damage accumulation zone amounts to $3 d_{max} = 9.45$ mm. Starting from the notch tip, it grows straight upwards, towards the load application point [64]. Throughout the entire test simulation, the rest of the structure is considered to remain undamaged.

The vertical support is modeled by blocking the vertical displacements of two neighboring nodes, positioned in a horizontal distance amounting to $0.04 D$ (Fig. 5.13). The external loading is considered through prescribing uniform vertical displacements over the three nodes of the damage accumulation zone, which are part of the top-surface of the analysis model (Fig. 5.13). Finally, the horizontal displacements of all nodes at the symmetry axis are blocked. The notch is considered by assigning a very large initial damage variable, namely $\omega_{notch,ini} = 10^4$,

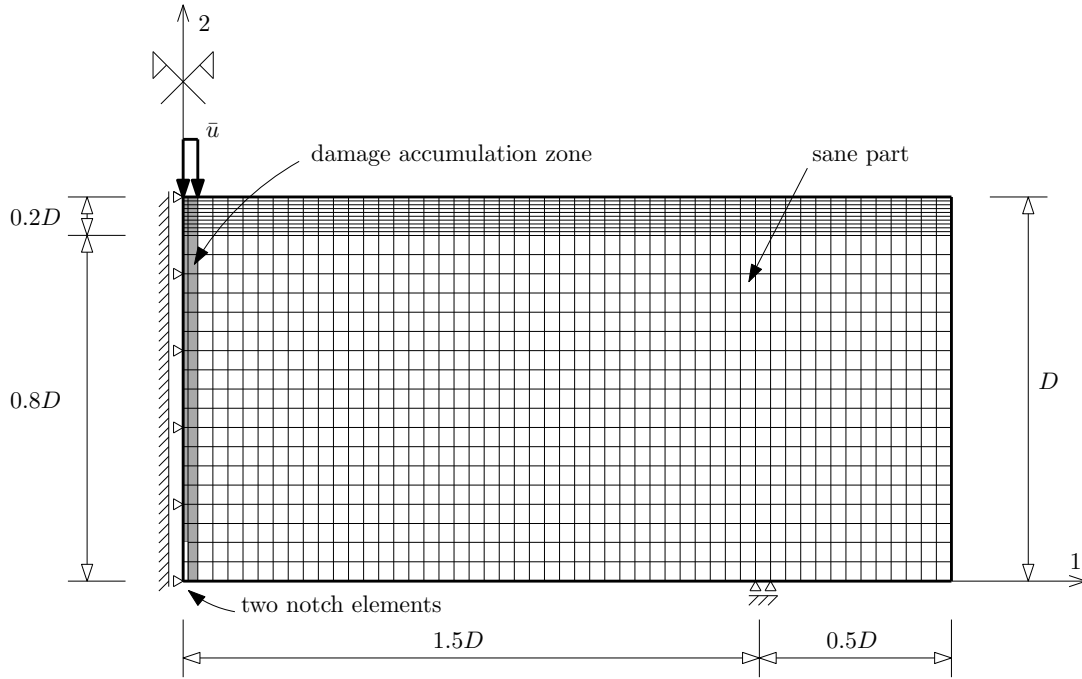


Figure 5.13: Finite Element mesh used for modeling three-point bending tests.

to the two finite elements which (i) are directly attached to the axis of symmetry, and which (ii) belong to the two bottom rows of the Finite Element mesh (Fig. 5.13).

The damage accumulation zone is subdivided, in damage propagation direction, into 28 layers of pairs of finite elements (Fig. 5.13). Each two elements belonging to the same layer, are considered to have, at any stage of the simulation process, the same crack density. Denoting the crack density parameter of the j -th layer as ω_j , we adopt the elasto-damage law (5.15), describing transversely isotropic behavior under plane stress conditions. In the standardly used notation of commercial Finite Element codes, it reads as:

$$\begin{bmatrix} \Sigma_{11} \\ \Sigma_{22} \\ \Sigma_{12} \end{bmatrix} = \begin{bmatrix} \frac{E_{mor}}{(1-\nu_{mor}^2)(1+\frac{16}{3}\omega_j)} & \frac{E_{mor}\nu_{mor}}{(1-\nu_{mor}^2)(1+\frac{16}{3}\omega_j)} & 0 \\ \frac{E_{mor}\nu_{mor}}{(1-\nu_{mor}^2)(1+\frac{16}{3}\omega_j)} & \frac{E_{mor}\left[1+\frac{16}{3}\omega_j(1-\nu_{mor}^2)\right]}{(1-\nu_{mor}^2)(1+\frac{16}{3}\omega_j)} & 0 \\ 0 & 0 & \frac{E_{mor}(2-\nu_{mor})}{2(1+\nu_{mor})\left[(2-\nu_{mor})+\frac{16}{3}\omega_j(1-\nu_{mor})\right]} \end{bmatrix} \cdot \begin{bmatrix} E_{11} \\ E_{22} \\ 2E_{12} \end{bmatrix} \quad (5.59)$$

For all finite elements referring to sane mortar, we employ (5.59) specialized for vanishing crack density, $\omega_j = 0$.

5.5.3 Finite Element model input

Upscaling elastic stiffness and fracture energy from nanoscopic solid C-S-H, see Eq. (5.1) and Table 5.1, up to the macroscale of mortar, follows Eqs. (5.8)–(5.21) and (5.31)–(5.35). Input values are the composition of mortar, see Table 5.2, as well as the degree of hydration ξ . The latter is set equal to 90 %, given that mortar specimens were tested 4 months after their production. For relevant volume fractions of gel, hydrates, and clinker, see Eqs. (5.17), (5.18), and (5.19), respectively. Notably, elastic properties and fracture energy change from scale to scale, but they stay on the same order of magnitude, see Table 5.5. The Weibull

Table 5.5: Upscaling of elastic and fracture energy from solid C-S-H up to macroscopic mortar.

	Solid C-S-H	C-S-H gel	Hydrate foam	Cement paste	Mortar	
Young's modulus	59.67*	28.04	22.32	23.79	41.13	GPa
Poisson's ratio	0.30*	0.26	0.26	0.26	0.22	–
Fracture energy	1.72**	0.85	0.66	0.75	1.24	J/m ²

*recalculated from k_{CSH} and μ_{CSH} given in Table 5.1

**taken from Bauchy et al. [11], see also Eq. (5.1)

modulus of mortar is set equal to the value considered for concrete: $m = 12$ (compare Table 5.6 with Table 5.4). The initial value of the characteristic crack

Table 5.6: Mortar properties considered for the re-analysis of the three-point bending tests performed by Le Bellego et al. [92].

property	value	source
maximum sand grain size	$d_{max} = 3.15$ mm	[93]
Young's modulus	$E_{mor} = 41.1$ GPa	upscaled (Table 5.5)
Poisson's ratio	$\nu_{mor} = 0.22$	upscaled (Table 5.5)
fracture energy	$G_{mor} = 1.24$ J/m ²	upscaled (Table 5.5)
Weibull modulus	$m = 12$	Table 5.4
tensile strength of mortar RVE	$\Sigma_{RVE}^{ult} = 5.77$ MPa	Eq. (5.61)
initial characteristic crack size	$a_{ini,RVE} = 1.27$ mm	Eq. (5.60)
dimensionless initial crack size	$a_{ini,RVE}/d_{max} = 0.402$	Table 5.4
damage evolution factor	$C = 0.396$	Table 5.4

size is obtained from multiplying the dimensionless quantity $(a_{ini,RVE}/d_{max}) = 0.402$ (compare Table 5.6 with Table 5.4) with the maximum sand grain size $d_{max} = 3.15$ mm resulting in

$$a_{ini,RVE} = 1.27 \text{ mm} \quad (5.60)$$

The tensile strength of the smallest cubic mortar RVE, with volume $V_{RVE} = (3 d_{max})^3 = 0.84 \text{ cm}^3$, see Eq. (5.43) and Table 5.6, is obtained as

$$\Sigma_{RVE}^{ult} = \sqrt{\frac{G_{mor} E_{mor} \pi}{4(1 - \nu_{mor}^2) a_{ini,RVE}}} = 5.77 \text{ MPa} \quad (5.61)$$

The elementary damage propagation law for each Finite Element reads as

$$\Sigma_{11}(\omega_j) \leq \sqrt{\frac{G_{mor} E_{mor} \pi}{4(1 - \nu_{mor}^2) d_{max}} \left[\frac{a_{ini,RVE}}{d_{max}} \left(\frac{V}{V_{RVE}} \right)^{\frac{2}{m}} + C \omega_j \right]^{-1}} \quad (5.62)$$

In Eq. (5.62), V denotes a subvolume of the specimen, in which virtually the same nominal tensile stress prevails. In accordance with the separation-of-scales principle, we set this volume equal to the one of a cuboid exhibiting a height of $3 d_{max}$, a width of $3 d_{max}$, and a depth of 40 mm (Fig. 5.12),

$$V = t (3 d_{max})^2 = 3.57 \text{ cm}^3 \quad (5.63)$$

5.5.4 Sequential elastic FE analyses technique with incremental increase of damage

We employ sequential elastic FE analyses with incremental increase of damage, as reported by Rots et al. [134]. In the first simulation, all elementary crack density parameters are set equal to zero, except for the two elements representing the notch. They exhibit a crack density of 10^4 (see above). A vertical displacement $u = 1 \text{ mm}$ is imposed to the top surface at the axis of symmetry of the Finite Element model. The resulting stresses, strains, and displacements are amplified by a proportionality factor obtained from dividing the maximum horizontal normal stress Σ_{11} by the initial tensile strength of the material, such that the damage propagation law is just satisfied in the most heavily loaded finite element of the row directly attached to the symmetry axis. The corresponding values for the external loading and the deflection at the beam center are stored. For the subsequent simulation, the crack densities of the above-identified most heavily loaded finite element and of its direct horizontal neighbor are increased incrementally: in case the two finite elements were undamaged before, the crack density parameter is set equal to 0.00375, resulting in an effective stiffness reduction by some 1.8 percent, see Eq. (5.57) specified for ν_{mor} according to Table 5.6. In case

the two elements were already damaged before, the crack density parameter is increased by multiplying the current crack density with a damage magnification factor $m_f = 2^{1/8}$. Thereafter, the same FE model is used for another linear elastic simulation where the load intensity factor is computed from the current (rather than the undamaged) tensile strength, in order to identify at which element the crack density will be amplified next. This procedure results in a stepwise increase of damage from simulation to simulation, and provides ordinates of the sought force-displacement diagram.

5.5.5 Comparison of model predictions with experimental data

Numerical simulations of three-point bending tests were carried out to reproduce the experiments by Le Bellego et al. [92]. The results for all three specimen sizes agree very well with the measurements in terms of ultimate forces, midspan deflections, and shape of the post peak regime, see Fig. 5.14 and Table 5.7. The quadratic correlation coefficients R^2 amount to $R_A^2 = 96.2\%$ for the series A, $R_B^2 = 99.2\%$ for series B, and $R_C^2 = 92.5\%$ for series C.

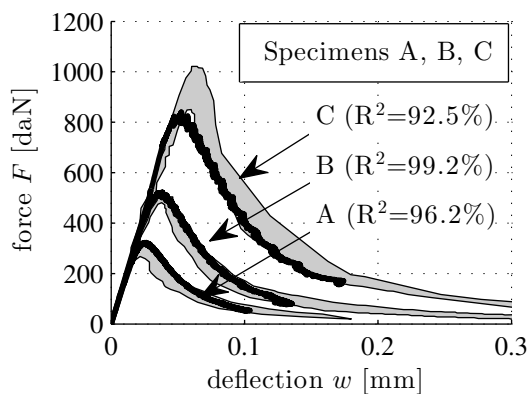


Figure 5.14: Force-deflection diagrams: shaded areas cover measurement data of Le Bellégo et al. [92], obtained from at least 4 tests for each specimen size; black solid lines represent the model prediction.

Since the model has survived a nontrivial attempt of falsification, it is strongly corroborated [126]. This underlines the quality of the developed multiscale model for tensile strength and tensile softening of cementitious materials, bridging all the scales from nanoscopic C-S-H to the macroscopic scale of a classical lab test.

Table 5.7: Numerical values obtained from simulating with the FE mesh shown in Fig. 5.13, with numerical inputs listed in Table 5.6.

size	D [m]	F^{elast} [daN]	F^{ult} [daN]	R^2 [%]
A	0.08	152.5	321.0	96.2
B	0.16	275.8	518.0	99.2
C	0.32	509.3	830.0	92.5

5.6 Discussion

In this paper, we have upscaled the fracture properties of concrete, starting from the fundamental level of C-S-H, where the fracture energy became recently accessible through molecular dynamics simulations [11]. Thereby, the fracture energy enters the resistance side of damage propagation law arising from thermodynamics considerations, while the fracture driving force follows from derivation of the elastic stiffness with respect to the crack density parameter. While the elastic stiffness follows well-validated multiscale micromechanics models [179, 180], two dimensionless quantities governing the crack propagation characteristics are determined from van Mier and van Vliet's size-effect studies in direct tension. The resulting model, when fed into Finite Element analyses of notched beams, delivers very good predictions of experimental results which are independent of those used for model development.

It is very instructive to discuss these novel developments in light of two topics which have been of continued interest in the engineering mechanics and structural engineering communities, namely (i) the fracture energy as used in so-called smeared crack approaches, and (ii) the scaling laws for the nominal ultimate structural stress level encountered with quasi-brittle materials.

While our mortar- or concrete-specific fracture energy ranges from 1 to 2 J/m² (see Tables 5.5 and 5.3), classical smeared crack approaches typically employ fracture energy values ranging from 100 to 200 J/m² [156, 51]. This seeming discrepancy can be explained as follows. In smeared crack approaches, the energy dissipated during a tension test is divided by the area of the final macrocrack. This way, the sum of all *actually* formed crack areas is underestimated significantly. In reality, namely, not only one crack forms during tensile failure of mortars and concretes, but many cracks of different sizes interact inside the damage accumulation zone, and not all microcracks coalesce into the final macrocrack, but most of them actually run into crack shielding, i.e. they return to stationarity and close

during failure of the material. These processes make is practically impossible to quantify, after a tension test, the sum of all actually formed crack areas. In contrast to the classical smeared crack approaches restricting the crack area to one single microcrack, our approach introduces multiple RVEs of cracked mortar or concrete, containing many cracks of different sizes; hence, a much larger crack area is considered. In order to estimate the total size of the latter, we consider the equivalence of the finally dissipated energy in both approaches, the classical smeared crack model and the presented multiscale micromechanical model,

$$G_{smeared} A_{macro} = G_{mat} A_{tot} \quad (5.64)$$

with $G_{smeared}$ as the fracture energy employed in smeared crack models, A_{macro} as the crack area of the single macrocrack, A_{tot} as the area of all cracks in the damage accumulation zone, and G_{mat} as the coverd-sphered-model-derived fracture energy at the mortar or concrete level, respectively, i.e. G_{mor} or G_{con} according to Eq.(5.34) or (5.35). Eq. (5.64) readily delivers that

$$\frac{G_{smeared}}{G_{mat}} = \frac{A_{tot}}{A_{macro}} \approx 100 \quad (5.65)$$

i.e. the total crack area is about one hundred times that of the macrocrack at the center of the damage accumulation zone.

As regards structural fracture scaling, it is instructive to relate the ultimate forces of Figure 5.14 to nominal stresses reading as [12]

$$\sigma_{Nu} = 4.5 \frac{F^{ult}}{t D} \quad (5.66)$$

These nominal stress values turn out to nicely follow Bazant's size effect law [12, 14]

$$\sigma_{Nu} = \frac{B f'_t}{\sqrt{1 + D/D_0}} \quad (5.67)$$

with the values B and D_0 as given in Table 5.8 for $w/c = 0.4$, obtained from a nonlinear regression based on the Levenberg-Marquardt algorithm, while computing f'_t from Eq. (5.54) with $V = V_{RVE}$ and $\omega = 0$. Repeating the same exercise for a water-to-cement ratio of $w/c = 0.50$ delivers virtually the same values for B and D_0 , see the right-hand side of Table 5.8. This clearly shows that B and

Table 5.8: Results of optimal B and D_0 parameters.

	$w/c = 0.40$	$w/c = 0.50$
$s/c = 2.16$	$B = 1.06, D_0 = 91.42 \text{ mm}$	$B = 1.08, D_0 = 90.09 \text{ mm}$
$s/c = 4.80$	$B = 1.02, D_0 = 86.42 \text{ mm}$	$B = 1.01, D_0 = 91.75 \text{ mm}$

D_0 are truly structural parameters which are virtually independent of the material composition. The latter, in turn, is strongly governing the tensile material strength, f'_t .

5.7 Conclusions

Here, it was shown that macroscopic (“effective” or “homogenized”) elastic stiffness properties and fracture energy of mortars and concretes are strongly related (i) to the corresponding mechanical properties of nanoscopic C-S-H, and (ii) to the scale-separated hierarchical organization of cementitious materials. Macroscopic elastic stiffness, for instance, results from (i) elastic properties of all microstructural constituents, (ii) their volume fractions, (iii) their characteristic shapes, and (iv) their characteristic interaction: either interaction between a continuous matrix and embedded inclusions, or direct mutual interaction between material constituents, resulting from a highly disordered “polycrystalline” arrangement. The macroscopic fracture energy, in turn, results from (i) the fracture energy of solid C-S-H, (ii) the volume fractions of all microstructural constituents, and (iii) their characteristic interaction, implying that cracks propagate along pathways with minimum material resistance, i.e. either through pores or around strong obstacles such as cement clinker, sand, and aggregate grains. The presented homogenization models allow for quantifying of elastic stiffness properties and fracture energy of mortars and concretes, based on the following three types of well-defined input parameters:

1. The initial material composition, quantified in terms of mass ratios between water, cement, sand, and aggregates, see van Vliet and van Mier [161] and Le Bellego et al. [93], and Table 5.2.
2. The material maturity, quantified in terms of hydration degree.
3. The grain size distribution of sand and aggregates, quantified in terms of the maximum grain diameter.

Homogenized properties intervene in a new microfracturemechanics damage model for damage accumulation zones in concrete and mortars. The model includes size effect and it allows for predicting the tensile strength of mortars and concretes as well as their tension-induced softening in the post-peak regime, characterized by the formation of a damage accumulation zone containing interacting cracks of different sizes.

Predictive capabilities of the *fully developed* model (i.e. of the model which does not contain any fitting parameters) were tested by predicting the expected behavior of a size-effect study consisting of three-point bending tests on mortar prisms, carried out by Le Bellego et al. [93]. It is important to emphasize that the direct tension tests on concretes considered for model development, on the one hand, and the three-point bending tests on mortars considered for model validation, on the other hand, differed in terms of raw materials, mix design, specimen shape, boundary conditions, as well as in terms of the labs, testing machines, and scientists who carried out the tests. Consequently, the chosen strategy for the assessment of the predictive capabilities represents – in the spirit of Karl Popper’s falsificationism [126] – a serious, nontrivial, and strictly quantitative attempt to falsify the developed model. It is remarkable that the model survived the falsification attempt, as is underlined by model predictions which agree very well with the observations of Le Bellego et al. [93]. We may conclude in the wording of Popper [126] that the model is strongly corroborated, which underlines that tension-induced failure of macroscopic structures made of cementitious materials can be explained based on elastic and fracture properties of nanoscopic C-S-H.

Acknowledgments

Funding of the first author provided by the industrial-academic nanoscience research network for sustainable cement and concrete “NANOCEM” (<http://www.nanocem.org>) within the framework of Core Project 10 entitled “Micromechanical Analysis of Blended Cement-Based Composites” is gratefully acknowledged. Interesting discussions with Dr. Klaus-Alexander Rieder, WR Grace / GCP Applied Technologies, are gratefully acknowledged.

Nomenclature

$\Delta\ell(\omega)$	total elongation of cuboid
ℓ	characteristic size of RVE
ℓ_{cp}	characteristic size of cement paste
ℓ_{gel}	characteristic size of hydrate gel
ℓ_{hf}	characteristic size of hydrate foam
$\mathbf{1}$	second-order identity tensor
Σ	macroscopic uniform stress
\mathbf{E}	macroscopic strain
\mathcal{G}_{df}	driving force for crack propagation
\mathcal{G}_{res}	resistance against crack propagation
\mathcal{L}	characteristic size of stress and strain fluctuations
\mathbf{A}_i	fourth-order strain concentration tensor of material phase i
\mathbf{C}_∞	fourth-order stiffness tensor of the infinite matrix in the Eshelby problems
\mathbf{C}_{dam}	fourth-order stiffness tensor of damaged material
\mathbf{C}_{gel}	fourth-order stiffness tensor of hydrate gel
\mathbf{C}_{hf}	fourth-order stiffness tensor of hydrate foam
\mathbf{C}_{hom}	fourth-order stiffness tensor of homogenized material
\mathbf{C}_i	fourth-order stiffness tensor of material phase i
\mathbf{C}_{mat}	fourth-order stiffness tensor of undamaged material
\mathbf{C}_{pore}	fourth-order stiffness tensor of porosity

\mathbb{I}	fourth-order unity tensor
\mathbb{I}_{dev}	deviatoric part of the fourth-order unity tensor
\mathbb{I}_{vol}	volumetric part of the fourth-order unity tensor
\mathbb{P}_i	fourth-order Hill tensor of material phase i
\mathbb{S}_i	fourth-order Eshelby tensor of material phase i
\mathbb{T}	fourth-order tensor accounting for the anisotropic damage effect of parallel cracks
μ_∞	shear modulus of the infinite matrix in the Eshelby problems
μ_{agg}	shear modulus of quartz aggregates
μ_{clin}	shear modulus of clinker
μ_{CSH}	shear modulus of C-S-H
μ_{pore}	shear modulus of pore
μ_{sand}	shear modulus of quartz sand
ν_{con}	Poisson's ratio of concrete
ν_{mat}	Poisson's ratio of the isotropic matrix material
ν_{mor}	Poisson's ratio of mortar
Ω	volume of damage accumulation zone
ω	Budiansky and O'Connell's crack density parameter
ϕ	standard variable for dissipation, with dimension energy per time per volume
ρ_{agg}	mass density of aggregates
ρ_{clin}	mass density of clinker
ρ_{H_2O}	mass density of water
ρ_{sand}	mass density of sand
Σ^{ult}	ultimate uniaxial tensile stress
Σ_{33}	uniaxial tensile stress in the \underline{e}_3 -direction

σ_{Nu}	nominal ultimate structural stress
Σ_{RVE}^{ult}	ultimate tensile stress of RVE
ξ	degree of hydration of ordinary Portland cement
a	representative crack size
a/c	initial aggregate-to-cement mass ratio
A_i	area of the i -th real crack
a_i	radius of i -th crack
$a_{ini,RVE}$	initial representative crack size in the smallest RVE
a_{ini}	initial value of the representative crack size
A_{macro}	crack area of a single macrocrack
A_{tot}	area of all cracks in the damage accumulation zone
B	fitting parameter of size effect fitting function
C	slope quantity
D	characteristic size of the structure
d	characteristic size of inhomogeneity
D_0	fitting parameter of size effect fitting function
d_{max}	maximum aggregate size
E_{con}	elastic modulus of concrete
E_{daz}	elastic modulus of damage accumulation zone in direction normal to the crack plane
E_{mat}	elastic modulus of material
E_{mor}	elastic modulus of mortar
$F(\omega)$	external tensile force acting on cuboid
f'_t	tensile strength
f_{agg}^{con}	volume fraction of aggregates within RVE of concrete
f_{clin}^{cp}	volume fraction of clinker within RVE of cement paste

f_{core}	volume fraction of core in covered sphere model
f_{cover}	volume fraction of cover in covered sphere model
f_{cp}^{mor}	volume fraction of cement paste within RVE of mortar
f_{CSH}^{gel}	volume fraction of C-S-H within RVE of hydrate gel
f_{gel}^{hf}	volume fraction of hydrate gel within RVE of hydrate foam
f_{gpor}^{gel}	volume fraction of gel pores within RVE of hydrate gel
f_{hf}^{cp}	volume fraction of hydrate foam within RVE of cement paste
f_{mor}^{con}	volume fraction of mortar within RVE of concrete
f_{pore}^{hf}	volume fraction of capillary porosity within RVE of hydrate foam
f_{sand}^{mor}	volume fraction of sand within RVE of mortar
G_{con}	fracture energy of concrete
G_{cover}	fracture energy of cover material in covered sphere model
G_{cp}	fracture energy of cement paste
G_{CSH}	fracture energy of C-S-H
G_{gel}	fracture energy of hydrate gel
G_{hf}	fracture energy of hydrate foam
G_{hom}	fracture energy of homogenized material
G_{mat}	fracture energy of material
G_{mor}	fracture energy of mortar
$G_{smeared}$	fracture energy employed in smeared crack models
k_{∞}	bulk modulus of the infinite matrix in the Eshelby problems
k_{agg}	bulk modulus of quartz aggregates
k_{clin}	bulk modulus of clinker
k_{CSH}	bulk modulus of C-S-H
$K_{Ic,mat}$	mode I fracture toughness of material
k_{pore}	bulk modulus of pore

k_{sand}	bulk modulus of quartz sand
L_s	characteristic size of dog bone-shaped specimens
m	Weibull modulus
m_f	damage magnification factor
r_{core}	radius of core in covered sphere model
r_{cover}	radius of cover in covered sphere model
s/c	initial sand-to-cement mass ratio
t	thickness of sample
V	volume of concrete body
V_{RVE}	smallest cubic RVE
w/c	initial water-to-cement mass ratio
f_i	volume fraction of material phase i
RVE	abbreviation for “representative volume element”

Conclusions and further research

The following research objectives were accomplished in the present thesis:

Chapter 1

- Microstructural phase assemblages of OPC and four blended cement-based pastes were obtained, documenting the point-wise evolution of material phases in time.
- Evolution of stiffness, compressive and tensile strength of investigated cement pastes was measured, starting one day after production up to 91 days.
- “CemBase” database was established. It contains detailed microstructural information from investigated pastes along with all measured results from the mechanical experiments carried out within this thesis. In addition, “CemBase” contains experimental data obtained from available literature.

Chapter 2

- A novel test setup for measuring unloading modulus of cement pastes is developed. It includes overdetermined deformation measurements using five Linear Variable Differential Transducers which minimize the eccentricity of the applied loading.

Chapter 3

- Four-level multiscale model for compressive strength of blended cement pastes is developed based on finite element homogenization. It uses C-S-H/space ratio as the primary microstructural descriptor and introduces a spatial C-S-H gradient, mimicking nonuniform distribution between individual grains.
- Most fundamental parameter for compressive/tensile strength of cement paste is the amount of C-S-H. Further factors are the volume of entrapped/entrained air and spatial gradient of C-S-H.
- Densification of the microstructure by forcing C-S-H to precipitate uniformly leads to increased compressive strength.

Chapter 4

- Hierarchical multiscale model for blended mortars is developed based on continuum micromechanics. The model accounts for stress peaks in representative volume element of cement paste, which are attached to the surface of sand grains, uses Mohr-Coulomb failure criterion for hydrates and extends the microstructural representation of hydrates from one *average* type towards individual types of hydrates.
- Uses strain energy-related (“higher-order”) stress averages to account for stress concentration from cement paste into the hydrate needle, because hydrate failure is very likely related to energy-driven shear cracking at nanometric scales inside hydrate needles.
- Strength predictions for blended mortars appear to be significantly more sensitive to the microstructural representation of hydrates either in form of just one average hydrate type or in form of several different types of hydrates. The latter more detailed representation appears to deliver better strength predictions.
- Finely ground inert fillers (quartz and limestone) exhibit a significant filler effect, i.e. they accelerate hydration kinetics and act as strength-increasing reinforcements of the hydrate foam.

- Supplementary cementitious materials (slag and fly ash) increase of the strength of hydrates which represent the weakest links of the microstructure.

Chapter 5

- Macroscopic (“effective” or “homogenized”) elastic stiffness properties and fracture energy of mortars and concretes are strongly related (i) to the corresponding mechanical properties of nanoscopic C-S-H, and (ii) to the scale-separated hierarchical organization of cementitious materials.
- The macroscopic fracture energy results from (i) the fracture energy of solid C-S-H, (ii) the volume fractions of all microstructural constituents, and (iii) their characteristic interaction, implying that cracks propagate along pathways with minimum material resistance, i.e. either through pores or around strong obstacles such as cement clinker, sand, and aggregate grains.
- The *covered sphere approach* is introduced to upscale fracture energy from nanoscopic solid C-S-H up to macroscopic mortar or concrete.
- A microfracturemechanics damage model for damage accumulation zones in concrete and mortars is introduced. The model includes size effect and it allows for predicting the tensile strength of mortars and concretes as well as their tension-induced softening in the post-peak regime, characterized by the formation of a damage accumulation zone containing interacting cracks of different sizes.

Further research

The following topics open interesting research opportunities:

- Recommendations and guidelines for testing compressive strength of cement pastes should be developed to minimize scatter of results.
- Experimental evidence on how C-S-H density distribution influences compressive strength is required.
- Scaling of strength for C-S-H: recent micro-bending tests on hydrated cement pastes identified tensile strength of inner product as high as 700

MPa [111]. Such strength is higher than those predicted by current models.

- Multiscale models need further elaboration for systems beyond the OPC basis producing C-S-H. Particularly alkali-activated systems (N-A-S-H gel), calcium aluminate cements (C-A-H gel), oxychloride, or phosphatic cements are of interest.
- Extension of model for tensile failure towards consideration of blended cements.
- Role of interfaces should be assessed to further improve model predictions.

Bibliography

- [1] A. C. I. A. C. 318. ACI 318-14: Building code requirements for structural concrete, 2014.
- [2] P. Acker. Micromechanical analysis of creep and shrinkage mechanisms. In F.-J. Ulm, Z. Bažant, and F. Wittmann, editors, *Creep, Shrinkage and Durability Mechanics of Concrete and other Quasi-brittle Materials*, 6th International Conference CONCREEP@MIT, pages 15–26, Amsterdam, 2001. Elsevier.
- [3] T. J. Ahrens, editor. *Mineral Physics & Crystallography: A Handbook of Physical Constants*. American Geophysical Union, 1995.
- [4] A. Allen, J. Thomas, and H. Jennings. Composition and density of nanoscale calcium-silicate-hydrate in cement. *Nature Materials*, 6(4):311–316, 2007.
- [5] M. Amieur. *Etude numérique et expérimentale des effets d'échelle et de conditions aux limites sur des éprouvettes de béton n'ayant pas le volume représentatif [Numerical and experimental study of scale effects and boundary conditions on concrete specimens having no representative volume]*. Doctoral thesis n°1256, École Polytechnique Fédérale de Lausanne (EPFL), Lausanne, 1994. In French. Available online at: <https://infoscience.epfl.ch/record/31734?ln=fr>.
- [6] ASTM. *Standard Test Method for Splitting Tensile Strength of Cylindrical Concrete Specimens*.
- [7] G. I. Barenblatt. *Scaling, Self-Similarity, and Intermediate Asymptotics*. Cambridge University Press, Cambridge, England, 1st edition, 1996.

-
- [8] A. J. C. Barré de Saint Venant. Mémoire sur la torsion des prismes, [Memory on twisting prisms], Mémoires des Savants étrangers [Memoires of foreign scholars]. *Comptes rendues de l'Académie des Sciences*, 14:233–560, 1855.
- [9] B. Bary. Estimation of poromechanical and thermal conductivity properties of unsaturated isotropically microcracked cement pastes. *International Journal for Numerical and Analytical Methods in Geomechanics*, 35(14):1560–1586, 2011.
- [10] M. Bauchy, M. Abdolhosseini Qomi, C. Bichara, F.-J. Ulm, and R. Pellenq. Nanoscale structure of cement: viewpoint of rigidity theory. *The Journal of Physical Chemistry C*, 118(23):12485–12493, 2014.
- [11] M. Bauchy, H. Laubie, M. A. Qomi, C. Hoover, F.-J. Ulm, and R.-M. Pellenq. Fracture toughness of calcium–silicate–hydrate from molecular dynamics simulations. *Journal of Non-Crystalline Solids*, 419:58–64, 2015.
- [12] Z. P. Bažant. Size Effect in Blunt Fracture: Concrete, Rock, Metal. *Journal of Engineering Mechanics*, 110(4):518–535, 1984.
- [13] Z. P. Bažant. Scaling of quasibrittle fracture: hypotheses of invasive and lacunar fractality, their critique and Weibull connection. *International Journal of Fracture*, 83(1):41–65, 1997.
- [14] Z. P. Bažant. Size effect on structural strength: a review. *Archive of Applied Mechanics*, 69(9-10):703–725, 1999.
- [15] Z. P. Bažant and B. H. Oh. Crack band theory for fracture of concrete. *Matériaux et Construction*, 16(3):155–177, 1983.
- [16] Z. P. Bažant and G. Pijaudier-Cabot. Measurement of Characteristic Length of Nonlocal Continuum. *Journal of Engineering Mechanics*, 115(4):755–767, 1989.
- [17] Z. P. Bažant and J. Planas. *Fracture and Size Effect in Concrete and Other Quasibrittle Materials*. CRC Press, 1998.
- [18] J. Beaudoin and V. Ramachandran. A new perspective on the hydration characteristics of cement phases. *Cement and Concrete Research*, 22(4):689–694, 1992.

- [19] D. P. Bentz. CEMHYD3D: A Three-Dimensional Cement Hydration and Microstructure Development Modeling Package. Version 3.0. Technical report, NIST Building and Fire Research Laboratory, Gaithersburg, Maryland, 2005.
- [20] D. P. Bentz, S. Mizell, S. Satterfield, J. Devaney, W. George, P. Ketcham, J. Graham, and J. Porterfield. The Visible Cement Data Set. *Journal of Research of the National Institute of Standards and Technology*, 107(2):137–148, 2002. <http://visiblecement.nist.gov>.
- [21] Y. Benveniste. A new approach to the application of Mori-Tanaka’s theory in composite materials. *Mechanics of Materials*, 6(2):147–157, 1987.
- [22] O. Bernard, F.-J. Ulm, and E. Lemarchand. A multiscale micromechanics-hydration model for the early-age elastic properties of cement-based materials. *Cement and Concrete Research*, 33(9):1293–1309, 2003.
- [23] S. Bishnoi and K. L. Scrivener. Studying nucleation and growth kinetics of alite hydration using uic. *Cement and Concrete Research*, 39(10):849–860, 2009.
- [24] S. Bishnoi and K. L. Scrivener. uic: A new platform for modelling the hydration of cements. *Cement and Concrete Research*, 39(4):266–274, 2009.
- [25] V. Bonavetti, V. Rahhal, and E. Irassar. Studies on the carboaluminate formation in limestone filler-blended cements. *Cement and Concrete Research*, 31(6):853–859, 2001.
- [26] C. Boulay, S. Staquet, M. Azenha, A. Deraemaeker, M. Crespini, J. Carette, J. Granja, B. Delsaute, C. Dumoulin, and Karaikos. Monitoring elastic properties of concrete since very early age by means of cyclic loadings, ultrasonic measurements, natural resonant frequency of composite beam (EMM-ARM) and with smart aggregates. In *Proceedings of the VIII International Conference on Fracture Mechanics of Concrete and Concrete Structures FraMCoS-8*, 2013. Available online at: <http://framcos.org/FraMCoS-8/p570.pdf> (last access: September 17 2014).
- [27] C. Boulay, S. Staquet, B. Delsaute, J. Carette, M. Crespini, O. Yazoghli-Marzouk, E. Merliot, and S. Ramanich. How to monitor the modulus of elasticity of concrete, automatically since the earliest age? *Materials and Structures/Materiaux et Constructions*, 47(1-2):141–155, 2014.

-
- [28] A. Boumiz, C. Vernet, and F. Cohen Tenoudji. Mechanical properties of cement pastes and mortars at early ages. *Advanced Cement Based Materials*, 3(3-4):94–106, 1996.
- [29] J. R. Bristow. Microcracks, and the static and dynamic elastic constants of annealed and heavily cold-worked metals. *British Journal of Applied Physics*, 11(2):81–85, 1960.
- [30] B. Budiansky. On the elastic moduli of some heterogeneous materials. 13(4):223–227, 1965.
- [31] J. Byfors. Plain concrete at early ages. Technical report, Swedish Cement and Concrete Research Institute, Stockholm, Sweden, 1980.
- [32] J. M. Carcione. Wave propagation in anisotropic, saturated porous media: Plane-wave theory and numerical simulation. *The Journal of the Acoustical Society of America*, 99(5):2655–2666, 1996.
- [33] J. M. Carcione. *Wave fields in real media : wave propagation in anisotropic, anelastic, porous and electromagnetic media*. Handbook of geophysical exploration. Pergamon, Amsterdam, London, New York, 2007.
- [34] A. Carpinteri. Fractal nature of material microstructure and size effects on apparent mechanical properties. *Mechanics of Materials*, 18(2):89–101, 1994. Special Issue on Microstructure and Strain Localization in Geomaterials.
- [35] A. Carpinteri, B. Chiaia, and G. Ferro. Size effects on nominal tensile strength of concrete structures: multifractality of material ligaments and dimensional transition from order to disorder. *Materials and Structures*, 28(6):311–317, 1995.
- [36] A. Carpinteri and G. Ferro. Size effects on tensile fracture properties: a unified explanation based on disorder and fractality of concrete microstructure. *Materials and Structures*, 27(10):563–571, 1994.
- [37] R. Chamrova. *Modelling and Measurement of Elastic Properties of Hydrating Cement Paste*. PhD thesis, École Polytechnique Fédéral de Lausanne, Lausanne, Switzerland, 2010.

- [38] P. Chindaprasirt, C. Jaturapitakkul, and T. Sinsiri. Effect of fly ash fineness on compressive strength and pore size of blended cement paste. *Cement and Concrete Composites*, 27(4):425–428, 2005.
- [39] P. Chindaprasirt, C. Jaturapitakkul, and T. Sinsiri. Effect of fly ash fineness on microstructure of blended cement paste. *Construction and Building Materials*, 21(7):1534–1541, 2007.
- [40] O. Chowaniec. *Limestone Addition in Cement*. PhD thesis, École Polytechnique Fédérale de Lausanne, 2012.
- [41] G. Constantinides and F.-J. Ulm. The effect of two types of C-S-H on the elasticity of cement-based materials: Results from nanoindentation and micromechanical modeling. *Cement and Concrete Research*, 34(1):67–80, 2004.
- [42] G. Constantinides and F.-J. Ulm. The nanogranular nature of C-S-H. *Journal of the Mechanics and Physics of Solids*, 55(1):64–90, 2007.
- [43] C. Coulomb. Sur une application des règles de maximis & minimis à quelques problèmes de statique, relatifs à l’architecture [On the application of rules of maxima and minima in problems of statics, related to architecture]. *Mémoires de Mathématiques et de Physique, Académie Royale des Sciences, Paris*, pages 343–382, 1776. In French.
- [44] G. Cusatis, Z. P. Bažant, and L. Cedolin. Confinement-Shear Lattice Model for Concrete Damage in Tension and Compression: II. Computation and Validation. *Journal of Engineering Mechanics*, 129(12):1449–1458, 2003.
- [45] G. De Schutter and L. Taerwe. Degree of hydration-based description of mechanical properties of early age concrete. *Materials and Structures/Materiaux et Constructions*, 29(190):335–344, 1996.
- [46] V. Deudé, L. Dormieux, D. Kondo, and S. Maghous. Micromechanical Approach to Nonlinear Poroelasticity: Application to Cracked Rocks. *Journal of Engineering Mechanics*, 128(8):848–855, 2002.
- [47] L. Dormieux, D. Kondo, and F.-J. Ulm. A micromechanical analysis of damage propagation in fluid-saturated cracked media. *Comptes Rendus Mécanique*, 334(7):440–446, 2006.

-
- [48] L. Dormieux, D. Kondo, and F.-J. Ulm. *Microporomechanics*. John Wiley & Sons, 2006.
- [49] L. Dormieux, A. Molinari, and D. Kondo. Micromechanical approach to the behavior of poroelastic materials. *Journal of the Mechanics and Physics of Solids*, 50(10):2203–2231, 2002.
- [50] W. Drugan and J. Willis. A micromechanics-based nonlocal constitutive equation and estimates of representative volume element size for elastic composites. *Journal of the Mechanics and Physics of Solids*, 44(4):497–524, 1996.
- [51] R. A. Einfeld and M. S. Velasco. Fracture parameters for high-performance concrete. *Cement and Concrete Research*, 36(3):576–583, 2006.
- [52] J. D. Eshelby. The Determination of the Elastic Field of an Ellipsoidal Inclusion, and Related Problems. *Proceedings of the Royal Society of London*, 241(1226):376–396, 1957.
- [53] D. K. Felbeck and A. G. Atkins. *Strength and Fracture of Engineering Solids*. New Jersey, Prentice-Hall, 1984.
- [54] R. Feldman, G. Carette, and V. Malhotra. Studies on mechanics of development of physical and mechanical properties of high-volume fly ash-cement pastes. *Cement and Concrete Composites*, 12(4):245–251, 1990.
- [55] I. Fischer, B. Pichler, E. Lach, C. Terner, E. Barraud, and F. Britz. Compressive strength of cement paste as a function of loading rate: experiments and engineering mechanics analysis. *Cement and Concrete Research*, 2014. Accepted for publication.
- [56] E. C. for Standardization. EN 1992 Eurocode 2 : Design of concrete structures, 2004.
- [57] A. Fritsch, L. Dormieux, and C. Hellmich. Porous polycrystals built up by uniformly and axisymmetrically oriented needles: homogenization of elastic properties. *Comptes Rendus Mécanique*, 334(3):151–157, 2006.
- [58] F. Ganneau, F.-J. Ulm, J. Gondzio, and E. Garboczi. An algorithm for computing the compressive strength of heterogeneous cohesive-frictional materials – Application to cement paste. *Computers and Geotechnics*, 34(4):254–266, 2007. Chemo-Mechanical Interaction in Geomaterials.

- [59] H. Gao. Application of fracture mechanics concepts to hierarchical biomechanics of bone and bone-like materials. *International Journal of Fracture*, 138(1-4):101–137, 2006.
- [60] E. Gartner. Industrially interesting approaches to “low-CO₂” cements. *Cement and Concrete Research*, 34(9):1489–1498, 2004.
- [61] E. M. Gartner and D. E. Macphee. A physico-chemical basis for novel cementitious binders. *Cement and Concrete Research*, 41(7):736–749, 2011.
- [62] T. Ghebrab and P. Soroushian. Mechanical Properties of Hydrated Cement Paste: Development of Structure-property Relationships. *International Journal of Concrete Structures and Materials*, 4(1):37–43, 2010.
- [63] J. Granja, M. Azenha, C. De Sousa, and C. Ferreira. Comparison between different experimental techniques for stiffness monitoring of cement pastes. *Journal of Advanced Concrete Technology*, 12(2):46–61, 2014.
- [64] P. Grassl, D. Grégoire, L. R. Solano, and G. Pijaudier-Cabot. Meso-scale modelling of the size effect on the fracture process zone of concrete. *International Journal of Solids and Structures*, 49(13):1818–1827, 2012.
- [65] P. Grassl and M. Jirásek. Meso-scale approach to modelling the fracture process zone of concrete subjected to uniaxial tension. *International Journal of Solids and Structures*, 47(7-8):957–968, 2010.
- [66] A. Griffith. Theory of rupture. In C. Biezeno and J. Burgers, editors, *First International Congress for Applied Mechanics*, pages 55–63, Delft, 1924.
- [67] C.-J. Haecker, E. Garboczi, J. Bullard, R. Bohn, Z. Sun, S. Shah, and T. Voigt. Modeling the linear elastic properties of Portland cement paste. *Cement and Concrete Research*, 35(10):1948–1960, 2005.
- [68] C. Hellmich and H. Mang. Shotcrete elasticity revisited in the framework of continuum micromechanics: From submicron to meter level. *Journal of Materials in Civil Engineering (ASCE)*, 17(3):246–256, 2005.
- [69] R. Helmuth and D. Turk. Elastic moduli of hardened Portland cement and tricalcium silicate pastes: Effect of porosity. *Symposium on structure of Portland cement paste and concrete*, 90:135–144, 1966. Highway Research Board, Washington, DC.

-
- [70] A. Hershey. The elasticity of an isotropic aggregate of anisotropic cubic crystals. *Journal of Applied Mechanics (ASME)*, 21:226—240, 1954.
- [71] R. Hill. A self-consistent mechanics of composite materials. 13(4):213–222, 1965.
- [72] M. Hlobil, V. Šmilauer, and G. Chanvillard. Micromechanical multiscale fracture model for compressive strength of blended cement pastes. *Cement and Concrete Research*, 83:188–202, 2016.
- [73] F. Holuj, M. Drozdowski, and M. Czajkowski. Brillouin spectrum of Ca(OH)₂. *Solid State Communications*, 56(12):1019–1021, 1985.
- [74] M. Irfan-ul Hassan, M. Königsberger, R. Reihnsner, B. Pichler, and C. Hellmich. How water-aggregate interactions affect concrete creep: a multiscale analysis. *submitted to the Journal of Nanomechanics and Micromechanics*, 2014.
- [75] H. Jennings. Model for the microstructure of calcium silicate hydrate in cement paste. *Cement and Concrete Research*, 30(1):101–116, 2000.
- [76] H. M. Jennings. A model for the microstructure of calcium silicate hydrate in cement paste. 30(6):101–116, 2000.
- [77] H. M. Jennings. Refinements to colloid model of C-S-H in cement: CM-II. 38(3):275–289, 2008.
- [78] M. Jirásek and Z. P. Bažant. *Inelastic analysis of structures*. John Wiley & Sons, Ltd., 2002.
- [79] M. Jirásek and S. Rolshoven. Localization properties of strain-softening gradient plasticity models. Part I: Strain-gradient theories. *International Journal of Solids and Structures*, 46(11–12):2225–2238, 2009.
- [80] T. Kanit, S. Forest, I. Galliet, V. Mounoury, and D. Jeulin. Determination of the size of the representative volume element for random composites: Statistical and numerical approach. *International Journal of Solids and Structures*, 40:3647–3679, 2003.
- [81] S.-M. Kim and R. K. A. Al-Rub. Meso-scale computational modeling of the plastic-damage response of cementitious composites. *Cement and Concrete Research*, 41(3):339–358, 2011.

-
- [82] C. Kohlhauser and C. Hellmich. Ultrasonic contact pulse transmission for elastic wave velocity and stiffness determination: Influence of specimen geometry and porosity. *Engineering Structures*, 47:115–133, 2013.
- [83] C. Kohlhauser, C. Hellmich, C. Vitale-Brovarone, A. R. Boccaccini, A. Rota, and J. Eberhardsteiner. Ultrasonic Characterisation of Porous Biomaterials Across Different Frequencies. *Strain*, 45(1):34–44, 2009.
- [84] H. Kolsky. *Stress waves in solids*. Courier Dover Publications, 1963.
- [85] M. Königsberger, B. Pichler, and C. Hellmich. Micromechanics of ITZ–Aggregate Interaction in Concrete Part I: Stress Concentration. *Journal of the American Ceramic Society*, 97(2):535–542, 2014.
- [86] M. Königsberger, B. Pichler, and C. Hellmich. Micromechanics of ITZ–Aggregate Interaction in Concrete Part II: Strength Upscaling. *Journal of the American Ceramic Society*, 97(2):543–551, 2014.
- [87] M. Königsberger, M. Irfan-ul-Hassan, B. Pichler, and C. Hellmich. Downscaling-based identification of non-aging power-law creep of cement hydrates. *Journal of Engineering Mechanics*, 2016. In print.
- [88] S. Kosse. Festigkeit zementgebundener Materialien: numerische Simulation und experimentelle Durchführung einaxialer Druckversuche an Zementsteinen, Mörteln und Betonen; [Strength of cementitious materials: numerical simulation and experimental realization of uniaxial strength tests for cement pastes, mortars, and concretes], 2015. Bachelors Thesis, TU Wien – Vienna University of Technology. In German.
- [89] E. Kröner. Berechnung der elastischen Konstanten des Vielkristalls aus den Konstanten des Einkristalls [Computation of the elastic constants of a polycrystal based on the constants of the single crystal]. *Zeitschrift für Physik A Hadrons and Nuclei*, 151(4):504–518, 1958. In German.
- [90] H. Kupfer, H. Hilsdorf, and H. Rusch. Behavior of concrete under biaxial stresses. *Am Concrete Inst-J*, 66(8):656–666, 1969.
- [91] L. Lam, Y. Wong, and C. Poon. Degree of hydration and gel/space ratio of high-volume fly ash/cement systems. *Cement and Concrete Research*, 30(5):747–756, 2000.

-
- [92] C. Le Bellégo, J. Dubé, G. Pijaudier-Cabot, and B. Gérard. Calibration of nonlocal damage model from size effect tests. *European Journal of Mechanics, A/Solids*, 22(1):33–46, 2003.
- [93] C. Le Bellégo, B. Gérard, and G. Pijaudier-Cabot. Chemo-Mechanical Effects in Mortar Beams Subjected to Water Hydrolysis. *Journal of Engineering Mechanics*, 126(3):266–272, 2000.
- [94] B. Lothenbach, K. Scrivener, and R. D. Hooton. Supplementary cementitious materials. *Cement and Concrete Research*, 41(12):1244–1256, 2011.
- [95] K. Luczynski, T. Brynk, B. Ostrowska, W. Swieszkowski, R. Reihnsner, and C. Hellmich. Consistent quasistatic and acoustic elasticity determination of poly-l-lactide-based rapid-prototyped tissue engineering scaffolds. *Journal of Biomedical Materials Research Part A*, 101(1):138–144, 2013.
- [96] L. Maia, M. Azenha, R. Faria, and J. Figueiras. Influence of the cementitious paste composition on the e-modulus and heat of hydration evolutions. *Cement and Concrete Research*, 41(8):799–807, 2011.
- [97] L. Maia, M. Azenha, R. Faria, and J. Figueiras. Identification of the percolation threshold in cementitious pastes by monitoring the e-modulus evolution. *Cement and Concrete Composites*, 34(6):739–745, 2012.
- [98] A. Malandrino, A. Fritsch, O. Lahayne, K. Kropik, H. Redl, J. Noailly, D. Lacroix, and C. Hellmich. Anisotropic tissue elasticity in human lumbar vertebra, by means of a coupled ultrasound-micromechanics approach. *Materials Letters*, 78(0):154–158, 2012. 30th Anniversary Special Issue.
- [99] H. Mang and G. Hofstetter. *Festigkeitslehre [Strength of Materials]*. Springer-Verlag, Wien, New York, 2000. In German.
- [100] F. McClintock and J. Walsh. Friction of Griffith cracks in rock under pressure. In *Proc. Fourth U.S. National Congress of Applied Mechanics*, pages 1015–1021, New York City, 1962.
- [101] J.-M. Mechling, A. Lecomte, and C. Diliberto. Relation between cement composition and compressive strength of pure pastes. *Cement and Concrete Composites*, 31(4):255–262, 2009.

- [102] H. Mihashi and N. Nomura. Correlation between characteristics of fracture process zone and tension-softening properties of concrete. *Nuclear Engineering and Design*, 165(3):359–376, 1996.
- [103] O. Mohr. Welche Umstände bedingen die Elastizitätsgrenze und den Bruch eines Materials [What reasons cause the elastic limit and the failure of a material]. *Zeitschrift des Vereins Deutscher Ingenieure*, 46(1524-1530):1572–1577, 1900. In German.
- [104] P. J. Monteiro and C. Chang. The elastic moduli of calcium hydroxide. *Cement and Concrete Research*, 25(8):1605–1609, 1995.
- [105] T. Mori and K. Tanaka. Average stress in matrix and average elastic energy of materials with misfitting inclusions. *Acta Metallurgica*, 21(5):571–574, 1973.
- [106] A. C. A. Muller, K. L. Scrivener, A. M. Gajewicz, and P. J. McDonald. Densification of c–s–h measured by 1h nmr relaxometry. *The Journal of Physical Chemistry C*, 117(1):403–412, 2013.
- [107] T. Mura. *Micromechanics of defects in solids*. Mechanics of elastic and inelastic solids. Kluwer Academic Publishers, 1998.
- [108] A. M. Neville. *Properties of Concrete*. John Wiley & Sons, Inc., 1997.
- [109] V. Nežerka and J. Zeman. A micromechanics-based model for stiffness and strength estimation of cocciopesto mortars. *Acta Polytechnica*, 52(6):29–37, 2012.
- [110] B. Newman and B. S. Choo. *Advanced concrete technology*. Elsevier Butterworth-Heinemann, 2003.
- [111] J. Němeček, V. Králík, V. Šmilauer, L. Polívka, and A. Jäger. Tensile strength of hydrated cement paste phases assessed by micro-bending tests and nanoindentation. *Cement and Concrete Composites*, 2015. , *submitted*.
- [112] J. Němeček, V. Šmilauer, and L. Kopecký. Nanoindentation characteristics of alkali-activated aluminosilicate materials. *Cement and Concrete Composites*, 33(2):163–170, 2011.
- [113] J. S. of Civil Engineers (JSCE). Standard specifications for concrete structures, 2010.

- [114] I. Pane and W. Hansen. Investigation of blended cement hydration by isothermal calorimetry and thermal analysis. *Cement and Concrete Research*, 35(6):1155–1164, 2005.
- [115] B. Patzák et al. Object Oriented Finite Element Method - OOFEM. <http://www.oofem.org>, since 1993.
- [116] R. J.-M. Pellenq, A. Kushima, R. Shahsavari, K. J. Van Vliet, M. J. Buehler, S. Yip, and F.-J. Ulm. A realistic molecular model of cement hydrates. *Proceedings of the National Academy of Sciences*, 106(38):16102–16107, 2009.
- [117] R. J.-M. Pellenq and H. Van Damme. Why Does Concrete Set?: The Nature of Cohesion Forces in Hardened Cement-Based Materials. *MRS Bulletin*, 29:319–323, 2004.
- [118] V. Pensée, D. Kondo, and L. Dormieux. Micromechanical Analysis of Anisotropic Damage in Brittle Materials. *Journal of Engineering Mechanics*, 128(8):889–897, 2002.
- [119] B. Pichler and C. Hellmich. Upscaling quasi-brittle strength of cement paste and mortar: A multi-scale engineering mechanics model. *Cement and Concrete Research*, 41(5):467–476, 2011.
- [120] B. Pichler, C. Hellmich, and J. Eberhardsteiner. Spherical and acicular representation of hydrates in a micromechanical model for cement paste – prediction of early-age elasticity and strength. *Acta Mechanica*, 203(3-4):137–162, 2009.
- [121] B. Pichler, C. Hellmich, J. Eberhardsteiner, J. Wasserbauer, P. Termkhajornkit, R. Barbarulo, and G. Chanvillard. The counteracting effects of capillary porosity and of unhydrated clinker grains on the macroscopic strength of hydrating cement paste—a multiscale model. In *Mechanics and Physics of Creep, Shrinkage, and Durability of Concrete: A Tribute to Zdenek P. Bazant – Proceedings of the 9th Int. Conf. on Creep, Shrinkage, and Durability Mechanics, CONCREEP 2013*, pages 40–47, 2013.
- [122] B. Pichler, C. Hellmich, J. Eberhardsteiner, J. Wasserbauer, P. Termkhajornkit, R. Barbarulo, and G. Chanvillard. Effect of gel–space ratio and microstructure on strength of hydrating cementitious materials: An engineering micromechanics approach. *Cement and Concrete Research*, 45(0):55–68, 2013.

- [123] B. Pichler, C. Hellmich, J. Eberhardsteiner, J. Wasserbauer, P. Termkhajornkit, R. Barbarulo, and G. Chanvillard. The Counteracting Effects of Capillary Porosity and of Unhydrated Clinker Grains on the Macroscopic Strength of Hydrating Cement Paste—A Multiscale Model. In *Mechanics and Physics of Creep, Shrinkage, and Durability of Concrete: A Tribute to Zdeněk P. Bažant*, pages 40–47. ASCE, 2013.
- [124] B. Pichler, C. Hellmich, and H. A. Mang. A combined fracture-micromechanics model for tensile strain-softening in brittle materials, based on propagation of interacting microcracks. *International Journal for Numerical and Analytical Methods in Geomechanics*, 31(2):111–132, 2007.
- [125] B. Pichler, S. Schneider, and C. Hellmich. From micron-sized needle-shaped hydrates to meter-sized shotcrete tunnel shells: micromechanical upscaling of stiffness and strength of hydrating shotcrete. *Acta Geotechnica*, 3(4):273–294, 2008.
- [126] K. Popper. *Logik der Forschung [Logic of scientific discovery]*. Springer, Wien, Austria, 1934. In German.
- [127] T. Powers and T. Brownyard. Studies of the physical properties of hardened portland cement paste. *Research Laboratories of the Portland Cement Association Bulletin*, 22:101–992, 1948.
- [128] T. C. Powers. Structure and physical properties of hardened Portland cement paste. *J. Am. Ceram. Soc.*, 41(1):1–6, 1958.
- [129] V. Presser, K. Gerlach, A. Vohrer, K. Nickel, and W. Dreher. Determination of the elastic modulus of highly porous samples by nanoindentation: a case study on sea urchin spines. *Journal of Materials Science*, 45(9):2408–2418, 2010.
- [130] A. Princigallo, P. Lura, K. van Breugel, and G. Levita. Early development of properties in a cement paste: A numerical and experimental study. 33(7):1013–1020, 2003.
- [131] I. Richardson. The nature of the hydration products in hardened cement pastes. *Cement and Concrete Composites*, 22(2):97–113, 2000.
- [132] I. Richardson. Tobermorite/jennite-and tobermorite/calcium hydroxide-based models for the structure of CSH: applicability to hardened pastes

- of tricalcium silicate, β -dicalcium silicate, Portland cement, and blends of Portland cement with blast-furnace slag, metakaolin, or silica fume. *Cement and Concrete Research*, 34(9):1733–1777, 2004.
- [133] P. Rossi, J.-L. Tailhan, F. Le Maou, L. Gaillet, and E. Martin. Basic creep behavior of concretes investigation of the physical mechanisms by using acoustic emission. *Cement and Concrete Research*, 42(1):61–73, 2012.
- [134] J. Rots, B. Belletti, and S. Invernizzi. Robust modeling of RC structures with an “event-by-event” strategy. *Engineering Fracture Mechanics*, 75(3-4):590–614, 2008.
- [135] M. Ruiz, A. Muttoni, and P. Gambarova. Relationship between non-linear creep and cracking of concrete under uniaxial compression. *Journal of Advanced Concrete Technology*, 5(3):383–393, 2007.
- [136] J. Salençon. *Handbook of continuum mechanics: general concepts, Thermoelasticity*. Springer Verlag, Berlin, Heidelberg, New York, 2001.
- [137] J. Sanahuja, L. Dormieux, and G. Chanvillard. Modelling elasticity of a hydrating cement paste. *Cement and Concrete Research*, 37(10):1427–1439, 2007.
- [138] E. Sarris and G. Constantinides. Finite element modeling of nanoindentation on C–S–H: Effect of pile-up and contact friction. *Cement and Concrete Composites*, 36:78–84, 2013.
- [139] S. Scheiner and C. Hellmich. Continuum microviscoelasticity model for aging basic creep of early-age concrete. *Journal of Engineering Mechanics (ASCE)*, 135(4):307–323, 2009.
- [140] G. Scherer, J. Zhang, J. Quintanilla, and S. Torquato. Hydration and percolation at the setting point. *Cement and Concrete Research*, 42(5):665–672, 2012.
- [141] G. W. Scherer. Structure and properties of gels. *Cement and Concrete Research*, 29(8):1149–1157, 1999.
- [142] K. L. Scrivener. Backscattered electron imaging of cementitious microstructures: understanding and quantification. *Cement and Concrete Composites*, 2004.

- [143] K. L. Scrivener, A. n. Crumbie, and P. Laugesen. The interfacial transition zone (ITZ) between cement paste and aggregate in concrete. *Interface Science*, 12(4):411–421, 2004.
- [144] S. Shah and R. Sankar. Internal cracking and strain softening response of concrete under uniaxial compression. *American Concrete Institute Materials Journal*, 84(3):200–212, 1987.
- [145] S. Shah and G. Winter. Inelastic behavior and fracture of concrete. *American Concrete Institute Journal Proceedings*, 63(9):925–930, 1966.
- [146] C. Shi, P. V. Krivenko, and D. Roy. *Alkali-activated cements and concretes*. Taylor & Francis, 2006.
- [147] S. Speziale, F. Jiang, Z. Mao, P. J. Monteiro, H.-R. Wenk, T. S. Duffy, and F. R. Schilling. Single-crystal elastic constants of natural ettringite. *Cement and Concrete Research*, 38(7):885–889, 2008.
- [148] L. Stefan, F. Benboudjema, J.-M. Torrenti, and B. Bissonnette. Prediction of elastic properties of cement pastes at early ages. *Computational Materials Science*, 47(3):775–784, 2010.
- [149] P. Suquet. *Continuum Micromechanics*, volume 377 of *CISM Courses and Lectures*. Springer Verlag, Wien New York, 1997.
- [150] J. Taplin. A method of following the hydration reaction in Portland cement paste. *Australian Journal of Applied Science*, 10(3):329–345, 1959.
- [151] H. F. W. Taylor. *Cement chemistry*. Thomas Telford Publishing, 2nd edition, 1997.
- [152] P. Termkhajornkit and R. Barbarulo. Modeling the coupled effects of temperature and fineness of Portland cement on the hydration kinetics in cement paste. *Cement and Concrete Research*, 42(3):526–538, 2012.
- [153] P. Termkhajornkit, Q. H. Vu, R. Barbarulo, S. Daronnat, and G. Chanvillard. Dependence of compressive strength on phase assemblage in cement pastes: Beyond gel–space ratio — Experimental evidence and micromechanical modeling. *Cement and Concrete Research*, 56(0):1–11, 2014.
- [154] The Cement Sustainability Initiative. 10 years of progress and moving on into the next decade, 2012.

- [155] J. Torrenti and F. Benboudjema. Mechanical threshold of cementitious materials at early age. *Materials and Structures/Materiaux et Constructions*, 38(277):299–304, 2005.
- [156] N. Trivedi, R. Singh, and J. Chattopadhyay. A comparative study on three approaches to investigate the size independent fracture energy of concrete. *Engineering Fracture Mechanics*, 138:49–62, 2015.
- [157] C. A. TU1404. Towards the next generation of standards for service life of cement-based materials and structures. <http://www.tu1404.eu>. Accessed: 2016-09-01.
- [158] M. I. ul Hassan, B. Pichler, R. Reihnsner, and C. Hellmich. Elastic and creep properties of young cement paste, as determined from hourly repeated minute-long quasi-static tests. *Cement and Concrete Research*, 82:36 – 49, 2016.
- [159] F.-J. Ulm and O. Coussy. Modeling of thermochemomechanical couplings of concrete at early ages. *Journal of Engineering Mechanics (ASCE)*, 121(7):785–794, 1995.
- [160] K. van Breugel. Numerical simulation of hydration and microstructural development in hardening cement-based materials. 25(2):319–331, 1995.
- [161] M. R. van Vliet and J. G. van Mier. Experimental investigation of size effect in concrete and sandstone under uniaxial tension. *Engineering Fracture Mechanics*, 65(2–3):165–188, 2000.
- [162] M. Vandamme. *The nanogranular origin of concrete creep: a nanoindentation investigation of microstructure and fundamental properties of calcium-silicate-hydrates*. PhD thesis, Massachusetts Institute of Technology, 2008.
- [163] K. Velez, S. Maximilien, D. Damidot, G. Fantozzi, and F. Sorrentino. Determination by nanoindentation of elastic modulus and hardness of pure constituents of Portland cement clinker. *Cement and Concrete Research*, 31(4):555–561, 2001.
- [164] N. Venkovic, L. Sorelli, B. Sudret, T. Yalamas, and R. Gagn. Uncertainty propagation of a multiscale poromechanics-hydration model for poroelastic properties of cement paste at early-age. *Probabilistic Engineering Mechanics*, 32:5–20, 2013.

- [165] G. J. Venta. Final Summary Report on the 3rd European Cement Conference. Technical report, Venta, Glaser & Associates, 2003.
- [166] J. Vorel, V. Šmilauer, and Z. Bittnar. Multiscale simulations of concrete mechanical tests. *Journal of Computational and Applied Mathematics*, 236(18):4882–4892, 2012.
- [167] V. Šmilauer. *Elastic properties of hydrating cement paste determined from hydration models*. Ph.D. Thesis, ČVUT in Prague, Faculty of Civil Engineering, 2006.
- [168] V. Šmilauer and Z. P. Bažant. Identification of viscoelastic C-S-H behavior in mature cement paste by FFT-based homogenization method. 40(2):197–207, 2010.
- [169] V. Šmilauer and Z. Bittnar. Microstructure-based micromechanical prediction of elastic properties in hydrating cement paste. 36(9):1708–1718, 2006.
- [170] V. Šmilauer, P. Hlaváček, and P. Padevět. Micromechanical Analysis of Cement Paste with Carbon Nanotubes. *Acta Polytechnica*, 52:35–41, 1998.
- [171] V. Šmilauer, P. Hlaváček, F. Škvára, R. Šulc, L. Kopecký, and J. Němeček. Micromechanical multiscale model for alkali activation of fly ash and metakaolin. *Journal of Materials Science*, 46(20):6545–6555, 2011.
- [172] Y. Wang, G. Ye, and K. van Breugel. Microstructure of cement paste blended with micronized sand (MS). In *Durability of Building Materials and Components*, pages 61–84. Springer, 2013.
- [173] W. Weibull. A statistical distribution function of wide applicability. *Journal of Applied Mechanics*, pages 293–297, 1951.
- [174] F. H. Wittmann. Crack formation and fracture energy of normal and high strength concrete. *Sadhana*, 27(4):413–423, 2002.
- [175] M. Wyrzykowski and P. Lura. Controlling the coefficient of thermal expansion of cementitious materials—A new application for superabsorbent polymers. *Cement and Concrete Composites*, 35(1):49–58, 2013.

-
- [176] G. Ye, X. Liu, G. De Schutter, A.-M. Poppe, and L. Taerwe. Influence of limestone powder used as filler in scc on hydration and microstructure of cement pastes. *Cement and Concrete Composites*, 29(2):94–102, 2007.
- [177] Z. P. Bažant. Can multiscale-multiphysics methods predict softening damage and structural failure? *International Journal for Multiscale Computational Engineering*, 8(1):61–67, 2010.
- [178] V. Zadeh and C. Bobko. Nanoscale mechanical properties of concrete containing blast furnace slag and fly ash before and after thermal damage. *Cement and Concrete Composites*, 37:215–221, 2013.
- [179] A. Zaoui. *Matériaux hétérogènes et composites [Heterogeneous materials and composites]*. Lecture Notes. Ecole Polytechnique, Paris, France, 1997. In French.
- [180] A. Zaoui. Continuum Micromechanics: Survey. *Journal of Engineering Mechanics*, 128(8):808–816, 8 2002.
- [181] B. Zech and F. H. Wittmann. A complex study on the reliability assessment of the containment of a PWR, Part II Probabilistic approach to describe the behaviour of materials. *Nuclear Engineering and Design*, 48(2-3):575–584, 1978.